



Ali Sobhani, Soroush (2020) *State-of-the-art InAs/GaAs quantum dot material for optical telecommunication*. PhD thesis.

.

<https://theses.gla.ac.uk/81398/>

Copyright and moral rights for this work are retained by the author

A copy can be downloaded for personal non-commercial research or study, without prior permission or charge

This work cannot be reproduced or quoted extensively from without first obtaining permission in writing from the author

The content must not be changed in any way or sold commercially in any format or medium without the formal permission of the author

When referring to this work, full bibliographic details including the author, title, awarding institution and date of the thesis must be given

Enlighten: Theses

<https://theses.gla.ac.uk/>
research-enlighten@glasgow.ac.uk

State-of-the-art InAs/GaAs Quantum Dot Material for Optical Telecommunication

Soroush Ali Sobhani



December 2019

A Thesis Submitted to the Division of Electronic and
Nanoscale of the James Watt School of Engineering

The University of Glasgow

In Fulfilment of the Requirements for The Degree of
Doctor of Philosophy (Ph.D.)

Abstract

This thesis reports on the characterization of the state-of-the-art In(Ga)As/GaAs quantum dot (QD) material grown by molecular beam epitaxy for optical telecommunication applications. A wide variety of characterization methods are employed to investigate the material properties and characteristics of a number of QD-based devices enabling future device optimization.

The motivation that prompted this study was predicated mainly upon two technological advantages. First, that the QDs gain spectra exhibits a symmetric gain shape, owing to their delta-function-like density of states, and thus the change of refractive index with respect to gain is negligible at the lasing wavelength. This is therefore expected to result in a zero or a very small linewidth enhancement factor (LEF), which is desirable for instance, for high-speed modulation purposes where frequency chirp under modulation, which is directly proportional to the LEF, may be substantially reduced.

Second, not only QDs exhibit a damped frequency response attributed to the carrier relaxation dynamics, but also the resilience of a laser to optical feedback is inversely proportional to the fourth power of the LEF. As such, QD lasers are expected to demonstrate a relatively higher feedback insensitivity. This bodes well for operating these devices isolator free, which would be greatly cost-effective.

The absorption and gain spectra of the QD active material are investigated in chapters 2 and 3, respectively. The LEF of QD lasers at a range of temperatures is studied in chapter 3, which confirms the expectation for the first time for In(Ga)As/GaAs QD lasers from $-10\text{ }^{\circ}\text{C}$ to $85\text{ }^{\circ}\text{C}$. Subsequently, the findings of chapters 2 and 3 are employed in chapter 4 with an electro absorption modulator device in mind which would be able to operate with chirp control.

In chapter 5, the modulation response of QD lasers is investigated through examining the relative intensity noise (RIN) spectra in the electrical domain. Subsequently, the resilience of the devices to external optical feedback is studied through the RIN characteristics at a range of temperatures in the context of compliance under deployment specific feedback levels.

Chapter 6 provides a summary of the thesis findings and possible future works that may be carried out as continuation to this project, which fell outside of the remit of this work.

Acknowledgements

To both of my life-couches, my late grandfathers, baba Sobhani and baba Jee: because I owe it all to you. Thank you!

A very special appreciation goes out to Professor Richard A. Hogg for providing the funding for this work and for being a fantastic supervisor and a friend throughout this process.

My gratitude also goes to Dr. David T.D. Childs, Dr. Nasser Babazadeh, Dr. Ben J. Stevens, and Professor Sorel for their input, guidance, and support.

I am grateful for the hard work and support of the staff at the III-V national center in Sheffield and the James Watt nanofabrication center here in Glasgow.

To Dr. Keizo Takemasa, Dr. Mitsuru Sugawara, and particularly Dr. Kenichi Nishi, the team at the QD Laser Inc. in Japan, it has been a privilege working with you. Thank you for your scientific support and advice.

I gratefully acknowledge the support of all my friends. Thank you: Dominic, Negin, Joshua, Aziz, Mert, Pavlo, Hannah, Simon, Kris, Ken, Jennie, Sarah, Graham, Francesco, Kseniya, Justin, Razvan, Affe, Richard, Lourdes, Lauren, Omar, Ellie, Armin, Tim, Mila, Kristof, and Ozaki-san.

A very particular gratitude goes out to my family back in Iran for the sublime support they have given me all my life and during my Ph.D.

The work carried-out in this thesis would not have been possible without the help and support from all of the above.

Publications

S. A. Sobhani, B. J. Stevens, N. Babazadeh, K. Takemasa, K. Nishi, M. Sugawara, R. A. Hogg, and D. T. D. Childs "Proposal for Common Active 1.3- μ m Quantum Dot Electroabsorption Modulated DFB Laser," IEEE Photon. Tech. Lett., Vol. 31, No. 6, pp. 419-422, Mar. 2019

<https://doi.org/10.1109/LPT.2018.2890641>,
<http://adsabs.harvard.edu/abs/2019IPTL...31..419S>

S. A. Sobhani, D.T.D. Childs, N. Babazadeh, B.J. Stevens, K. Nishi, M. Suguwara, K. Takemasa, and R.A. Hogg, "Study of electro-absorption effects in 1300nm In(Ga)As/GaAs quantum dot materials," Proc. SPIE 9742, Physics and Simulation of Optoelectronic Devices XXIV, Edited by B. Witzigmann, M. Osinski, and Y. Arakawa, Mar 2016

<https://dx.doi.org/10.1117/12.2213187> ,
<http://adsabs.harvard.edu/abs/2016SPIE.9742E..0SS>

I. M. E. Butler, W. Li, S. A. Sobhani, N. Babazadeh, I. M. Ross, K. Nishi, K. Takemasa, M. Sugawara, D. T. D. Childs, and R. A. Hogg, "Size anisotropy inhomogeneity effects in state-of-the-art quantum dot lasers," App. Phys. Lett., Vol. 113, 012105, Jul. 2018

<https://doi.org/10.1063/1.5021774> ,
<http://adsabs.harvard.edu/abs/2018ApPhL.113a2105B>

I. M. E. Butler, W. Li, S. A. Sobhani, N. Babazadeh, I. M. Ross, K. Nishi, K. Takemasa, M. Sugawara, N. Peyvast, D. T. D. Childs, and R. A. Hogg "Incorporating structural analysis in a quantum dot Monte-Carlo model", Proc. SPIE 10553, Novel In-Plane Semiconductor Lasers XVII, 105530G, Feb. 2018

<https://doi.org/10.1117/12.2291004>

I. M. E. Butler, W. Li, S. A. Sobhani, N. Babazadeh, I. M. Ross, K. Nishi, K. Takemasa, M. Sugawara, D. T. D. Childs, and R. A. Hogg, "Object orientated Monte-Carlo model incorporating quantum dot size anisotropy effects in state-of-the-art quantum dot lasers," in JSAP-OSA Joint Symposia, paper 21p_211B_6, 2018

https://www.osapublishing.org/abstract.cfm?uri=JSAP-2018-21p_211B_6

Conferences

S. A. Sobhani, D.T.D. Childs, K. Nishi, K. Takemasa, M. Sugawara, and R.A. Hogg, "Temperature-insensitive zero linewidth enhancement factor in state-of-the-art In(Ga)As/GaAs quantum-dot lasers", Physics and Simulation of Optoelectronic Devices XXVI, 1052602, SPIE Photonics West - San Francisco, 2018

S.A. Sobhani, D.T. Childs, N. Babazadeh, B.J. Stevens, K. Nishi, M. Suguwara, K. Takemasa, and R.A. Hogg, "Investigation of the quantum confined stark effect in 1300nm In(Ga)As/GaAs quantum dot materials", UK Semiconductors 2017

S.A. Sobhani, D.T. Childs, N. Babazadeh, B.J. Stevens, K. Nishi, M. Suguwara, K. Takemasa, and R.A. Hogg, "Study of electro-absorption effects in 1300nm In(Ga)As/GaAs quantum dot materials," Physics and Simulation of Optoelectronic Devices XXVI, SPIE Photonics West - San Francisco, 2016

Contents

Chapter 1

Introduction	1
1.1 Historical context	1
1.2 P-n junctions and heterostructures	6
1.3 Lattice matching and 1.3 μm lasing	8
1.4 Optical transitions in semiconductors	12
1.5 Lasing	14
1.6 Quantum dot rate equation model	16
1.7 Quantum confined structures and density of states	18
1.8 Inhomogeneous broadening in quantum dots	20
1.9 QDs for optical telecommunication	22
1.10 Thesis outline	23
References	27

Chapter 2

Study of Electro-absorption Effects	32
2.1 Introduction	32
2.2 Background and motivation	33
2.3 Gaps in knowledge	34
2.4 Modulation	36
2.5 Photodetection	39
2.6 Photocurrent process	40
2.6.1 Experimental set-up	42
2.7 Results	43
2.8 Application – electro absorption modulator (EAM)	53
2.9 Application - avalanche photodetector (APD)	55
2.10 Discussion	57
2.11 Conclusion	59
2.12 Future work	59
References	62

Chapter 3

Temperature-insensitive Zero Linewidth Enhancement Factor	69
3.1 Introduction	69
3.2 Background and motivation	71

3.3	Gaps in knowledge.....	76
3.4	Experimental techniques for the measurement of LEF	79
3.5	Measurement of LEF	82
3.5.1	Devices.....	83
3.5.2	Hakki-Paoli gain measurement.....	84
3.5.3	H-P gain measurement considerations	86
3.5.4	Differential gain (dg/dI).....	87
3.5.5	Spontaneous emission	87
3.5.6	Measurement issues.....	87
3.5.6.1	Correcting for thermal effects	88
3.6	Experimental Results	90
3.6.1	L-I-V measurement	90
3.6.2	Differential output power	91
3.6.3	Characteristic temperature T_0	92
3.6.4	External differential quantum efficiency (η_d)	94
3.6.5	Lasing spectra	95
3.6.6	RMS linewidth	96
3.6.7	Maintaining a constant junction-temperature	98
3.6.8	Temperature-dependent gain spectra	100
3.6.9	Comparison of material gain and differential gain spectra	105
3.6.10	Mode shift correction	105
3.6.11	LEF results	108
3.6.12	Accuracy of measurement	110
3.7	Discussion.....	111
3.8	Conclusion	113
3.9	Future work	114
	References.....	116

Chapter 4

	Proposal for a Common Active Layer In(Ga)As Quantum Dot Electroabsorption Modulated DFB Laser at 1.3-μm	126
4.1	Introduction.....	126
4.1.2	Extinction ratio and insertion loss	128
4.2	Background and motivation.....	129
4.3	Gaps in knowledge.....	130
4.4	Proposed device.....	133
4.5	Results and analysis	133
4.5	Conclusion	141
4.6	Future work	142
	References.....	144

Chapter 5

	Relative Intensity Noise: Temperature-Dependent Study of Modulation and External Optical Feedback.....	148
5.1	Introduction.....	148

5.2	Background and motivation.....	153
5.3	Gaps in knowledge.....	157
5.4	Measurement of RIN	159
5.4.1	Limitations of RIN measurement.....	162
5.4.1.1	Laser noise	163
5.4.1.2	Shot noise	163
5.4.1.3	Thermal noise	163
5.4.1.4	Mode partition noise.....	165
5.5	Measurement methods	165
5.5.1	Subtraction method.....	166
5.5.2	Quantum noise calibration method.....	168
5.5.3	Low noise reference laser calibration method	169
5.5.4	RIN under external optical feedback.....	169
5.6	Results	172
5.6.1	Free-running RIN.....	173
5.6.2	RIN under external optical feedback.....	187
5.7	Discussion	198
5.8	Conclusions.....	200
5.9	Future work	201
	References.....	203
Chapter 6		
	Summary and Future Work.....	209
6.1	Summary.....	209
6.2	Future works.....	212
	References.....	216
Appendix		
A.1	Laser Theory.....	218
A.1.1	Steady-state solutions.....	220
A.1.2	Differential investigation of rate equations.....	220
A.1.3	Small-signal modulation.....	222
A.1.4	Equivalent circuit for SSM	225
	References.....	227
B.1	Hakki - Paoli Gain and More (Data Analysis) – Matlab Code	229

Chapter 1

Introduction

1.1 Historical context

The initial idea for a laser was put forth by Einstein considering emission from a ‘Planck resonator’ in 1917 [1]. However, the world had to wait until 1960 to witness this in practice. Javan *et. al.* invented one of the most practical and widely used types of lasers, the gas discharge laser, having published his initial idea a year earlier [2]. This was done utilizing an electrically pumped He-Ne gas mixture emitting in the infrared region of the spectrum at the Bell Laboratories, Murray Hill – New Jersey in 1960 [3]. Most notably they were the first to demonstrate continuous wave operation, i.e. a continuous beam of light. The next day, they used the light to place a phone call. It was the first time that a laser beam had been used to transmit a telephone conversation [4]. Two years after that, Hall *et. al.* demonstrated the first semiconductor-based laser diode [5]. The laser was a $\sim 400 \mu\text{m}$ cube of GaAs which had ohmic contacts formed on the top and the bottom creating a p-n junction within it. Lasing was achieved with the device immersed in liquid nitrogen, with a threshold current density of $\sim 20 \text{ kA/cm}^2$. In the same year, an internal quantum efficiency, i.e. conversion of electron-hole pairs into photons, of close to unity was demonstrated in a GaAs-based laser [6] and research efforts went into developing semiconductor growth procedures fundamentally for the purposes of realizing structures with lower threshold currents and high temperature operation. The use of semiconductors started to be investigated as a lasing medium attributed to their small size, manufacturability, operation reliability, and the ability to be electrically pumped.

The early bulk semiconductor lasers were comprised of a GaAs homojunction p-n junction whereby gain was provided by carrier recombination in the depletion region, waveguiding was provided by a small change in refractive index in the cladding from doping, and the optical

feedback was provided by cleaving facets at either end of the cavity. Initial semiconductor lasers operated with very high threshold current densities attributed to the poor carrier and photon confinement due to the immaturity of the technology.

The introduction of the double heterostructure laser, where the p and n materials were the same but the intrinsic region was of a different material reduced the threshold current densities considerably. By using a lower refractive index and lattice matched material above and below the active region (cladding) as a waveguide, the optical mode was confined more to the active region. Secondly, using cladding material with a higher band gap than the intrinsic region concentrated the carriers in the active region and reduced absorption in the cladding.

In 1970, Hayashi *et. al.* achieved room temperature continuous wave lasing operation of a GaAs/AlGaAs double heterostructure laser [7]. The double heterostructure essentially consisted of a sandwich of GaAs between AlGaAs with one slice of the AlGaAs being p-doped and the other n-doped. Along with intrinsic GaAs in the middle to form a p-i-n structure which allows for more efficient electrical injection of carriers, confines those carriers injected to the GaAs region (due to the larger bandgap of AlGaAs), and provides index guiding for the optical mode simultaneously.

The next breakthrough came in 1974 when Dingle and Henry showed [8] that a step-like characteristic of the density of states can be obtained by shifting from free-electron-moving bulk semiconductor systems to thin films. Quantum confinement shows that if the size of one of the spatial dimensions is reduced (going from bulk to thin film) to the order of ~ 10 nm (see section 1.7) then in that dimension the electrons freedom reduces to a series of confined quantized states. Consequently, the degree of freedom of an electron in its associated band reduces from 3 degrees of freedom (bulk) to 2 (thin film or quantum well (QW)) with the third dimension having a series of confined energy states. In other words, the density of electrons in a state transforms from an increase as a function of $(\text{carrier energy})^{1/2}$ for bulk materials, to a step like increase in the density of states as a function of carrier energy for a QW.

Arakawa and Sakakai carried this notion further by hypothesizing that materials with complete carrier confinement in all three spatial dimensions would exhibit a lasing threshold current density that is insensitive to temperature [9]. In 1982 they modelled the threshold current density of a laser as a function of temperature for devices with increasing carrier quantization

from 3-D to 0-D confinement. The result is shown in fig. 1.1 and exhibits a considerable improvement in the characteristic temperature, T_0 , which is a measure of the sensitivity of threshold current density to temperature, with the degree of quantization. This improvement was suggested to be attributed to increasing carrier confinement leading to a reduction in thermalization of carriers as confinement energy became $> K_B T$. To validate the model a dual heterostructure bulk laser was subjected to a 30 T magnetic field introducing confinement within the bulk plane thereby going from 3 to 2 degrees of freedom. The experimental increase in T_0 going from 3D to 2D matched that of the model and opened the doors for the prospects of an infinite T_0 in a 0D or a quantum dot (QD) laser.

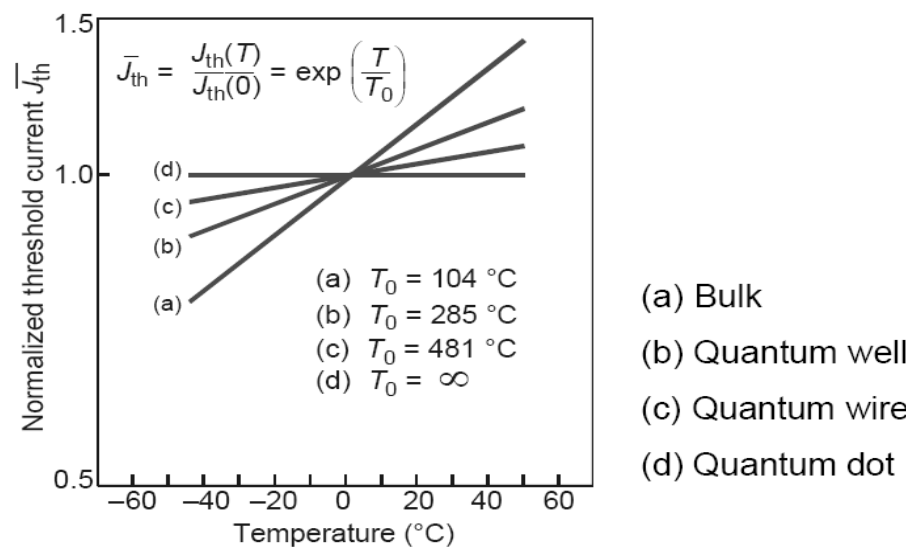


Figure 1.1: Predicted T_0 Improvement with quantization from ref [9].

Asada et al. [10] showed in 1986 that quantum ‘box’ lasers, based on lattice-matched growth and etching to a zero-dimensional state, had the prospects of exhibiting higher gain and lower threshold current densities than less confined semiconductor systems. These two properties are essential for low cost devices for the telecoms and other similar high specification markets. However, progress on perfecting the quantum box laser was slow. Etching the material into boxes small enough to be quantized proved difficult, resulting in a low number of boxes and boxes that were not very uniform in shape due to the lithographic step and etchants used.

Figure 1.2 plots the calculated modal gain as a function of current density for different systems in terms of the material’s carrier confinement [10]. It can be seen that the lowest threshold

current density and the highest material gain is achieved in the Box (QD) material system which is ascribed to its highest degree of carrier confinement.

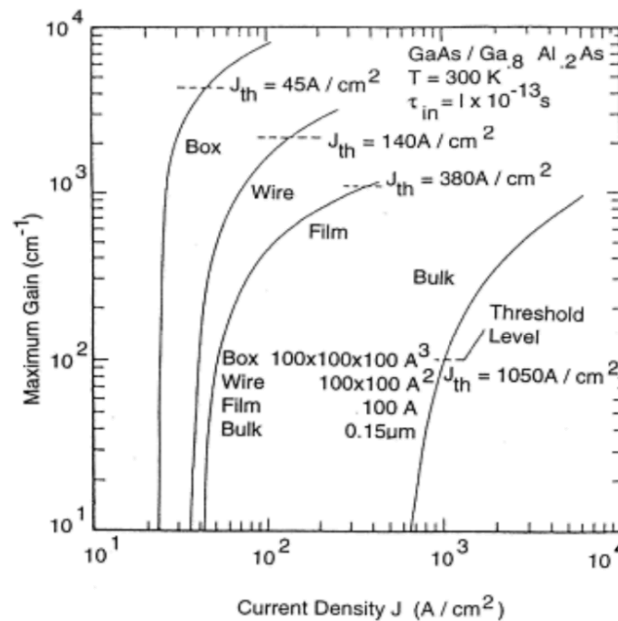


Figure 1.2: Calculated gain as a function of current density for different systems [10]

The next major phase was initiated by Kirstaedter *et al.* [11] in 1994. By growing lattice-mismatched In_xGa_{1-x}As layers of different proportions, zero-dimensional QDs were formed. Mismatching the lattice strains forced the layers to relax, which created dot islands, as the relaxed material energy was lowest in this form. Not in relation to QD lasers, however, the groundworks for this idea were laid in 1937 when Stranski and Krastanow (S-K) grew dot islands on a heteroepitaxial surface [12]. Also, it is noteworthy that InAs islands were grown on a GaAs substrate with a 7% lattice mismatch reported in 1985 by Goldstein [13], again not in relation to QD lasers but laying the groundworks.

The addition of InGaAs reduces the bandgap primarily and adds more strain to GaAs QW lasers thereby increasing the lasing wavelength beyond the unstrained GaAs wavelength to 980 nm. Nevertheless, GaAs/InGaAs lasers were unable to reach 1.3 μm attributed to the strain limit found to be at ~ 1.1 μm after which defects develop extensively precipitating failure to lase. InP-based QW lasers are used for 1.3 μm lasing in that InP needs very little change in lattice constant (<< 0.1 Å) to reach the telecoms wavelength of 1.3 μm compared to ~ 0.2 Å for InGaAs/GaAs, as (discussed in lattice matching section - shown in fig. 1.5. Not only InP has

smaller band offsets compared to InGaAs/GaAs which will ultimately result in a lower T_0 , it is also quite a fragile and comparatively difficult material to work with. Consequently, there is continual research on producing high quality In(Ga)As/GaAs QD lasers since they reach 1.3 μm and beyond. GaAs is also a much stronger material so devices can be grown on larger wafers, and it is expected to exhibit a much higher T_0 due to the higher band offset. Though physicists might argue that 6-inch GaAs wafers exist due to the electronics influence.

InGaAs QDs formation on GaAs was demonstrated in 1994 [14] emitting at 1.3 μm . Successively, in 1998 a method of consistently growing dots on GaAs by MBE emitting at 1.3 μm was provided [15].

The next major development was by Lester *et. al.* [16] in 1999, producing the first Dot-in-Well laser (DWELL), which was comprised of placing InAs dots in a quantum well. The advantage of this method was to increase the carrier capturing ability of the dot by confining the carriers in the well and thus acted as a carrier reservoir for the dots. Without the well the electrons had a much lower probability of being captured by the dots and so introducing the DWELL reduced the threshold current. The DWELL also allowed for a better reservoir for In for dot formation when InGaAs was used to encompass the dots and form the QW. As such, the wavelength could be tailored more precisely.

Although the theoretical predictions point to the temperature insensitivity of QD lasers, such advancement were yet to be realized in practice. The aforementioned simulations by Arakawa anticipated an infinite T_0 . However, the finite confinement potential of the QDs and the smaller energy spread of the hole levels due to their higher effective mass precipitates carrier thermalization out of the ground state at lower temperatures than hypothesized. Consequently, the dots were nonetheless temperature sensitive.

Later-on in 2002 it was demonstrated that modulation p-doping the active layer of QD lasers can considerably increase the T_0 to 161K between 0 and 80 $^{\circ}\text{C}$. However, this came at the cost of a higher threshold current [17]. Moreover, a low threshold current density of 19A/cm² was realized in oxide-confined InGaAs/GaAs QD lasers [18]. Also, enhanced small-signal modulation bandwidth of 15GHz and a T_0 of 237k at 278K < T < 318K were reported in [19]. Furthermore, QD lasers optical gain was shown to be improved by increasing the QD density and stacking QD layers vertically. QD areal density in the order of 6¹⁰ cm⁻² was reported by

QD Laser Inc., Fujitsu Laboratories and the University of Tokyo in 2007 [20] working on self-assembling InAs QDs on GaAs substrates emitting at 1.3 μ m.

Retaining a higher T_0 removes the requirement for incorporation of a costly Peltier packaged device typically utilized for the laser to operate at a fixed temperature. This is alongside the associated complexity of the feedback isolation circuitry, which is used with InP-based QW lasers to inhibit external optical feedback into the laser. Feedback effects will be discussed in chapter 5. Threshold current increases with temperature which will negatively affect modulation speeds as higher currents will be required to maintain the 0 to 1 intensity change of e.g. ~1mW to 10mW. If not corrected, the signal to noise ratio reduces precipitating the eye diagram closure and a lower bit error ratio. Research currently focuses on increasing the T_0 as much as possible. The telecoms market not only necessitates wavelength stability but also a high modulation bandwidth. Study is ongoing to find out the maximum possible speed at which the lasers can be modulated and practical methods to increase this. Current InP QW lasers have been commercially used at 10 Gb/s and higher. In 2000 researchers [21] calculated a theoretical eye open pattern at 5 Gb/s followed in 2002 by [22] who calculated a theoretical maximum bandwidth of 30 GHz increasing to 60 GHz with a reduction of inhomogeneous linewidth broadening for a QD laser. Results in [23] showed a temperature insensitive 1.3 μ m In(Ga)As QD laser at 10 Gb/s.

Semiconductor QD lasers have theoretically been shown to be much better than bulk and QW lasers considering their higher material gain, higher T_0 , lower threshold current, smaller linewidth enhancement factor, smaller wavelength chirp, smaller intensity noise, and resilience to optical feedback. However, achieving these advantages has not been as streamlined practically and are the subjects of this thesis.

1.2 P-n junctions and heterostructures

In this thesis a range of semiconductor optoelectronic devices were investigated including mesa diode LEDs (light emitting diodes) and lasers. The principle of operation of these devices are rather alike irrespective of the device type as they incorporate a common active area.

The p-n junction is a fundamental operational building block in semiconductor devices [24]. P-doped semiconductor material is grown on top of an n-doped layer and both are electrically connected. In a p-n junction the excess of electrons on the n-side and the excess of holes on the p-side recombine in a region around the interface of the two doped materials. The recombination produces a depletion of excess carriers over a small region around the junction until the Fermi levels of the holes on the p side and electrons on the n side are in equilibrium. This equilibrium prevents further carrier flow by producing a potential barrier [25] as shown in fig. 1.3 a). The charge from the ionized donors and acceptors causes an E-field, which causes a drift of carriers in the opposite direction. The diffusion of carriers continues until the drift current balances the diffusion current, i.e. reaching thermal equilibrium as indicated by a constant Fermi energy.

As forward bias is applied the potential of the electron levels in the n side is reduced relative to the p side electron levels and electrons can flow if the applied bias is high enough to the lower potential barrier for electron escape. The same applies to holes. With a forward bias more than the built-in potential (voltage), carriers flow through the depletion region experiencing almost no resistance. Recombination of electrons and holes may then take place with this carrier flow in the depletion region as shown in fig. 1.3 b). In a direct band gap semiconductor e.g. InAs/GaA, the minimum of conduction band is coincident with the maximum of the valance band in the energy vs crystal momentum. Thus, electrons can transition to the lower state, without a change in momentum, and recombine radiatively with a hole at a wavelength determined by the energy difference of the conduction and valance bands known as the bandgap energy. This is the standard for p-n homojunctions.

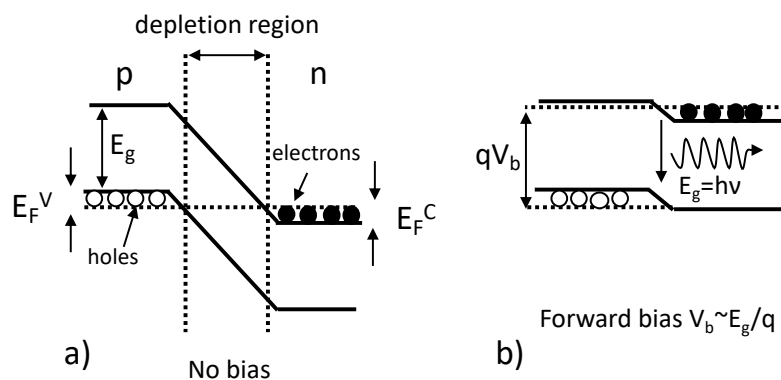


Figure 1.3: Band diagram of a p-n junction. (a) at zero bias, and (b) under forward bias $V_b \sim E_g/q$. The dotted lines illustrate the corresponding Fermi levels, which are aligned when $V_b = 0$. Electrons in the n-region recombine with holes in the p- region at the junction, emitting light at frequency ν .

The room temperature operation of laser devices, at an efficient current density level, requires simultaneous confinement of carriers and photons in the active region, a controllable recombination layer between the p and n sides, and mitigation of photon re-absorption after emission. To achieve these, hetero-structures were introduced [26]. A schematic of a double hetero structure with schematic of the relative refractive index and band gaps is provided in fig. 1.4. In a double hetero structure, an intrinsic layer of a lower band gap material (higher refractive index) is sandwiched between doped layers of higher band gap (lower refractive index). In this case the p and n layers are referred to as the cladding layers. Due to high refractive index and low band gap of the intrinsic material, photons and carriers are confined in this region. The increased refractive index confines photons to the intrinsic region, while due the lower bandgap side, photons emitted have a lower energy to be absorbed by the p and n cladding layers.

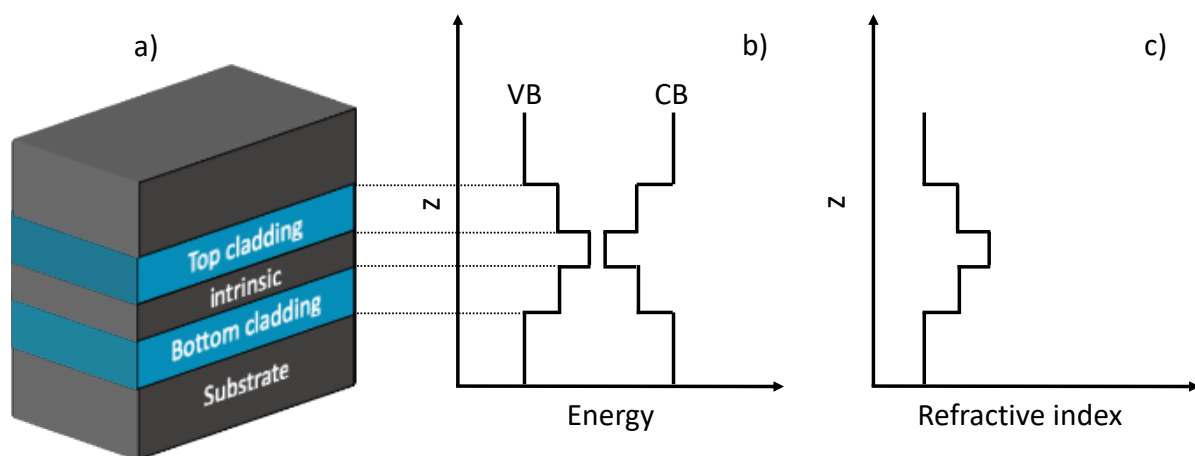


Figure 1.4: (a) schematic of a double hetero structure, (b) its band gap energy, and (c) its refractive index profile in the growth direction, z

The intrinsic layer is usually too thin to confine the light effectively. In order to solve this problem separate confinement heterostructures (SCH) were introduced by adding another two layers with a lower refractive index on the either side of the existing ones.

1.3 Lattice matching and 1.3 μm lasing

From figure 1.3 b), it can be seen that the bandgap of the material where recombination occurs determines the wavelength of the emitted light. This in conjunction with fig. 1.5, which shows

the bandgap of various important direct and indirect gap semiconductor materials and their lattice constants, means the choice of emission wavelength can be determined by the material used. By straining the semiconductor material with the addition of a third material to form a ternary alloy, the bandgap can be altered, although too much strain can cause relaxation in the crystal forming defects which can be detrimental to the system. For self-assembled QDs strain relaxation without defect formation is fundamental.

Figure 1.5 plots the band-gap energy of some of the most significant III–V semiconductors with respect to their lattice constant, wavelength is also indicated on the second vertical axis.

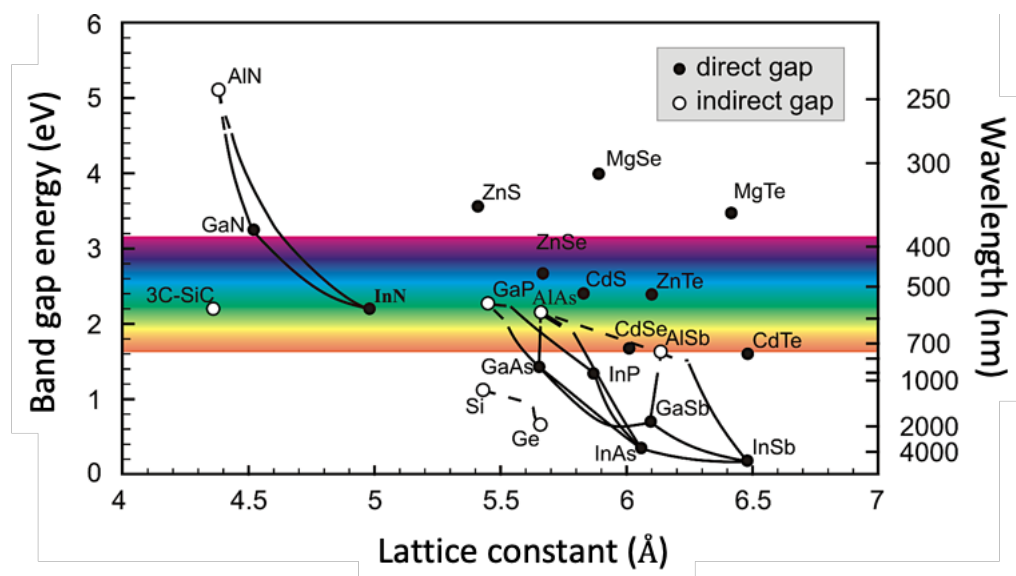


Figure 1.5: Bandgap energy and lattice constant for semiconductors at 300K [27].

Most devices for the red and near-infrared wavelength are grown on GaAs or InP substrates. For instance, an epitaxial layer of GaAs grown on a GaAs substrate would emit at 873 nm or 1.42 eV, due to their bandgap energy ($E=hc/\lambda$) as explained in section 1.2. This wavelength is acceptable for applications involving short-range transmission down optical fibers. However, for long distances we require emission at 1.3 μm or 1.55 μm , while for many other applications we require emission in the visible spectral region.

Optical fibers based on fused-silica (SiO_2) glass exhibit a number of resonant frequencies. Figure 1.6 shows the refractive index of SiO_2 with respect to frequency from the infrared to the X-ray spectral expanse. The general characteristics presented in fig. 1.6 are usual in optical

transparent materials. The transmission range of transparent materials is based on the electronic absorption in the ultraviolet and the lattice vibrational absorption in the infrared regions [28].

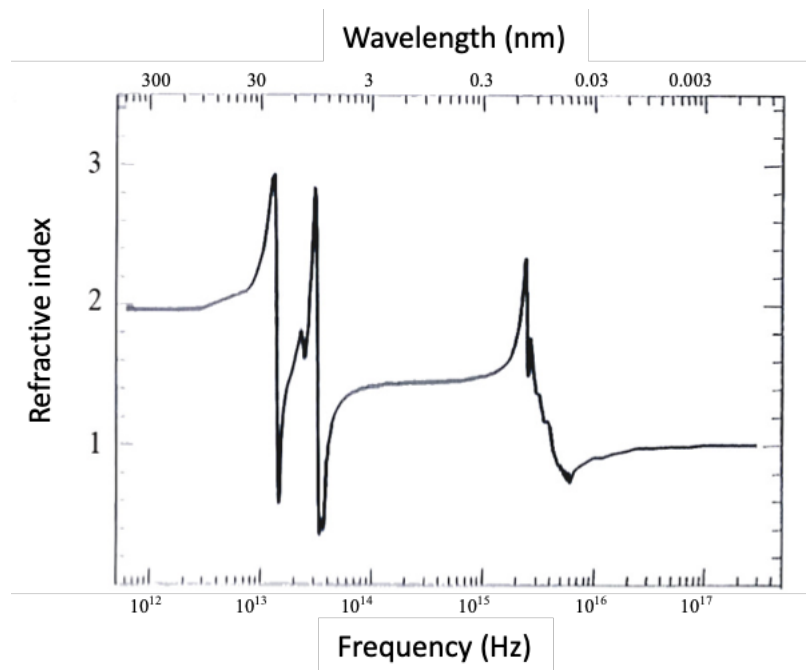


Figure 1.6: Real part of the refractive index as a function of photon energy for SiO₂ optical fiber [28.1].

Absorption of light around these resonant frequencies results in an increase in refractive index below the absorption frequency and a decrease in refractive index above the absorption frequency. Between the resonant peaks at 150 nm (2×10^{15} Hz) and 9.1 μ m (3.3×10^{13} Hz), from the high refractive index at wavelengths longer than 150nm, to low refractive index at wavelengths shorter than 9.1 μ m, the refractive index reduces with wavelength or increases with frequency. One of the consequences of this dispersion is that light with different frequencies takes a different amount of time to travel through a material. In order to satisfy the uncertainty principle $\Delta\nu\Delta t \sim 1$, a pulse of light of duration t_p must necessarily contain a spread of frequencies given approximately by [28]:

$$\Delta\nu \approx 1/t_p \quad 1.1$$

Dispersion will result in pulse broadening (in time) as it travels through the medium. This can become a stern problem for the transmission of very short pulses through a long length of a

standard single mode optical fiber, which is the case in high speed optical-fiber telecommunications systems.

In SiO₂ at the spectral wavelength range between the UV absorption tail (causing the refractive index to reduce) and the IR absorption tail (causing the refractive index to increase), these effects balance out so the change in refractive index is ~ 0 . This window occurs at 1.3 μm for SiO₂ fibers and the resultant zero dispersion is the reason for using lasers of this wavelength for telecoms applications. Although 1.3 μm is not at the lowest absorption minima (0.5dB/Km), which is 1.55 μm (0.2 dB/Km), it is importantly used for local area optical and enterprise optical network transmission, where pulse shaping is too expensive and distances are short enough not to require optical amplification.

Optical losses from a fiber are conveniently expressed through the fiber's attenuation coefficient in decibels per kilometer (dB/km). Correspondingly, the well-known fused silica glass fiber's attenuation coefficient is plotted in figure 1.7 with respect to wavelength.

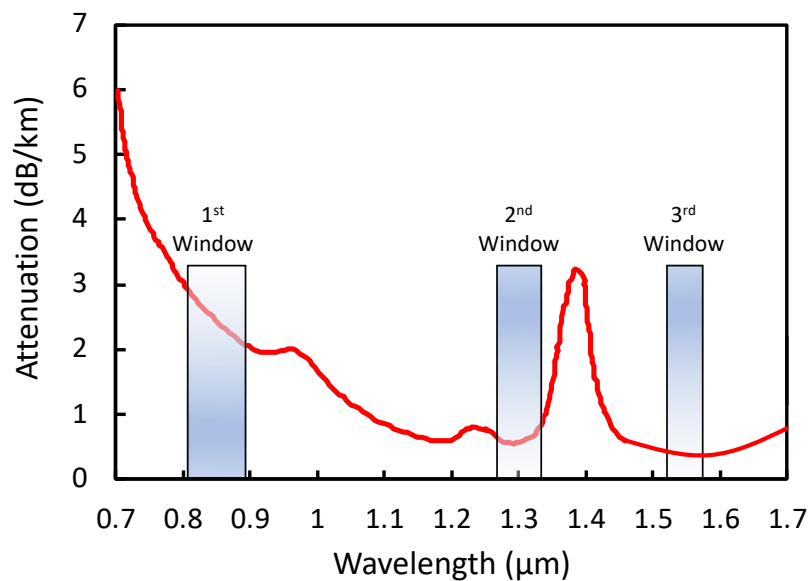


Figure 1.7: Attenuation spectrum of fused-silica as a function of wavelength [29]

The simplest case of epitaxial growth for emission is a layer of GaAs grown on a GaAs substrate, which emits at 873 nm. This wavelength is reasonable for applications involving short-range transmission down optical fibers. This falls under the first window illustrated in fig. 1.7 and is the first band used for fiber-optic communication in the 1970s and early 1980s.

It can still be utilized for low cost optical sources and detectors as far as telecommunication is concerned. However, for longer haul transmission and modulation purposes the second and the third windows are utilized. This is the band around 1310 nm which came into use in the mid 1980s. This band is more effective as there is zero dispersion (on single-mode fiber). While sources and detectors for this band are pricier than for the short-wave band, the attenuation is ~ 0.4 dB/km. The third window between about 1510 nm and 1600 nm has the lowest attenuation available on the current standard single mode optical fiber (~ 0.26 dB/km). It is more difficult thus more expensive, particularly for QDs, to make optical sources and detectors that operate in this region (quaternary InGaAsP QWs cover 1200-1600 nm). In addition, contrary to the 1300 nm window there is a finite amount of dispersion associated with this band.

1.4 Optical transitions in semiconductors

Imagine an isolated atom that can either exist in the state of lowest energy (ground state), with energy E_0 , or in a higher energy state (excited state), with energy E_x . There are 3 mechanisms by which the atom can move from one state to another, i.e. absorption, spontaneous, and stimulated emission

With respect to absorption, fig. 1.8 a) presents the atom originally in ground state. When the atom is put under an electric field which is alternating at frequency ν , the atom can absorb an amount of energy $h\nu$ from that field and move to the higher energy state. Due to the principle of conservation of energy we have $h\nu = E_x - E_0$. This process is called absorption.

As for spontaneous emission, in fig. 1.8 b) the atom is initially in excited state with no external radiation around. After a finite amount of time, the atom will drop on its own accord to its ground state, whereby it will emit a photon of energy $h\nu$. This is called spontaneous emission, spontaneous since the incident was not caused by any external influence. Normally, the mean life of excited atoms before spontaneous emission occurs is about 10^{-8} s. However, for some excited states, this mean life is perhaps as much as 10^5 times longer. We call such long-lived states metastable; they play an important role in laser operation.

As far as stimulated emission is concerned, fig. 1.8 c) presents the atom in excited state. In this instance, radiation with a frequency given by $h\nu = E_x - E_0$ is provided. A photon of energy $h\nu$

can stimulate the atom to relax to its ground state, during which process the atom emits an additional photon, whose energy is also $h\nu$. This is called stimulated emission. Stimulated since the incident was caused by an external photon. The emitted photon has identical quantum properties to the stimulating photon i.e. the same energy, phase, polarization, and direction of travel.

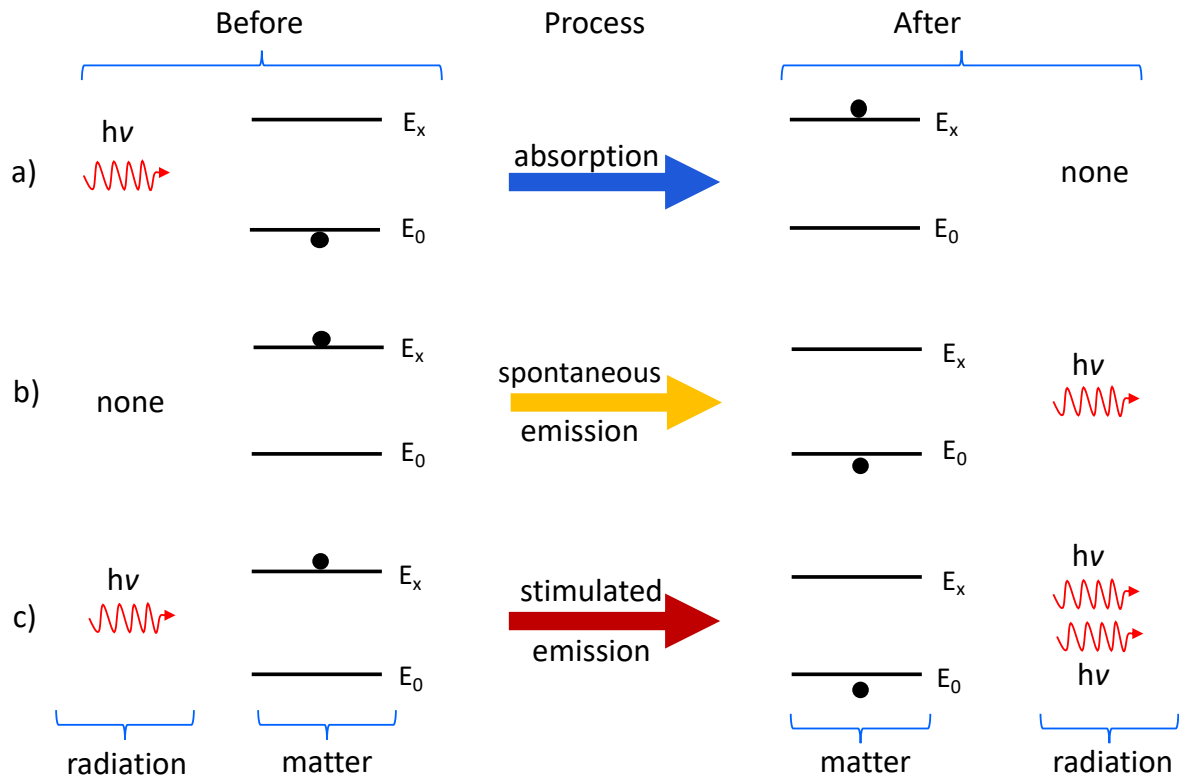


Figure 1.8: a) absorption, b) spontaneous emission, and c) stimulated emission of a photon

In the absorption process, an incident photon, with energy greater than the band-gap, is annihilated and its energy is transferred to an electron which is promoted to the conduction band, leaving a positively charged hole. For high absorption probabilities an empty conduction band and full valence band are required. In the absence of non-linear effects, such as a two-photon absorption process, the semiconductor will be transparent for the photons with energies less than the band gap. In semiconductors there is always a possibility that a carrier in the conduction band recombines spontaneously with a hole in the valence band giving rise to a photon with energy equal to the bandgap. These spontaneously emitted photons are generated with random phase, frequency, and direction and are sources of noise in semiconductor optical amplifiers (SOAs) and lasers.

In the stimulated emission process a photon with suitable energy interacts with an electron and hole, stimulating their recombination and emission of a photon with exactly the same energy, phase and frequency as the incident photon. These two photons may then contribute to the stimulation of further carrier recombination.

Figure 1.8 c) portrays stimulated emission for an individual atom. Assume now that a sample contains a large number of atoms in thermal equilibrium at temperature T . Before any radiation is directed at the sample, a number N_0 of these atoms are in their ground state with energy E_0 and a number N_x are in the excited state, E_x . Boltzmann demonstrated that N_x is defined in terms of N_0 as:

$$N_x = N_0 e^{-(E_x - E_0)/kT} \quad 1.2$$

Where, k is Boltzmann's constant. Also, because $E_x > E_0$, eqn. (1.2) requires that $N_x < N_0$ i.e. there will always be fewer atoms in the excited state than in the ground state. This is what we expect if the level populations N_0 and N_x are determined only by the action of thermal agitation.

To produce laser light, net amplification is required i.e. there must be more photons emitted than absorbed. In other words, there must be a situation in which stimulated emission dominates. Consequently, more atoms are needed in the excited state than in the ground state. However, because such a population inversion is not consistent with thermal equilibrium, a laser is electrically pumped to achieved this.

1.5 Lasing

Laser operation is predicated on light amplification by stimulated emission of radiation (laser), as the acronym describes. Needless to mention that stimulated emission is the key to the operation of laser diodes. Radiative emission rates increase in a laser as the current density is increased. At low carrier injection, the absorption and spontaneous emission rates are higher than the stimulation emission rate and thus no amplification (gain) will be achieved. As a laser is injected with a current above a certain threshold for the carriers to accomplish efficient conduction within the diode, a number of consequences occur contingent upon the amount of carrier density. Firstly, if a small number of carriers are injected into the ground state of the conduction band and recombine radiatively then the light emitted may travel down the

waveguide where it can be reabsorbed by the active region as the numbers of carriers in the conduction band is low. If the carrier concentration in the conduction band increases, more photons are emitted which can stimulate further emission. However, if the conduction band occupancy remains low, absorption again dominates attenuating the light. In the ideal case, with no cavity loss assumed, when the carrier concentration increases the absorption probability reduces due to carrier build up in the conduction band. When the carrier density in the conduction band is equal to that of the valence band, emitted photons are absorbed and stimulated in equal numbers. This is called the transparency point. If the carrier concentration in the conduction band is increased above transparency numbers, a population inversion is reached and amplification of stimulated photons dominates absorption. In the real case there are cavity losses to contend with so the population inversion must be exceeded to achieve transparency and subsequently lasing.

Figure 1.9 shows a schematic of the round trip of stimulated light through a laser cavity.

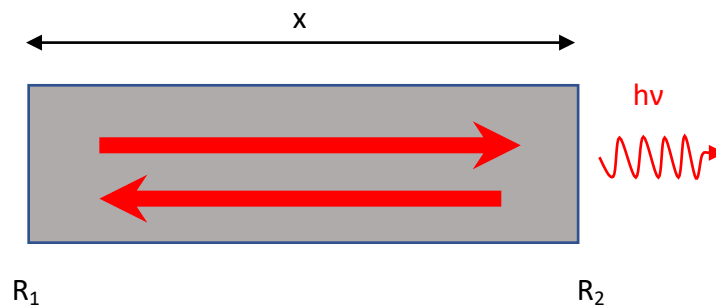


Figure 1.9: Schematic representation of a laser cavity of length x formed by reflection from end mirrors R_1 and R_2 ($R_1 \gg R_2$)

Photons which transit through the cavity with a population inversion result in amplification (i.e. gain) of the light intensity (I) as the distance (x) light travels increases, thus incremental amplification or gain (g) can be defined as [28]:

$$dI = g \cdot dx I(x) \tag{1.3}$$

This is the same as the absorption coefficient in Beer's law, except intensity is growing with distance rather than diminishing. By integrating equation (1.3), the intensity can be calculated as:

$$I(x) = I_0 e^{gx} \tag{1.4}$$

For lasing oscillation, the increase of the intensity due to the gain must exactly equal the losses from the imperfect reflectivity of the end mirrors (mirror losses) and any other losses that may be present in the medium (internal losses). From fig. 1.9, following the light at frequency ν around a round trip of the cavity, the lasing condition may be written as:

$$R_1 R_2 e^{2gL} e^{-2\alpha_i L} = 1 \quad 1.5$$

Where, the factor of 2 in both of the exponents accounts for the round trip and α_i represents the internal losses, which accounts for scattering losses and absorption from processes other than interband transitions such as impurity absorption.

The oscillation condition defined in eqn 1.5 may be re-phrased for threshold gain (g_{th}) and scaled with a confinement factor, Γ . This is because the light produced in the cavity is not totally confined to the active region where carriers are injected. The cavity volume occupied by photons is often larger than the active region volume occupied by electrons [30].

The oscillation condition can therefore be re-written as [28]:

$$g_{th} = \Gamma g_{mat} = \alpha_i + \frac{1}{2l} \ln \left(\frac{1}{R_1 R_2} \right) = \alpha_i + \alpha_m \quad 1.6$$

Where, the mirror loss term $\left(\frac{1}{2l} \ln \left(\frac{1}{R_1 R_2} \right) \right)$ is summarized as α_m . Increasing the drive current in a bulk laser increases the gain until threshold condition is met where the gain equals the losses (g_{th}), though for a QD laser gain saturation can occur resulting in non-linear gain increase with current and is discussed further in chapter 3. For an ideal laser above threshold, the gain remains constant (clamps) and additional carriers recombine to emit more photons. Therefore, excess current above threshold increases the stimulated emission optical power out but does not increase the gain. This important point is discussed further in chapter 3 as a prerequisite to measuring the linewidth enhancement factor.

1.6 Quantum dot rate equation model

Figure 1.10 is a schematic band diagram of the simplified dynamics taking place in QD lasers. The energy diagram of the laser active region is shown including the self-assembled QDs and

the relaxation process of carriers into the ground state. It forms the foundation of the rate equations which are solved to determine the QD specific relative intensity noise function which can be used to extract the D-factor and the k-factor limited modulation bandwidth.

In this model [31], due to the increased degeneracy and low occupation probability of the excited states compared to the ground state, they are simplified into one continuum. As a result, only a single main transition and relaxation time are considered i.e. from the continuum to the ground state.

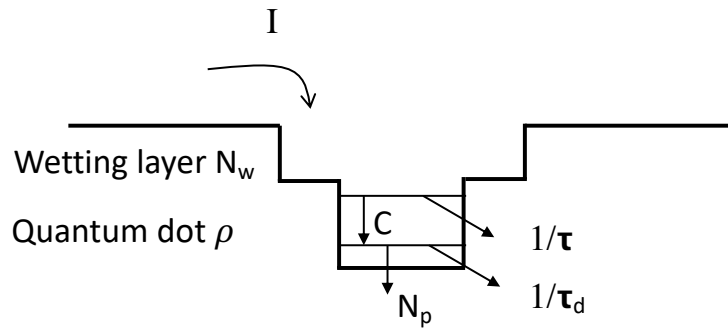


Figure 1.10 Energy diagram of the active layer of the quantum dot laser

As mentioned above, only a single discrete electron and hole ground state is assumed to be formed inside of a QD. Moreover, charge neutrality is assumed to always hold in each QD that is electrons and holes are treated as excitons. The injected carriers diffuse through the separate confinement heterostructure, relax into the QW, and subsequently, relax into the dots.

The QD specific transfer function can be written as [31]:

$$RIN = \frac{\frac{H}{\omega^2} + A\omega^2 + B}{(\omega - \omega_r^2)^2 + \gamma^2 \omega^2} \quad 1.7$$

The new factor, H, appear in this expression as compared to the classical relative intensity noise (RIN) transfer function provided in the appendix section A.1.3 (small signal modulation) eqn. A.19. It describes the interaction between the wetting layer and the QD. This factor's function is to increase the noise at low frequencies.

1.7 Quantum confined structures and density of states

In semiconductors, the number of electrons at each energy is obtained by multiplying the number of states with the probability of that state being occupied. As such, density of states (DoS) is the number of states per unit energy, per unit volume. The DoS is dependent on the degree and form of carrier confinement. In bulk material, due to a continuum of states in all three dimensions, carriers can potentially have any energy within their band structure. The DoS in bulk semiconductors varies as $E^{1/2}$. By decreasing the size in one-dimension quantum effects on the density of states can be obtained. A quantum-confined structure is one in which the motion of the electrons (and/or holes) are confined in one or more directions by potential barriers. Figure 1.11 schematically plots the density of states for different degrees of confinement in semiconductors.

Quantum theory entails if a particle is confined in one of the spatial directions, the confinement energy increases as confinement distance (x) is decreased. This follows from Heisenberg's uncertainty principle:

$$\Delta p \sim \frac{\hbar}{\Delta x} \quad 1.8$$

Given the particle is free with mass (m), the additional kinetic energy obtained from the confinement can be written as [28]:

$$E_{Conf} = \frac{\Delta p^2}{2m} \sim \frac{\hbar^2}{2m\Delta x^2} \quad 1.9$$

This confinement energy is considerable when it is comparable to or greater than the kinetic energy of the particle from its thermal motion in the x direction. The principle of equipartition of energy indicates a thermal energy of $k_B T / 2$ for each degree of freedom of the motion. Therefore, quantum size-effects matter when:

$$\Delta x < \sqrt{\frac{\hbar^2}{mk_B T}} \quad 1.10$$

This is equivalent to saying that Δx must be comparable to or smaller than the de Broglie wavelength $\lambda_{deB} \equiv h/p_x$ for the thermal motion. The criterion given in eqn 1.10 provides an idea of how small the structure must be if we are to observe quantum confinement effects. At room

temperature, we find that we must have $\Delta x \leq 5 \text{ nm}$ for an electron in a typical semiconductor with $m_e^* = 0.1m_0$.

By quantizing the states in one direction the carrier motion is limited in that direction. Quantum-confined structures are generally classified by their dimensionality. Figure 1.11 shows the three major types of quantum-confined structures, QW, quantum wire, and QD.

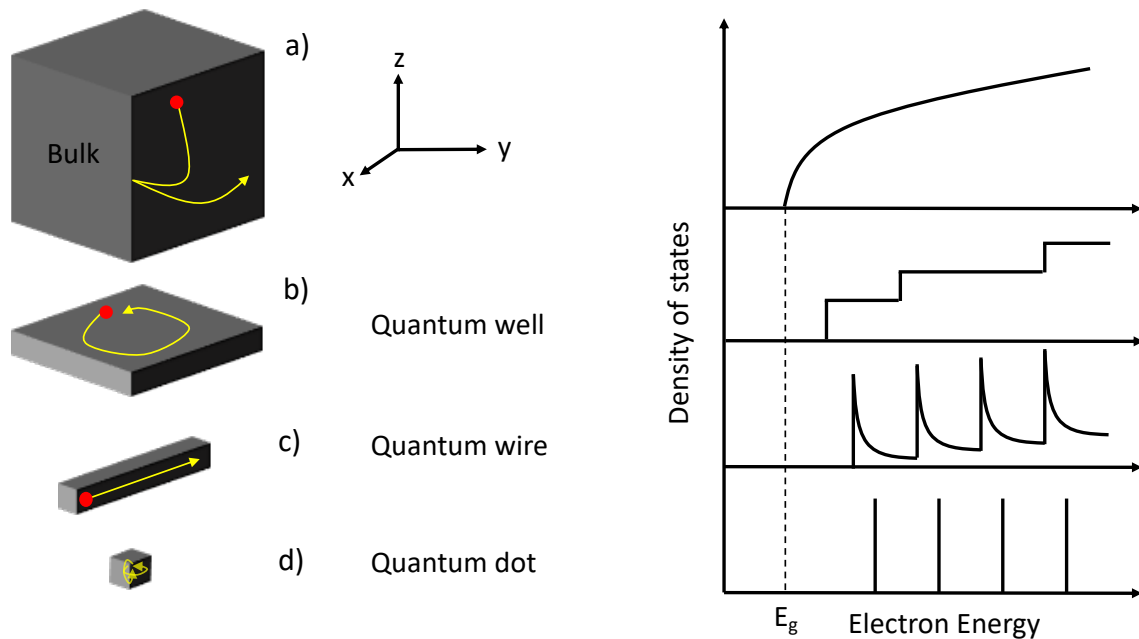


Figure 1.11: Schematic comparison of density of states for different quantum confinement degrees [28].

The quantization of the motion of the carriers not only causes an increase in the energy of a particle at rest by the confinement energy but also changes the form of the density of states. The effect of quantum confinement on carrier density and gain profile will be discussed in chapter 3.

The conduction band electrons in a bulk semiconductor (Fig. 1.11a) can have any energy above the band gap energy E_g and the density of states is proportional to $(E - E_g)^{1/2}$. This is a consequence of the free motion in all three dimensions. The Dos for a QW (Fig. 1.11b) is determined by the 2-D free motion and the shift of the energy due to the quantum confinement. The DoS increases as a series of steps, one for each quantized level. The band edge is essentially shifted to higher energy by the quantized energy for the quantum-confined motion in the third direction. The argument can be repeated for 1-D quantum wire and 0-D QD systems

(Fig. 1.11 c and d). In the case of quantum wires, the DoS has an $E^{-1/2}$ dependence which leads to peaks at each new quantized state. In QDs the motion is quantized in all three directions and there are no continuous bands at all. The density of states consists of a series of Dirac δ -functions for each quantized level. In this sense, QDs behave like ‘artificial atoms’ in which the electrons have discrete energies rather than continuous bands.

To summarize, the number of degrees of freedom associated with the type of quantum confinement explained above is tabulated in table 1.

Structure	Quantum confinement	Number of free dimensions	Density of states
Bulk	none	3	$E^{1/2}$
Quantum well	1-D	2	E^0
Quantum wire	2-D	1	$E^{-1/2}$
Quantum dot	3-D	0	Dirac δ -functions

Table 1: Structures degrees of freedom with respect to the dimensionality of the quantum confinement.

1.8 Inhomogeneous broadening in quantum dots

The most standard instance of S-K growth mode is self-assembling InAs on GaAs. InAs has a narrow bandgap with a 7% larger unit cell size than GaAs. The deposition of thin layers of In molecules on GaAs during MBE growth helps create the dots. The InAs molecules try to match the lattice constant of GaAs which gives rise to the formation of a highly strained layer known as the ‘wetting layer’ on the surface of the crystal. The energy necessary to strain the layer is so great that it stops being satisfactory to form a uniform layer when the thickness exceeds only a few atoms. The InAs molecules coalesce into clusters instead, which leads to the formation of InAs QDs on top of the wetting layer. By depositing layers of GaAs on top of the dots, known as capping, the electrons and holes are consequently confined in both the vertical and the lateral directions. Ultimately, highly strained layers are grown, resulting in the formation of islands having zero dimensional properties. Dots created by this method are not identical in size and composition. This causes the inhomogeneous broadening of the gain and spontaneous emission from the ensemble that can be approximated by a Gaussian function [32]. This is schematically presented in fig. 1.12.

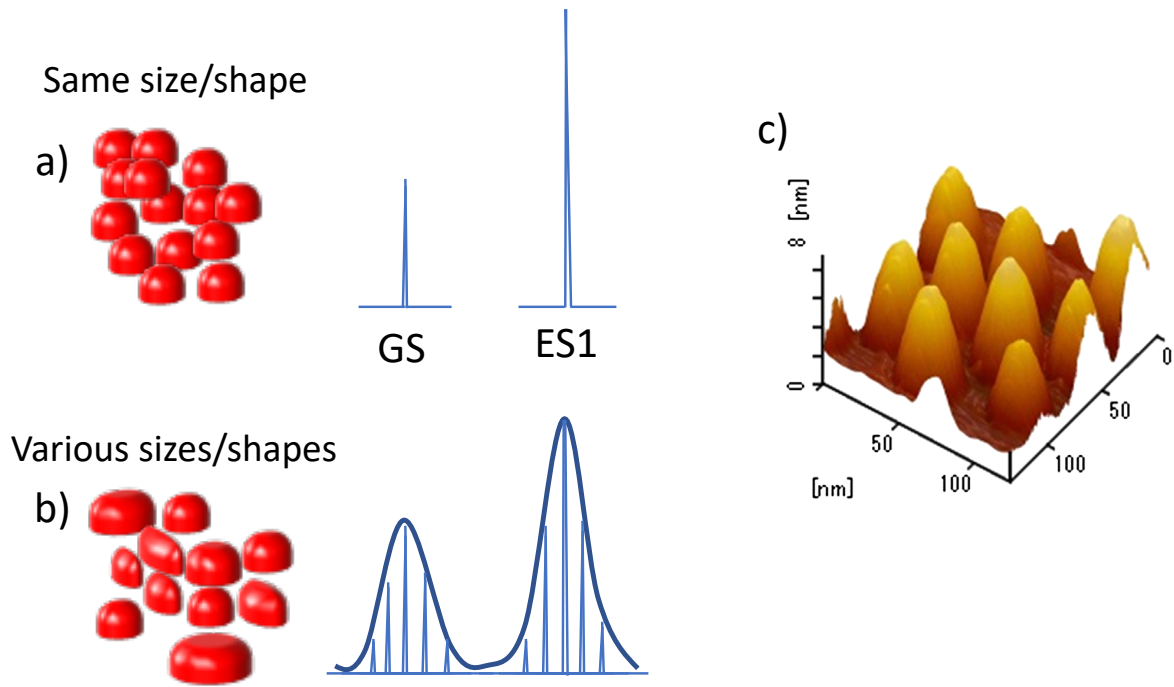


Figure 1.12: (a) Identical size QDs and the resultant delta function like density of states. (b) Self assembled QDs in variable sizes and the resultant Gaussian density of states, (c) real QDs grown by S-K method, 3-D graph is produced from an atomic force microscopic image [33].

This broadening results in lower peak gain due to a spread over a wide range of wavelengths, which may be attributed the self-assembled nature of the QDs causing size and composition fluctuations across the QD ensemble. This is disadvantageous for lasers which require high gain, but makes wider spectral emission possible for applications where low coherence length is an important figure of merit such as for interferometric imaging purposes e.g. in optical coherence tomography or for broadband emitters such as super-luminescent diodes (SLD) and also semiconductor optical amplifiers (SOA).

Another reason for this low gain is the saturation of the states at relatively low current such that increasing the current offers no increase in gain at the ground state (e.g. 1300 nm) but rather an increase in the excited state (e.g. 1220 nm) [34, 35]. This enables emission from more than one state leading to very broadband emission (e.g. in an SLD [36]).

In QD structures the size and shape of dots define the electronic structure, i.e. the number of carriers which can be contained, and their confinement energies. The shape of a dot is dependent on the material they are made of and the growth method and conditions. These

structures are sometimes referred to artificial atoms due to the similarity of the physics at play. As explained previously, the confinement of carriers results in quantized, delta-function-like, energy levels in a QD in theory but in real QDs broadening of this transition is expected due to both homogeneous broadening and the previously described inhomogeneous broadening. Homogeneous broadening of the QDs is a consequence of the finite carrier life time, carrier-carrier, and carrier-phonon interactions [37].

1.9 QDs for optical telecommunication

With a tremendous increase in data transmission precipitated by the advent of internet-based communications, there is a need for devices that could transfer data faster, further and more efficiently down an optical fiber. This led to the drive in InP-based QW lasers as InP could readily cover the 1550 nm minimum loss window in optical fibers. Opto-electronic integrated circuits (OEIC) were realized which may consist of a tuneable distributed feedback laser integrated wavelength locker, a power monitor, and a Mach-Zender type modulator inside of a standard butterfly package [38]. This butterfly package would typically be sold with all driver circuitries and could be plugged into a fiber-optic transmitter unit. Achieving OEIC in the InP platform required developing advanced growth and processing capabilities e.g. selective area growth, overgrowth, and butt coupling technologies [39].

Traditionally GaAs addresses the wavelengths between 650 – 1064 nm with III-nitrides being used for shorter wavelengths and InP for longer. GaInAs quantum wells (QW) in GaAs are limited in their emission wavelength (to ~1100 nm) due to the excess strain in the material for QWs of longer emission wavelength. However, incorporation of a small amount of nitrogen to give a GaInNAs QW successfully extends the emission wavelength to 1.3 μm where the light has zero dispersion in optical fiber. The emission wavelength has been extended to 1.5 μm [40] but does not seem to be being used successfully for devices yet. This makes GaInNAs of interest for developing 1.3 μm transmitters and detectors for short haul (1.55 μm is used for longer distance due to lower loss) fiber-optic communications.

For GaAs-based QDs, developments go hand in hand with new processing techniques in order to make new devices feasible. Devices that address market needs in novel areas as well as the conventional. Applications are as diverse as frequency doubling for laser projection displays,

broadband or swept source light sources for optical coherence tomography, low cost uncooled and potentially isolator-free direct or external modulation lasers for fiber to the home or the next generation of Ethernet, and for use in harsh environments at elevated temperatures.

The fact that QDs can be formed directly during epitaxial growth means that they can be easily incorporated into laser diode structures. Also, the result of the delta-function like DoS is a reduction in the carriers required to form a population inversion compared to bulk material. This is beneficial in reducing threshold current density and increasing material gain. The delta function like density of states also results in: a narrow lasing linewidth, coincident material-gain peak wavelength and differential-gain peak wavelength, and if the confinement between energy levels is high enough a reduction in the temperature sensitivity of the threshold. These theoretical characteristics make QDs ideal for operation as commercial communication lasers. Nonetheless, the reality is yet to reach theory. As such, it is the basis of this thesis to understand some of the current limits of QD lasers, based on In(Ga)As/GaAs III-V semiconductors and systematically study methods of improving their performance for device designs.

1.10 Thesis outline

This thesis is predicated upon the empirical analysis of the static and dynamic performance of the state of the art 1.3 μm In(Ga)As/GaAs QD material for the purposes of better understanding the physical mechanisms behind their operation in order to develop the next generation of lasers, detectors, and modulator devices. This will enable the further evolution of GaAs-based QDs for fiber to the home telecommunications incorporated in transmitters, receivers, and modulators as a sturdier, more scalable, and less temperature sensitive alternative to the InP platform.

In chapter 2, I will carry out a photocurrent (PC) spectroscopic study of the high quality 1300 nm In(Ga)As/GaAs QD materials grown by MBE. The experiments are performed on p-i-n mesa-diode structures under electric fields of up to 450 kV/cm applied to the QDs. These materials exhibit a comparatively low inhomogeneous line-width, large state-separation, and constrained tunneling breakdown (i.e. very low dark current). The quantum confined Stark shift (QCSS) in the QD states under applied electric field is analyzed, and the permanent dipole moment compared to other reports in the literature of QDs at shorter wavelengths. The dark-

current and responsivity are compared to comparable reports in the literature and also commercial devices. Subsequently, the QCSS of the QDs is compared to reports for various QW systems (GaAs/AlGaAs, InGaAs/GaAs, InGaAsP/InP) operating at a range of wavelengths (800 nm to 1600 nm).

In chapter 3, a temperature-dependent investigation of the LEF (spectral and also as a function of current) is presented with high-resolution. This is particularly interesting in that the LEF is expected to increase at higher temperatures as the differential gain decreases due to carrier thermalization to higher states. However, the alpha-Henry values are pinned close to zero even at higher temperatures ascribed to the strong carrier localization within the dots providing ample gain. Additionally, knowledge of the spectral and current dependent LEF values at particular wavelengths and drive currents, respectively is useful for e.g. intensity modulation purposes. Furthermore, by investigating the carrier related mode shift with respect to drive current an interesting interplay was observed, for the first time, in terms of a correlation between the change in linewidth and the carrier related modal shift above the lasing threshold. This is due to subtle effects which will be discussed in the results section. Ultimately, an essentially zero LEF (spectral and current dependent) is demonstrated for the first time in GaAs-based QDs at the full temperature range of measurement (-10 to 85C).

In Chapter 4, I will re-present the electric-field and temperature dependent investigation of optical gain and absorption performed on the state-of-the-art 1.3- μm In(Ga)As/GaAs QD devices with a device design in mind. It will be demonstrated that the distinctive shape of the gain and absorption spectra, which stems from the QDs density of states (DoS), can be utilized for a number of potential modulation configurations based on the selected laser wavelength detuning from the gain maximum. Intensity modulation and the corresponding change in absorption spectra, leading to operation with negative chirp, are demonstrated via absorption spectroscopy and gain measurement of the QD-active material. This device would be able to provide positive or negative chirp dependent upon modulation scheme and gain peak wavelength detuning.

In Chapter 5, a temperature-dependent RIN spectroscopy of the state-of-the-art QD lasers is carried out at a temperature range beyond the current standards' commercial window [41] to establish noise characteristics and modulation capabilities at elevated temperatures. Generally, in a transmission communication system, knowledge of the RIN characteristics of the source

is crucial because it is a measure of the signal to noise ratio (SNR) of the link. Since optical transmission systems have a critical limitation due to this noise source, it is important to know how it can be defined and measured. RIN is a measure in order to quantify how noisy the laser, as the transmitter of the transmission link, is. Consequently, in order to achieve a certain data rate in the transmission in a digital system, a certain bit error rate needs to be achieved which entails employment of a laser diode with a certain noise performance.

The free-running RIN results are presented along with their analysis to probe the modulation capabilities of the QD lasers prior to delving into the investigation of the external optical feedback effects under various feedback rates and for the first time at different temperatures, which clearly demonstrates the expected increase in RIN with feedback in terms of compound cavity modes height with a mode-spacing dictated by the length of the external cavity.

The experimental results presented in chapter 3 indicates an essentially zero LEF across all of the positive gain region and also up to the threshold current at all measurement temperatures. Therefore, the devices are also expected to demonstrate a rather high resilience towards external optical feedback, since the critical feedback ratio for coherence collapse is inversely proportional to the fourth power of the LEF as derived in [42]. Also, it will be shown that the critical feedback level fundamentally depends on the damping rate. The heavier the damping, the larger the critical feedback level would be for the onset of the coherence collapse. The difference in the K factor alone is predicted to result in over 10 dB of increase in f_{crit} for QD lasers compared to QWs. Furthermore, considering the fact that QD lasers exhibit lower LEF values, even larger increases to the critical feedback level for coherence collapse are expected.

Accordingly, with the demonstration of an ultra-low and temperature-insensitive threshold current [43, 44] and potential tolerance to optical feedback [45], QD active media are strong candidates for cooler- and isolator-free operation in optical transmitters. The latter is the direct subject of investigation of the final chapter of this project.

And lastly, a conclusion and future work study will be provided in chapter 6 in order to conclude this thesis, and provide the investigations that could be carried out as complementary work or continuation to this study but fell outside of the remit of this work.

References

- [1]: A. Einstein, "Zur Quantentheorie der Strahlung or (To) The Quantum Theory of Radiation", in *Physikalische Zeitschrift*, Vol. 18, 121, 1917
- [2]: A. Javan, "Possibility of production of negative temperature in gas discharges", *Phys. Rev. Letts.*, Vol. 3, No 2, pp. 87-89, Jun. 1959
- [3]: A. Javan, W.R. Bennett Jr., and D.R. Herriott, "Population inversion and continuous optical Maser oscillation in a gas discharge Containing a He-Ne mixture", *Phys. Rev. Letts.*, Vol. 6, No. 3, pp. 106-110, Dec. 1960
- [4]: From web link: <https://lemelson.mit.edu/resources/ali-javan>, acquired on 21/01/2019
- [5] R.N. Hall, G.E. Fenner, J.D. Kingsley, T.J. Soltys and R.O. Carlson, "Coherent Light Emission from GaAs Junction, *Phys. Rev. Letts.*, Vol. 9, No. 9, 366, 1962
- [6]: T.M. Quist, R.H. Rediker, R.J. Keyes, W.E. Krag, B. Lax, A.L. McWhorter and H.J. Zegler, "Semiconductor Maser of GaAs", *Appl. Phys. Letts.*, Vol. 1, No. 4, pp. 91-92, 1962
- [7] I. Hayashi, M.B. Panish, P.W. Foy, and S. Sumski, "Junction Lasers which operate Continuously at Room temperature", *Appl. Phys. Letts.*, Vol. 17, No. 3 109 (1970).
- [8] R. Dingle, W. Wiegmann and C.H. Henry, "Quantum States of Confined Carriers in very Thin $\text{Al}_x\text{Ga}_{1-x}\text{As}$ -GaAs- $\text{Al}_x\text{Ga}_{1-x}\text{As}$ Heterostructures" *Phys. Rev. Letts.*, 33, 827 (1974).
Epitaxy by Periodic Annealing, A.Y. Cho, *Surface Sci.* 17, 494 (1969).
- [9]: Y. Arakawa and H. Sakaki, "Multidimensional quantum well laser and temperature dependence of its threshold current," *Appl. Phys. Letts.*, Vol. 40, No. 11, pp. 939-941, Mar. 1982
- [10]: M. Asada, Y. Miyamoto and Y. Suematsu, "Gain and the threshold of three-dimensional quantum-box lasers," *IEEE Jnl. Quant. Elect.*, vol. 22, iss. 9, pp. 1915-1921, 1986.
- [11]: N. Kirstaedter, N. N. Ledentsov, M. Grundmann, D. Bimberg, V. M. Ustinov, S. S. Ruvimov, M. V. Maximov, P. S. Kop'ev, Zh. I. Alferov, U. Richter, P. Werner, U. Gösele and J. Heydenreich, "Low threshold, large To injection laser emission from (InGa)As quantum dots," *Elect. Letts.*, vol. 30, iss. 17, pp. 1416-1418, 1994.
- [12]: I.N. Stranski and L. Krastanow "Zur Theorie der orientierten Ausscheidung von Ionenkristallen aufeinander". *Abhandlungen der Mathematisch-Naturwissenschaftlichen Klasse Iib. Akademie der Wissenschaften Wien.* 146: 797–810, 1938

- [13]: L. Goldstein, F. Glas, J. Y. Marzin, M. N. Charasse and G. Le Roux, "Growth by molecular beam epitaxy and characterization of InAs/GaAs strained-layer superlattices," *Appl. Phys. Lett.* 47, 1099, 1985
- [14]: K. Mukai, N. Ohtsuka, M. Sugawara and S. Yamazaki, "Self-formed In_{0.5}Ga_{0.5}As quantum dots on GaAs substrates emitting at 1.3 μm ," *Japan. Jnl. Appl. Phys.*, vol. 33, iss. 12A, pp. L1710-1712, 1994
- [15]: D. L. Huffaker, G. Park, Z. Zou, O. B. Shchekin and D. G. Deppe, "1.3 μm room-temperature GaAs-based quantum-dot laser," *Appl. Phys. Letts.*, vol. 73, iss. 18, pp. 2564-2566, 1998
- [16]: L. F. Lester, A. Stintz, H. Li, T. C. Newell, E. A. Pease, B. A. Fuchs and K. J. Malloy, "Optical characteristics of 1.24- μm InAs quantum-dot laser diodes," *IEEE. Photon. Tech. Letts.*, vol. 11, iss. 8, pp. 931-933, 1999
- [17]: O. B. Shchekin and D. G. Deppe, "1.3 μm InAs quantum dot laser with $T_0 = 161$ K from 0 to 80 $^\circ\text{C}$," *Appl. Phys. Letts.*, vol. 80, iss. 18, pp. 3277-3279, 2002
- [18]: G. Park, O. B. Shchekin, D. L. Huffaker, and D. G. Deppe, "Low-threshold oxide-confined 1.3- μm quantum-dot laser," *IEEE Photon. Technol. Lett.*, 13, 3, 230–232, 2000
- [19]: P. Bhattacharya and S. Ghosh, "Tunnel injection In_{0.4}Ga_{0.6}As/ GaAsIn_{0.4}Ga_{0.6}As/ GaAs quantum dot lasers with 15 GHz modulation bandwidth at room temperature," *Appl. Phys. Lett.* 80, 3482, 2002
- [20]: M. Ishida, K. Watanabe, N. Kumagai, Y. Nakata, N. Hatori, H. Sudo, T. Yamamoto, M. Sugawara, and Y. Arakawa, 19th International Conference on Indium Phosphide and Related Materials (IPRM2007) FrB1-3, Matsue, Japan, 2007
- [21]: M. Grundmann, "Feasibility of 5 Gbit/s wavelength division multiplexing using quantum dot lasers," *Appl. Phys. Letts.*, vol. 77, iss. 26, pp. 4265-4267, 2000
- [22]: D. G. Deppe, H. Huang and O. B. Shchekin, "Modulation characteristics of quantum-dot lasers: the influence of p-type doping and the electronic density of states on obtaining high speed," *IEEE Jnl. Quant. Elect.*, vol. 38, iss. 12, pp. 1587-1953, 2002
- [23]: K. Otsubo, N. Hatori, M. Ishida, S. Okumura, T. Akiyama, Y. Nakata, H. Ebe, M. Sugawara and Y. Arakawa, "Temperature-insensitive eye-opening under 10-Gb/s modulation of 1.3- μm P-doped quantum-dot lasers without current adjustments," *Japan. Jnl. Appl. Phys.*, vol. 43, iss. 8B, pp. L1124-L1126, 2004
- [24]: C. Sah, R. N. Noyce and W. Shockley, "Carrier Generation and Recombination in P-N Junctions and P-N Junction Characteristics," in *Proceedings of the IRE*, vol. 45, no. 9, pp. 1228-1243, Sept. 1957

- [25]: J. R. Hook and H. E. Hall, "Solid state physics," – Chapter 6, Wiley, 1996.
- [26]: Z. I. Alferov, V. M. Andreev, E. L. Portnoy, and M. K. Trukan, "AlAs–GaAs heterojunction injection lasers with a low room-temperature threshold", *Fiz. Tekh. Poluprovodn.* 3, 1328, 1969
- [27]: From web link: http://gorgia.no-ip.com/phd/html/thesis/phd_html/node4.html acquired on 30/1/19
- [28]: Mark Fox "Optical Properties of Solids", Oxford master series in condensed matter physics, Oxford University Press, 2001
- [28.1]: Taken from [28] after E.D. Palik, Handbook of optical constants of solids. Vol. 3. Academic press, pp. 753 1998.
- [29]: From web link: <https://www.newport.com/t/fiber-optic-basics> acquired on 30/1/19
- [30]: L. A. Coldren and S. W. Corzine, "Diode lasers and photonic integrated circuits," 2nd edition, Wiley, 1995
- [31]: J. Hayau, P. Besnard, O. Dehaese, F. Grillot, R. Piron, S. Loualiche, A. Martinez, K. Merghem, and A. Ramdane "Effect of the wetting layer on intensity noise in quantum dot laser," 2009 35th European Conference on Optical Communication, Vienna, pp. 1-2, 2009
- [32]: M. Sugawara, N. Hatori, H. Ebe, M. Ishida, Y. Arakawa, T. Akiyama, K. Otsubo, and Y. Nakata, "Modeling room-temperature lasing spectra of 1.3 μ m self-assembled InAs/GaAs quantum-dot lasers: Homogeneous broadening of optical gain under current injection", *J. Appl. Phys.* 97, 043523, 2005
- [33]: K. Nishi, T. Kageyama, M. Yamaguchi, Y. Maeda, K. Takemasa, T. Yamamoto, M. Sugawara, Y. Arakawa, "Molecular beam epitaxial growths of high-optical-gain InAs quantum dots on GaAs for long-wavelength emission", *Journal of Crystal Growth*, 378, 459–462, 2013
- [34]: M. V. Maximov, L. V. Asryan, Y. M. Shernyakov, A. F. Tsatsul'nikov, I. N. Kaiander, V. V. Nikolaev, A. R. Kovsh, S. S. Mikhrin, V. M. Ustinov, A. E. Zhukov, Z. I. Alferov, N. N. Ledenstov, and D. Bimberg, "Gain and Threshold Characteristics of Long Wavelength Lasers Based on InAs/GaAs Quantum Dots Formed By Activated Alloy Phase Separation," *IEEE J. Quantum Electron.*, 37, 676, 2005
- [35]: A. Markus, J. X. Chen, C. Paranthoën, A. Fiore, C. Platz, and O. Gauthier Lafaye "Simultaneous two-state lasing in quantum-dot lasers" *Appl. Phys. Lett.*, 82, 1818, 2003
- [36]: S. K. Ray, H. Y. Liu, T. L. Choi, K. M. Groom, S. L. Liew, M. Hopkinson, and R.A. Hogg, "Molecular Beam Epitaxial Growth of High Power Quantum Dot Super-Luminescent Diodes," *Jpn. J. Appl. Phys.*, 46, 2418, 2007

- [37]: A. V. Uskov, I. Magnusdottir, B. Tromborg, J. Mørk, and R. Lang, “Line broadening caused by Coulomb carrier-carrier correlations and dynamics of carrier capture and emission in quantum dots”, *Appl. Phys. Lett.* 79, 1679, 2001
- [38]: Datasheet: TL7000NCD, www.bookham.com, retrieved 21/08/2009.
- [39] B. Mason, S.P. Den Baars and Larry A. Coldren “Tuneable Sampled-Grating DBR Lasers with Integrated Wavelength Monitors”, *IEEE Phot. Tech. Letts.*, 10(8), 1085 (1998).
- [40]: H. Zhao, S.M. Wang, Q.X. Zhao, M. Sadeghi, and A. Larsson “Growth and characterization of GaInNAs by molecular beam epitaxy using a nitrogen irradiation method”, *J. Cryst. Growth*, 311, 1723, 2009
- [41]: “Cisco GPON SFP” Datasheet, April 25, 2016, document ID:1461606040226191
- [42]: H. Helms and K. Petermann, “A simple analytic expression for the stable operation range of laser diodes with optical feedback,” *IEEE J. Quantum Electron.*, vol. 26, pp. 833-836, 1990
- [43]: S. Fathpour, Z. Mi, P. Bhattacharya, A. R. Kovsh, S. S. Mikhrin, I. L. Krestnikov, A. V. Kozhukhov and N. N. Ledentsov, “The role of Auger recombination in the temperature-dependent output characteristics ($T_0=\infty$) of p-doped 1.3 μm quantum dot lasers,” *Appl. Phys. Lett.*, 85, no. 29, 5164-5166, 2004
- [44]: H. Y. Liu, D. T. Childs, T. J. Badcock, K. M. Groom, I. R. Sellers, M. Hopkinson, R. A. Hogg, D. J. Robbins, D. J. Mowbray and M. S. Skolnick, “High-performance three-layer 1.3 - μm InAs–GaAs quantum-dot lasers with very low continuous-wave room-temperature threshold currents,” *IEEE Photon. Tech. Lett.*, 17, no. 6, 1139-1141, 2005
- [45]: D. O'Brien, S. P. Hegarty, G. Huyet, J. G. McInerney, T. Kettler, M. Laemmlin, D. Bimberg, V. M. Ustinov, A. E. Zhukov, S. S. Mikhrin and A. R. Kovsh, “Feedback sensitivity of 1.3 μm InAs/GaAs quantum dot lasers,” *Elect. Letts.*, vol. 39, no. 25, pp. 1819- 1820, 2003

Chapter 2

Study of Electro-absorption Effects

2.1 Introduction

The last two decades have seen research into a wide-ranging number of optical devices based on quantum dots (QDs) [1], most notably, lasers and optical amplifiers for high speed communication systems. The optical characteristics of the inter-band transitions of QDs have been investigated either for a pure physical understanding [2-5], or for employment in lasers [6, 7]. However, less attention has been given to absorption-based devices e.g. modulators and photodetectors.

Photocurrent (PC) spectroscopy allows direct measurement of the absorption spectra in the active region of a light source. This absorption probing of the active elements yields essential information about inter-band optical transitions such as the oscillator strength, transition energies, selection rules, and polarization [8]. In PC spectroscopy, the absorption of incident light is measured as a function of wavelength. The technique works by shining monochromatic light onto the facet of a p-i-n structure, this is then propagated along the layers of the device where it can be absorbed. The absorption of light results in the generation of electron-hole pairs, that are rapidly swept towards the contacts by the field, and hence into the external circuit. Under the influence of an electric field, the optical transition energy is modified, leading to a quantum-confined Stark shift (QCSS) [9]. Since the PC spectra contain energy transition features, the QCSSs of the QD ground-state, excited-states, the wetting layer, and the band-

edge transitions can all be clearly observed. Therefore, the study of the QCSS in a QD system may provide information that can be utilized for tailoring the optical properties of InAs QDs for absorption-based device applications.

Photoluminescence-excitation spectroscopy, which has been utilized expansively to measure the properties of higher-dimensional systems [10], requires a broadly tunable laser source and does not replicate absorption spectra directly, but instead reflects intra-dot relaxation features which arise from the emission of multiple LO phonons [11]. On the other hand, other methods utilized in the measurement of absorption spectra either involve the highly sensitive direct probing of transmission that requires extremely sensitive techniques which would precipitate operation with acquisition times of several hours per scan [12], or the use of extremely low-temperature method of calorimetric absorption spectroscopy that seem to produce broadened spectra [13].

PC spectroscopy is a relatively simple, sensitive, direct, and low-noise method of measuring essentially the absorption spectra of active material and is therefore utilized in this work. Analysis under applied electric field is demonstrated to produce important information on the carrier wave functions in quantum wells (QWs) and QDs.

2.2 Background and motivation

Self-assembled InAs/GaAs QDs present close to ideal zero-dimensional systems [1]. Carriers are confined within the QDs in all 3 dimensions resulting in a delta-function like density of states (DoS). This provides a number of technological advantages as opposed to the band-like nature in the higher dimensional structures.

The discrete energy levels may open up new applications for QDs since in QWs light with an energy greater than the band-gap energy is absorbed. In QDs, however, there are transparent regions between the discrete levels, given the inhomogeneous broadening is relatively small. This will be discussed later for EAM applications whereby if the off signal is coincident on the wavelength of these transparent regions an infinite extinction ratio (ER) could be achieved (as will be seen later essentially $ER = ON\ Power / OFF\ Power$).

Furthermore, a very small change in the refractive index is expected for the changes in carrier density in the QDs at the resonant wavelength. This can be attributed to the symmetric shape of QDs gain curve yielding an unchanging refractive index at its peak. This will yield a very small linewidth enhancement factor value and thus wavelength chirp under modulation in QD lasers, as will be investigated in chapter 3. In standard optical fibers, the dispersion of the signal light at 1.55 μm often limits the maximum distance attainable because zero dispersion exists at 1.3 μm . As QDs can cover all wavelengths from the O- to L- bands, the same principle of operation applies with respect to EAM operation at this wavelength range.

On the other hand, discrete energy levels affect carrier dynamics as well. If the LO-phonon energy does not coincide with the level separation, carrier energy relaxation will be slow [1]. This could be advantageous for photodetectors because it helps to achieve a low dark current attributed to weaker thermionic emission from the QDs with 3D carrier confinement as compared to QWs [14]. Therefore, the detectivity, which is proportional to the signal (PC) to noise (dark current) ratio, $D=I_{pc} / I_{Dark}$, could be increased because of the low dark current in QDs. Moreover, QDs are sensitive to normal incident radiation attributed to the breaking of the polarization selection rule [15]. While QWs are also capable of detecting normal incident light [16], the absorption, photoconductive gain, and responsivity are lower attributed to the large hole effective mass and low hole mobility. Furthermore, the absorption peak in QDs is expected to be more robust to higher E-fields as compared to QWs due to higher carrier wavefunction localization. This advantage can be utilized at higher fields when there is a potential for impact ionization for avalanche photodetection purposes.

Considering the above-mentioned advantages, it is reasonable to consider that QDs may be used as a potential active medium in semiconductor absorption-based devices such as optical modulators and photodetectors as competitors to their QW counterparts.

2.3 Gaps in knowledge

Modulators based on QD material have not been extensively investigated, and less attention has been given to a spectral investigation of the absorption characteristics carried out for these purposes. Previous PC spectroscopic studies of InAs/GaAs QD structures have concentrated on short wavelength structures, and have been concerned with the determination of the electron-hole wavefunction alignment within the QD [17-19]. The work in this chapter was prompted

with a view to explore the possibilities of use of QDs as absorptive elements e.g. in an EAM or for detection applications.

QD material offer promise as photodetectors. For the near-infra red (IR) applications, InAs QDs have been employed, fabricated on a native III-V substrate, as high-speed photodetectors and shown responsivity values as high as 0.5 A/W (under edge-illumination) for the wavelength range of 1510-1630 nm. This was done with less than 1 nA of dark current up to -20 V bias. In the avalanche regime, multiplication factors as high as 12 were achieved with 3 μ A dark current [20]. At the 1.3 μ m window, QDs grown on Si have shown an internal responsivity of 0.9 A/W and a dark current of less than 0.8 nA at -1 V [21]. InAs/GaAs QDs monolithically grown on Si have been proposed as photodetectors with an avalanche gain (multiplication factor) of 8 and dark current densities of 5 mA/cm² at -25 V [22]. More work using InAs/AlInGaAs/InP devices have shown promise as high sensitivity photodetectors with a dark current of 1 nA at 20 V and an avalanche multiplication factor of 12 at -27.8 V [23]. Additionally, QD photodetectors heterogeneously integrated on Si were reported in [24] that were using the same epitaxial layers and fabrication process as a QD laser on Si. Dark current of as low as 10 pA (1×10^{-6} A/cm²) were achieved with a maximum external responsivity of 0.34 A/W at 1310 nm and 0.9 A/W at 1280 nm.

A spectroscopic investigation of high quality QDs has not been carried with a view to EAM and photodetector applications. Consequently, a comprehensive absorption spectroscopic study of high quality self-assembled InAs/GaAs QD materials is carried out with a view for incorporation in modulation and photodetection applications.

In this chapter, I describe a PC spectroscopic study of high quality 1300nm In(Ga)As/GaAs QD materials grown by molecular beam epitaxy (MBE). The experiments are executed in p-i-n diode structures, which allows electric fields of up to 450 kV/cm to be applied to the QDs. These materials exhibit comparatively low inhomogeneous line-width, large state-separation, and limited tunnelling breakdown (i.e. very low dark current). I analyze the quantum confined Stark effect (QCSE) in the QD states under applied electric field, and compare the permanent dipole moment to other reports in the literature of QDs at shorter wavelengths.

The dark-current and responsivity are compared to comparable reports in the literature and also commercial devices. I go on to compare the QCSE of the QDs to reports for various QW

systems (GaAs/AlGaAs, InGaAs/GaAs, InGaAsP/InP) operating at a range of wavelengths (800 nm to 1600 nm). I show that the rate of shift of the QD ground-state absorption peak is smaller than that of most QW systems (~ 0.1 meV/kVcm $^{-1}$ *c.f.* 0.15-0.2 meV/kVcm $^{-1}$). I then go on to show that the QD absorption strength is relatively insensitive to applied electric field as compared to the reports for QWs. Both observations are attributed to the strong carrier localization of the QD states. As a consequence, we observe a strong QD absorption peak at all biases up to avalanche breakdown, which is not observed in QW systems. Subsequently, I will explore possible future uses of 1300 nm QDs as an absorptive element for modulation and detection purposes.

2.4 Modulation

By the discovery of QCSE in GaAs-based QWs, an enhanced electro-optic effect was demonstrated, which was attributed to the large band-edge optical absorption shift to lower energies due to an electric field perpendicular to the QW growth direction [25]. This electro-absorption was readily utilized in an intensity modulator. A later demonstration at the communications wavelength of 1.55 μm made use of an InGaAs/InP waveguide device [26]. The QCSE have further been used successfully in integrated laser-modulators at 2.5, 10, and 40 Gb/s [27, 28, 29].

In optical communication systems information is encoded into a digital optical signal by turning the light on and off. This is the process of optical intensity modulation that is widely used in various optical links and is referred to as intensity modulation (IM) or amplitude shift keying (ASK). IM is implemented in an optical modulator that modifies one or more characteristics of an optical signal for the purpose of conveying information. There are fundamentally three kinds of IM modulators that have been employed for commercial use: the directly modulated diode (DM), the lithium niobate based Mach-Zehnder interferometer (LiNbO $_3$ OR LN- MZI), and the electro-absorption modulator (EAM).

The directly modulated laser diodes have several advantages such as the simplicity of modulation through changing the injection current, and no insertion loss as compared to external modulators. DM systems are simple and compact in configuration, which leads to stability. However, the large frequency chirp associated with the direct modulation of laser

diodes operating at a few GHz presents a problem for high-speed, long-distance optical-fibre communication [30].

1550 nm systems are limited to distances below 100 km even at a bit rate of 2.5 Gb/s because of the frequency chirp [31]. Still, higher bit rates (up to 10 Gb/s) and longer distances at 2.5 Gb/s can be achieved by use of some compensating techniques, such as negative dispersive fibres [32,33], fibre gratings [34,35] and light injection [36]. These schemes, however, increase the system complexity and cost. To bypass the chirp limitation of DMs, external modulators may be employed, e.g. the LN-modulator. The LN-modulator has an MZI configuration and the lithium niobate is chosen because of its high electrooptic coefficients. Chirp-free or chirp-tunable modulation can be realized using a LN-modulator at bit rates up to 40 Gb/s [37,38].

As a competitor to the LN-modulator, an EAM realizes the direct amplitude modulation by changing the absorption of the light propagating in the waveguide. An EAM is basically a reverse-biased p-i-n diode and when a light beam is incident on the EAM it is absorbed by the medium given the incident photon energy is larger than the bandgap. If the absorption edge is adjusted through an external electric field, then the light absorption and therefore the intensity of the optical output will follow the change of the modulating electrical signal. EAMs provide various advantages e.g. low frequency chirp, broad wavelength range, and compactness. Furthermore, EAMs can be monolithically integrated with other devices providing high optical output and high system reliability.

Figure 2.1 compares a QW and a QD intensity modulator in terms of their absorption and change in refractive index spectra. Note that the chirp parameter is directly proportional to the Δn spectra.

The comparison of the gain/absorption shape of QWs and QDs, and also investigation of the alpha-Henry parameter are the subjects of investigation in the next experimental chapter. For now, let us consider the idea of a negative chirp modulator utilizing the unique feature of QDs, the discrete energy levels as compared to the band-like nature in higher dimensional structures. A transparent region can be obtained on the shorter wavelength side (blue side) of the absorption peak, in contrast to the QW or bulk, where there is no transparent region on the blue side of the band edge attributed to the continuous energy levels.

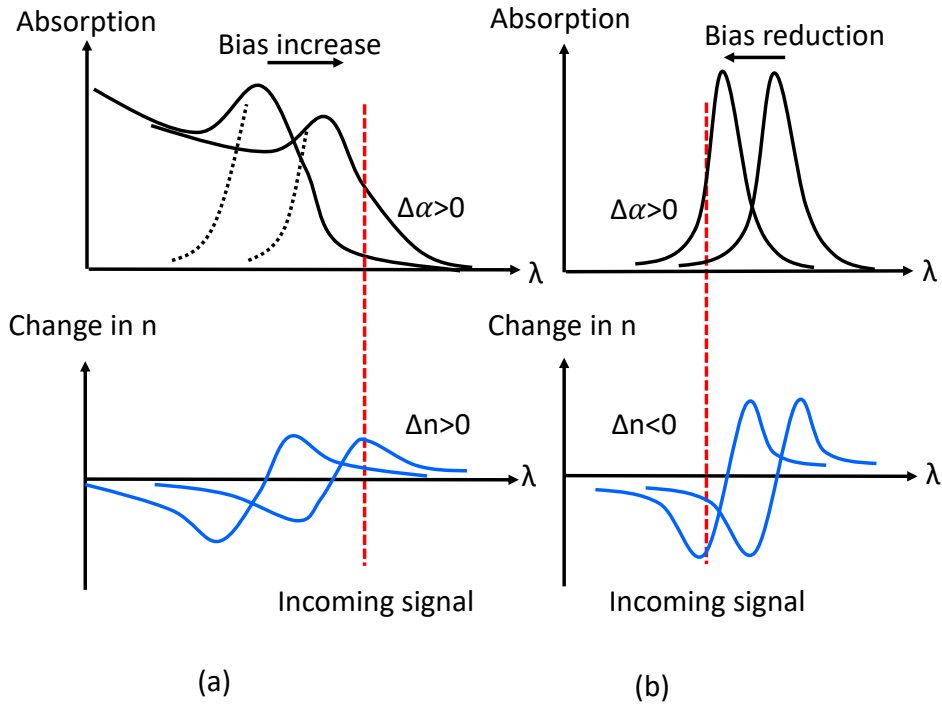


Figure 2.1: Comparison of the absorption and the change in refractive index in a) QW modulator and b) QD modulator.

In the case of a conventional QW modulator, an electric field is applied to obtain absorption, this entails the signal wavelength will be on the red side of the absorption peak. Corresponding to the shift of the peak wavelength, the refractive index increases yielding a positive alpha parameter.

On the other hand, in the case of QDs, due to their discrete absorption peak, the signal wavelength can be put at the blue side of the absorption peak. With the signal wavelength on the blue side under the application of the electric field, the reduction of the electric field causes the wavelength shift of the absorption peak to increase the absorption at the signal wavelength. Correspondingly, the refractive index reduces. The refractive index change is opposite to that of the QWs, thus yielding a negative alpha value.

In other words, for the operation of the novel modulator, the electric field is applied to the modulator for the light-on state and is reduced for the light-off state, in an opposite manner to the conventional configuration. When the light is turned off, electric field is reduced from the high field to the lower field. At this high field region alpha is negative yielding blue chirp to compress the light signal pulse.

2.5 Photodetection

The full breadth of different types of photodetectors would require another thesis, thus provided in this section is a brief introduction to photodiodes followed by the photocurrent process.

Photodetectors are widely employed in telecommunication systems for optical signal detection. The photodetector absorbs the incident photons by atomic interactions in the material. These interactions produce photo-excited carriers or photocarriers. The generation of a photocarrier corresponds to the formation of an electron-hole pair. When these photocarriers transport charge they form an electrical photocurrent that can be processed.

To achieve high responsivity and bandwidth, photodiodes with waveguide structures have become a well-known route. Optical waveguides are utilized with embedded absorbing material in a PIN diode. The general operation of a PIN photodiode is explained in the next section.

Another type of photodiode is known as the avalanche photodiode (APD). In contrast to the conventional PIN photodiodes, which produce a single electron-hole pair in response to photon absorption, an APD can generate many electron-hole pairs from a single photon absorption. This internal gain makes APDs attractive for use in making sensitive receivers.

When a p-n junction is subjected to a high reverse bias, there are two breakdown mechanisms that can occur. The first one is when the atoms directly ionize due to the applied field (Zener breakdown). This is employed in voltage-regulating diodes. The second mechanism is due to high velocity carriers resulting in impact ionizations within the semiconductor that generate additional carriers (avalanche breakdown). This forms the principle of APDs operation.

QDs have potential to be employed as absorbing material for photodetection applications, e.g. high-efficiency solar cells [39, 40]. QDs have been proposed to increase the maximum achievable conversion efficiency of solar photons to up to $\sim 66\%$ through exploiting hot photogenerated carriers. This is based on the hot carriers in QD solar cells to generate and collect additional electron-hole pairs through impact ionization [39]. In QDs, the absorption

peak is expected to be resilient to carrier ionization at high biases due to the high carrier localization.

Furthermore, as explained in the motivation section, QDs exhibit a number of other advantages for employment in photodetectors, such as sensitivity to normal-incident radiation [41 –43], and low dark currents [44, 45] which precipitates high detectivity. The latter is due to the weak thermionic coupling between the ground state and excited states, which is expected to result in lower thermal excitation and, therefore lower dark current and higher operating temperature. The corresponding increase in the lifetimes of excited carriers should enable higher responsivities as carriers have more time to escape and contribute to the PC before relaxing to the ground state [46-47].

2.6 Photocurrent process

PC is the current generated from the electrons and holes created by photons absorbed in a photosensitive device such as a mesa- or a photo-diode. As in the case of a photodiode, these photo-generated carriers must be quickly swept out of the active region before they get a chance to recombine. Therefore, a reverse bias is applied to the terminals of the device and the current is measure in an external circuit.

Figure 2.2 provides a schematic representation of this process. An aerial view of the optical access mesa diode is also shown.

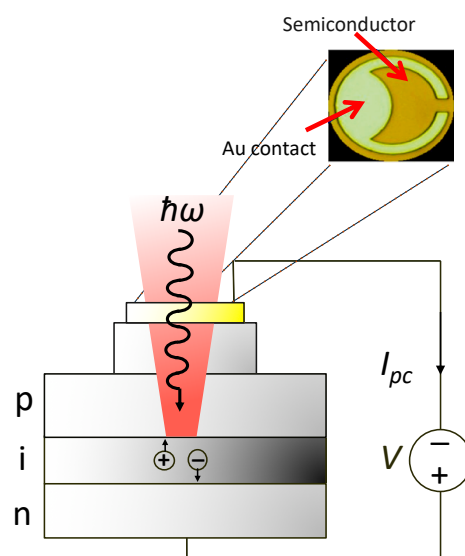


Figure 2.2 Schematic representation of the photocurrent process and the aerial view of the optical contact mesa diode

The diode is comprised of a p-n junction and a thin intrinsic active layer within the depletion region. The diode is operated in reverse bias with a positive voltage V applied to the n-region. This will in turn generate a strong DC E-field across the intrinsic region which would rapidly sweep the photogenerated electrons and holes towards the contacts and into the external circuit. This is the PC, I_{pc} .

Figure 2.3 shows a schematic band diagram of a p-i-n structure under reverse-bias. This will inhibit flow of current in the circuit when there is no light incident on the device. Nonetheless an insignificant amount of current still flows in the circuit under such regime. The process of carrier escape from the dots is expected to involve a mixture of thermionic emission and tunneling through the barrier as shown schematically below.

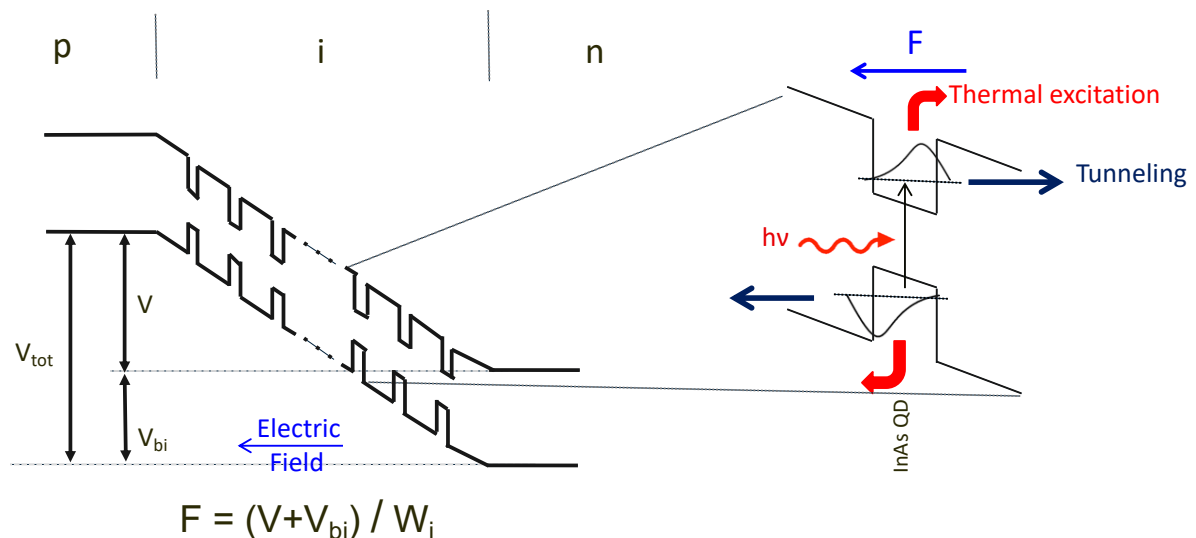


Figure 2.3 a) Schematic band diagram of a p-i-n structure under reverse bias, b) carrier escape occurs either through tunneling or thermal excitation.

The inter-band absorption and the subsequent escape processes are illustrated in Figure 2.3 b). PC can be measured to obtain a very good indication of the absorption spectrum of the active elements, which is determined by the overlap of the electron and hole wave functions, and the mechanism by which carriers escape into the external circuit.

The fraction of PC generated per incident optical power P of the incoming light beam is defined as responsivity, and is given by:

$$R = \frac{I_{PC}}{P} = \frac{\eta e}{\hbar\omega} (1 - e^{-\alpha l}) A/W \quad 2.1$$

The PC term in the numerator is made up of absorption of photons that generate electron-hole pairs at a certain quantum efficiency. Consequently, a high responsivity can be obtained with a large absorption and high quantum efficiency. From an engineering point of view, in an ideal situation both absorption and quantum efficiency are close/equal to unity so that the responsivity is simply given by $e/\hbar\omega$. This is the upper limit on the highest achievable responsivity. For instance, the highest achievable responsivity for a 620 nm photon is 0.5 A/W. Meticulously engineered photodetectors responsivity figures approach this limit quite closely.

2.6.1 Experimental set-up

Samples were first mounted and bonded onto gold tiles for characterization. A schematic diagram of the measurement system is presented in figure 2.4. White light source is provided from a tungsten halogen lamp at 24 V (power density ~ 3 mW/cm²). An optical chopper was utilized to modulate the intensity of light at 216 Hz to lower white noise and to employ lock-in amplification, as the PC signal will also be modulated at this frequency. The light was passed through a long-pass filter (transmitting > 800 nm), and then dispersed by the monochromator to select the appropriate wavelength. The monochromator was connected to the computer, through a stepper motor, to enable wavelength selection.

The widths of the entrance and exit slits were set to 300 μ m (provided the grating contains 600 1/mm) yielding a resolution of 1.92 nm. A cylindrical collimating and a focusing lens were then used to focus the monochromatic light onto the 400 μ m annular contact of the mesa diodes at room temperature.

The resultant PC was detected through standard lock-in techniques. The lock-in amplifier, the Stanford research systems SR 830 unit, was referenced through a phase locked loop to the operating frequency of the optical chopper. A Keithley 4200 semiconductor characterization system was utilized in order to apply DC voltage across the device, along the growth direction.

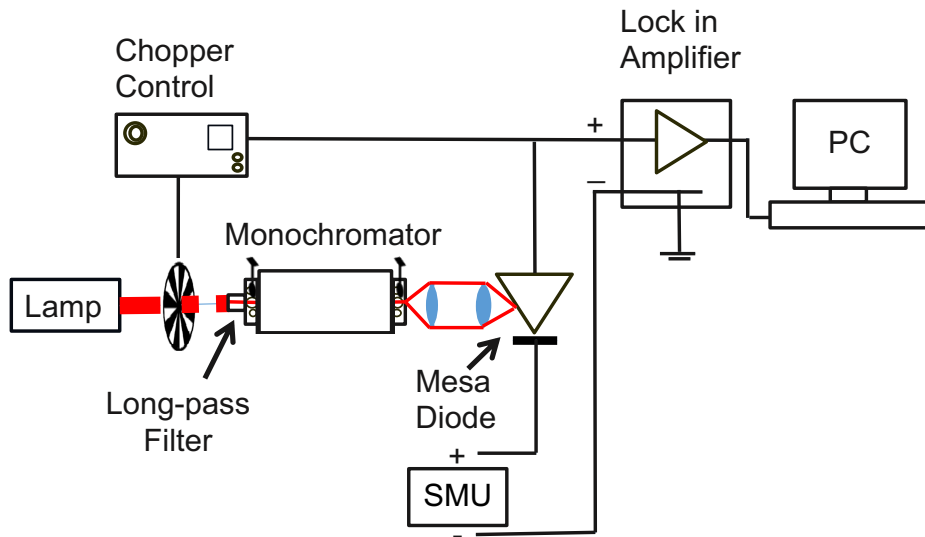


Figure 2.4 schematics of the photocurrent experimental set-up.

The low incident power ($\sim 3 \text{ mW/cm}^2$ with bandwidth of $\sim 8\text{meV}$) results in very low carrier occupancies in the QDs therefore, many carrier occupation effects can be neglected [48]. It is worthy to note that the amplitude of modulation regulates the bandwidth of the detected signal, as the bandwidth monotonically increases with modulation frequency.

2.7 Results

In this section the correction and normalization processes to obtain responsivity from the PC spectra are presented first. Subsequently, the responsivity spectra at a number of different reverse biases are provided, and the shift and magnitude of the observed absorption peaks are investigated.

The PC spectra of a range of QD and QW and hybrid QD/QW devices were extracted. However, their corresponding analysis and discussion would fall outside the scope of this project. The devices considered in this work are comprised of QDs only. The layer structure of the epitaxial material is shown schematically in Figure 2.5. The growth of the active region (QD containing intrinsic region of the p-i-n diode) begins with 60nm of un-doped GaAs, followed by 8 repeats of InAs QDs (InAs QDs and GaAs barriers). Each repeat is comprised of 2.5 ML of self-assembling InAs QDs, an InGaAs strain reducing layer (shown in blue color in the Figure), and a 40 nm GaAs buffer. The intrinsic region is sandwiched between p- and n-doped AlGaAs cladding layers, constituting a 485nm active region, and the structure is grown on a silicon

doped GaAs substrate. All wafers were provided by a commercial supplier, QD Laser Inc., Japan.

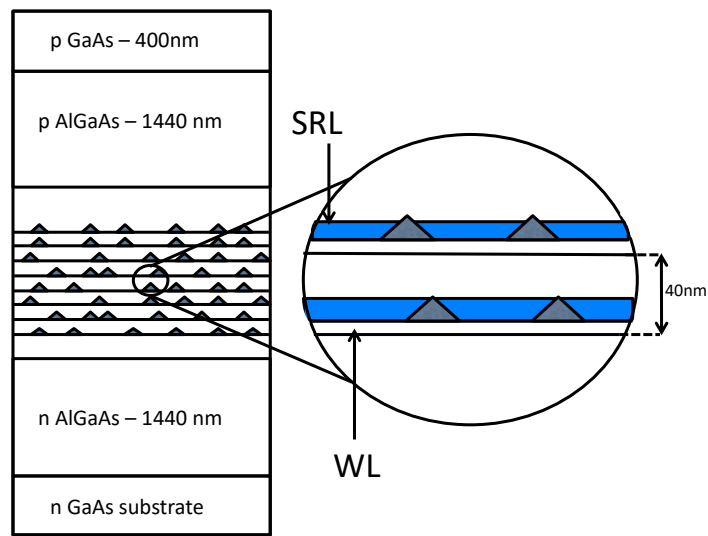


Figure 2.5 schematic diagram of the diode's layer structure.

The InAs QDs are embedded in an $\text{In}_x\text{Ga}_{1-x}\text{As}$ matrix, the so-called strain reducing layer (SRL), which acts to relax the stress on InAs dots induced by lattice mismatch between InAs and GaAs, thereby pushing ground state emission to longer wavelengths [49].

The current vs bias characteristics of the device is examined first. This is carried out on the optical access mesa diodes and the results are presented in figure 2.6. Turn on and break down voltages, as shown in fig. 2.6 a) and b), are at 0.8 and -20 V, respectively.

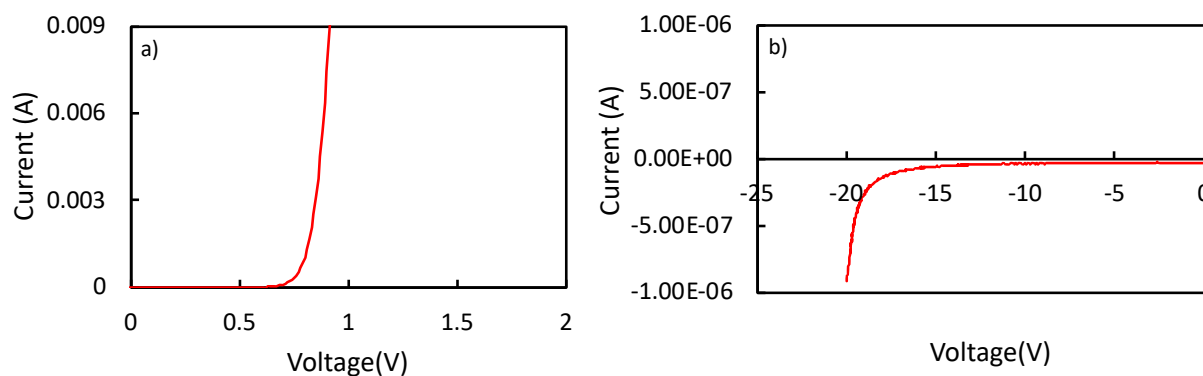


Figure 2.6 I-V characteristics of sample AD

In a reverse bias configuration, E-field is applied with a relatively small dark current density ($\sim 600 \text{ nA/cm}^2$ at -5 V) up to 20 V , which is a lower value compared to previous reports by ~ 3 orders of magnitude [22,23]. However, these reports were for large mesa diodes fabricated on epitaxial material grown on Si [22], and on very small diameter devices where surface leakage may be dominant [23]. Table 2 reflects a comparison of dark currents in these reports and some commercial photodetector devices.

Material	Device Diameter (μm)	Dark Current ($\times 10^{-9} \text{ A/cm}^2$)	Comment	Reference
InAs/GaAs QDs	400	~ 600	-	This Work
InAs/GaAs QDs on Si	400	$\sim 800,000$	Grown on Si – direct comparison difficult	[22]
InAs/AlInAs/InP QDs	14	$\sim 300,000$	Small device – sidewall leakage	[23]
Bulk InGaAs/InP	200	~ 100	InP substrate	Hamamatsu G11193-02R
Bulk GaAs	80	~ 600	Bulk GaAs – good comparison	Kyosemi KPDG008

Table 2 Dark current comparison

Considering the non-optimized structure under study here, identical dark current values are achieved in a commercial bulk GaAs based photodetector with a 5 times smaller diameter. This exhibits one of the advantageous aspects of using QD active medium for photodetection.

Figure 2.7 plots the short circuit PC spectrum as a function of energy. There is a notch at around $1 \mu\text{m}$ (1.241 eV) which is attributed to the PC measurement system.

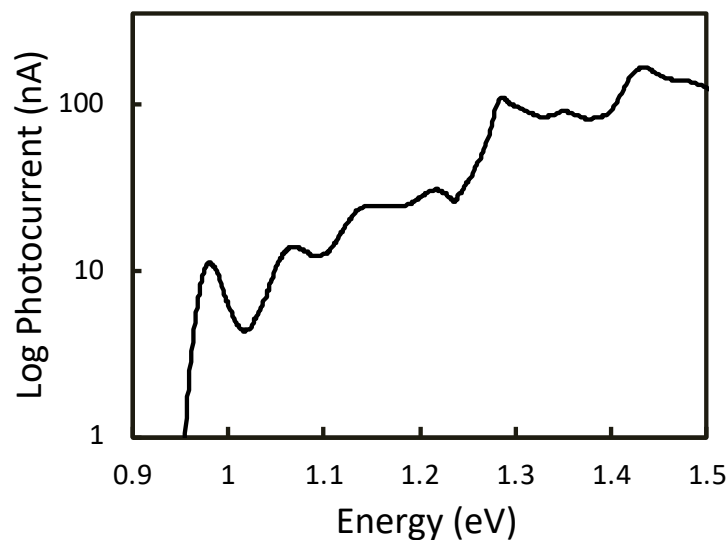


Figure 2.7 Sample AD 0V original photocurrent spectrum

This feature is caused by the combination of all the optics involved in producing the monochromatic light. As mentioned before, photo-responsivity is defined as the current generated as a result of the incident optical power. To obtain responsivity, the system's power spectrum is needed. Thus, an InGaAs photodetector with known responsivity versus wavelength was used. The relevant spectra are shown in Figure 2.8.

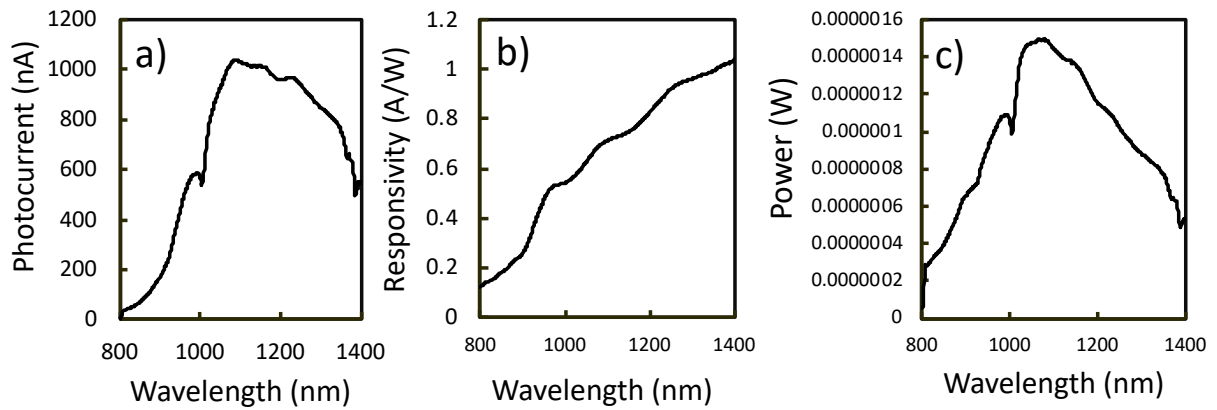


Figure 2.8 a) Measurement system PC spectrum, b) Photodetector's responsivity, and c) The corresponding power spectrum

Subsequently the power spectrum in 2.8 c) was utilized to normalize the raw PC spectra to obtain responsivity. Figure 2.9 plots the corresponding normalized responsivity spectrum from fig. 2.7. The resonant features are in good agreement to reports in an identical structure [50]

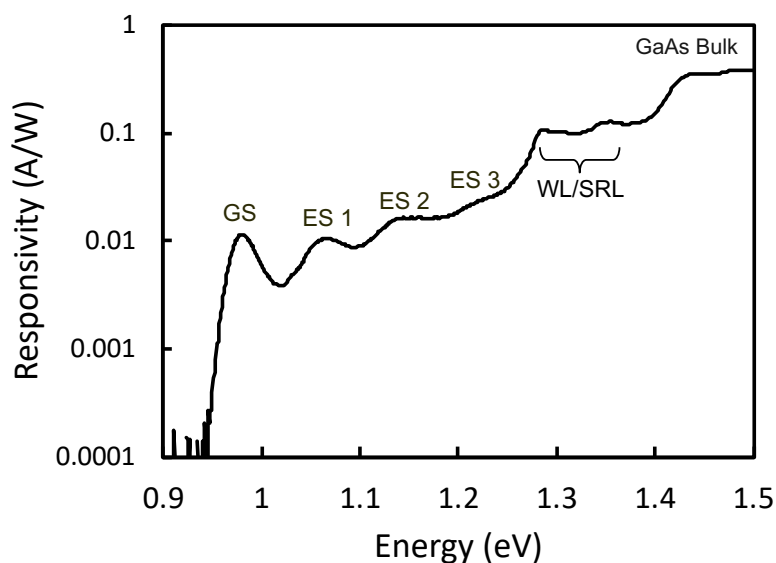


Figure 2.9 Normalized responsivity spectrum of sample AD

The spectrum is made up of several well-resolved features. The first four are ascribed to the inter-band transitions of the QDs ground state (GS) and excited states (ES) 1 to 3. Then two features attributed to the 2-D wetting layer/strain reducing layer transitions, and one last feature that is due to the GaAs band edge. Notably, the full width at half maximum (FWHM) of the GS absorption is 28 meV, which is very small relative to the limited number of PC spectroscopy reports in the literature [17-19]. This underscores the high uniformity of these QDs.

Moreover, investigation of the PC spectra under electric field provides important information about the modification of the carrier wave functions and thus the above features with respect to energy.

Figure 2.10 plots the spectra of sample AD as a function of electric field as a function of energy. The applied DC field tilts the potential barriers and distorts carrier wave functions, as the electrons tend to move towards the anode and the holes towards the cathode. This has an important implication. All QD associated transitions shift to lower energies due to the electrostatic interaction between the electric dipole in QDs and the field (QCSS).

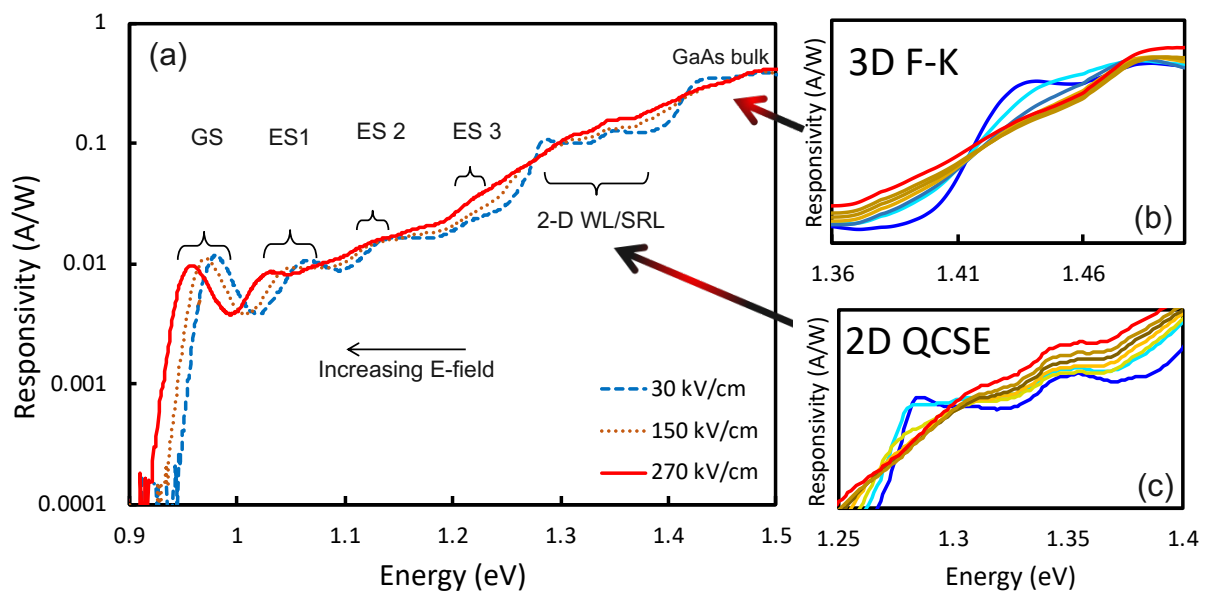


Figure 2.10 a) Spectra of sample AD as a function of bias (0,6,and 12V), b) Band edge, and c) WL/SRL (0-12 at every 2V)

PC responsivity spectra of the QD optical contact mesa diode is presented in figure 2.10 a) at reverse biases of 0, 6, and 12 V at room temperature. These biases correspond to electric fields

of 30, 150, and 270 kV/cm, respectively. As before, the spectra are comprised of 4 features due to the inter-band transitions of the QDs, 2 features that are attributed to the 2-D wetting layer/strain reducing layer transitions, and one last feature that is from the bulk GaAs band edge transition at 1.42 eV. The QD transitions are superimposed on a broad background signal that increases with energy. From the calculated energy levels for an identical structure [50], the bound-to-bound QD transitions are expected to occur at energies of up to ~ 1.22 eV, afterwards bound (hh) to continuum (e) absorption increases as $E^{-1/2}$. At 1.28 eV, a step-like absorption continuum is observed, attributed to the 2-D WL/SRL region of the QD active element.

The spectra in Figure 2.10 (b and c) are taken at biases of 0-12 V (30-270 kV/cm), and data are shown in 2 V (40kV/cm) intervals for clarity. Fig. 2.10 b) plots the PC spectra with respect to applied bias in the energy range 1.36 to 1.51 eV. This region corresponds to absorption within the bulk GaAs of the active region. It is observed that as a result of the applied electric field absorption is increased below the band gap (1.37 – 1.39 eV) and an oscillatory behavior occurs above the band gap (1.43 -1.44 eV). This is attributed to the Franz-Keldysh effect [51, 52] that is a consequence of the penetration of the wavefunctions into the band gap as electric field is applied. The application of E-field distorts the plane wave electron and hole wavefunctions to Airy functions, thereby resulting in the characteristics seen in Figure 2.10 b. In other words, these effects occur as the additional electric potential results in solution of the Schrödinger equation to become Airy functions, which decay exponentially into the forbidden energy gap. This causes an increased absorption of photons whose energies are lower than the gap energy. The alteration in the absorption of photons with higher energy than the gap energy exhibits an oscillatory behavior due to interferences of airy functions in the conduction band.

Figure 2.10 c) plots PC as a function of bias in the energy range 1.25 to 1.4 eV. This region corresponds to the optical transitions from the 2-D WL/SRL within the QD structure. The PC spectra display the classic QCSE behavior, showing a quadratic shift of peak energy, and a monotonic reduction in oscillator strength with increasing applied E-field [53]. This effect is more severe for the lowest level ($n=1$) since its orbit is distorted more severely than the higher levels. This is evident in Figure 2.10 c), since the e_1hh_1 transition of the QW, located at energy of 1.27 eV, quenches at a field of 110 kV/cm, while e_2hh_2 at 1.35 eV is still resolvable at an E-field of 270 kV/cm. The E-field dependent optical absorption in 2-D QW structures has been extensively studied [54], and the red shift of exciton energy has been calculated [56].

With respect to the QD ground state transitions, a clear shift of the spectra to lower energies is observed, indicative of QCSE. As mentioned previously, this is a result of the applied electric field in the growth direction, which shifts the electron and holes wave functions out of their overlap causing a decrease in the oscillator strength. The magnitude of this DC electric field is

$$F = \frac{V_{built-in} + V_{bias}}{L_i} \quad 2.2$$

Where L_i is the total thickness of the active region. $V_{built-in}$ is the band-gap voltage of the GaAs doped regions (~ 1.4 V from its transition energy).

Figure 2.11 plots the evolution of QD ground state PC spectrum in the energy region of 0.92 to 1.0 eV for E-fields from 30 to 270 kV/cm with 40 kV/cm intervals. At a first glance, it appears that the shift is almost linear with applied E-field. The peak absorption initially increases at 70 kV/cm, which is attributed to the E-field reaching a strong enough magnitude to efficiently sweep carriers out of the dots before they recombine. The peak absorption decreases monotonically thereafter, which is attributed to the reduction of e-h wavefunction overlap (oscillator strength) as the E-field is increased giving rise to the 0-D QCSE, which is also evident in the observed red shift of the peaks observed.

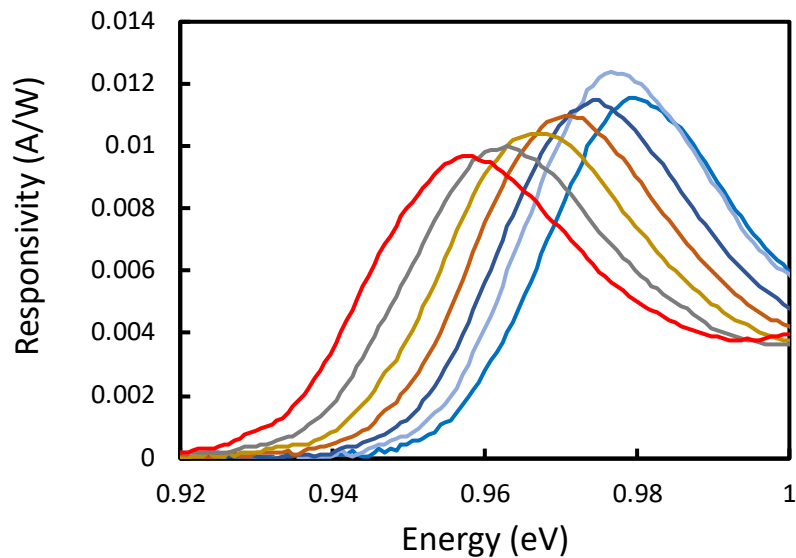


Figure 2.11 QCSE in the QDs ground state of sample AD

At low reverse biases, a responsivity of ~ 12.3 mA/W is observed, in line (considering the higher number of layers and higher areal density) with previous reports [17-19]. The E-field acts to distort the e-h wavefunctions in a very similar manner to that observed for the 2-D WL/SRL. However, because of the extra dimension of quantization in QDs, the wavefunctions are much more strongly localized compared to the QWs and hence the absorption strength does not fall off as significantly as it does for the 2-D system and persist at higher fields. This change in (essentially) the absorption spectra can be utilized for modulation purposes but for now let's investigate the dipole moment.

The field dependence of the transition energies can be described to a very reasonable approximation by the quadratic equation:

$$E = \beta F^2 + pF + E_0 \quad 2.3$$

Where E_0 is the transition energy at 0 field, p arises from the non-zero dipole moment, and β is a coefficient of polarization of the dots in the applied field. The maximum transition energy occurs at a non-zero field, this asymmetry about $F=0$ is the direct result of the permanent dipole moment (p). At higher fields the exciton dipole moment saturates at a value limited by $p=er$.

Figure 2.12 shows a quadratic fit to the series of transition energies as a function of applied E-field.

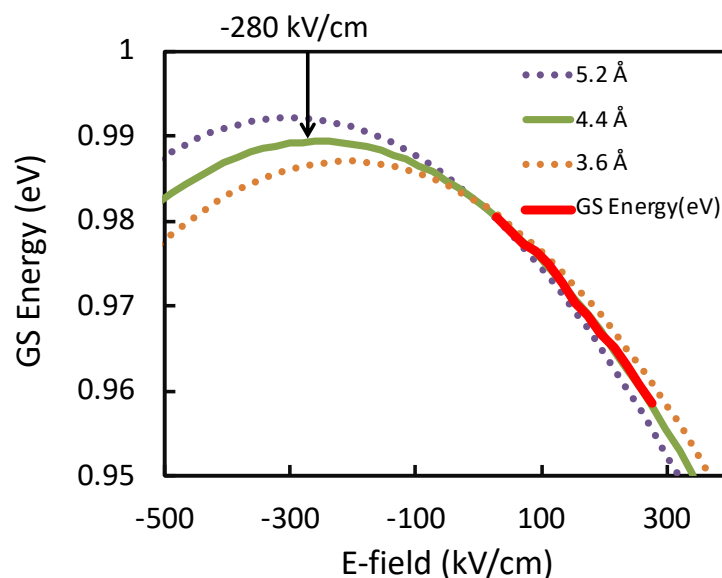


Figure 2.12 GS transition energies of sample AD as a function of electric field with a quadratic fit

A good fit to the data is obtained using values of p and β of 5.64×10^{-29} Cm and $0.98 \mu\text{eV}/(\text{kV}/\text{cm})^2$, respectively. The error range is investigated by contouring the quadratic fit above and below the energy curve for best fit. The fit indicates a clear asymmetry about $F=0$, with a maximum energy at a field of $280 \text{ kV}/\text{cm}$, giving rise to a permanent dipole moment of $p= 5.64 \times 10^{-29}$ Cm. By including the fit analysis, this would correspond to an electron-hole separation of $4.4 \pm 0.5 \text{ \AA}$ that is in line with other values reported in the literature [19, 57] for shorter wavelength structures. It can be seen that the maximum GS transition energy occurs for a negative field. This demonstrates that a permanent dipole with the hole above the electron is a general property of these QDs. For photodetection and modulation purposes using QDs, this entails choosing the correct bias to harness the maximum GS energy for higher detectivity and higher extinction ratios, respectively.

Figure 2.13 is a schematic representation of the inverted e-h alignment within a single QD.

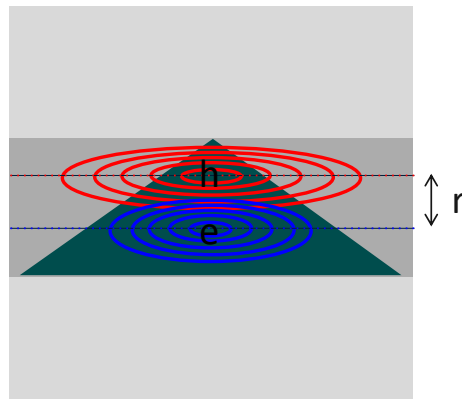


Figure 2.13 Schematic presentation of electron and hole alignment within the QDs

The measurements on the QD device transitional states are compared to QCSE data for a range of QW structures in the following.

Fig. 2.15 plots the energy shift of QD GS peaks (QCSS) with respect to the applied E-field compared to a number of QW structures from the literature with respect to applied electric field. The almost linear shift of the QD absorption peak is in stark contrast to the quadratic behavior of the QWs. It is observed that the QDs also demonstrate a lower rate of peak shift with applied E-field (~ 0.1 *c.f.* $\sim 0.2 \text{ meV}/\text{kVcm}^{-1}$). This characteristic is also attributed to the strong localization of the wavefunctions within the dots.

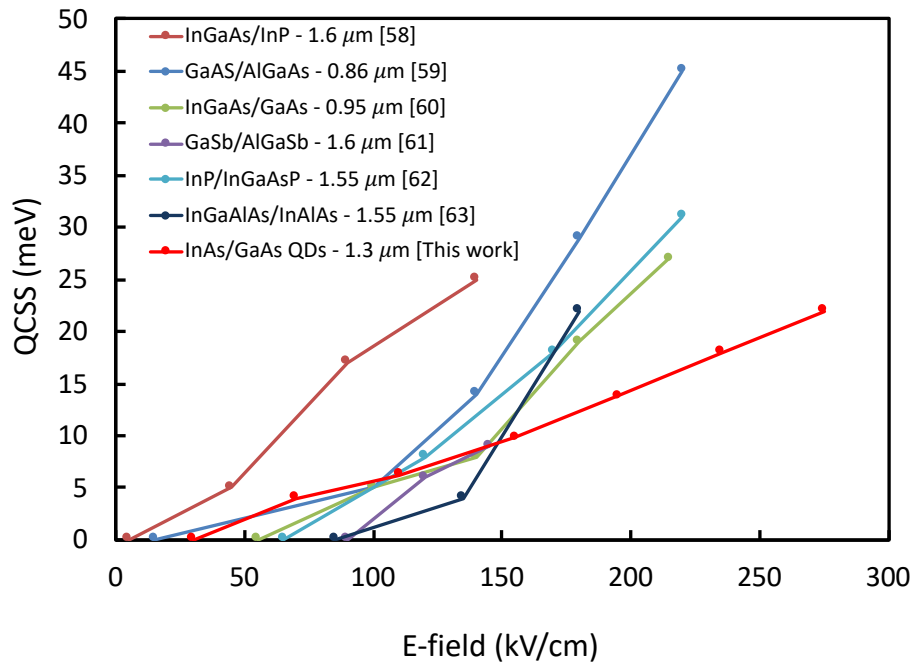


Figure 2.15 Quantum-confined Stark shift (QCSS) of typical QW absorption peaks as a function of E-field

Figure 2.16 plots the normalized amplitude of the ground state absorption peaks of the QD device and the same QWs studies.

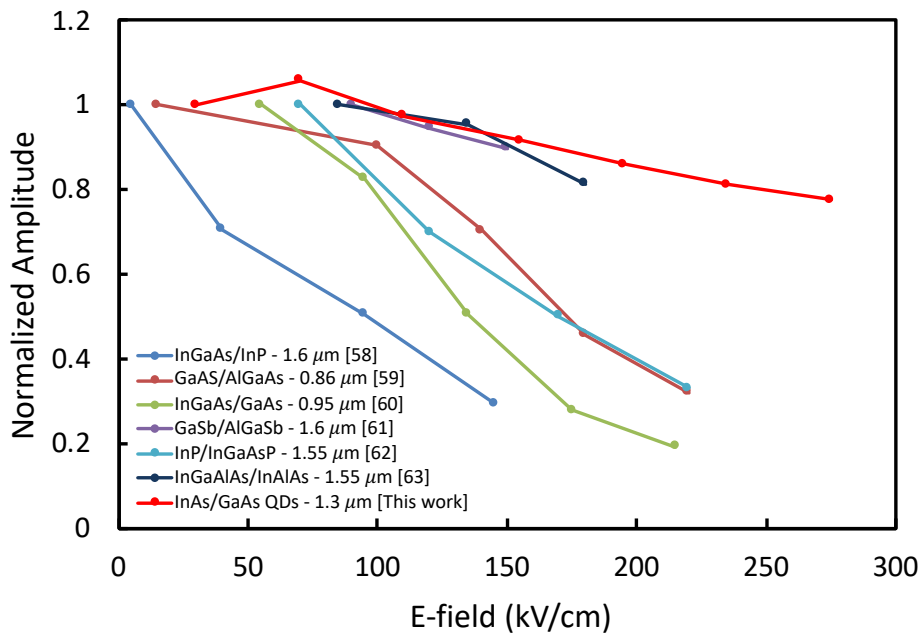


Figure 2.16 Normalized amplitude of absorption as a function of E-field

It is evident that the QDs studied in this work maintain a higher normalized absorption as reverse bias is increase, while the excitons within the QWs are more readily ionized with increasing E-field due to the comparatively lower degree of wavefunction localization.

2.8 Application – electro absorption modulator (EAM)

In this section the GS responsivity data is utilized with a view for employment in EAM applications.

Figure 2.17 plots the 0 and 12 V spectra in the GS region of measurement as a function of energy.

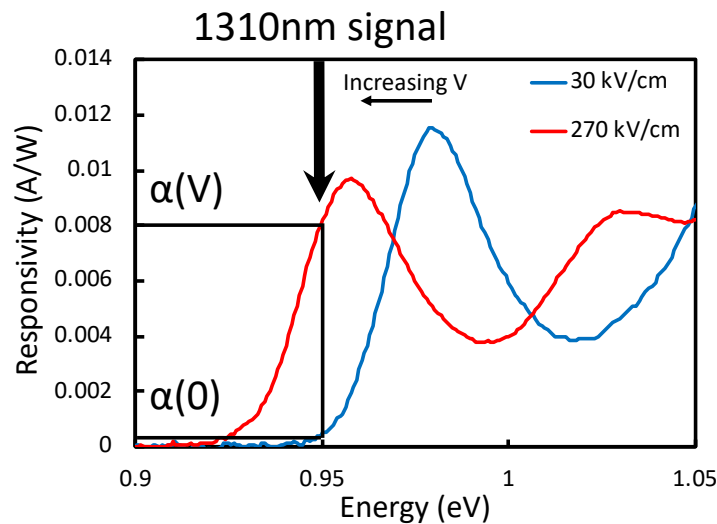


Figure 2.17 0 and 12 V responsivity spectra as a function of energy for conventional EAM application

In a conventional EAM configuration, the signal is blocked ('0') by the application of E-field (270 kV/cm) and is transmitted ('1') by stepping the absorption edge out of the incoming signal when 0V is applied (30 kV/cm). A peak shift of 23 meV is obtained in the figure above from 0-12V compared to the 28 meV linewidth of the GS. Considering the ER is given as the ratio of the on and off powers as:

$$ER = \frac{P_{out}(V_{on} = V)}{P_{out}(V_{off} = 0)} = \frac{e^{-\alpha(V)L}}{e^{-\alpha(0)L}} \quad 2.4$$

An ER of 20 dB can be achieved using this conventional configuration.

Figure 2.18 a) replots the above figure but for a novel configuration of modulation to obtain negative alpha leading to blue chirping. 2.18 b) plots the change in absorption spectrum to highlight the positive and the negative change in absorption for these modulation configurations. Note that this change in the absorption spectrum could be presented in terms of modal loss, with the unit of cm^{-1} . This needs knowledge of the absorption/gain spectra which will be investigated in the next chapter and the data will thus be utilized to present the modal loss in chapter 4.

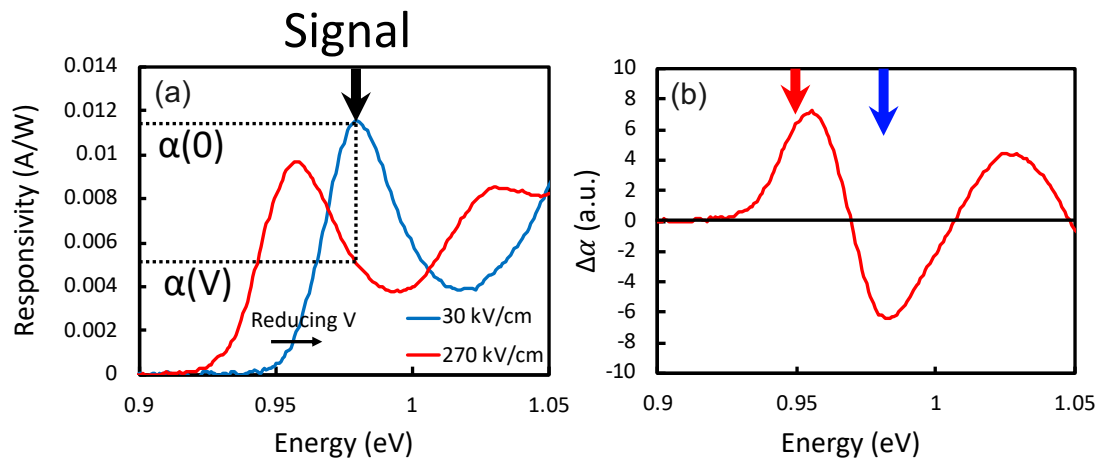


Figure 2.18 a) 0 and 12 V responsivity spectra as a function of energy for novel EAM application with negative chirp. b) Change in absorption spectrum, red and blue arrows indicate the signs of the final acquired chirp for novel and conventional EAM configurations, respectively

Although negative chirp can be obtained utilizing the novel configuration, smaller ER values are achieved as compared to the conventional mode. Also, it must be noted that the voltage swings are larger in the results presented above as compared to the typical QW EAM counterparts which employ $\sim 3\text{V}$ pk-pk drivers therefore, modulation efficiency is expected to be relatively modest. This may be attributed to the lower QCSS in QDs *c.f.* QWs as investigated in fig. 2.15.

It is noted that the emission wavelength of the GS of the QDs of a laser active would be at $\sim 0.98\text{ eV}$ (see 0 bias curve in Figure 2.11), and at high bias this corresponds to the dip in absorption, being halfway between the absorption energies of the GS and ES (see high bias curve in Figure 2.17). It is anticipated that in a QD structure possessing an in-plane symmetry, the first ES transition would have double the degeneracy of that of the GS transition [66]. Nonetheless, the measured PC spectra does not reflect this. Furthermore, for this QD ensemble

with ground-state linewidth of 28 meV and a state separation of 85 meV, there should be minimal absorption between the GS-ES1 states. However, this is not evident in our findings and there is finite absorption at 1.02 eV. This characteristic is attributed to the asymmetry of the QDs in the major and minor flat orientations via high angle annular dark field imaging of the active media provided by my colleague, Dr. Wei Li, and became the subject of a separate study [64].

2.9 Application - avalanche photodetector (APD)

Another interesting feature of this device is the exhibition of impact ionization at higher reverse biases, above 15V, where the responsivity of the diode was investigated in the vicinity of break down region. Figure 2.20 plots the PC spectra at reverse biases of 15-20 V incremented by 1V, corresponding to E-field values of 340-440 kV/cm with 20kV/cm intervals. The 30kV/cm (0V) spectrum is also shown for comparison in the solid black line. A total shift of 40meV from zero applied bias to breakdown is observed. This is smaller than that observed for 1300nm InAs/GaAs QDs grown on Si substrates (*c.f.* 60meV) which may be due to a difference in the average QD height, brought about by the details of the SRL and capping process in MBE.

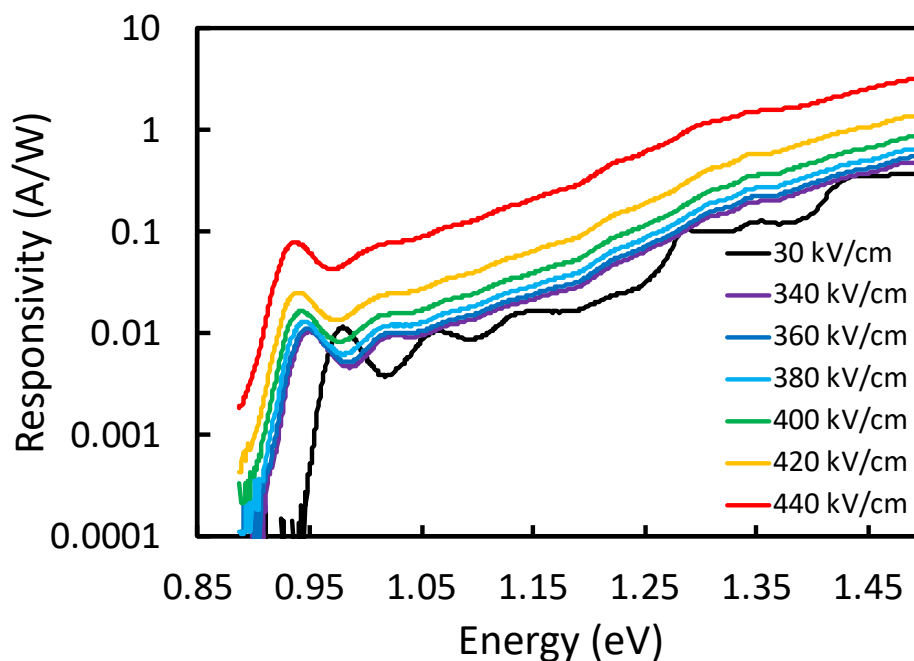


Figure 2.20 Responsivity at higher E-fields (15-20 V)

In this bias region, a clear increase in the PC spectra is observed at all wavelengths. Avalanche gain increases the PC exponentially and the GS absorption peak is still resolvable due to QDs carrier localization. This is attributed to photons being absorbed by the QDs, 2-D WL/SRL, and GaAs bulk layers and being subsequently subjected to impact ionization due to the high E-fields in the GaAs. The onset of the increase in PC with increasing reverse bias occurs at a bias of ~ 340 kV/cm, in good agreement with expected breakdown fields of ~ 430 kV/cm [64]. This behavior underscores the prospects of this material system for incorporation in a separate absorption and multiplication avalanche photodetector (SAM-APD).

The multiplication factor from the avalanche gain is obtained by taking the fraction of the PC, subtract the dark current contribution, and divide by the unity current (the linear region in which PC does not vary with the applied field) [65]:

$$M(V) = \frac{I_{PC} - I_{dark}}{I_{unity}} \quad 2.5$$

Figure 2.21 plots the multiplication factor due to the avalanche effect as a function of E-field.

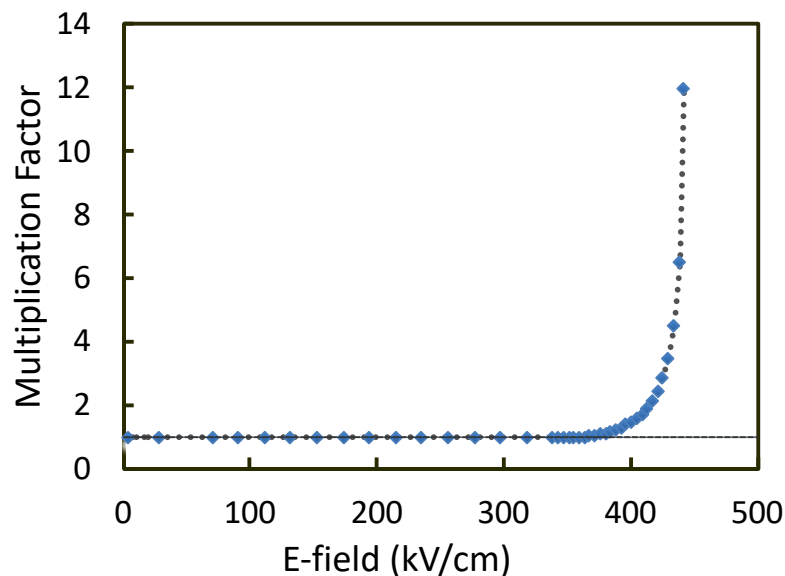


Figure 2.21 Ground state multiplication factor. Dotted line between the points is to show the trend. Dashed line indicative of unity current

It can be seen that PC increases 12-fold at an applied E-field of 440 kV/cm across the device. Previous reports for InAs/GaAs QDs grown monolithically on Si observed a small increase in avalanche gain for E-fields >180 kVcm $^{-1}$ which was attributed to an increase in PC due to the

QCSE [22]. Our results show no such abnormal behavior, suggesting that either the growth on Si, or specifics of the electronic structure of QDs grown using a different optimization process, gave rise to that observed behavior.

The occurrence of impact ionization/avalanche breakdown effects underscores the high level of material quality with limited evidence for Zener breakdown, and very low dark-current for these highly strained structures. The presence of impact ionization effects, coupled with strong QD absorption simultaneously and at very high E-fields is attractive. From the unbiased curve in fig. 2.20 shown in black, the emission wavelength of the GS of the QDs of a laser active would be at ~ 0.98 eV. This coincides with the dip in absorption in the 440 kV/cm biased spectrum shown in red, halfway between the the GS and ES. Nevertheless, it can be seen that carrier multiplication results in a significant increase in the PC at this wavelength and considerably compensates for the low absorption due to QCSE. Although these devices were not optimized for photodetection purposes these results suggest that a QD laser active element may be used as an avalanche photodiode for possible applications in sensing, range finding, and/or imaging where arrays of lasers and photodetectors may be utilized without the need for intricate epitaxial structures.

2.10 Discussion

The ground state shows a linewidth of 28 meV which is the result of the comparatively smaller inhomogeneous broadening in these QDs due to their high uniformity. Although narrower broadening and a state-splitting of 85 meV was expected to largely reduce the absorption loss between discrete levels to result in much larger modulation extinction ratios, a finite amount of absorption exists between the ground and the first excited state. In a transmission electron microscopic (TEM) study, these QDs were shown to have an anisotropy in the inhomogeneity of the QD size distribution [66]. This causes a modification to the shape of the DoS relative to the case of an isotropic size inhomogeneity. The PC spectrum shown in fig 2.9 along with the reported measured electroluminescence spectra are shown to be in good agreement with a simulation carried out on the shape of the DoS that utilizes the TEM data to define the size distribution of the QD ensemble.

Additionally, it is expected that the first excited state transition would exhibit twice the degeneracy of that of the GS in a QD material with in-plane symmetry [67]. Nevertheless, fig. 2.9 shows the first excited state to have its peak below that of the ground state. The TEM data identified that inhomogeneity is more noticeable in the 110 crystallographic direction than the $1\bar{1}0$. These findings suggest further advancement of QDs need to consider this anisotropic broadening for future development.

With respect to photodetector applications, the multiplication gain is created by carriers experiencing impact ionization in the multiplication region to amplify the input signal. Carrier ionization occurs as carriers are transported into the multiplication region toward higher electric field. High E-fields of around 600–700 kV/cm in an avalanche multiplication layer are commonly required for bulk / QW-based APDs [68]. From the presented results, the QD material exhibits avalanche multiplication under considerably lower electric fields due to the thinner intrinsic layer. For instance, in a conventional InGaAs bulk photodetector [22], the maximum electric field was limited to under 300 kV/cm at 20 V which yielded a multiplication factor of 12. In other InAs QD reports, a bias of 27.8 V was required to achieve a multiplication factor of 12 [23], 27.7 V (with the onset of impact ionization at 20 V) in [20], and a multiplication factor of 10 at 19.6 V for InP based QDs in [64]. In the presented results, electrons start to impact ionize when the electric field is sufficiently high (at 15 V or 340 kV/cm) compared to 600 kV/cm in [23] and ~ 450 kV/cm in [20], given their active layer was just over double the thickness of the presented work here.

Furthermore, a relatively small dark current density of ~ 600 nA/cm² was recorded at -5 V. This is lower by about 3 orders of magnitude compared to previous reports [22,23]. It is acknowledged that these reports were for large mesa diodes and were fabricated on epitaxial material grown on Si [22]. Also, the devices had very small diameters causing surface leakage to become dominant [23].

The absorption and also multiplication factor are expected to be improved by increasing the vertical stacking of the QD layers. An important design consideration for a photodiode structure is predicated upon the trade-off between responsivity and bandwidth [69]. A higher bandwidth generally necessitates a thinner absorption layer, which results in a lower responsivity. Also, a thinner absorption layer increases junction capacitance.

2.11 Conclusion

This chapter described and demonstrated a PC spectroscopic analysis of highly uniform QD material at 1.3 μm . The intensity and shift of the transitions have been compared with reports in the literature on QWs. It was shown that the comparison of QDs shift of PC peaks investigated in this work to a number of QW absorption reports indicated that the QDs maintain a high peak GS absorption up to high E-fields, and exhibit a lower Stark-shift as compared to their QW counterparts. This is attributed to the strong carrier confinement in QDs. We show that by contrast to the QW system, absorption from the QDs remains strong as E-field is increased. The absorption remains strong until impact ionization effects (in the GaAs intrinsic region) occur. I have gone on to discuss possible applications in which such properties may be exploited for absorption-based devices. Thus, prospects for employment in an EAM with potential of producing blue chirp under modulation and also in a SAM-APD with a relatively low dark current and a reasonable avalanche multiplication gain were investigated.

2.12 Future work

The material investigated in this chapter was designed for emission applications. Considering the prospects of highly uniform QDs for employment in absorption-based devices in the results presented in this chapter, optimizing this material for incorporation in detection and modulation devices is expected to be rewarding. For instance, it was shown that there is a finite amount of absorption half-way between the GS and ES1 which goes against the predicted transparent regions expected to result from the discrete energy levels. Therefore, growth optimization with the purpose of alleviating this characteristic could significantly improve the ER particularly for the novel EAM configuration scheme.

Also conducting this absorption study under different temperatures could provide valuable information particularly about the dark current. The major contributing component to dark current in APDs is typically attributed to the surface leakage current associated with the mesa [67]. Whereas, if the dark current increases with temperature in a manner consistent with the temperature dependence of the band gap of GaAs, tunneling current in the GaAs avalanche layer would be the factor causing it as reported in [67]. In this case, a current blocking AlGaAs layer can be employed to further lower the dark current count and therefore improve the

detectivity. Considering the low dark currents obtained from the presented structure, it seems that the field is confined effectively to the i region of the p-i-n diode. It would also be interesting to drive these devices above the breakdown limit in a pulsed manner to investigate the increase in the multiplication factor for photodetection purposes.

The findings of this chapter along with the gain studies in the following chapter are also utilized, with the design of a novel device in mind, to investigate the viability of an electro-absorption modulated laser in chapter 4.

References

- [1]: M. Sugawara, "Self-Assembled InGaAs/GaAs Quantum Dots," in *Semiconductors and Semimetals*, vol. 60, Academic Press- CA, 1999
- [2] D. Leonard, M. Krishnamurthy, C. Reaves, S. Denbaars, and P. Petroff, "Direct formation of quantum-sized dots from uniform coherent islands of InGaAs on GaAs surfaces," *Appl. Phys. Lett.* 63, 3203, 1993
- [3]: S. Fafard, R. Leon, D. Leonard, J. L. Merz, and P. M. Petroff, "Phonons and radiative recombination in self-assembled quantum dots," *Phys. Rev. B* 52, 5752, 1995
- [4]: N. N. Ledentsov, V. Shchukin, M. Grundmann, N. Kirstaedter, J. Bohrer, O. Schmidt, D. Bimberg, V. M. Ustinov, A. Y. Egorov, A. E. Zhukov, P. S. Kop'ev, S. V. Zaitsev, N. Yu. Gordeev, Z. Alferov, A. Borovkov, A. Kosogov, S. Ruvimov, P. Werner, U. Gosele, and J. Heydenreich, "Direct formation of vertically coupled quantum dots in Stranski-Krastanow growth," *Phys. Rev. B* 54, 8743, 1996
- [5]: L. Chu, M. Arzberger, G. Bohm, and G. Abstreiter, "Influence of growth conditions on the photoluminescence of self-assembled InAs/GaAs quantum dots," *J. Appl. Phys.* 85, 2355, 1999
- [6]: Y. Arakawa and S. Sakaki, "Multidimensional quantum well laser and temperature dependence of its threshold current," *Appl. Phys. Lett.* 40, 939, 1982
- [7]: Q. Xie, A. Kalburge, P. Chen, and A. Madhukar, "Observation of lasing from vertically self-organized InAs three-dimensional island quantum boxes on GaAs (001)," *IEEE Photon. Tech. Lett.* 8, 965, 1996
- [8]: R.T. Collins, K.V. Klitzing, and K. Ploog; "Photocurrent Spectroscopy of GaAs/Al_xGa_{1-x}As Quantum Wells in an Electric Field" *Physical Review B*, Vol. 33, No. 6, 1986
- [9]: D. A. B. Miller, D. S. Chemla, T. C. Damen, A. C. Gossard, W. Wiegmann, T. H. Wood, and C. A. Burrus, "Band-Edge Electroabsorption in Quantum Well Structures: The Quantum-Confined Stark Effect", *Phys. Rev. Lett.* 53, 2173, Nov 1984
- [10]: C. Weisbuch, R. Dingle, A. C. Gossard, and W. Wiegmann, "Optical Characterization of Interface Disorder in GaAs-Ga-AlAs Multiple Quantum Well Structures", *Solid State Commun.* 38, 709, 1981
- [11]: R. Heitz, M. Grundmann, N. N. Ledentsov, L. Ekey, M. Veit, D. Bimberg, V. M. Ustinov, A. Yu. Egorov, A. E. Zhukov, P. S. Kop'ev, and Zh. I. Alferov, "Multiphonon-relaxation processes in self-organized InAs/GaAs quantum dots", *Appl. Phys. Lett.* 68, 361, 1996

- [12]: R. J. Warburton, C. S. Dürr, K. Karrai, J. P. Kotthaus, G. Medeiros-Ribeiro, and P. M. Petroff; “Charged Excitons in Self-Assembled Semiconductor Quantum Dots”, *Physical Review Letter*, Vol. **79**, No. 26, (1997)
- [13] M. Grundmann, J. Christen, N. N. Ledentsov, J. Bohrer, and D. Bimberg, S. S. Ruvimov, P. Werner, U. Richter, U. Gosele, and J. Heydenreich, V. M. Ustinov, A. Yu. Egorov, A. E. Zhukov, P. S. Kop'ev, and Zh. I. Alferov; “Ultrannarrow Luminescence Lines from Single Quantum Dots”, *Physical Review Letters* Vol **74**, No. 20, (1995)
- [14] V. Ryzhii, “The theory of quantum-dot infrared phototransistors”, *Semicond. Sci. Technol.*, vol. 11, no. 5, pp. 759–765, 1996
- [15]: S Kim, H Mohseni, M Erdtmann, E Michel, C Jelen and Manizheh Razeghi , “ Growth and characterization of InGaAs/InGaP quantum dots for midinfrared photoconductive detector,” *Appl. Phys. Lett.* Vol 73, No 7, pp. 963-965, 1998
- [16] J Hoff, M Razeghi, and Brown G J, “Effect of the spin split-off band on optical absorption in p-type $Ga_{1-x}In_xAs_yP_{1-y}$ quantum-well infrared detectors,” *Phys. Rev. B* 54 10773, 1996
- [17]: P. Jin, C. M. Li, Z. Y. Zhang, F. Q. Liu, Y. H. Chen, X. L. Ye, B. Xu, and Z. G. Wang, “Quantum-confined Stark effect and built-in dipole moment in self-assembled InAs/GaAs quantum dots,” *Appl. Phys. Lett.*, 85, 2791– 2793 (2004).
- [18]: P.W. Fry et al., “Photocurrent spectroscopy of InAs/GaAs self-assembled quantum dots: Observation of a permanent dipole moment,” *Physica*, E 7, 408 – 412, 2000
- [19]: P.W. Fry, I.E. Itskevich, D.J. Mowbray, M.S. Skolnick, J.J. Finley, J.A. Barker, E.P. O'Reilly, L.R. Wilson, I.A. Larkin, P.A. Maksym, M. Hopkinson, M. Al-Khafaji, J.P.R. David, A.G. Cullis, G. Hill, J.C. Clark, “Inverted Electron-Hole Alignment in InAs-GaAs Self-Assembled Quantum Dots,” *Phys. Rev. Lett.*, 84, 334, 2000
- [20]: T. Umezawa, K. Akahane, A. Kanno, and T. Kawanishi, “Investigation of a 1.5- μ m-wavelength InAs-quantum-dot absorption layer for high-speed photodetector,” *Appl. Phys. Express* 7, 032201, 2014
- [21]: Y. Wan, Z. Zhang, R. Chao, J. Norman, D. Jung, C. Shang, Q. Li, M. Kennedy, D. Liang, C. Zhang, J. Shi, A. C. Gossard, K. M. Lau, and J. E. Bowers, “Monolithically integrated InAs/InGaAs quantum dot photodetectors on silicon substrates,” *Opt. Express* 25, 27715–27723, 2017
- [22]: I. Sandall, J. Ng, J. David, C. Tan, T. Wang, and H. Liu, “1300 nm Wavelength InAs Quantum Dot Photodetector Grown on Silicon,” *Opt. Express* 20, 10446-10452, 2012

- [23]: T. Umezawa, K. Akahane, N. Yamamoto, A. Kanno, T. Kawanishi, "Highly Sensitive Photodetector Using Ultra-High-Density 1.5- μm Quantum Dots for Advanced Optical Fiber Communications," *IEEE Journal of Selected Topics Quant. Electronics*, 20, 147-153, 2014
- [24]: P. Martyniuk and A. Rogalski, "Quantum-dot infrared photodetectors: Status and outlook," *Progress Quantum Electron.*, vol. 32, pp. 89–120, 2008
- [25]: D. A. B. Miller, D. S. Chemla, T. C. Damen, A. C. Gossard, W. Wiegmann, T. H. Wood, and C. A. Burrus. Electric field dependence of optical absorption near the band gap of quantum-well structures. *Phys. Rev. B*, 32(2):1043–1060, Jul 1985
- [26]: U Koren, TL Koch, H Presting, and BI Miller, "InGaAs/InP multiple quantum well waveguide phase modulator", *Appl. Phys. Lett.*, 50(7):368–370, 1986
- [27] M Aoki, N Kikuchi, K Sekine, S Sasaki, M Suzuki, T Taniwatari, Y Okuno, A Takai, and T Kawano. Low drive voltage and extremely low chirp integrated electroabsorption modulator/DFB laser for 2.5 Gbit/s 200 km normal fibre transmission. *Electronic Letters*, 29, pp. 1983–1984, 1993
- [28] K Wakita, O Mitomi, I Kotaka, S Nojima, and Y Kawamura. High-speed electrooptic phase modulators using InGaAs/InAlAs multiple quantum well waveguides. *IEEE Ph Tech. Lett.*, 1(12), pp 441–442, 1989
- [29] M Aoki, N Kikuchi, K Sekine, S Sasaki, M Suzuki, T Taniwatari, Y Okuno, A Takai, and T Kawano. Low drive voltage and extremely low chirp integrated electroabsorption modulator/DFB laser for 2.5 Gbit/s 200 km normal fibre transmission. *Electronic Letters*, 29, pp. 1983–1984, 1993
- [30]: J. C. Cartledge, and G. S. Burley, "The effect of laser chirping on lightwave system performance", *J. Lightwave Technol.*, vol. 7, no. 3, pp. 568-573, 1989
- [31]: R. A. Linke, "Modulation induced transient chirping in single frequency lasers", *J. Quantum Electron.*, vol. QE-21, no. 6, pp. 593-597, 1985
- [32]: E. S. Awad, P. S. Cho, C. Richardson, N. Moulton, J. Goldhar, "Optical 3R regeneration with all-optical timing extraction and simultaneous wavelength conversion using a single Electro-Absorption Modulator", in *Proceedings of ECOC'02*, paper 6.3.2, 2002
- [33]: A. Filios, et al., "16 channel, 10 Gb/s DWDM transmission of directly modulated lasers with 100 GHz channel spacing over 100 km of negative dispersion fiber", in *Proceedings of LEOS'01*, paper. ThK3, 2001
- [34] P. Paoletti, et al., "10 Gbit/s ultra-low chirp 1.55 μm directly modulated hybrid fiber grating – semiconductor laser source", in *Proceedings of ECOC'97*, pp. 107- 110, 1997

- [35] F. N. Timofeev, et al., “Low-chirp, 2.5 Gbit/s directly modulated fiber grating laser for WDM networks”, in Proceedings of OFC’97, paper ThM1, 1997
- [36]: S. Mohrdiek, H. Burkhard and H. Walter, “Chirp reduction of directly modulated semiconductor lasers at 10 Gb/s by strong CW light injection”, *J. Lightwave Technol.*, vol. 12, no. 3, pp. 418-442, 1994
- [37] J. Kondo, et al., “Low-drive-voltage 40 Gb/s modulator on X-cut LiNbO₃ wafer”, in Proceedings of ECOC, We.F.3.3, 2001
- [38] M. Sugiyama, et al., “Drive-less 40 Gb/s LiNbO₃ modulator with sub-1 V drive voltage”, in Proceedings of OFC, FB6-1, 2002
- [39]: A. J. Nozik, “Quantum dot solar cells”, *Physica E*, vol. 14, pp. 115–120, 2002
- [40]: A. Luque, A. Marti, “Increasing the efficiency of ideal solar cells by photon induced transitions at intermediate levels”, *Phys. Rev. Lett.*, Vol. 78, No. 26, 1997
- [41]: V. Ryzhii, “The theory of quantum-dot infrared phototransistors”, *Semicond. Sci. Technol.*, vol. 11, no. 5, pp. 759–765, 1996
- [42]: J. Phillips, “Evaluation of the fundamental properties of quantum dot infrared detectors”, *J. Appl. Phys.*, vol. 91, no. 7, pp. 4590–4594, 2002
- [43]: D. Pan, E. Towe, and S. Kennerly, “Normal-incidence intersubband (In, Ga) As/GaAs quantum dot infrared photodetectors”, *Appl. Phys. Lett.*, vol. 73, pp. 1937–1939, 1998
- [44]: S. Chakrabarti, XH Su, P Bhattacharya, G Ariyawansa, and AU Perera, "Characteristics of a multicolor InGaAs-GaAs quantum-dot infrared photodetector." *IEEE Photonics technology letters* 17.1, 178-180, 2004
- [45]: AD Stiff, S Krishna, P Bhattacharya, and SW Kennerly “Normal-incidence, high-temperature, mid-infrared, InAs-GaAs vertical quantum-dot infrared photodetector,” *IEEE Jour of Quant. Electron.* 37(11):1412-9, 2001
- [46]: L. Chu, A. Zrenner, G. Böhm, and G. Abstreiter, “Normal-incident intersubband photocurrent spectroscopy on InAs/GaAs quantum dots”, *Appl. Phys. Lett.*, vol. 75, pp. 3599–3601, 1999
- [47]: J. Urayama, T. B. Norris, J. Singh, and P. Bhattacharya, “Temperature dependent carrier dynamics in InGaAs self-assembled quantum dots”, *Phys. Rev. Lett.*, vol. 86, p. 4930, 2001
- [48]: R. J. Warburton, C. S. Durr, K. Karrai, J. P. Kotthaus, G. Medeiros-Ribeiro, and P. M. Petroff, “Charged Excitons in Self-Assembled Semiconductor Quantum Dots,” *Phys. Rev. Lett.* 79, 5282, 1997

- [49]: K. Nishi, H. Saito, S. Sugou, and J.S. Lee, "A narrow photoluminescence linewidth of 21 meV at 1.35 μm from strain-reduced InAs quantum dots covered by $\text{In}_{0.2}\text{Ga}_{0.8}\text{As}$ grown on GaAs substrates," *Appl. Phys. Lett.*, vol. 74, no. 8, pp. 1111–1113, Feb. 1999
- [50]: J. Kim and S.L. Chuang, "Theoretical and Experimental Study of Optical Gain, Refractive Index Change, and Linewidth Enhancement Factor of p-Doped Quantum-Dot Lasers", *IEEE J. Quant. Elec.*, Vol. 42, No. 9, 2006
- [51]: L. V. Keldysh, "Behavior of non-metallic crystals in strong electric fields," *J. Exp. Theor. Phys. (USSR)* 33, 994 (1957); translation *Sov. Phys. JETP*, 6, 763, 1958
- [52] W. Franz, "Einfluß eines elektrischen Feldes auf eine optische Absorptionskante," *Z. Naturforsch., Teil A* 13, 484, 1958
- [53]: D. A. B. Miller, "Optical Physics of Quantum Wells" in "Quantum Dynamics of Simple Systems," ed. G. -L. Oppo, S. M. Barnett, E. Riis, and M. Wilkinson, Institute of Physics, London, 239-266, 1996
- [54]: J. Weiner, D. A. B. Miller, and D. S. Chemla, "Quadratic Electro-Optic Effect due to the Quantum- Confined Stark Effect in Quantum Wells," *Appl. Phys. Lett.*, 50, 842-844, 1987
- [55]: G. Bastard, "Wave mechanics applied to semiconductor heterostructures," *Les Editions de Physique, Les Ulis, France*, 247-248, 1988
- [56]:
- [57]: Peng Jin, C. M. Li, Z. Y. Zhang, F. Q. Liu, Y. H. Chen, X. L. Ye, B. Xu, and Z. G. Wang, "Quantum-confined Stark effect and built-in dipole moment in self-assembled InAs / GaAs quantum dots," *Appl. Phys. Lett.*, 85, 2791, 2004
- [58]: I. Bar-Joseph, C. Klingshirn, D.A.B. Miller, D.S. Chemla, U. Koren, B.I. Miller, "Quantum-confined Stark effect in InGaAs/InP quantum wells grown by organometallic vapor phase epitaxy," *Appl. Phys. Lett.*, 50, 1010-1012, 1987
- [59]: D. A. B. Miller, J. S. Weiner and D. S. Chemla, "Electric Field Dependence of Linear Optical Properties in Quantum Well Structures: Waveguide Electroabsorption and Sum Rules," *IEEE J. Quantum Electron. QE - 22*, 1816-1830, 1986
- [60]: T.E. Van Eck, P. Chu, W. Chang, H. Wieder, "Electroabsorption in an InGaAs/GaAs strained-layer multiple quantum well structure," *Appl. Phys. Lett.*, 49, 135-136, 1986
- [61]: T. Miyazawa, S. Tarucha, Y. Ohmori, Y. Suzuki, and H. Okamoto "Observation of Room Temperature Excitons in GaSb–AlGaSb Multi-Quantum Wells," *Japanese J. of Appl. Phys.*, 25, 1986
- [62]: K. Sato, I. Kotaka, K. Wakita, Y. Kondo, M. Yamamoto, "Strained-InGaAsP MQW electroabsorption modulator integrated DFB laser," *Electronics Lett.*, 29, 1993

- [63] K. Wakita, I. Kotaka, O. Mitomi, H. Asai, Y. Kawamura, and M. Naganuma, "High-speed InGaAlAs /InAlAs Multiple Quantum Well Optical Modulators," *J. of Lightwave Tech.*, 8, 1990
- [64]: M Nada, Y. Muramoto, H. Yokoyama, N. Shigekawa, T. Ishibashi, and S. Kodama "Inverted InAlAs/InGaAs Avalanche Photodiode with Low–High–Low Electric Field Profile," *Jpn. J. Appl. Phys.* 51, 02BG03, 2012
- [65]: P. Yuan, K. A. Anselm, C. Hu, H. Nie, C. Lenox, A. L. Holmes, B. G. Streetman, J. C. Campbell, and R. J. McIntyre, "A New Look at Impact Ionization - Part II: Gain and Noise in Short Avalanche Photodiodes," *IEEE Tran. On Electron Devices*, 46, 1632, 1999
- [66]: I. M. E. Butler, W. Li, S. A. Sobhani, N. Babazadeh, I. M. Ross, K. Nishi, K. Takemasa, M. Sugawara, D. T. D. Childs, and R. A. Hogg, "Size anisotropy inhomogeneity effects in state-of-the-art quantum dot lasers," *App. Phys. Lett.*, Vol. 113, 012105, 2018
- [67]: H. Drexler D. Leonard, W. Hansen, J. P. Kotthaus, and P. M. Petroff. "Spectroscopy of quantum levels in charge-tunable InGaAs quantum dots." *Physical review letters* 73, no. 16 2252, 1994
- [68]: K. F. Brennan and Y. Wang, "Field and special geometry dependence of the electron and hole ionization rates in GaAs/AlGaAs multi-quantum well APD's," *IEEE Trans. Electron. Devices*, vol. 35, no. 5, pp. 634–641, May 1998
- [69]: T. Li, A.E. Willner, and I. Kaminow, "Optical Fiber Telecommunications Volume A: Components and Subsystems", Academic Press, pp. 221-259, 2010

Chapter 3

Temperature-Insensitive Zero Linewidth Enhancement Factor

3.1 Introduction

The linewidth of solid-state and gas-based lasers can be predicted with high precision using the Schawlow-Townes theory [1]. In semiconductor laser diodes, however, this predicted linewidth is considerably smaller than the linewidth that is measured. Fleming and Moradian [2] reported a measurement of laser spectral linewidth as a function of optical power which demonstrated 50 times higher linewidth as compared to the expectation by theory. Even though they corrected their analysis for optical dispersion and considered that the spontaneous emission factor is greater than unity in semiconductor lasers, the measured linewidth was still 30 times wider than the prediction. Henry, subsequently, demonstrated that the Schawlow-Townes linewidth is increased or enhanced relative to other types of lasers, such as solid-state or gas-based lasers [3]. New theory was developed by Vahala and Yariv [4,5] showing the expected enhancement of the linewidth to be of the form:

$$\Delta\nu = \Delta\nu_{S-T}(1 + \alpha_H^2) \quad 3.1$$

Where, $\Delta\nu$ is the spectral linewidth of the laser, $\Delta\nu_{S-T}$ is the predicted Schawlow-Townes linewidth, and α_H is the enhancement factor.

The linewidth enhancement factor (LEF), also known as the alpha-Henry or the alpha factor, is commonly used to describe this behaviour of semiconductor lasers with respect to other types of lasers and influences several fundamental aspects. A large value of LEF is undesirable in

that it precipitates many detrimental effects such as the increased lasing linewidth [3, 6], frequency chirp under modulation [7], the laser's intolerance to external optical feedback [8], as well as the occurrence of the filamentation in broad-area lasers [9].

The main source of noise in semiconductor lasers is due to spontaneous emission. The spontaneously emitted photons have random vector and scalar properties i.e. wavelength, polarization, direction, and phase, and may overlap or coincide with the vector and scalar properties of the coherent fields of the stimulated emission photons (lasing mode). The consequence of this 'contamination' is the generation of fluctuations in both the output intensity and output frequency of the laser.

Although the number of photons introduced into the lasing mode through spontaneous emission can be made small compared to the photons produced through stimulated emission, they can never be entirely removed, entailing that perfect coherence in a laser can never be achieved. This noisy characteristic is further exacerbated since in addition to the instantaneous phase changes due to the spontaneous emission photons perturbing the stimulated emission ones, there also exists a delayed phase change resulting from the instantaneous change in the field intensity. This occurs because in order to re-establish the steady-state field intensity, the laser goes through relaxation oscillation.

The intensity fluctuations are described by relative intensity noise (RIN), which will be considered in chapter 5. On the other hand, the frequency fluctuations are responsible for the enhancement of the spectral linewidth of semiconductor lasers, characterized through the LEF, which will be investigated in this chapter. Thus, in a fiber-optic communications system, there are two limitations to consider for maintaining a given bit error ratio for the transmission line. Firstly, intensity noise may result in the signal being indistinguishable from noise. Secondly, broadening of the optical pulses may result in inter-symbol interference by overlapping the train of optical pulses.

For typical quantum well (QW) lasers LEF values of the order of 2-6 have been reported [6,8]. For quantum dot (QD) lasers, simple models suggest very small LEF values close to zero. Different values have been achieved in experimentations occasionally even reaching negative values. Nevertheless, in spite of the desirable low LEF values reported in QD lasers, high-resolution, spectral or current dependent LEF studies at a range of temperatures are nebulously scattered in the literature. This is presumably due to noisy gain spectra, particularly at elevated

temperatures, yielding even noisier differential gain spectra which precipitates high fluctuations in the final extracted LEF spectra. Thus, reports in the literature demonstrate single LEF values at lasing wavelength or a limited number of data points in a relatively wide positive gain wavelength range. In this chapter, firstly the background knowledge and the motivation behind this LEF study is provided. Subsequently, in order to place this work in perspective, the gaps in knowledge are presented before delivering the outline of the chapter at the end of the section.

3.2 Background and motivation

Alpha-Henry, α_H , or the LEF can be explained in its most general form as the coupling between the real and the imaginary parts of the refractive index of a semiconductor material [3]:

$$LEF = \frac{d(n)/dN}{d(n')/dN} \quad 3.2$$

Where, n and n' are the real and the imaginary parts of the refractive index, respectively and N is the carrier density.

During relaxation oscillation mentioned above, there will be a net gain change of [3]:

$$\Delta g(t) = -2 \left(\frac{\omega}{c} \right) \Delta n'(t) \quad 3.3$$

Where, g is modal gain, ω is the frequency, C the speed of light, and $\Delta n'(t)$ is the deviation of the imaginary part of the refractive index from its steady-state value.

The variations in gain, $\Delta g(t)$, may be viewed in more detail considering the cause, which is variations in photon and carrier densities [10], *c.f.* eqn. A.13:

$$\Delta g(t) = g_N \Delta N - g_P \Delta N_p \quad 3.4$$

Where g_N and g_P are the gain derivatives due to carrier and photon densities, N and N_p , respectively. Note that the negative sign convention is to reflect the gain is increased with increasing carrier density and is decreased or compressed with increasing photon density.

The change in n' is caused by a change in carrier density, which will also alter the real part of the refractive index, n . Subsequently, substituting K , the free space wavevector [11], in eqn. (3.3) for $\frac{\omega}{c}$ and manipulating for $\Delta n'(t)$, eqn. (3.2) can be rewritten as:

$$LEF = -2k \frac{dn/dN}{dg/dN} \quad 3.5$$

These equations (3.2 and 3.4) show that gain and refractive index are correlated and their dependence can be quantified using the Kramers-Kronig relations [12].

Spectral purity of the lasing mode has always been a very important issue since the early stages of laser development. While gas-based and solid-state lasers typically operate with a comparatively narrower linewidth than their semiconductor counterparts, the former are poorer in terms of reliability, cost, and size. A plethora of research has been carried out to narrow down the linewidth in semiconductor lasers. Several device designs and configurations, most important of which the external cavity arrangement [2, 13, 14] and distributed feedback lasers (DFBs) [15], have been recommended for obtaining narrower linewidths.

The external cavity configurations are based on a laser chip typically with one end anti-reflection coated. The laser resonator is then completed with e.g. a collimating lens and an external mirror to couple the light back into the cavity. It should be noted that this is one of the very few cases where controlled optical feedback into the laser could be useful. Another type of external-cavity laser uses a resonator based on an optical fiber rather than on free-space optics. Narrow wavelength band optical feedback can then come from a fiber Bragg grating.

Mode-locking is another interesting feature of the external cavity configuration which is used to produce ultra-short laser pulses. Mode-locking stems from a frequency-domain interpretation, where in the mode-locked state many axial resonator modes oscillate with a locked relative phase.

In the case of the DFB laser design, note that if one or both of the end mirrors are replaced with a periodically structured element (a diffraction grating), the device then becomes a DBR laser (Distributed Bragg Reflector). These longitudinal diffraction grating mirrors reflect the light back in the cavity based on their interference. Due to this selectivity, diffraction grating mirrors reflect a narrower band of wavelengths than normal cleaved facet mirrors. This limits the number of standing waves that can be supported in the cavity. As a result, DBR lasers tend to be more spectrally stable than Fabry-Perot (FP) lasers with broadband mirrors. For DFB lasers, the grating and hence the reflection is typically continuous along the laser cavity, rather than at the either ends. This changes the modal characteristics and makes the laser more stable in terms of frequency and intensity fluctuations. In real-world applications, single-mode DFB

lasers with narrow spectral linewidth are essential for various applications, such as coherent sources and local oscillators for optical communication systems [16].

Another approach to reduce the LEF is through the modification of the density of states (DoS). New semiconductor materials, for instance, strained QWs [17] and also QDs, to be considered in what follows, have been recommended for narrower linewidth operation. In this section lowering the LEF through the use of lower dimensional structures is investigated.

The solutions to eqn. (3.2) were investigated by Yamanaka et. al. [18]. They pointed out that lasing oscillation near the peak of the differential gain spectrum rather than the peak in gain could be critical in reducing the LEF to zero. Given the differential and material gain peaks are coincident at the same wavelength, an LEF of zero may be acquired. Figure 3.1 plots their results for a QW laser at a lasing wavelength of 1.55 μm .

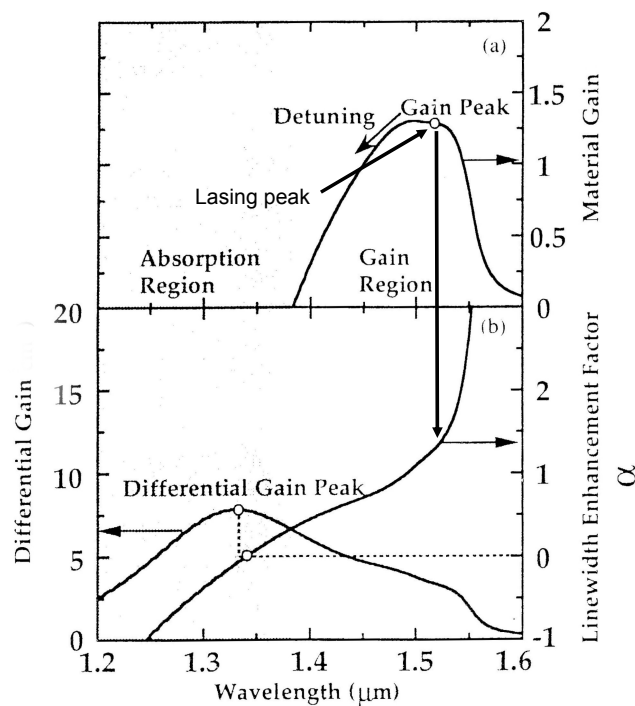


Figure 3.1: Changes of LEF vs wavelength with zero value at differential gain peak [18].

The plot shows material gain and differential gain as a function of wavelength for the laser and indicates the corresponding LEF value at the material gain peak. This suggests that a QW laser will have a positive LEF because the material gain peak is on the short wavelength side of the differential gain peak as will be seen in figure 3.2. It can be observed that if the material gain peak was at the same wavelength as the differential gain peak (or within the positive material gain region as suggested by the paper), then the resulting LEF is expected to be zero.

Figure 3.2 provides a depiction of the key differences in QW and QD lasers. Note that the DoS is portrayed here for a single QD, while carrier density is depicted for an ensemble of QDs which undergo inhomogeneous broadening due to differing QD sizes, shapes, and compositions.

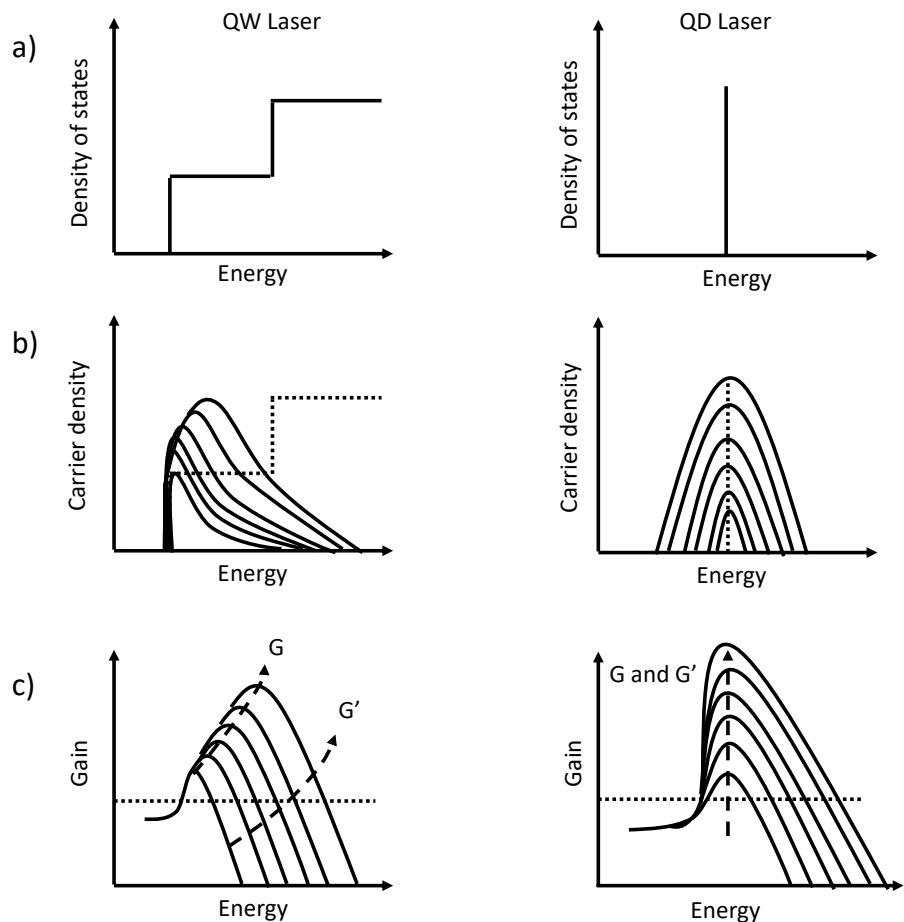


Figure 3.2: QW and QD lasers comparison in terms of: (a) theoretical density of states as a function of energy, (b) practical state filling with increasing carrier density (N.B. ensemble of dots), and (c) corresponding gain spectra as a function of energy. Differential gain ($G' = dg/dI$) and peak gain evolution with carrier density are indicated

QW materials exhibit a step-like DoS, where each step accounts for the addition of a new subband transition pair (state). Therefore, as carrier density increases, the states start to fill up, thereby saturating gain. This results in a jagged gain spectrum but lineshape (homogeneous) broadening tends to even out the edges into rounded features for each state. In other words, as current is increased the material gain peak shifts to higher energies (shorter wavelengths). When gain saturates, the differential gain peak will therefore appear at the relatively less populated higher energy (shorter wavelength) side of the peak in material gain.

In regard to a QD laser, there is an electron degeneracy of 2 in the ground state. This is caused by their discrete DoS and the Pauli exclusion principle. Consequently, as the carrier density is increased the mean dot carrier occupancy increases and the ground state occupation probability becomes higher. Conversely, the probability of carrier-capture into a dot and relaxing to the ground state becomes lower. This leads to QD lasers having an earlier onset for the gain saturation *c.f.* QW counterparts which possess a continuous DoS with an electron degeneracy much higher than 2 in the ground state. In other words, gain saturates at considerably higher currents in a QW laser. Therefore, for a QD laser at low carrier densities the gain is linear with current, but as the occupation probability of the ground state approaches 1, near threshold, gain saturates. This dynamic is reflected in fig 3.3 where gain evolution with carrier density is depicted for QW and QD lasers.

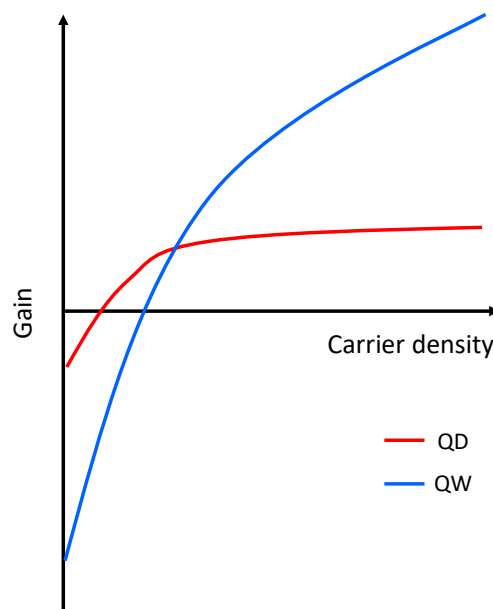


Figure 3.3: Gain with respect to carrier density for the QD and QW active material

It can be seen that for a QD laser, gain increases linearly initially before saturating at higher currents while this is not the case for a QW laser yet. In QD the δ -function-like, discrete states, are spaced a quantisation energy apart, which is normally much greater than the amount of $k_B T$ at room temperature (26 meV) for GaAs-based QDs. GaAs-based QD lasers have become promising alternatives to the InP-based counterparts. This is attributed to their better temperature performance, lower substrate cost, and lower threshold current. On the other hand, an ensemble of different sizes, shapes, and compositions of the QDs, each having slightly different energies, inhomogeneously broadens the ground state transitional energy. As long as the amount of this inhomogeneous broadening is smaller than the state separation, this will not

affect the gain development with current. If this is provided, the material and the differential gain peak wavelengths are expected to be equivalent with that of the ground state. Therefore, given operation in the linear gain region with unoccupied excited states, a QD laser may exhibit zero LEF [18]. Additionally, it has been proposed that QDs may exhibit negative LEF, if when the carrier density is increased, the gain peak moves towards the excited state, considering the inhomogeneous broadening should still be small [19]. Moreover, the reported high resilience of QD lasers to feedback compared to QWs [20], is very much indicative of lower photon and carrier coupling in the cavity, i.e. low LEF values [21]. Additionally, theoretical calculations indicate that the population inversion factor is lower in QD lasers as compared to the QW counterparts [22], considering $n_{sp} = (1 / 1 - \exp (E_{21} - \Delta E_F / k_B T))$. Where, E_{21} is the separation energy of the conduction and valance bands, k_B is the Boltzmann constant, T is the temperature, and ΔE_F is the difference in their associated Fermi levels. As the total linewidth of a semiconductor laser is directly proportional to n_{sp} [23], QDs are expected to have narrower linewidths than QW lasers.

3.3 Gaps in knowledge

In order to more clearly synthesize the canon, a review of the reports in the literature is summarized in terms of their key figures of merit in table 3 below.

Up to the present time, small LEF values have been reported in the literature from QD lasers operating over a range of wavelengths from O- to L-band. These values are notably smaller than those reported for the QW counterparts [25]. For instance, the LEF of a similar QD and QW laser structure are compared in [26]. The QD device is demonstrated to have half the LEF values of the QW.

LEF values of as low as 0.01 has been reported in p-doped QD lasers also reaching negative values [27]. A comparative study of the linewidth enhancement factor in p-doped and undoped QD lasers based on a combination of theoretical and experimental investigations was carried out to study the effect of the p-type dopants. It was found that the p-doped QD lasers exhibited a lower linewidth enhancement factor near threshold relative to the undoped QD lasers [28]. This observation showed that as the doping level increases LEF becomes negative. This was attributed to the reduced transparency carrier density enabled by the combination of p-type modulation doping and a low DoS semiconductor system.

In [29], LEF of chirped InAs/GaAs QDs were investigated and it was found that due to lower differential gain, attributed to gain dispersion, the LEF was slightly higher (0.07-1 vs 0.4-0.6 in chirped structure).

Other work on 1.3 μm p-doped tunnel injection QD lasers have shown LEF values close to zero [30]. Additionally, an LEF of zero at 98% of threshold in QD lasers emitting at 964 nm has been reported [32]. In the telecoms 1.3 μm QD lasers, LEF of 1 have been found on a 2mm device [33]. On the other hand, larger values have also been reported from many other groups [26, 34-44]. For InP-based QDs, the pressing problem of small band offsets at the hetero boundary occurs which acts to exacerbate the carrier photon coupling and produce large LEF values as compared to the GaAs-based counterparts.

Ref <i>et. al.</i>	Year	Material	λ (nm)	G_{sat} (cm^{-1})	LEF	T ($^{\circ}\text{C}$)	Spectral	Method	Type
Ukhanov [26]	2004	InGaAs	1250	5	2.4 at $0.8 \times I_{\text{th}}$	20	Yes, 14 points	H-P	F-P
Newell [25]	1999	InGaAs	1220	8.5	0.1 at $0.79 \times I_{\text{th}}$	20	No	Pulsed H-P	F-P
Kim [28]	2006	InGaAs	1288	15	-1 to 2 at $0.9 \times I_{\text{th}}$	20	Yes	CW and pulsed H-P	F-P
Fathpour [30]	2005	InGaAs	1057	15	0.5 - 0.73 at $0.9 \times I_{\text{th}}$	20	Yes 9 points	Pulsed H-P	F-P
Xu [32]	2004	InGaAs	964	15	0 at $0.98 \times I_{\text{th}}$	20	No	Pulsed H-P	Filtered BAL
Muszalski [33]	2004	InGaAs	1310	~ 10	1 - 3 at $0.9 \times I_{\text{th}}$	20	No	Pulsed H-P	F-P
Rodriguez [36]	2005	InGaAs	980	~ 15	2-8 at $0.9 \times I_{\text{th}}$	20	Yes	CW and pulsed H-P	F-P
Dagens [37]	2005	InGaAs	1290	~ 5	10 - 60 at I_{th}	20	No	M-Z interfer'r	F-P
Schneider [35]	2004	InGaAs	1100	12	0.5 - 1.1 at I_{th}	-223 to 27	No	Time-resolved pump/probe	F-P
Azouigui [38]	2011	InGaAs	<u>1300</u>	14	2.5 at I_{th}	25-85	No	M-Z interfer'r	DFB
Carroll [31]	2006	InGaAs	<u>1300</u>	~ 10	2-5 at I_{th}	20-50	No	H-F Mod	BAL
Cong [34]	2008	InGaAs	<u>1300</u>	~ 10	3.2 at I_{th}	20-80	No	H-F Mod	F-P
Martinez [40]	2005	InGaAs	<u>1300</u>	15	0.6 - 2.2 at $1.1 \times I_{\text{th}}$	20	Yes 3 modes	H-F Mod	F-P
Martinez [39]	2008	InAs/InP	1520	10	1.8 - 6.6 at I_{th} - $1.1 \times I_{\text{th}}$	20	No	H-F Mod	F-P
Alexander [27]	2007	InGaAs	<u>1300</u>	9-17	0.01 to -0.001 at $0.95 \times I_{\text{th}}$	20	No	Pulsed H-P	F-P
Lelarge [41]	2005	InAs/InP	1500	12	2.2 - 9 at I_{th}	20	Yes 6 modes	H-P	BRS
Kondratko [42]	2003	InGaAs	1090	10	3.3 at $0.9 \times I_{\text{th}}$	20	Yes	H-P	F-P
Grillot [43]	2011	InAsP/InP	1560	5	2.2 - 13 Above I_{th}	20	No	H-F Mod	F-P
Kim[29]	2010	InGaAs	<u>1300</u>	6.8	At I_{th}	20	Yes	H-P	F-P
Zubov [44]	2013	InGaAs	1255	7	0.2 -3.3 ($0.95 I_{\text{th}}$)	20-50	Yes	H-P	F-P
Sobhani	2019	InGaAs	1300	45	0.0001 at $0.9 I_{\text{th}}$	-10 to 85	Yes	H-P	F-P

Table 3: Published LEF values. Key: H-P: Hakki-Paoli, M-Z: Mach-Zender interferometry, HF: high frequency modulation, F-P: Fabry-Perot, BAL: broad area laser, DFB: distributed feedback, BRS: buried ridge stripe

As tabulated above, the majority of the reports in the literature demonstrate single LEF values at or in the vicinity of lasing oscillation. For 1300nm In(Ga)As QD lasers on GaAs, there has only been one report published on spectral LEF (with respect to wavelength or energy) and it only consists of 3 modes. Notably, gain is lower across all reports as compared to the QDs under test in this work. There are no spectral LEF reports, to my knowledge, published at a range of temperatures for this QD system at this wavelength, presumably due to the noisy gain spectra producing even noisier LEF results particularly at elevated temperatures. More current dependent LEF studies were reported comparatively but similarly, high resolution experimental current dependent LEF studies are scarce in the literature, let alone at a range of temperatures for 1300nm devices.

Knowledge of the high resolution spectral and current dependent LEF is valuable for the design of the next generation of devices incorporating QDs. This information is particularly useful for instance for modulation purposes where knowledge of the LEF value at a particular drive current and wavelength is needed to optimize the chirp characteristics under modulation. Also, considering the previously-mentioned temperature-insensitive characteristics of QD lasers as compared to the QW counterparts, it is important to investigate the LEF particularly at elevated temperatures as it applies to the state-of-the-art, high density/high gain QD devices not only for fiber optic telecoms but also for deployment in a variety of harsh environments for e.g. optical sensing.

Consequently, in order to fill this gap, a high-resolution current and temperature dependent study of LEF was carried out in order to investigate the degree of carrier/photon coupling inside the laser, which is expected to be lower *c.f.* QWs as mentioned before. Also, other interesting characteristics were observed, for the first time, such as the imprint of the laser linewidth in the corrected carrier related modal shift above threshold which will be discussed in the results section.

In this chapter, a high-resolution and temperature-dependent study of the spectral LEF and also with respect to current is provided. This is particularly interesting in that the LEF is expected to increase at higher temperatures as the differential gain decreases due to carrier thermalisation to higher states. However, the alpha values are pinned close to zero even at higher temperatures ascribed to the strong carrier localization within the dots providing ample gain. Additionally, knowledge of the spectral and current dependent LEF values at particular wavelengths and drive currents, respectively is useful for e.g. intensity modulation purposes. Furthermore, by

investigating the carrier related mode shift with respect to drive current an interesting interplay was observed, for the first time, in terms of a correlation between the change in linewidth and the carrier related modal shift above the lasing threshold. This is due to subtle effects which will be discussed in the results section.

In what follows, a review of different measurement techniques that are typically used to calculate the LEF of semiconductor lasers is given. I will then detail out the method utilized in this study, which is the Hakki-Paoli technique, as explained in section 3.6.2. As shown subsequently, the measurements are convoluted by the thermally induced refractive index change, which need to be removed to obtain the correct LEF. This will be discussed under the measurement issues in section 3.6.6. These methods are subsequently applied to 8-layer stack QD-active fiber-pigtailed lasers at two different lengths at a range of temperatures. The LEF of the QD lasers are successively quantified with respect to wavelength and drive current and the final results are presented in section 3.7.11. Consequently, a discussion is provided to reflect upon the findings prior to the conclusion and future works sections which will summarize this chapter and provide the investigations that could be carried out as continuation to this study but fell outside of the remit of this work.

3.4 Experimental techniques for the measurement of LEF

As there are many different methods of measuring the LEF in lasers [45], assessment against the literature can be complicated. A number of different techniques have been utilized to measure the α_H -factor, without any thorough comparison between the results achieved [46,47]. It should also be noted that the number of the proposed measuring methods have been increasing while novel types of lasers such as those based on QDs have arisen, for which the determination of the LEF may be particularly of interest [48]. A brief review of the most common experimental methods, both below and above threshold, utilized in the determination of the LEF is provided in this section, and the method chosen for this work is outlined at the end.

Among the above-threshold techniques used for measuring the α_H -factor, the linewidth method relies on the measurement of laser's linewidth, and on fitting the results to known laser's parameters, so that the α_H -factor can be extracted by applying eqn. (3.5) from Henry [3]. By considering that the laser's linewidth exhibits different slopes below and above threshold, a method to determine the α_H -factor in a single-mode laser was proposed in [49]. Additionally,

there is the modified linewidth method [50], which relies on the measurement of laser's linewidth as a function of emitted power below and above the laser's threshold, and the ratio of the slopes of the linewidths as a function of the inverse power gives the α_H -factor value directly. This method has been more recently generalized to FP lasers [51]. These methods based on the laser's linewidth both require a systematic characterization of the specific device under test and suffer from a poor accuracy due to the complex dependence of the laser's linewidth on several parameters.

The other above threshold measurement methods of α_H -factor rely on injection locking or on optical feedback techniques. Notably, light from a master laser is injected into the slave laser resulting in the locking of the slave's optical frequency to that of the master's. The locking region is investigated in terms of the injected power level and frequency detuning, showing an asymmetry in frequency due to the nonzero LEF [52, 53]. An accurate measurement of the effective injection level is generally difficult because there always exists a mode profile mismatch between the master beam projected onto the slave laser facet and the slave-guided mode. Such mismatch can reduce the effective injection to a value that is 10–50% of the total facet power meaning that the accuracy is limited.

On the other hand, the optical feedback method is based on the self-mixing interferometry configuration and, according to the Lang–Kobayashi theory [54], the α_H -factor is determined from the measurement of specific parameters of the resulting interferometric waveform. In contrast with the injection-locking method, the accuracy appears to be better so long as the data on the effective feedback level is not required [55]. It is also important to stress that a theoretical and experimental investigation of the reflectograms obtained for a distributed feedback (DFB) laser using a phase-controlled high-resolution optical low-coherence reflectometer (OLCR) was carried out in [56]. Among other results, it is shown that the α_H -factor can be directly deduced from the OLCR measurements.

Alternatively, the determination of the LEF can be conducted through high-frequency techniques. The laser current modulation generates both amplitude (AM) and optical frequency (FM) modulation [57]. The ratio of the FM over AM components gives a direct measurement of the α_H -factor [58, 59, 60, 61]. The AM term can be measured by direct detection via a high-speed photodiode, while the FM term is related to sidebands intensity that can be measured using a high-resolution scanning FP filter. Although the FM/AM method requires modulation well above the laser's relaxation oscillation frequency, this technique gives the device α_H -factor

under direct modulation.

The fiber transfer function method, originally proposed for electro-absorption modulators (EAMs) [61] exploits the interaction between the chirp of a high-frequency-modulated laser and the chromatic dispersion of an optical fiber, which produces a series of minima in the amplitude transfer function versus modulation frequency. Such a technique has then been generalized to diode lasers by introducing the adiabatic term as shown by [62, 63] and by fitting the measured transfer function, the α_H -factor can be retrieved. This method has been shown to be reliable as long as precise measurement of the fiber dispersion is made and as long as the power along the fiber is kept sufficiently low to avoid nonlinear effects. Compared to the FM/AM technique, the main disadvantage of such a method is that several fitting parameters have to be determined to access the α_H -factor.

Recently, another technique based on a tuneable Mach–Zehnder (MZ) interferometer has been utilized to determine the AM and FM responses both in amplitude and in phase in addition to the LEF value [64]. Although both Michelson and MZ interferometers have already been used in the past to measure the laser’s FM responses [65, 66, 67, 68], the suggested method not only enables evaluation of the LEF but it also allows determination of the adiabatic chirp and the thermal effects. As considered in [64], the proposed technique is also much quicker as compared to the fiber transfer one and can easily be converted to a large-signal analysis configuration [69].

In this study, the α_H -factor is evaluated using the Hakki–Paoli [70] technique to measure the net modal gain. It is the usual method used to extract gain as a special fabrication run is not required, given a single-mode laser is available. The net gain can be obtained from the amplified spontaneous emission spectra as pump current is incremented. Furthermore, the ability to maintain a constant junction temperature in the Hakki-Paoli method, explained in section 3.7.7, brings about two experimental advantages. Firstly, it is not necessary to drive the device in pulsed mode to circumvent thermal effects. This would entail a complex setup for impedance matching and necessitates time-gated signal detection, which results in long data acquisition times. Secondly, the constant junction temperature gain measurement enables the characterization of a device where any self-heating effects can be removed. In this case isolated free carrier effects can be analyzed in detail. Consequently, the Hakki-Paoli method can be employed to differentiate the characteristics of the laser material at both constant heat-sink and constant junction temperature conditions, enabling the evaluation of free carrier and thermal

effects. This method also provides a good indication of laser gain spectra above threshold [71].

3.5 Measurement of LEF

The α_H -factor of a semiconductor laser may be found as the ratio of the refractive index change with respect to carrier density (dn/dN) to the gain change with carrier density (dg/dN). Substituting for K in eqn. 3.5:

$$LEF = \frac{-4\pi}{\lambda} \frac{dn/dN}{dg/dN} \quad 3.6$$

where, λ is the wavelength, N the carrier density, and g is the net modal gain. Using the equation for the F-P free spectral range (FSR) [72], $\delta\lambda = \frac{\lambda^2}{2n_g L}$, and replacing for n_g (the group index), the LEF expression above may be streamlined for practical measurement purposes to:

$$LEF = \frac{-2\pi}{\delta\lambda L} \frac{d\lambda/dI}{dg/dI} \quad 3.7$$

Where, $\delta\lambda$ is the FP mode spacing, L is cavity length, $d\lambda/dI$ is the carrier related wavelength shift with drive current, and dg/dI is the rate of change of net modal gain with respect to current.

In order to measure LEF, the wavelength shift of an individual FP mode and also gain change with current were measured. The setup shown in fig. 3.4 was used to follow an individual FP mode with increasing drive current to determine $d\lambda/dI$ at a particular temperature. Section 3.5.6, LEF measurement issues, further discusses issues relating to measuring the correct $d\lambda/dI$ due to the influence of thermal effects on the shifting of the wavelength.

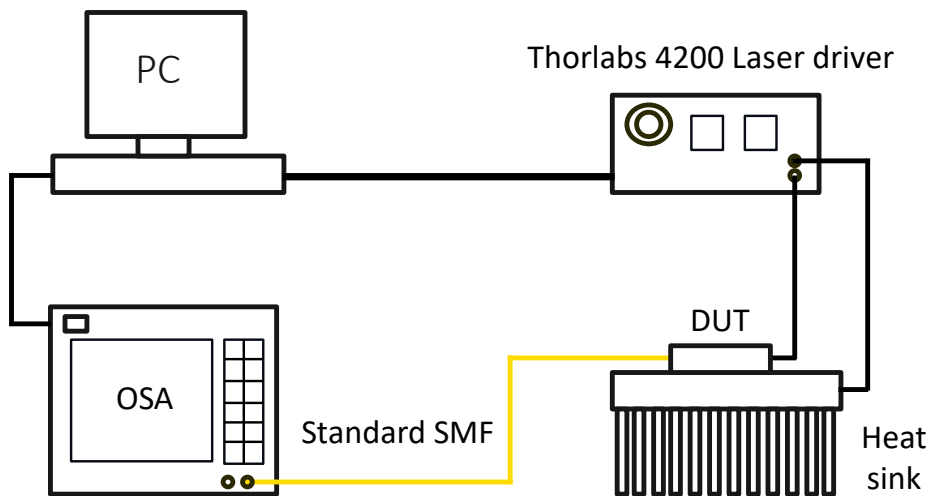


Figure 3.4: Experimental set-up for temperature-dependent optical spectrum measurements

Figure 3.4 shows the setup for measuring the Hakki-Paoli net modal gain spectrum. A Thorlabs 4100 laser driver, a 5 W rated thermoelectric cooler (TEC), a PT100 thermistor used for temperature feedback, and a CPU heatsink unit were used to keep DUT temperature constant during testing. Unless stated otherwise this is the standard equipment used in all succeeding measurements. Below threshold, light out of the fiber pigtailed laser was collected via a standard single-mode-fibre with a coupling loss of 25.8 % and fed into the optical spectrum analyser. The OSA resolution is critical since F-P mode spacing or the FSR reduces with increasing cavity length.

3.5.1 Devices

The state-of-the-art QD structures provided by QD Laser inc., Japan, were grown by molecular beam epitaxy consisting of 8 stacks of QDs each comprising of self-assembling InAs. An areal density of $5.9 \times 10^{10} \text{ cm}^{-2}$ is achieved with the growth of highly uniform QDs [73]. This can be observed in the AFM image in fig. 3.5 a). This material was incorporated in 375 and 750- μm fiber-pigtailed single-mode ridge-waveguide commercial lasers. The rear and front facets were high reflectivity coated (94%) and as-cleaved (34%) for the short device, and both as cleaved (34%) for the long device, with a coupling loss 25.8% for both devices. The facets are coated as such so that both devices exhibit similar threshold gains.

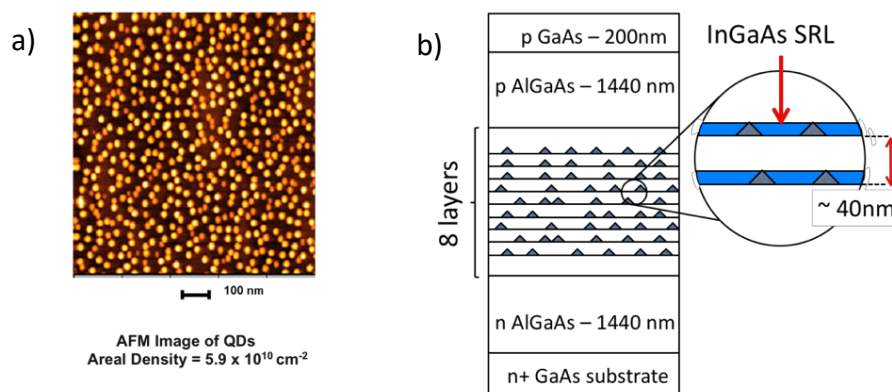


Figure 3.5: a) Atomic force microscope image of the dots [73], and b) Active layer composition of the laser

The mechanism for higher uniformity in order to increase maximum optical gain is based on a similar principle by Wasilewski et al 1999 [74]. In this method indium out-diffusion from the dots is suppressed during the capping process. Under a conventional coverage sequence, indium out-diffusion occurs which degrades the uniformity due to inhomogeneous diffusion, level

separation also decreases. With the suppression of In out-diffusion, initial uniformity is preserved increasing the symmetry in the gain spectral shape. Initial energy states are also preserved which would decrease the thermal carrier distribution. In general, higher density yields higher gain while higher uniformity narrows down the inhomogeneous broadening further increasing gain and temperature insensitivity.

3.5.2 Hakki-Paoli gain measurement

This method, presented by Hakki and Paoli in 1975 [70], has been cited over 900 times as of the time of writing this thesis. The technique is based on a round trip method and is typically utilized in case of short-cavity FP devices. This method is based on comparatively higher resolution spectroscopy i.e. requiring the length of the cavity to be small enough to enable the full resolution of the electroluminescence spectrum as far as individual FP modes are concerned. Net modal gain below threshold is calculated based on the modulation depth of the resolved peaks and valleys of the acquired electroluminescence spectrum. Operation is therefore in the linear gain region in the absence of saturation effects. The ratio in the intensity between the maxima and the minima of the F-P fringes, where gain is constructive and destructive, respectively allows the determination of gain and spontaneous emission. Figure 3.6 shows an example of an electroluminescence spectrum from the short device in the vicinity of the lasing oscillation. In other words, the Hakki-Paoli technique utilises FP resonances to determine the net modal gain of a laser. Round trip interference of spontaneously emitted light causes spectral modulation in the below threshold emission spectra. From the peak to valley ratio of this modulation, the gain spectrum can be derived. Figure 3.4 shows the setup for measuring the optical spectra from which Hakki-Paoli gain could be extracted.

The ratio of the maxima (P_i) and minima (V_i) of each F-P mode is measured and the gain calculated from that through [70]:

$$r_i = \frac{P_i + P_{i+1}}{2V_i} \quad 3.8$$

$$gain = \frac{1}{L} \ln \left(\frac{r_i^{\frac{1}{2}+1}}{r_i^{\frac{1}{2}-1}} \right) + \frac{1}{L} \ln(R) \quad 3.9$$

Figure 3.6 plots and indicates the consecutive peak (P_i) and valley (V_i) of each F-P mode to be measured for gain calculations.

In all cases, extraction of the peak to valley ratio was completed through data analysis in the Matlab software. The peak and trough ratio of consecutive modes was extracted using the peakfinder function with pre-defined mode spacing values. The ratios were subsequently utilized to calculate the net modal gain spectra with respect to drive current. The Matlab code is included in the appendix section.

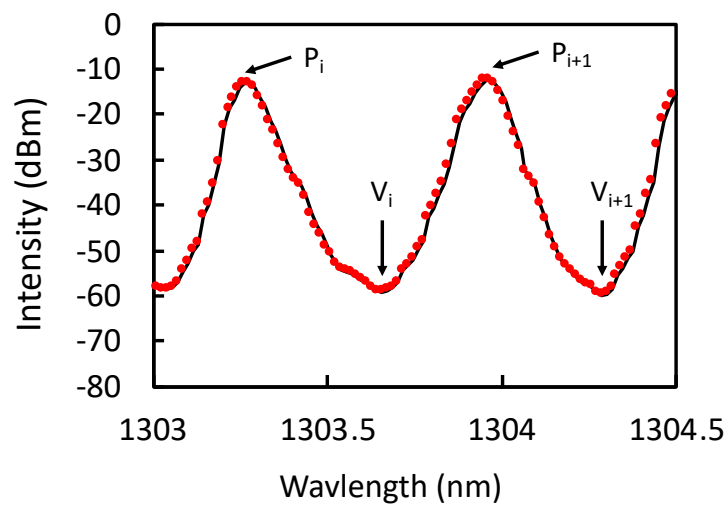


Figure 3.6: Consecutive peaks and valleys

An HP 8111 OSA was used with a resolution of 0.08 nm, which is sufficient to resolve the peak to valley ratio for cavity lengths up to 1mm. This limit is set by the mode spacing, $\delta\lambda = \frac{\lambda^2}{2n_g L}$, as defined before eqn. 3.7 (0.6 and 0.3 nm for the 375 and 750 μm devices, respectively).

On a practical note, beside setting the resolution of the OSA, the number of points measured in the required wavelength range should be adjusted to ensure enough data points are measured within one periodic cycle of the F-P modes.

Calculation of the gain at each F-P mode enables extraction of a net modal gain spectrum as shown in figure 3.7 for the 375 μm device at 25 C under $0.8 \times I_{th}$ of drive current, where internal losses are also indicated.

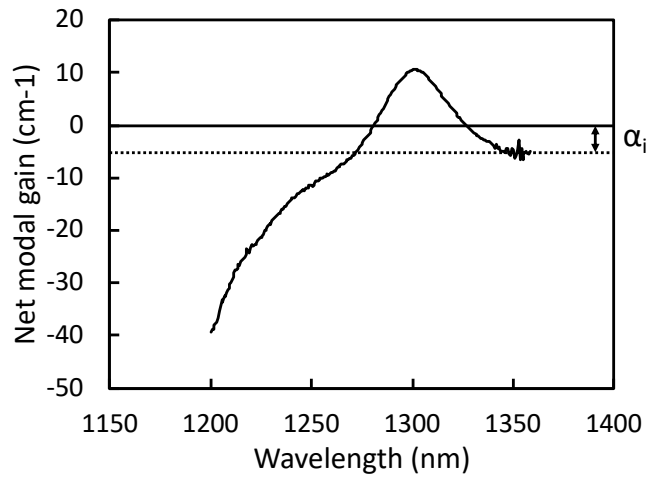


Figure 3.7: Net modal gain spectrum of the 375 μm device at 25 C under $0.8 \times I_{\text{th}}$ of current

Subsequently, from the spectrum, the mirror loss can be found which corresponds to the maximum gain found before lasing threshold. Internal loss can be estimated from the asymptote of the long wavelength tail of the gain plot [70].

3.5.3 H-P gain measurement considerations

It is important to select the appropriate spectroscopic resolution as when resolving the FP peaks and valleys a reduced throughput degrades the signal to noise ratio of the data. In order to optimize, a series of spectra were obtained at different resolution settings for the devices described in section 3.6.7.

The gain was then calculated using eqn. 3.9. It was observed that an underestimation of the valleys' depth is caused by a combination of mode partition noise and insufficient resolution. The low-resolution results in an underestimation of the gain. Therefore, the optimum spectroscopic resolution was determined at the point just before the onset of this reduction in calculated gain, corresponding to the maximum in light throughput and hence the maximum signal to noise ratio. This resolution was 0.1 nm and 0.08 nm for the 375- and 750 μm devices, respectively.

Hakki-Paoli analysis is carried out up to the lasing threshold. It is noted that above threshold measurements may be hampered by scattered, stray lasing light inside the OSA which could act as some type of external cavity and modulate the measured F-P spectrum, thereby resulting in erroneous gain measurements as shown later on in Fig. 3.21 erroneous data in the vicinity of lasing in a form of a “hump”.

3.5.4 Differential gain (dg/dI)

Once the Hakki-Paoli gain spectra has been calculated as a function of current (Fig. 3.17), the differential gain can be found by calculating the change of gain at a single wavelength as a function of drive current.

3.5.5 Spontaneous emission

Through the measurement of the peak to valley ratio, gain could be computed via eqns. (3.8) and (3.9) which consider the round-trip gain in the cavity. By taking out the round-trip amplification from these equations, the single pass non-amplified spontaneous emission (Sp.E.) can be calculated using the following equation [70]:

$$Sp. E. = \frac{P_i V_i}{\left(1/2[P_i^{1/2} + V_i^{1/2}]\right)^2} \quad 3.10$$

Extraction of the intensities of the peaks and valleys was done in the same manner as for the Hakki-Paoli gain above.

3.5.6 Measurement issues

Driving at low current densities (below threshold), nonlinear optical effects such as gain saturation and hole burning, spatial or spectral, can be omitted as they are all caused above threshold at high gain. However, as mentioned before, measurement of $d\lambda/dI$ is convoluted by thermal effects. With increasing carrier density, the refractive index changes and so does the wavelength ($d\lambda_{Carrier}$), this is the $d\lambda/dI$ required in eqn. (3.7). Nevertheless, as the devices have non-zero resistance, incrementing current causes heating and a corresponding red shift of the wavelength ($d\lambda_{Thermal}$). Thus, total wavelength shift is:

$$d\lambda_{Total} = d\lambda_{Thermal} + d\lambda_{Carrier} \quad 3.11$$

Therefore, the thermal component of the wavelength shift must be removed for the correct carrier related wavelength shift. The following sections detail-out the method for dealing with thermal effects.

3.5.6.1 Correcting for thermal effects

The following section explains the LEF calculation process using a continuous wave method. This method [76] is predicated on the fact that in a laser diode, above threshold, the carrier density and hence the gain is nearly clamped. Therefore, wavelength shifts with injected current above threshold may be considered as purely thermal. This shift can be removed from the below threshold wavelength shift to yield the carrier density related shift only ($\frac{\delta n_N}{\delta I}$). Although, in [76] the carrier related shift $\frac{\delta n_N}{\delta I}$ was calculated via eqn. (3.12), an identical value of $\frac{\delta n_N}{\delta I}$ was considered for both above and below threshold. As a result, this approach disregards the important fraction of the injected power that is transformed into optical power and does not contribute to the device heating. Consequently, the junction heating below threshold was underestimated and therefore also the modal change of index and the LEF. This may be alleviated by considering sub- and above- threshold dissipated power separately.

In this case, the measured change of refractive index with current ($\delta n_M / \delta I$) is a function of the sum of carrier-related refractive index change with current ($\delta n_N / \delta I$) and the temperature-related refractive index change with current ($\delta n_T / \delta I$):

$$\frac{\delta n_M}{\delta I} = \frac{\delta n_N}{\delta I} + \frac{\delta n_T}{\delta I} \quad 3.12$$

Eqn. 3.12 may be rearranged in terms of carrier density, N, and temperature, T, such that:

$$\frac{\delta n_M}{\delta I} = \frac{\delta N}{\delta I} \frac{\partial n}{\partial N} + \frac{\delta T}{\delta I} \frac{\partial n}{\partial T} \quad 3.13$$

Temperature increase, δT , in the device is dependent upon thermal resistance, R_T , and dissipated power, δW_{dis} as:

$$\delta T = R_T \delta W_{dis} \quad 3.14$$

Considering dissipated electrical power (W_{dis}) is the power into the laser sub-threshold (IV) and above threshold, power into the laser minus the stimulated emission power out (P_{opt}):

$$W_{dis} = \begin{cases} IV & I \leq I_{th} \\ IV - P_{opt} & I \geq I_{th} \end{cases} \quad 3.15$$

Utilizing eqn. (3.13) and (3.14) and rearranging to find carrier related refractive index change

with current:

$$\frac{\delta n_N}{\delta I} = \frac{\delta n_M}{\delta I} - \frac{\partial n}{\partial T} R_T \frac{\delta W_{dis}}{\delta I} \quad 3.16$$

Considering $\frac{\partial n}{\partial T} R_T = \frac{\partial n}{\partial W_{dis}}$, the index change due to carrier variations may be written as a function of the measured index change, the dissipated power, and the index change due to thermal effects:

$$\frac{\delta n_N}{\delta I} = \frac{\delta n_M}{\delta I} - \frac{\partial n}{\partial W_{dis}} \frac{\delta W_{dis}}{\delta I} \quad 3.17$$

Where, ∂W_{dis} is the dissipated thermal power and δW_{dis} the dissipated electrical power. Above threshold, we have $\delta n_N / \delta I = 0$ attributed to carrier clamping, then any remaining wavelength shift is exclusively due to thermal effects.

At first, the L-I-V characteristics of the device were measured at increasing currents at a fixed temperature. Subsequently, utilizing the experimental setup described in section 3.5 the lasing F-P mode was chosen and its wavelength shift with current was traced and measured at increasing current steps from below threshold to well above threshold. This was then converted into a change of the refractive index. The above threshold changes in refractive index with current ($\delta n_M / \delta I$) was then calculated from this data.

From eqn. (3.15) using above threshold L-I-V measurement, the rate of change of dissipated electrical power with current ($\delta W_{dis} / \delta I$) can be calculated. From eqn. (3.17) and given $\delta n_N / \delta I$ is negligible above threshold due to carrier clamping, the measured $\delta n_M / \delta I$ is only due to thermal effects.

The below threshold index change with current, $\delta n_N / \delta I$, can now be calculated using (3.17) from $\delta n_M / \delta I$ and $\delta W_{dis} / \delta I$ for each current step below threshold using the I-V data. The carrier-related only $\delta n_N / \delta I$ is calculated by removing the thermal component, $\partial n / \partial W_{dis}$.

At this stage, as the carrier-related refractive index change with current is known, and also differential gain, dg/dI , can be calculated from the Hakki-Paoli gain measurements, eqn. 3.7 can be consequently used to calculate the LEF.

3.6 Experimental Results

This section firstly presents the general figures of merit of the laser operation at a range of temperatures. This includes the light-current-voltage operation, characteristic temperature, external differential quantum efficiency, lasing spectra, and the corresponding RMS linewidths. Subsequently gain spectra are provided and temperature correction methods utilized before demonstrating the spectral and the current dependent LEF values.

3.6.1 L-I-V measurement

One of the most important characteristics of laser devices is the light output as a function of drive current. L-I measurement is carried out using Labview software to communicate between the instruments and record the results. The devices are fiber pigtailed, and the fiber is connected to the optical power head for light measurement via the lightwave multimeter.

Figure 3.8 plots the light-current-voltage characteristics of the 375 μm device. From the L-I graph numerous parameters such as threshold current, slope efficiency, etc can be determined.

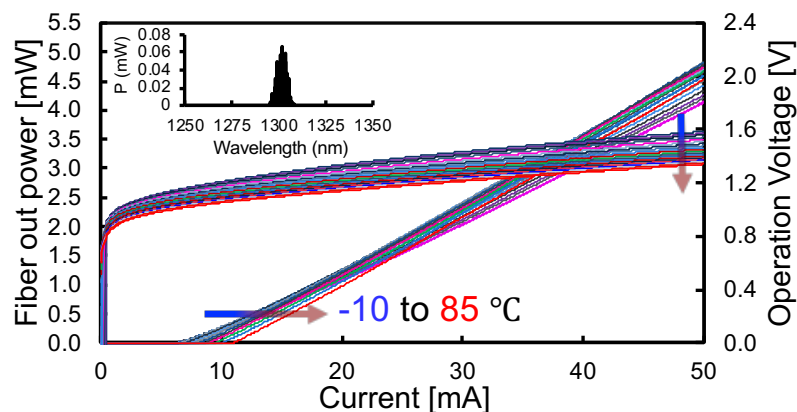


Figure 3.8: LIV characteristics of the device from -10 to 85 °C, inset shows the lasing spectrum at 25 °C under 30-mA of drive current.

The threshold currents were determined at the intersection of the above and below threshold linear fits and at 25 C for the 375 μm device was 6.85 mA and 13.7 mA for the 750 μm device or 600 A/cm² for both devices assuming a ridge width of 3 μm (same mirror losses). The current density for 1mW of output power is 1.7 and 2.3 kA/cm² for the short and long devices, respectively.

3.6.2 Differential output power

The dP/dI characteristics as a function of heatsink temperature from -10 to 85 °C is plotted in figure 3.9 for the 375 μm device at every 5 degrees Celsius. Black line in inset is the 25 °C.

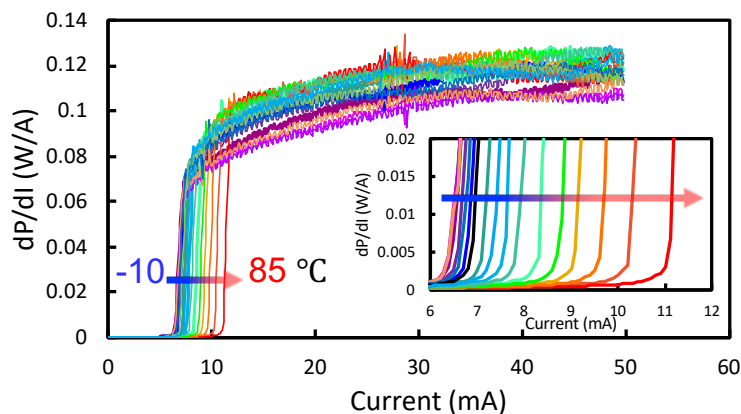


Figure 3.9: differential power with respect to current, black line in inset is for 25 °C.

This provides another measure for the threshold current determination and also a slope to determine η_d above threshold. A slow increase in threshold current up to 25 °C is observed and then the increase becomes continually faster. This may be attributed to a number of subtle mechanisms to be considered in the next section e.g. the nonradiative recombination mechanism that accompanies the thermalized carriers to the QD upper energy levels and also the wetting layer at higher temperatures [77].

As temperature increases, homogeneous broadening becomes comparable and/or exceeds the inhomogeneous broadening [78]. Hence, lasing takes place from not only carriers of the resonant dots, but also from dots within the full extent of the homogeneous broadening. This would improve the slope efficiency as the lasing mode photons obtain gain from both the energetically resonant dots and from the other non-resonant dots that are within the scope of the homogeneous broadening. This behavior is unique to quantum dot material and is distinguished from their QW counterparts where slope efficiency degrades as temperature is increased.

On the other hand, temperature increase causes carriers to thermalize to higher energy states. The threshold current increases because the increased number of carriers in the excited states are consumed predominantly via nonradiative recombination [79].

3.6.3 Characteristic temperature T_0

The theory of QD lasers suggests that in the case of an infinite confinement potential, a 0-D discrete DoS laser, with a ground state to excited state transition energy much greater than the amount of $K_B T$ (26 meV at RT *c.f.* $\Delta E = 85$ meV in these devices), should have an unchanging threshold current as temperature increases [80]. In real QD lasers, threshold current will inevitably increase with increasing temperature due to thermalization of carriers to higher states with a higher nonradiative recombination rate due to an increased number of recombination paths.

Characteristic temperature, T_0 , is a measure of how sensitive the laser is to temperature changes. Higher values of T_0 indicate that the threshold current density and the external differential quantum efficiency of the device increase less rapidly with increasing temperature, which means the laser is more thermally stable. The value of T_0 is calculated by measuring the threshold current density of a laser at increasing device temperatures [81]:

$$T_0 = \frac{\Delta T}{\Delta \ln(J_{th})} \quad 3.19$$

Figure 3.10 plots the natural log of threshold current versus temperature for characteristic temperature calculations. Slope efficiency is also plotted on the right vertical axis.

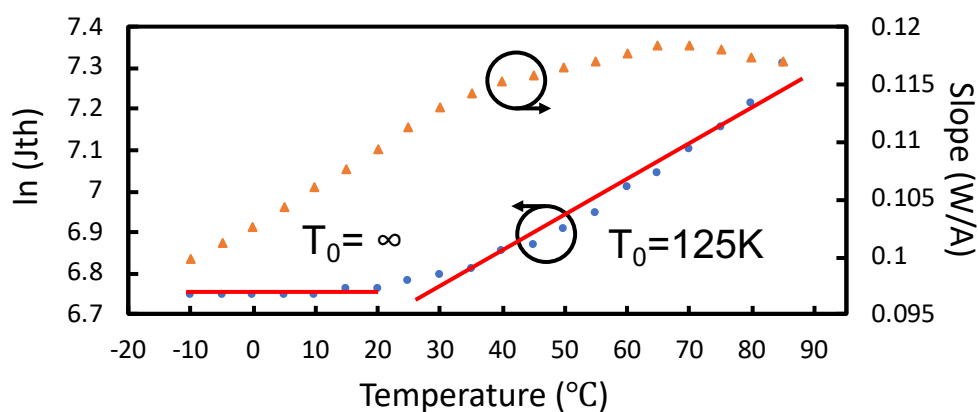


Figure 3.10: Natural logarithm of threshold current density and slope with respect to mount temperature

The behavior observed in the figure above was qualitatively explained in the L-I-V measurements in section 3.6.1, which ascribed nonradiative recombination via thermalized carriers to higher states as temperature is increased. The slope efficiency is 0.1 W/A at 1 mW for the short chip and 0.03 W/A for the long chip.

Additionally, an almost completely flat linear behavior is observed up to about 20 °C yielding a characteristic temperature of $T_0 = \infty$. As temperature is increased, carriers start thermally distributing into excited states where they are also subject to more nonradiative recombination via impurities or defects, thus we see a super-linear increase in the threshold current above 20 °C onward which results in a $T_0 \sim 125\text{K}$ for the temperature range 20-85°C.

There is not a unanimous agreement in the literature as far as the origin of the infinite T_0 is concerned. A number of possible mechanisms have been proposed to describe it, including: suppression of thermal hole broadening [82], Auger process having a $1/T$ dependence on the scattering rate [83], a deeper confinement potential for electrons within the p-doped QDs caused by Coulomb attraction [84] [85], mixed Auger recombination [86], and a photon coupling mechanism [87].

Threshold current characteristics of InGaAs QD lasers were studied under a temperature range of -200 to 100 C [88] and ascribed the infinite characteristic temperature in the noted temperature region to a balancing of I_{th} reducing process due to an increase in the homogeneous linewidth, and the I_{th} increasing process due to carrier thermalization causing non-radiative recombination.

At the higher temperature region (80 C) a thermal activation energy of ~ 250 meV was calculated in [88] from an Arrhenius plot of the threshold current, suggesting carrier escape into the well. This is equivalent to a wavelength of 980 nm consistent with emission wavelength of the 2-D wetting layer. It is this rapid carrier escape that must be counteracted in order to produce devices that operate at high temperatures for uncooled applications.

One approach to circumnavigate this carrier escape is the incorporation of higher potential barriers around the QDs [89]. Nonetheless, the use of AlGaAs has so far proved unsuccessful due to poor quality growth at the low temperatures necessary in order to maintain a high indium composition within the QDs [88], essential for emission at $1.3\mu\text{m}$.

3.6.4 External differential quantum efficiency (η_d)

Measurement of the gradient of the L-I slope when the device is lasing gives a measure of the percentage conversion efficiency of injected carriers to photons out of the facets or η_d . In an ideal laser one electrically injected electron-hole pair is converted into one photon and emitted from the laser. For this case one carrier of charge q results in one photon at the lasers wavelength (hc/λ), where h is Planck's constant and c the velocity of light. Therefore, the dimensionless ratio of $q/(hc/\lambda) = 1$ or 100%.

Nevertheless, in a real laser only a percentage of the electron-hole pairs are converted to photons in the lasing mode (internal efficiency η_i). This is attributed to the injection current leakage created by possible shunt paths around the active region. Furthermore, the possibility of carrier leakage by thermionic emission or by lateral diffusion (if no lateral confinement in place) before recombining further decrease η_i . Thus, this leakage precipitates a loss of carriers in the active region that could be otherwise used to produce light. On the other hand, the emitted photons can be reabsorbed or scattered in the waveguide instead of being emitted from the laser facet (internal loss α_i). Consequently, the probability of one injected electron-hole pair then resulting in an emitted photon is the probability of generating a photon (η_i) multiplied by the probability of the photon being emitted via the mirror loss (α_m) and not being lost in the cavity via internal loss, α_i :

$$\eta_d = \eta_i \frac{\alpha_m}{\alpha_m + \alpha_i} \quad 3.20$$

The real external efficiency of conversion of injected e-h pairs to photons out of a laser's facets is calculated from the slope efficiency of the L-I graph when lasing occurs. The ratio of the real response $\Delta P/\Delta I$ to the ideal response ($q\lambda/hc$) gives the percentage of the external differential efficiency [81]. The factor of 2 is to account for the emissions from the back facet:

$$\eta_d = 2 \frac{\Delta P}{\Delta I} \left[\frac{q\lambda}{hc} \right] \quad 3.21$$

Fig. 3.11 plots the external differential quantum efficiency (DQE) as a function of mount temperature for the 375 μm device (without the factor 2) considering a coupling efficiency of 25.8 %.

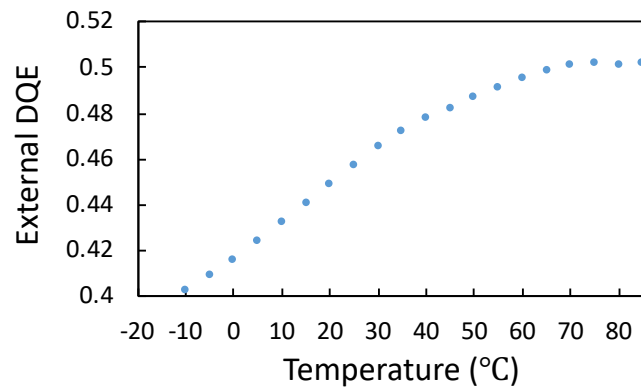


Figure 3.11: External differential quantum efficiency with respect to mount temperature for the 375 μm device

The slope efficiency and the external DQE plots follow the same behavior, namely linearly increasing in line with the increase in dP/dI above threshold with temperature up to 25°C and gradually start to roll off as the aforementioned non-radiative recombination rates turn the fraction of those carriers which would otherwise contribute to the optical power into heat or vibration.

3.6.5 Lasing spectra

Figure 3.12 plots the lasing spectra as a function of mount temperature at 30 mA.

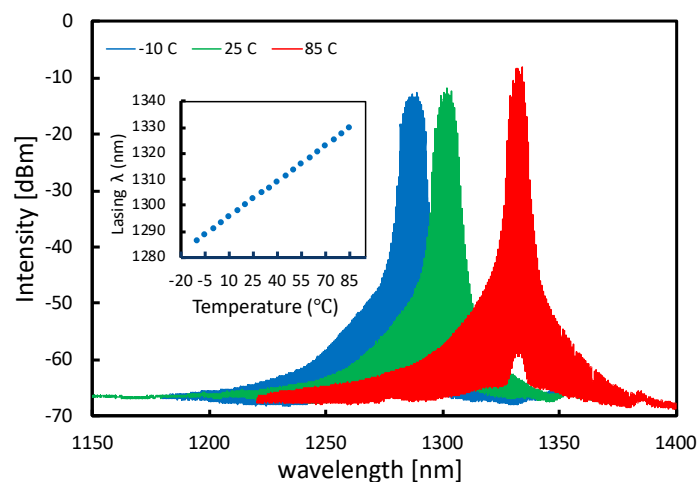


Figure 3.12: Lasing spectra with respect to wavelength, inset shows the shift of lasing wavelength with temperature

The device exhibits a mode packet 3 dB width of 6 nm under 30 mA at 25 °C. Moreover, shift of the whole spectra, namely all emission peaks, (0.26 nm/°C for lasing wavelength) to higher wavelengths (lower energies) is observed which is due to the temperature dependence of the band gap as the energy gap reduces with increasing temperature from the increase in the interatomic spacing (the inset shows the lasing wavelength shift). Additionally, a temperature-dependent narrowing of the lasing spectra is observed which is then reflected and discussed in figure 3.13. It is interesting to note that the emission intensity increases slightly as temperature is increased to 85 °C. This is because the threshold gain has increased, as explained before, triggered by the increase in the non-radiative mechanism of the thermalized higher states carriers, possibly even in the wetting layer [90].

3.6.6 RMS linewidth

The root-mean-square linewidth, $\Delta\lambda_{\text{rms}}$, is calculated using a standard deviation function and the mean of a normal distribution (Gaussian function) as [91]:

$$\Delta\lambda_{\text{rms}} = \sqrt{ \left\{ \left(\sum [P_i \times (\lambda_i - \lambda_c)^2] \right) / P_0 \right\} } \quad 3.22$$

Where, $P_0 = \sum P_i$, and P_i is the power of each FP mode's maxima, λ_i is its wavelength, and the center wavelength is calculated as:

$$\lambda_c = \left(\sum \lambda_i \times P_i \right) / P_0 \quad 3.23$$

Figure 3.13 plots the root mean square lasing spectral width at -10, 25, and 85 °C. In general, there is a decrease in the lasing linewidth with increasing temperature. At all temperatures, the lasing linewidth increases with current.

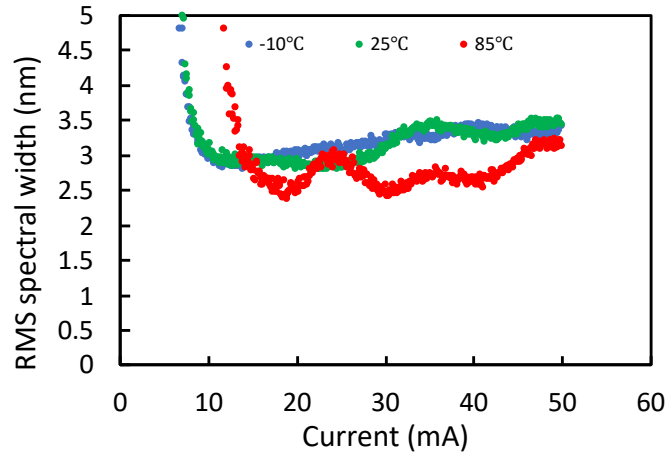


Figure 3.13: RMS linewidth of the 375 μm device with respect to drive current at the temperature range

At 85 $^{\circ}\text{C}$, homogeneous broadening is comparable or exceeds inhomogeneous broadening [78]. Lasing mode photons are emitted not only from energetically resonant dots, but also from other non-resonant dots within the scope of homogeneous broadening, eventually leading to collective lasing of the dot ensemble. Thus, the number of broadened longitudinal modes significantly decreases, resulting in a smaller lasing mode broadening as temperature is increased to 85 $^{\circ}\text{C}$.

Moreover, the continual increase in the linewidth with current at all temperatures is due to an additional broadening caused as the carriers begin to populate the excited state of the QDs with increasing current. Coulomb interactions, carrier-carrier scattering, and phonon-carrier scattering between the confined carriers in QDs and free carriers in the wetting layer continually alter the instantaneous number of carriers in the QDs [92] which results in frequency fluctuations in the ground state transition. Hence, an increase in excitation energy causes an increase in the interaction between carriers inside the QDs which leads to an additional increase in the dephasing rate acting to further broaden the linewidth.

On the other hand, there are fluctuations in the measured linewidth as injection current is increased. The largest of these changes is observed in the 85 $^{\circ}\text{C}$ spectrum between 20 and 30mA. Such instabilities are expected to be mitigated once the laser chip's junction temperature is maintained, explained in the next section.

It must be noted that the mount temperature was stable to ± 0.5 °C utilizing the combination of a PT100 thermistor, a TEC, and a CPU heatsink unit. The temperature sensing settings of the Thorlabs 4100 laser driver unit was subsequently used to reach the highest accuracy possible through the PID loop.

Moreover, further improvement was achieved firstly with a certain level of trial and error e.g. with the A/C system of the laboratories needing to be turned off as the difference of readings between the A/C's sensor and the mount's thermistor (caused by the location difference) resulted in increase in fluctuations. Secondly the mount was placed inside of an improvised chamber under dry air flow. This brought the temperature precision up to ± 0.2 °C.

Ultimately, in order to maintain a constant junction temperature, a careful calibration was employed by making use of the F-P mode wavelength as a thermometer.

3.6.7 Maintaining a constant junction-temperature

The method to keep the junction temperature constant for the laser devices is explained in this section. Figure 3.14 plots the wavelength of a FP mode of the 375 μm device as a function of heat-sink temperature from 70 to 80 °C at a constant current of 30 mA with 1°C increments.

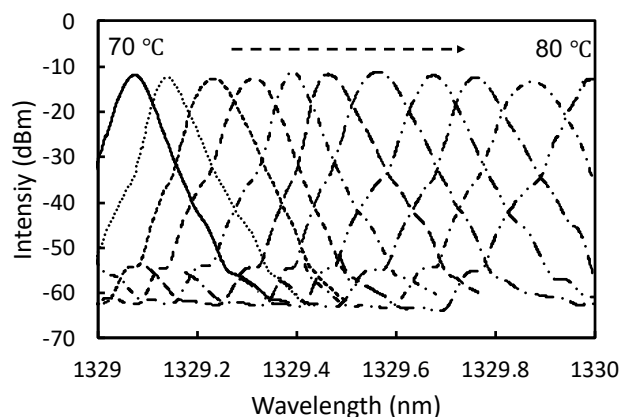


Figure 3.14: modal shift in the vicinity of lasing as a function of current

Figure 3.15 shows a plot of shift the FP peak position as a function of heatsink temperature. It can be observed that there is a linear relationship between temperature increase and FP peak wavelength shift and this shift is attributed to crystal expansion and the change in refractive index of the cavity material due to thermal effects [76] as outlined in eqn. (3.11).

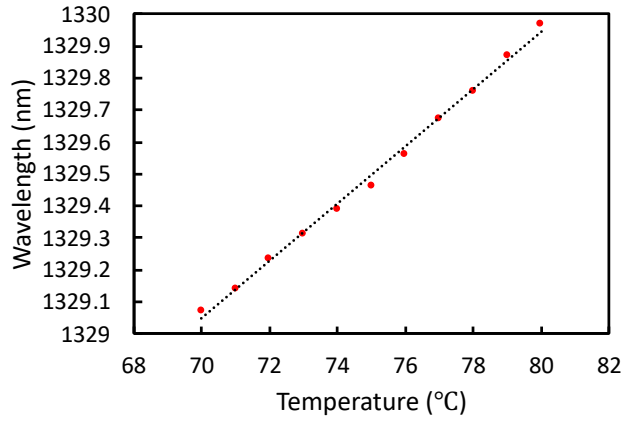


Figure 3.15: modal shift in the vicinity of lasing as a function of current

The slope of the linear fit, $\Delta\lambda/\Delta T$, is measured to be 0.1 nm/°C i.e. a mode-shift of 0.1 nm for every 1 °C of temperature increase. From the inset of figure 3.12, the modal shift is converted to an increase in cavity temperature of 0.195 °C/mA.

The heatsink temperature can now be adjusted at every current increment to counter the effects of self-heating in the chip. Figure 3.16 plots the RMS linewidth at 85 °C under constant junction temperature.

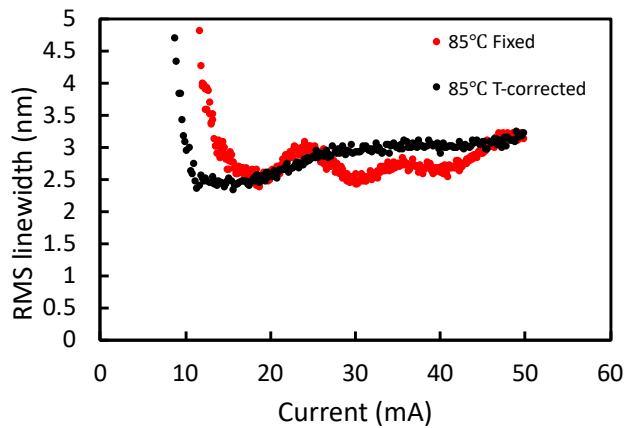


Figure 3.16: RMS linewidth at 85 °C with and without temperature correction for constant junction temperature

The results of maintaining the junction temperature constant can be observed from the relative stabilization of the fluctuations in the linewidth spectra which is shown in fig 3.16. It is acknowledged that there still exist slight variations in the linewidth evolution with current over threshold. This will be further discussed in the mode shift correction section 3.6.10.

3.6.8 Temperature-dependent gain spectra

Incorporating the previously explained methods and techniques, a temperature-dependent study of the net modal gain spectra is presented in this section.

Figure 3.17 plots the net modal gain (NMG) spectra measure using the Hakki Paoli technique below threshold in the region of the ensemble of quantum dot ground and the first excited state (ES_1) at $-10\text{ }^\circ\text{C}$. The ES_1 peak is not observed, in the positive NMG region, in that it falls behind noise floor as there is not enough spontaneous emission from the dots.

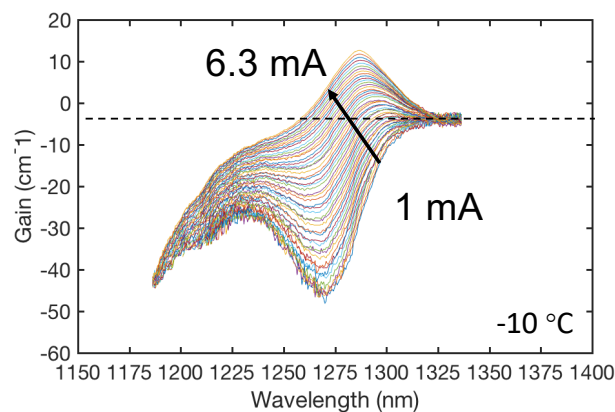


Figure 3.17: Hakki-Paoli net modal gain at $-10\text{ }^\circ\text{C}$

As current increases, gain peak shifts to lower wavelength (higher energy) due to state filling. On the other hand, at the longer wavelength end of the spectrum (lower energies), the limited number of energy states available in the dots lead to strong saturation in both spontaneous emission and gain spectra. The internal losses are estimated from the asymptote of the low energy side of the gain curves [70] and amount to $3.5 \pm 0.5\text{ cm}^{-1}$. Figure 3.18 a) and b) plot NMG at $25\text{ }^\circ\text{C}$ and $85\text{ }^\circ\text{C}$, respectively. Shift of the gain peaks with temperature are due to the band gap shrinkage as mentioned before. Lasing threshold was at 6.35, 6.85, and 11.25 mA for -10 , 25 , and $85\text{ }^\circ\text{C}$ mount temperatures, respectively. Above this injection current level, the gain at the non-lasing wavelengths is predominantly pinned and does not further increase with current. Extra carriers above threshold result in increasing lasing power, rather than increased gain, this is also observed in the L-I-V characteristics. As a result, the wavelength shift above threshold can be related to thermal effects alone.

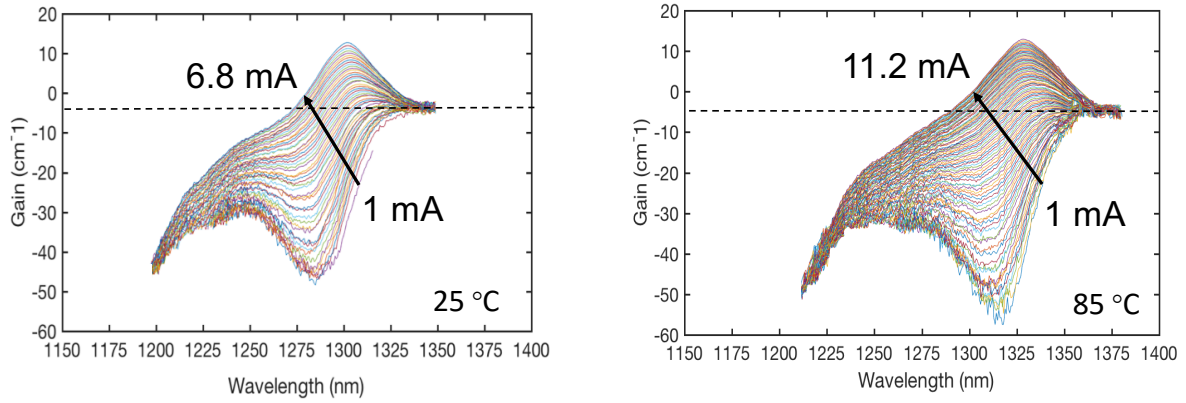


Figure 3.18: Hakki-Paoli net modal gain at a) 25 and b) 85 °C

It is noted that in Fig 3.18 a) the energy shift between the peak in absorption (1285 nm) and the peak in gain (1301 nm) is ~ 13 meV with an increase in FWHM of ~ 5 meV (linear). This is a similar behavior across all temperatures. The maximum of gain is not coincident with the maximum of absorption in wavelength owing to carrier distribution and many-body effects causing additional broadening and a renormalization shift to the transition energy [93].

Figure 3.19 plots the net modal gain (NMG) spectra for the 750 μm device from -10 to 85 °C. Spectra are similarly plotted up to threshold currents of 13.3, 13.7, and 18.7 mA, respectively at -10, 25 and 85 °C.

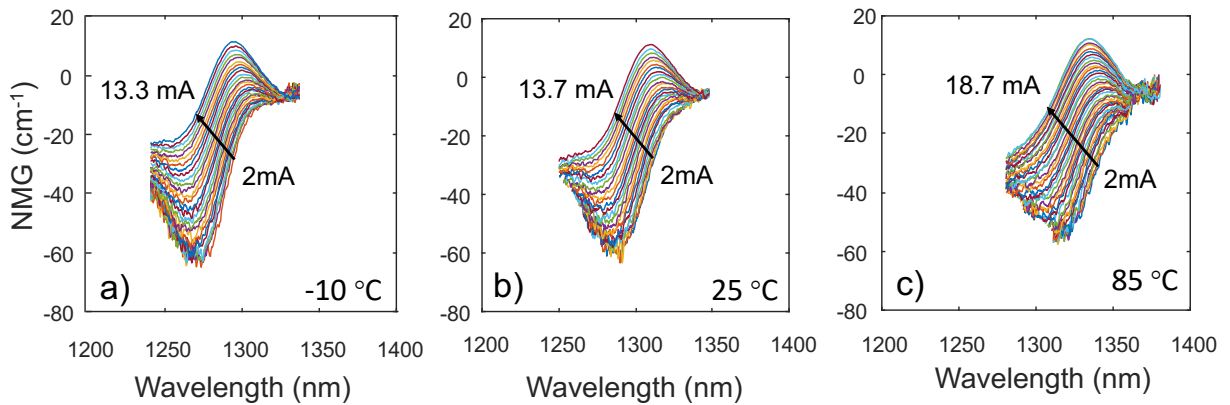


Figure 3.19: Hakki-Paoli net modal gain (NMG) at a)-10, b) 25, and c) 85 °C from the 750 μm device

The peak gain that reaches threshold as a function of current density is plotted for both devices in fig. 3.20. The short chip lases at 15 cm^{-1} with 94% HR coating. Long chip lases at 13 cm^{-1} with as cleaved facets. J_{th} for both devices is 600 A/cm^2 .

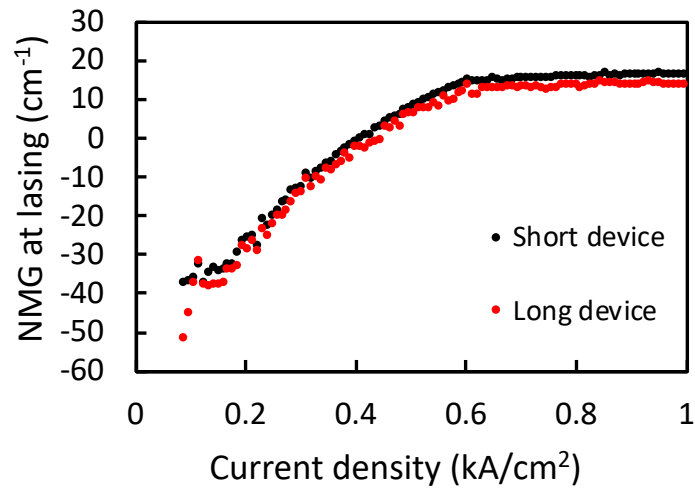


Figure 3.20: Gain vs current density of both device lengths at 10nm shorter than lasing wavelength

A 30:1 ratio can be inferred from the slope of dg/dJ below and above threshold, thus it is reasonable to consider gain clamped above threshold.

A three-dimensional rendering of the net modal gain spectra with respect to energy as a function of drive current of the 375 μm device at 25 $^{\circ}\text{C}$ up to 95% of threshold current is provided in figure 3.21 for the purposes of displaying the laser operation in a different light where gain and absorption may be viewed more pictorially.

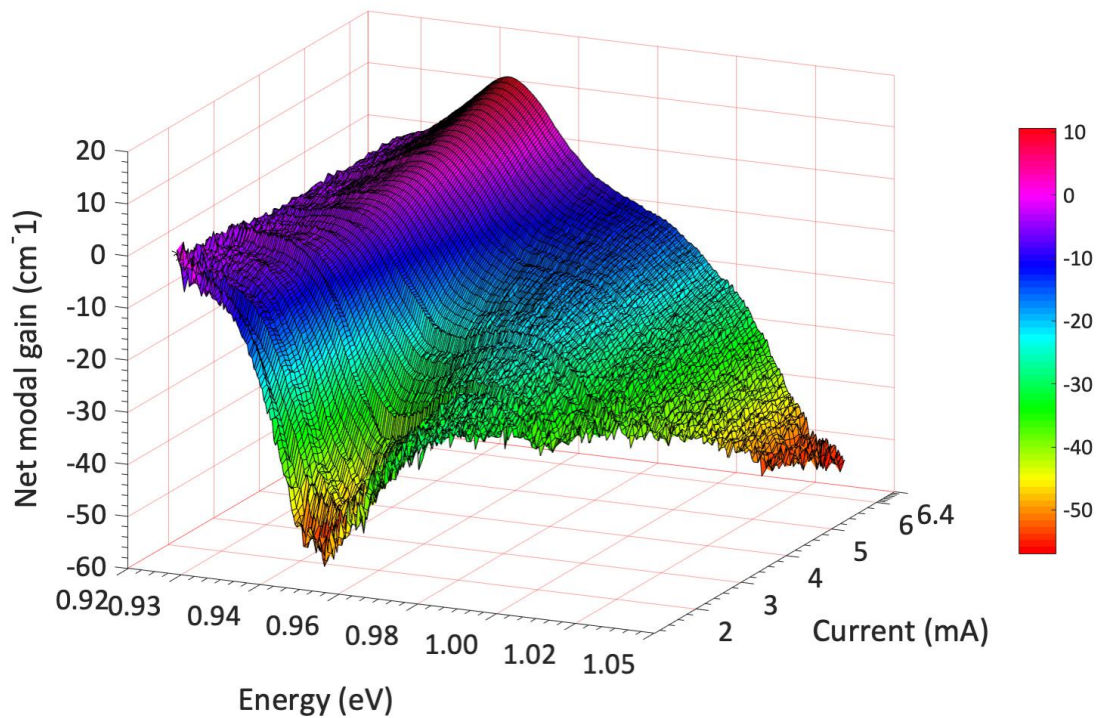


Figure 3.21: 3-D Hakki-Paoli net modal gain spectra at 25 $^{\circ}\text{C}$ from the short device

Figure 3.22 plots the net modal gain at $\sim 90\%$ of threshold current from the short device at the temperature range for comparison with respect to wavelength. Gain is measured at 5.9 mA ($0.90 I_{th}$), 6.1 mA ($0.89 I_{th}$), and 10.2 mA ($0.91 I_{th}$) for mount temperatures of -10 , 25 , and 85 $^{\circ}\text{C}$, respectively.

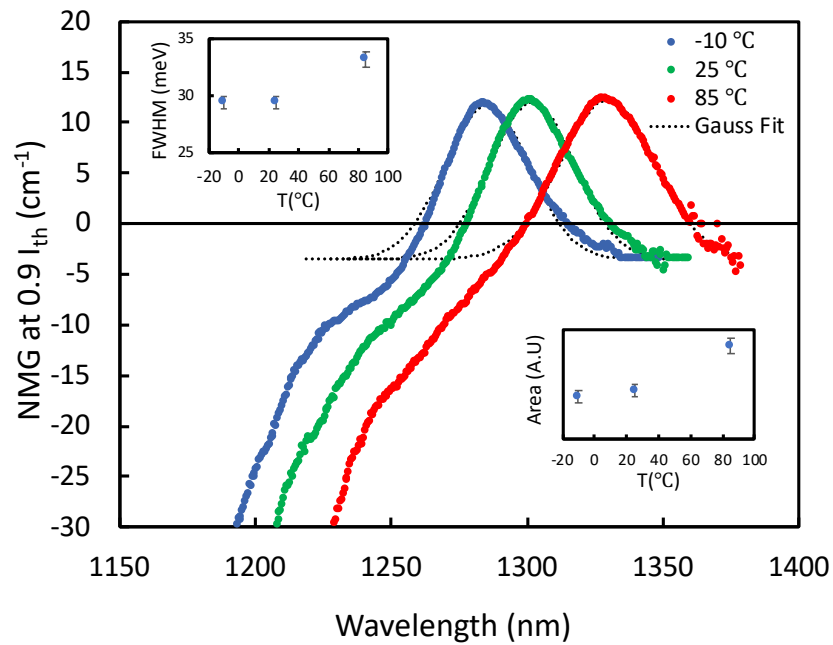


Figure 3.22: Hakki-Paoli net modal gain (NMG) at $\sim 90\%$ threshold current with respect to wavelength at different temperatures from the short device

The inset shows the FWHM evolution in line with the fact that homogeneous broadening results in the interaction of energetically and spatially isolated dots by photons, which precipitates collective lasing. This interaction leads to a narrow lasing line at room temperature via the collective interaction of energetically non-resonant and spatially isolated dots.

As temperature is increased, carriers thermally redistribute into the ESs, possibly including the wetting layer [90]. As mentioned previously, this increases the threshold gain as these carriers recombine non-radiatively. Furthermore, a redshift of $0.33 \text{ meV}/^{\circ}\text{C}$ is observed in the gain peak as temperature is increased due to band-gap shrinkage.

The corresponding differential gain (dg/dI) spectra at $0.9 \times I_{th}$ are plotted with respect to wavelength and as a function of temperature in figure 3.23 for the short chip. Maximum differential gain at 85 $^{\circ}\text{C}$ is reduced to about quarter of its value at 25 and -10 $^{\circ}\text{C}$.

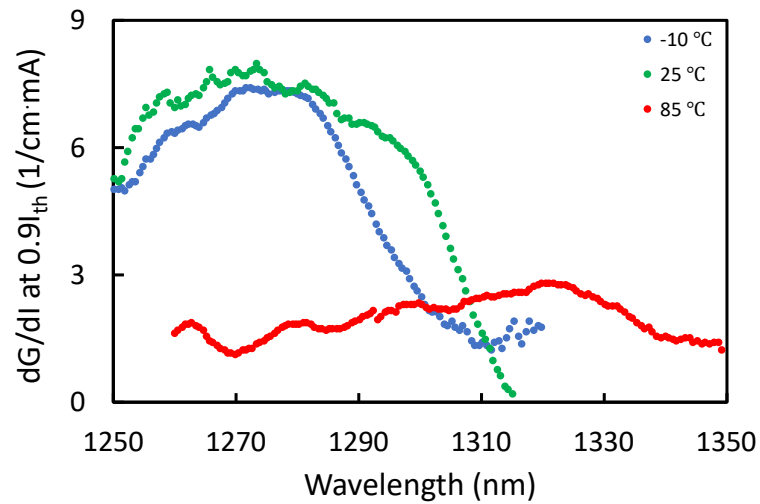


Figure 3.23: differential gain at 90% threshold current with respect to wavelength at different temperatures

This dG/dI reduction is attributed to the thermal excitation of carriers out of the QDs GS which precipitates a lower gain at elevated temperatures. For the 750 μm device, dG/dI has a max of 4.2 /cm/mA at 25 C at $0.9 \times I_{th}$.

Fig. 3.24 plots the Sp.E spectra at 90% threshold current with respect to wavelength at the temperature range. The linewidth increase reflected in the inset is in line with the increase in the homogeneous linewidth.

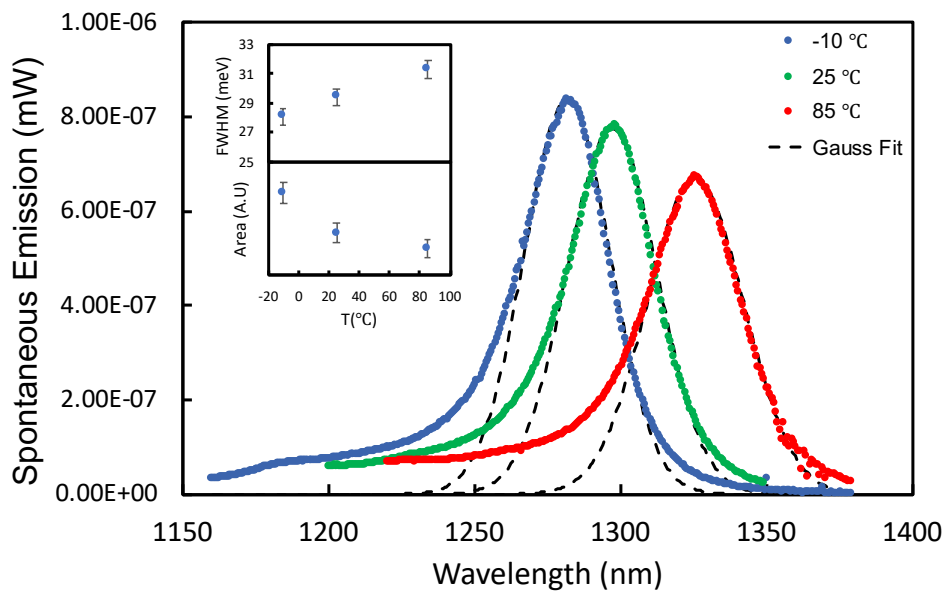


Figure 3.24: Spontaneous emission at 90% threshold current with respect to wavelength at different temperatures

The intensities fall with increasing temperature, also reflected in the area in the inset, in line with the carrier distribution to higher states where they are more likely to recombine non-radiatively. Temperature induced decrease in spontaneous emission efficiency has also been reported in [94], correspondingly reported to be attributed to the nonradiative recombination rates of carriers in higher states.

3.6.9 Comparison of material gain and differential gain spectra

Figure 3.25 shows the comparison of the positive gain region, differential gain, and the lasing emission spectra at different temperatures.

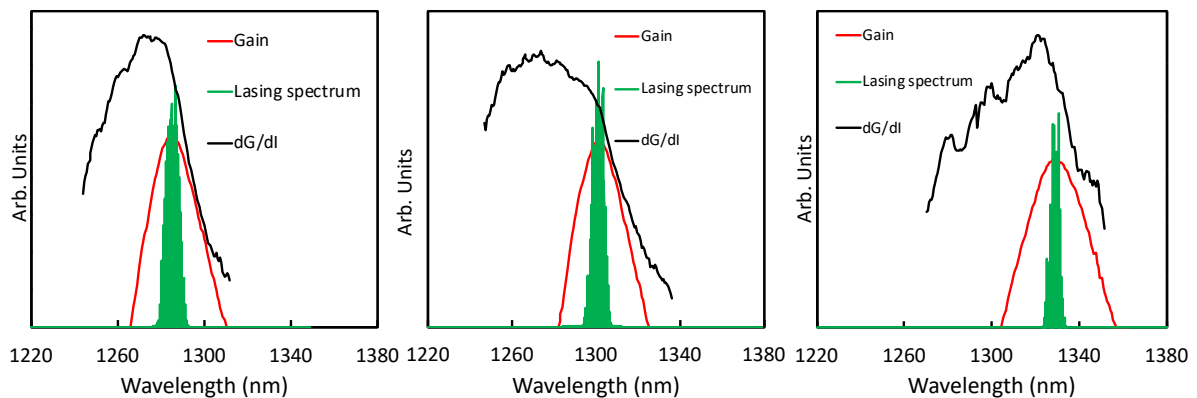


Figure 3.25: Positive gain, differential gain, and lasing spectrum with respect to wavelength at a) -10, b) 25, and c) 85 °C for the 375 μm device

From the Hakki-Paoli gain measurements the modal and differential gains were calculated. The gain peak is coincident with the peak lasing wavelength at all temperature. The differential gain is not exactly coincident on the peak lasing wavelength but very much within the positive gain region. Referring back to fig. 1 and comparing the wavelength difference of the gain and differential gain peaks, a 25 nm $\Delta\lambda$ at 25 °C is expected to result in a value of ~ 0.1 for the LEF for these samples. This difference is larger for 25 °C as the dg/dI spectrum has a larger FWHM.

3.6.10 Mode shift correction

The change in refractive index was obtained by measuring the wavelength shift of the FP modes up to the threshold for a given change in the injection current. Since the lasers were operated under CW conditions in my measurements, the wavelength shift caused by thermal effects must

be considered. Below threshold, the wavelength shift ($d\lambda$) with respect to the increase in current is caused by the refractive index change (dn) due to the injection of carriers, the active region temperature-increase-induced refractive index change (dn_t) and thermal expansion of the laser cavity (dL):

$$d\lambda_{sub-threshold} = \left(\frac{dn}{n} + \frac{dn_t}{n} + \frac{dL}{L} \right) \lambda \quad 3.24$$

Above threshold, the carrier density is clamped and the wavelength shift is only caused by the thermal effect:

$$d\lambda_{above-threshold} = \left(\frac{dn_t}{n} + \frac{dL}{L} \right) \lambda \quad 3.25$$

The above-explained dynamic can be qualitatively observed below where Fig. 3.26 plots the electroluminescence intensity as a function of wavelength in the vicinity of lasing oscillation.

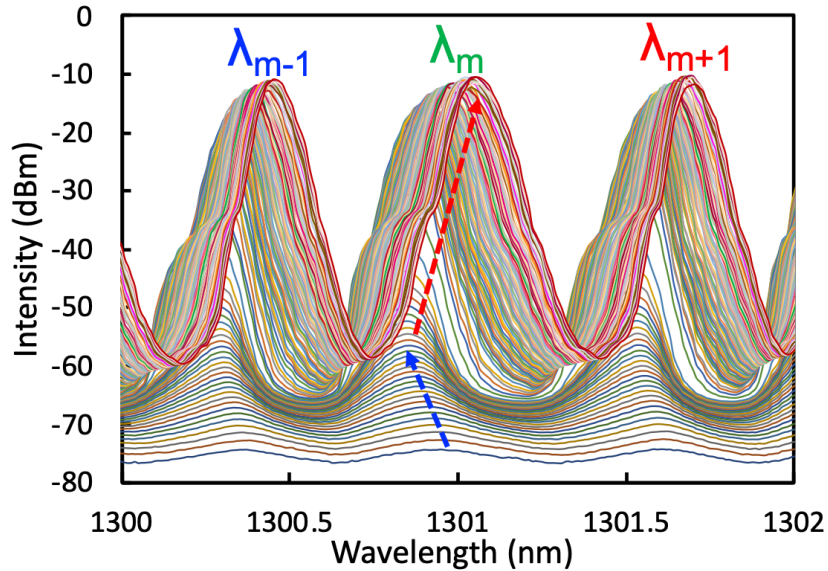


Figure 3.26: Modal shift in the vicinity of lasing wavelength of the 375 μm device at 25 $^{\circ}\text{C}$, up to 20 mA. Lasing mode ± 1 . The blue and red arrows show the below and above threshold shifts, respectively

It can be observed from above that the mode spacing for the short chip is 0.619 nm at 1300 nm which gives an effective index of 3.67 using the FSR eqn provided before ($\delta\lambda = \frac{\lambda^2}{2nL}$). Given the refractive index of GaAs = 3.4 and AlAs = 2.9 considering device structure presented in Fig. 3.5b, the higher calculated effective index suggests that the length of the device is 410 μm .

For the long chip, this mode spacing is 0.311 nm at 1305nm yielding an effective index of 3.65 also suggesting that the length of the device is 805 μm . Lengths were assumed at 375 and 750 μm in the calculations for mirror losses and current density.

In the state-of-the-art QD material used in this study, the gain from ground state is at least 3 times higher than reports in the literature summarized in table 3, and as mentioned before the ES1 contribution is limited. Nonetheless, non-ideal carrier clamping can be observed in the gain spectra above threshold whereby there is no increase in gain in the non-lasing wavelengths as current is increased above threshold. This can be seen in figure 3.27. This indicates a certain level of carrier clamping of QD carriers, and possibly also of those in the wetting layer (referring back to fig. 3.20 with a ratio of 30:1). If carriers surrounding the QDs are not pinned due to the capture process, this correction process would slightly underestimate the value of the LEF.

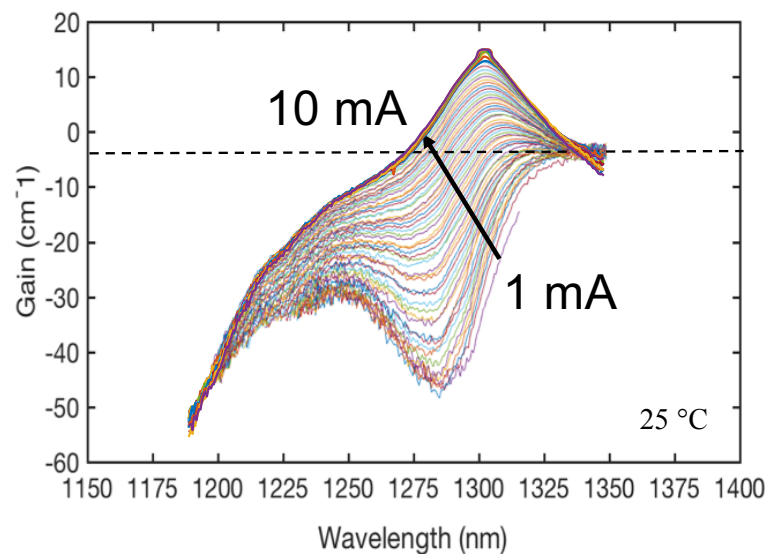


Figure 3.27: Net modal gain as a function of wavelength above threshold, 375 μm device at 25 $^{\circ}\text{C}$

Extra carriers above threshold cause an increase in the lasing power rather than the gain, this is also shown in the L-I plot of fig. 3.8.

Figure 3.28 plots the carrier-related wavelength shift and the RMS linewidth as a function of current.

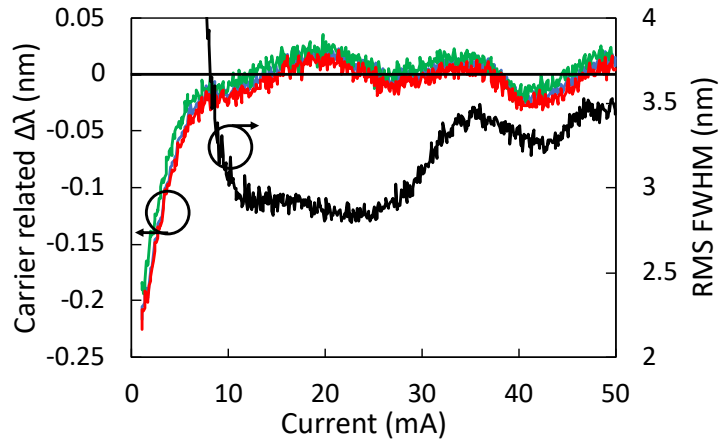


Figure 3.28: Temperature-corrected carrier related modal shift and RMS linewidth at 25 °C

An imprint of the RMS linewidth can be seen in the corrected modal shifts in fig 3.28, which may be attributed to a degree of non-ideal carrier clamping. This may be explained by extrapolating to the dynamic case of complete carrier clamping for the QDs, whereas as mentioned before the lack of clamping of excited state carriers in QD lasers has been previously reported [96]. With respect to accuracy of measurement, this yields an error in $\Delta\lambda$ of ± 0.05 nm (second term in eqn. 3.24). Thus, in this case, this warning is noted to be revisited briefly in the conclusions section.

3.6.11 LEF results

Now that the carrier related modal shift and the differential gain are acquired, LEF can be calculated from measured data. Figure 3.29 plots LEF at lasing wavelength as a function of drive current at the temperature range of measurement for the 375 μm device.

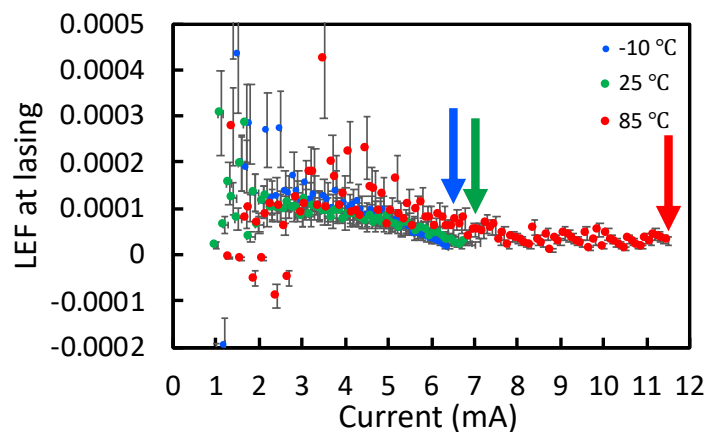


Figure 3.29: LEF at lasing vs current at the temperature range of measurement. Threshold current are indicated by arrows for the 375 μm device

An essentially zero LEF is observed at the gain peak up to threshold. A slight decrease is observed in the LEF as dg/dI increases near threshold in QD lasers. This will be further discussed in section 3.7.

Figure 3.30 plots the spectral LEF in the positive gain region as a function of wavelength at the temperature range of measurement at 90% of threshold current for the 375 μm device.

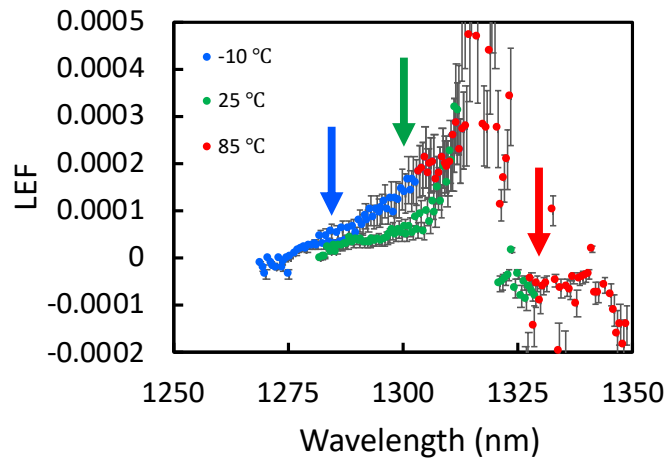


Figure 3.30: Spectral LEF with respect to wavelength at the temperature range of measurement at 90% of threshold for the 375 μm device. Arrows indicate lasing wavelength at the associated temperature

The LEF is effectively zero across the spectral range corresponding to positive net modal gain at the temperature range of measurement. Similarly, the net modal gain at 90 % of threshold current and also the corresponding values of the current dependent LEF at lasing are plotted in figure 3.31 for the 750 μm device.

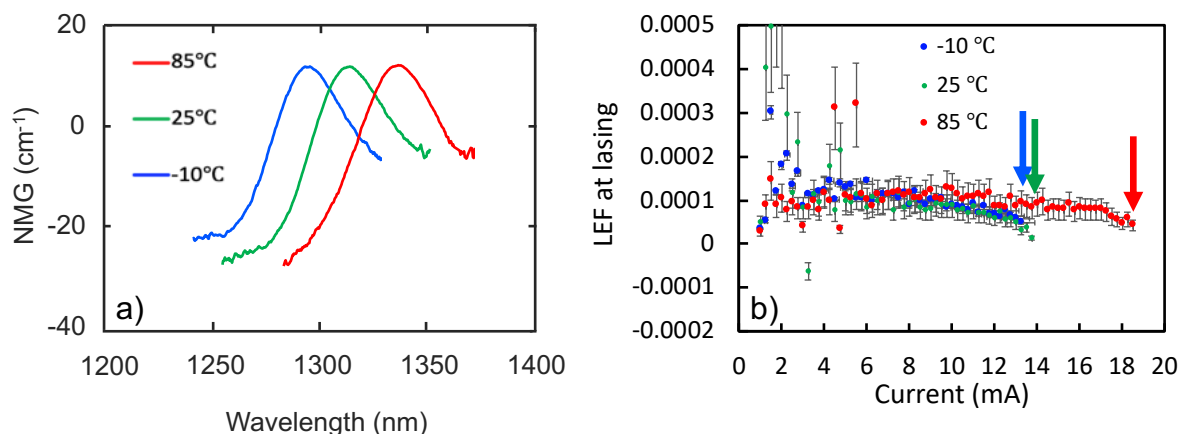


Figure 3.31: Net modal gain spectra as a function of temperature and the current dependent LEF at lasing at the temperature range of measurement at 90% of threshold for the 750 μm device. Arrows indicate threshold current

Accordingly, figure 3.32 plots the spectral LEF for the 750 μm device.

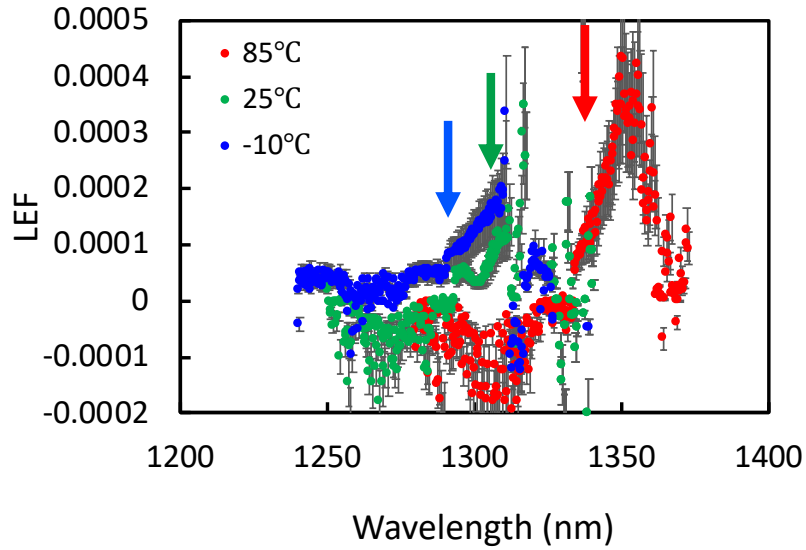


Figure 3.32: Spectral LEF at 90% of threshold at the temperature range of measurement for the 750 μm device. Lasing wavelengths are indicated by arrows

Both devices demonstrate close to zero spectra and current dependent LEF values at all measurement temperatures. From fig. 3.30-32 an LEF of 2.6×10^{-5} , 5×10^{-5} , and -8.9×10^{-5} is measured at lasing wavelength for the 375 μm device, and 5.14×10^{-5} , 7.6×10^{-5} , and 11×10^{-5} for the 750 μm device at -10, 25 and 85 C, respectively. The trends and observations are discussed in section 3.7.

3.6.12 Accuracy of measurement

Within the calculated error bars, LEF values found were all close to zero. The error bars derived from calculating LEF are from the culmination of errors in calculating the different terms of eqn. (3.2):

$$\left(\frac{\Delta \text{LEF}}{\text{LEF}}\right)^2 = \left(\frac{\Delta \delta \lambda}{\delta \lambda}\right)^2 + \left(\frac{\Delta d \lambda / d I}{d \lambda / d I}\right)^2 + \left(\frac{\Delta d g / d I}{d g / d I}\right)^2 + \left(\frac{\Delta L}{L}\right)^2 \quad 3.26$$

Where, the first term on the right-hand-side relates to the error in the F-P mode spacing, the second term to the error on calculating the wavelength shift with current, the third term to the error on calculating the differential gain, and the fourth term to the error on the cavity length deduction.

In comparison to the rest of the errors, the error on the F-P mode spacing and cavity length will be negligible due to the uncertainty in the cavity length being $\sim 1\%$ from the tolerance of the cleaving machine and that of the lasing wavelength to be $\sim 1\%$ from the calibrated OSA. The error on the second term will be small as it is calculated from the amount of above-threshold fluctuations that could be due to extrapolating to the dynamic case of total gain clamping above threshold. From the graph the error is estimated to be $\sim 5\%$. The main source of error derives from the measurement of the differential gain due to the number of steps required to obtain the gain spectrum using the Hakki Paoli technique. This average error is $\sim 20\%$ giving a total error of $\sim 30\%$ which gave a maximum error of ± 0.0003 for the LEF results.

3.7 Discussion

For both devices, the spectral and current dependent LEF values were found to be essentially zero. The general impairment of typical QDs is believed to be slow carrier relaxation through the QD energy levels resulting in excess carriers in the continuum of states in the wetting layer and well surrounding the dot. This is expected to increase the measured values of the LEF due to the free carrier effect which causes a reduction in refractive index [93]. Increasing the dot density not only increases the gain, but it also introduces more relaxation pathways for the carriers from the continuum to dots states thereby increasing the relaxation rate. This dynamic may be expected to result in a reduction of the carrier density in the continuum which can be attributed to for the achievement of very small LEF in this study relative to reports in table 3. It can be seen from the spectral LEF values plotted in figures 3.30 and 3.32, that the LEF grows with increasing wavelength. This mainly reflects the differential gain trends plotted in fig. 3.23 as the carrier related wavelength shift is smaller comparatively. This agrees with previous reports [29,44].

On the other hand, LEF values with respect to drive current presented experimentally [28, 48] or theoretically [96] for QD lasers are shown to increase monotonically with current, and in [48] it is shown to increase and then collapse at higher drive currents due to gain saturation and the occurrence of ES lasing as mentioned earlier in section 3.4. However, in the subthreshold data presented in figures 3.29 and 3.31 b) and because of the increase in dg/dI close to threshold, the QDs studied here present the opposite effect and LEF decreases close to threshold. This characteristic has also been observed in [25 and 39], where the differential gain

increases as the current nears threshold, causing a decrease in the LEF. As such, my results are also consistent with electroluminescence efficiency measurements in [97].

This can be qualitatively explained by considering that differential gain is the incremental gain obtained from e–h pairs injected in the active region, and is therefore independent of the nature of the active region, so long as all injected carriers relax to the lasing state (GS). However, above threshold, in QDs the differential gain decreases considerably with injection current, which is a ramification of gain compression linked to the QD intra-band relaxation dynamics [98]. These QD trends are at odds with that of QW counterparts [99] as the differential gain is highest at low current densities and gradually decreases with increasing current since states that are associated with the GS transition fill up. Furthermore, as electrons and holes do not fill the dots in pairs necessarily, the gain is small until a significant number of dots are filled, from then onwards it increases super-linearly. Conversely, for a QW laser their continuous DoS triggers a sub-linear increase in gain with current [25].

Additionally, as all the LEF values are very close to zero, there is the possibility of underestimation of the measurement error. Nonetheless, the absolute values are sizably smaller than that of the QW laser counterparts and other reports in QD lasers.

While the LEF comparison between QW and QD is not like-for-like in terms of material, and emission energy, it does show a greater reduction in the linewidth enhancement of QD lasers compared to QW lasers. However, it does suggest QD lasers have superior direct modulation performance than QW lasers, as far as linewidth is concerned, owing to their discrete DoS giving rise to symmetric gain shapes, particularly in terms of the inherent adiabatic positive chirp under modulation.

This sub-threshold method of calculating LEF provides a good indication of the realistic above threshold LEF values at low ground state population densities [96], i.e. well below ground state gain saturation. For CW operation at high injection current densities, thermal effects may take over. Another interesting consideration which is distinctive of QD lasers is the possibility the ground state becoming fully populated, gain saturation results in dg/dI approaching zero resulting in LEF approaching infinity.

3.8 Conclusion

In this chapter the up-to-date experimental techniques to measure the LEF were first outlined. A temperature correction technique was utilized to remove the thermal related wavelength shift yielding a measurement of solely the carrier-related LEF. Additionally, a constant junction temperature method was then utilized to account for the temperature increase as current density is increased. Finally, LEF of QD lasers has been calculated from measured data at a range of temperatures.

The 1300 nm QD lasers investigated in this chapter were demonstrated for the first time to have both spectral and current dependent LEF values that are essentially zero over all positive net modal gain region of the devices at the full temperature range of -10 to 85 °C, which goes beyond the commercial window as specified in guidelines [107]. This is attributed to the high gain from the GS, the symmetrical gain shape profile, and peak of differential gain being in the vicinity of the peak in net modal gain. It should be noted that the smallest LEF results, using the same experimental method, were previously reported in [27] which considered the effect of p-doping in QD laser dynamics, and the presented results here are an order of magnitude smaller attributed to the higher differential gain. As chirp is directly proportional to the LEF, these findings bode well for employment in a pre-chirp managed optical telecommunication system. It must be noted that although dispersion is zero at the 1300 nm window, QDs can cover all the O- through to the L- bands and the same principle of operation would apply as far as LEF is concerned here.

In the meantime, and to be studied in chapter 5, because the resilience of a semiconductor laser to external optical feedback is inversely proportional to the fourth power of its alpha-H parameter, when LEF is small [100], the presented QD lasers, with essentially zero-LEF values, are expected to demonstrated a rather high resilience towards external optical feedback. This will be considered in chapter 5, where I will investigate the RIN characteristics, which is the other inherent ramification of photon/carrier densities coupling inside a semiconductor laser as mentioned in the introduction. RIN under feedback will also be investigated.

Additionally, an imprint of the fluctuations in the laser linewidth with increasing current above threshold was observed for the first time in the corrected modal shift of the QD devices. This correlation can be ascribed to spectral hole burning in the lasing mode and a certain degree of

non-ideal carrier clamping above threshold varying the inhomogeneous linewidth in an oscillatory manner. These variations were mitigated via the constant junction temperature method but still visibly persist.

Furthermore, from a device stand-point, the essentially zero LEF values at the full temperature spectrum bode well for e.g. modulation purposes where adiabatic chirp (directly proportional to LEF) is the limiting factor on the signal degradation and hence the achievable transmission distance of the system. Since both gain and absorption spectra have been measured on these state-of-the-art active materials, light source and modulator characteristics can be investigated from a devices point of view. As a result, in the next chapter a novel integrated common active 1.3- μm electro-absorption modulated DFB QD laser is proposed.

3.9 Future work

The prospects of a monolithic integration of these QD materials in an EAM will be investigated in the next chapter. Additionally, as mentioned earlier the free running and also under external feedback RIN characteristics of these material will be studied in chapter 5.

The smallest achievable linewidth, at higher drive currents above threshold, is normally limited by gain compression [101, 102], linewidth re-broadening due to mode instability [103], the development of side modes [104], or spatial-hole burning [105, 106]. The latter three of these ramifications are predominantly related to the device structure and can be mitigated or circumvented via device design optimization. However, gain compression is fundamentally related to the timescales precipitated from the carrier relaxation dynamics in the semiconductor laser active media and is enhanced in a QD gain medium. Therefore, investigating the trade-offs involved in a dynamic operation, e.g., under modulation and above threshold would be a desirable extension to this work.

On the other hand, as shown in Fig 3.23, the differential gain follows a decreasing trend with increasing temperature due to hot carrier effects. This results in an increase in the LEF which is not very well pronounced in the results presented here up to 85 °C, as the final values are very close to zero. It would be noteworthy to investigate these QD devices LEF performance at higher temperatures as there is interest for these devices to operate in harsh environments often under high temperatures.

References

- [1]: A. L. Schawlow and C.H. Townes, "Infrared and optical masers", *Phys. Rev.* 112/6, pp. 1940-1949, 1958
- [2]: M.W. Fleming and A. Moradian, "Spectral characteristics of external-cavity controlled semiconductor lasers", *IEEE J. Quantum Electron.* 17, pp. 44–59, 1981
- [3]: C.H. Henry, "Theory of the linewidth of semiconductor lasers", *IEEE J. Quantum Electron.* 18, pp. 259–264, 1982
- [4]: K. Vahala and A. Yariv, "Semiclassical theory of noise in semiconductor lasers - Part I," in *IEEE Journal of Quantum Electronics*, vol. 19, no. 6, pp. 1096-1101, 1983
- [5]: K. Vahala and A. Yariv, "Semiclassical theory of noise in semiconductor lasers - Part II," in *IEEE Journal of Quantum Electronics*, vol. 19, no. 6, pp. 1102-1109, 1983
- [6]: H. Su, L. Zhang, R. Wang, T. C. Newell, A. L. Gray and L. F. Lester, "Linewidth study of InAs-InGaAs quantum dot distributed feedback lasers," in *IEEE Photonics Technology Letters*, vol. 16, no. 10, pp. 2206-2208, 2004
- [7]: K. Petermann (1991). *Laser Diode Modulation and Noise*. Kluwer Academic Publisher, Dordrecht
- [8]: H. Su et al., "High external feedback resistance of laterally loss-coupled distributed feedback quantum dot semiconductor lasers," in *IEEE Photonics Technology Letters*, vol. 15, no. 11, pp. 1504-1506, 2003
- [9]: J. R. Marciante and G. P. Agrawal, "Nonlinear mechanisms of filamentation in broad-area semiconductor lasers," in *IEEE Journal of Quantum Electronics*, vol. 32, no. 4, pp. 590-596, 1996
- [10]: L. A. Coldren and S. W. Corzine, "Diode lasers and photonic integrated circuits – 2nd edition," Willey, pp. 258, 2012
- [11]: M. Fox, "Optical properties of solids," Oxford University Press, 2001.
- [12]: R. de L. Kronig, "On the Theory of Dispersion of X-Rays," *J. Opt. Soc. Am.* 12, pp. 547-557, 1926
- [13]: Matthews, M. R., Cameron, K. H., Wyatt, R., and Devlin, W. J., "Packaged frequency-stable tunable 20 kHz linewidth 1.5 μm InGaAsP external cavity laser", *Electron. Lett.* 21, 113–115, 1985
- [14]: Patzak, E., Sugimura, A. S., Saito, S., Mukai, T., and Olesen, H., "Semiconductor laser linewidth in optical feedback configurations", *Electron. Lett.* 19, 1026–1027, (1983)

- [15]: Okai, M., “Spectral characteristics of distributed feedback semiconductor lasers and their improvements by corrugation-pitch-modulated structure”, *J. Appl. Phys.* 75, 1–29., 1994
- [16]: G. P. Agrawal, “Fiber-Optic Communication Systems” Wiley Inter-science, New York, pp. 478–512, 2002
- [17]: Takano, S., Sasaki, T., Yamada, H., Kitamura, M., and Mito, I. “Sub-MHz spectral linewidth in 1.5 μm separate-confinement-heterostructure (SCH) quantum-well DFB LDs”, *Electron. Lett.* 25, 356–357., 1989
- [18]: T. Yamanaka, Y. Yoshikuni, K. Yokoyama, W. Lui and S. Seki, “Theoretical study on enhanced differential gain and extremely reduced linewidth enhancement factor in quantum-well lasers,” *IEEE Jnl. Quant. Elect.*, vol. 29, no. 6, pp. 1609-1616, 1993
- [19]: O. Qasaimeh et. al, “Linewidth enhancement factor of quantum dot lasers,” *Opt. and Quant. Elect.*, vol. 37, no. 5, pp. 495-507, 2005
- [20]: D. O’Brien et al.: ‘Feedback sensitivity of 1.3 μm InAs/GaAs quantum dot lasers’, *Electron. Lett.*, 39, (25), pp. 1819–1820, 2003
- [21]: H. C. Schneider, W. W. Chow and S. W. Koch, “Anomalous carrier-induced dispersion in quantum-dot active media,” *Phys. Rev. B*, vol. 66, art. no. 041310, 2002
- [22]: T. W. Berg and J. Mork, “Quantum dot amplifiers with high output power and low noise,” *Appl. Phys. Lett.*, vol. 82, pp. 3083–3085, 2003
- [23]: L. A. Coldren and S. W. Corzine, “Diode lasers and photonic integrated circuits – 2nd edition,” Willey, pp. 307, 2012
- [25]: T. C. Newell, D. J. Bossert, A. Stintz, B. Fuchs, K. J. Malloy and L. F. Lester, “Gain and linewidth enhancement factor in InAs quantum-dot laser diodes,” *IEEE Photon. Tech. Letts.*, vol. 11, no. 12, pp. 1527-1529, 1999
- [26]: A. A. Ukhanov, A. Stintz, P. G. Eliseev and K. J. Malloy, “Comparison of the carrier induced refractive index, gain, and linewidth enhancement factor in quantum dot and quantum well lasers,” *Appl. Phys. Letts.*, vol. 84, pp. 1058-1060, 2004
- [27]: R. Alexander, D. Childs, H. Agarwal, K. Groom, H.Y. Liu, M. Hopkinson, R.A. Hogg “Zero and Controllable Linewidth Enhancement Factor in p-Doped 1.3 μm Quantum Dot Lasers” in *Japanese Journal of Applied Physics*. 46. pp. 2421-2423, 2007
- [28]: J. Kim, H. Su, S. Minin and S. L. Chuang, “Comparison of linewidth enhancement factor between p-doped and undoped quantum-dot lasers,” *IEEE Photon. Tech. Letts.*, vol. 18, no. 9, pp. 1022-1024, 2006
- [29]: J. Kim, Su, H., Minin, S., and Chuang, S.-L., “Gain-dependent linewidth enhancement factor in the quantum dot structures,” in *Nanotechnology* 21, 134010, 2010

- [30]: Sasan Fathpour, Z. Mi and P. Bhattacharya, "High-speed quantum dot lasers," *Jrnl. Phys. D: Appl. Phys.*, vol. 38, no. 13, pp. 2103-2111, 2005
- [31]: O. Carroll, I. O'Driscoll, S. P. Hegarty, G. Huyet, J. Houlihan, E. A. Viktorov, and P. Mandel, "Feedback induced instabilities in a quantum dot semiconductor laser," *Opt. Express* 14, pp. 10831-10837, 2006
- [32]: Z. Xu, D. Birkedal, M. Juhl and J. M. Hvam," Submonolayer InGaAs/GaAs quantum-dot lasers with high modal gain and zero-linewidth enhancement factor," *Appl. Phys. Letts.*, vol. 85, pp. 3259-3261, 2004
- [33]: J. Muszalski, J. Houlihan, G. Huyet and B. Corbett, "Measurement of linewidth enhancement factor in self-assembled quantum dot semiconductor emitting lasers at 1310nm," *Elect. Letts.*, vol. 40, no. 7, pp. 428-430, 2004
- [34]: D.Y. Cong, A. Martinez, K. Merghem, A. Ramdane, J.-G. Provost, M. Fischer, I. Krestnikov and A. Kovsh, "Temperature insensitive linewidth enhancement factor of p-type doped InAs/GaAs quantum-dot lasers emitting at 1.3 μ m," *Appl. Phys. Letts.*, vol. 92, art. no. 191109, 2008
- [35]: Stephan Schneider, Paola Borri, Wolfgang Langbein, Ulrike Woggon, Roman L. Sellin, D. Ouyang, and Dieter Bimberg, "Linewidth Enhancement Factor in InGaAs Quantum-Dot Amplifiers", *IEEE JQE*, Vol. 40, No. 10, pp. 1423-1429, 2004
- [36]: D. Rodríguez, I. Esquivias, S. Deubert, J. P. Reithmaier, A. Forchel, M. Krakowski, M. Calligaro, and O. Parillaud, "Gain, Index Variation, and Linewidth-Enhancement Factor in 980-nm Quantum-Well and Quantum-Dot Lasers", *IEEE JQE*, Vol. 41, No. 2, pp. 117-126, 2005
- [37]: B. Dagens, A. Markus, J.X. Chen, J.-G. Provost, D. Make, O. Le Gouezigou, J. Landreau, A. Fiore and B. Thedrez, "Giant linewidth enhancement factor and purely frequency modulated emission from quantum dot laser", *Electronic Letters*, Vol. 41 No. 6, 2005
- [38]: S. Azougui, D.-Y. Cong, A. Martinez, K. Merghem, Q. Zou, J.-G. Provost, B. Dagens, M. Fischer, F. Gerschütz, J. Koeth, I. Krestnikov, A. Kovsh, and A. Ramdane , " Temperature Dependence of Dynamic Properties and Tolerance to Optical Feedback of High-Speed 1.3- m DFB Quantum-Dot Lasers", *IEEE Photon. Tech. Lett.*, Vol. 23, No. 9, 2011
- [39]: A. Martinez, K. Merghem, S. Bouchoule, G. Moreau, A. Ramdane, J.G. Provost, F. Alexandre, F. Grillot, O. Dehaese, R. Piron, and S. Loualiche, "Dynamic properties of InAs/InP In As / In P (311)B quantum dot Fabry–Perot lasers emitting at 1.52 μ m", *Appl. Phys. Lett.* 93:2, 2008

- [40]: A. Martinez, A. Lemaître, K. Merghem, L. Ferlazzo, C. Dupuis, A. Ramdane, J.-G. Provost, B. Dagens, and O. Le Gouezigou, "Static and dynamic measurements of the α - factor of five-quantum-dot-layer single-mode lasers emitting at 1.3 μ m 1.3 μ m on GaAs" Appl. Phys. Lett. 86:21, 2005
- [41]: F. Lelarge, B. Rousseau, B. Dagens, F. Poingt, F. Pommereau and A. Accard, "Room temperature continuous-wave operation of buried ridge stripe lasers using InAs-InP (100) quantum dots as active core," in IEEE Photonics Technology Letters, vol. 17, no. 7, pp. 1369-1371, 2005
- [42]: P.K. Kondratko, S.L. Chuang, G. Walter, T. Chung, and N. Holonyak Jr. "Observations of near-zero linewidth enhancement factor in a quantum-well coupled quantum-dot laser," in Appl. Phys. Lett., 83, pp. 4818, 2003
- [43]: F. Grillot and N. Dubey, "Influence of the Linewidth Enhancement Factor on the Modulation Response of a Nanostructure based Semiconductor Laser Operating under External Optical Feedback" in Proc. of SPIE Vol. 7933, 2011
- [44]: F. I. Zubov Yu. M. Shernyakov M. V. Maximov A. E. Zhukov D. A. Livshits A. S. Payusov A. M. Nadtochiy A. V. Savelyev N. V. Kryzhanovskaya N. Yu. Gordeev, "spectral dependence of the linewidth enhancement factor", in Physics of Semiconductor Devices, Volume 47, Issue 12, pp 1656–1660, 2013
- [45]: G. Giuliani, "Linewidth enhancement factor in semiconductor lasers," COST 288-WG2, 2004
- [46]: Giuliani, G., Donati, S., Villafranca, A., Lasobras, J., Garces, I., Chacinski, M., Schatz, R., Kouloumentas, C., Klonidis, D., Tomkos, I. "Round-Robin Measurements of Linewidth Enhancement Factor of Semiconductor Lasers" in COST 288 Action, CB9-2- WED. CLEO Europe/IQEC, 2007.
- [47]: M. Osinski and J. Buus, "Linewidth broadening factor in semiconductor lasers-An overview," in IEEE Journal of Quantum Electronics, vol. 23, no. 1, pp. 9-29, 1987
- [48]: F. Grillot, B. Dagens, J. Provost, H. Su and L. F. Lester, "Gain Compression and Above-Threshold Linewidth Enhancement Factor in 1.3-um InAs–GaAs Quantum-Dot Lasers," in IEEE Journal of Quantum Electronics, vol. 44, no. 10, pp. 946-951, 2008.
- [49]: Z. Toffano, A. Destrez, C. Birocheau, and L. Hassine, "New linewidth enhancement determination method in semiconductor lasers based on spectrum analysis above and below threshold," Electron. Lett. 28, 9-11 (1992).

- [50]: A. Villafranca, J. A. La'zaro, I. Salina, and I. Garcé's, "Measurement of the Linewidth Enhancement Factor in DFB Lasers Using a High-Resolution Optical Spectrum Analyzer", *IEEE Photon. Technol. Lett.* 17, 2268–2270, 2005
- [51]: Villafranca, A., Giuliani, G., and Garces, I., "Mode-resolved measurements of the linewidth enhancement factor of a Fabry–Pérot laser", *IEEE Photon. Technol. Lett.* 21, 1256–1258, 2009
- [52]: Hui, R., Mecozzi, A., D'Ottavi, A., and Spano, P., "Novel measurement technique of alpha factor in DFB semiconductor lasers by injection locking" *Electron. Lett.* 26, 997–998, 1990
- [53]: Liu, G., Jin, X., and Chuang, S. L., "Measurement of linewidth enhancement factor of semiconductor lasers using an injection-locking technique" *IEEE Photon. Technol. Lett.* 13, 430–432, 2001
- [54]: R. Lang and K. Kobayashi, "External optical feedback effects on semiconductor injection laser properties," in *IEEE Journal of Quantum Electronics*, vol. 16, no. 3, pp. 347-355, 1980
- [55]: Yu, Y., Giuliani, G., and Donati, S., "Measurement of the linewidth enhancement factor of semiconductor lasers based on the optical feedback self-mixing effect" *IEEE Photon. Technol. Lett.* 16, 990–992, 2004
- [56]: Palavicini, C., Campuzano, G., Thedrez, B., Jaouen, Y., and Gallion, P., "Analysis of optical-injected distributed feedback lasers using complex optical low-coherence reflectometry," *IEEE Photon. Technol. Lett.* 15, pp. 1683–1685, 2003
- [57]: Harder, C., Vahala, K., and Yariv, "Measurement of the linewidth enhancement factor α of semiconductor lasers", *A. Appl. Phys. Lett.* 42, 328–33, 1983
- [58]: Kruger, U., and Kruger, K, J., "Simultaneous measurement of the linewidth, linewidth enhancement factor α , and FM and AM response of a semiconductor laser" *Lightw. Technol.* 13, 592–597, 1995
- [59]: Schimpe, R., Bowers, J. E., and Koch, T. L., "characterisation of frequency response of 1.5 μ m InGaAsP DFB laser diode and InGaAs PIN photodiode by heterodyne measurement technique" *Electron. Lett.* 22, 453–454, 1986
- [60]: Zhang, T., Zhu, N. H., Zhang, B. H., and Zhang, X., "Measurement of chirp parameter and modulation index of a semiconductor laser based on optical spectrum analysis", *IEEE Photon. Technol. Lett.* 19, 227–229, 2007
- [61]: Devaux, F., Sorel, Y., and Kerdiles, J. F., *J. Lightw. Technol.* "Simple measurement of fiber dispersion and of chirp parameter of intensity modulated light emitter", *Technol.* 11, 1937–1940, 1993

- [62]: Royset, A., Bjerkan, L., Myhre, D., and Hafskjaer, L., “Use of dispersive optical fibre for characterisation of chirp in semiconductor lasers,” *Electron. Lett.* 30, 710–712, 1994
- [63]: Srinivasan, R. C., and Cartledge, J. C., “On using fiber transfer functions to characterize laser chirp and fiber dispersion”, *IEEE Photon. Technol. Lett.* 7, 1327–1329, 1995
- [64]: J. G. Provost and F. Grillot, “Measuring the Chirp and the Linewidth Enhancement Factor of Optoelectronic Devices with a Mach-Zehnder Interferometer,” *IEEE Photon. J.* 3, 476-488, 2011
- [65]: Goobar, E., Gillner, L., Schatz, R., Broberg, B., Nilsson, S., “Measurement of a VPE-transported DFB laser with blue-shifted frequency modulation response from DC to 2 GHz”, and Tanbunek, T., *Electron. Lett.* 24, 746–747. 1988
- [66]: Sorin, W. V., Chang, K. W., Conrad, G. A., and Hernday, P. R., J., “Frequency Domain Analysis of an Optical FM Discriminator”, *Lightw. Technol.* 10, 787–793, 1992
- [67]: Vodhanel, R. S., and Tsuji, S., “12 GHz FM bandwidth for a 1530 nm DFB laser”, *Electron. Lett.* 24, 1359–1361., 1988
- [68]: Wellford, D., and Alexander, S. B., J., “Magnitude and phase characteristics of frequency modulation in directly modulated GaAlAs semiconductor diode lasers”, *Lightw. Technol.* 3, 1092–1099, 1985
- [69]: Saunders, R. A., King, J. P., and Hardcastle, I., “Wideband chirp measurement technique for high bit rate sources”, *Electron. Lett.* 30 (16), 1336–1338, 1994
- [70]: B. W. Hakki and T. L. Paoli, “Gain spectra in GaAs double- 328 heterostructure injection lasers,” *J. Appl. Phys.*, vol. 46, no. 3, 329 pp. 1299–1306, 1975
- [71]: Henning, I. D., and Collins, J. V., “Measurements of the semiconductor laser linewidth broadening factor”, *Electron. Lett.* 19, 927–929., 1983
- [72]: L. A. Coldren and S. W. Corzine, “Diode lasers and photonic integrated circuits – 2nd edition,” Willey, pp. 58, 2012
- [73]: Kenichi Nishi et. al., “Molecular beam epitaxial growths of high-optical-gain InAs quantum dots on GaAs for long-wavelength emission,” *J. Cryst. Growth*, Vol. 378, pp. 459-462., 2013
- [74]: Z.R. Wasilewski et al., “Size and shape engineering of vertically stacked self-assembled quantum dots”, *Journal of Crystal Growth*, Vol. 201–202, pp.1131-1135, 1999
- [75]: R.R. Alexander, “GaAs based quantum dot lasers for 1.3 μ m optical communications”, in PhD thesis, University of Sheffield, pp.64, submitted 2010

- [76]: B. Zhao, T. R. Chen, S. Wu, Y. H. Zhuang, Y. Yamada, and A. Yariv, “Direct measurement of linewidth enhancement factors in quantum well lasers of different quantum well barrier heights,” *Appl. Phys. Letts.*, Vol. 62, No. 14, 1993
- [77]: D.G. Deppe, D. L. Huffaker, S. Csutak, Z. Zou, G. Park, and O. B. Shchekin, “Spontaneous emission and threshold characteristics of 1.3 μm InGaAs/GaAs quantum dot GaAs-based lasers”, *IEEE J. Quantum Electron.* 35 (1999) 1238–1246.
- [78]: M. Sugawara, K. Mukai, Y. Nakata, and H. Ishikawa, “Effect of homogeneous broadening of optical gain on lasing spectra in self-assembled $\text{In}_x\text{Ga}_{1-x}\text{As}/\text{GaAs}$ quantum dot lasers,” *Phys. Rev. B* 61, 11, 2000
- [79]: M. Sugawara, K. Mukai, and H. Shoji, “Effect of phonon bottleneck on quantum-dot laser performance”, *Appl. Phys. Lett.* 71 (19), 2791, 1997
- [80]: Y. Arakawa and H. Sakaki, “Multidimensional quantum well laser and temperature dependence of its threshold current,” *Appl. Phys. Letts.*, vol. 40, pp. 939-941, 1982
- [81]: K. S. Mobarhan, “Test and characterization of laser diodes: Determination of principal parameters,” Newport Application Note 1.
- [82]: O. B Shchekin and D. G. Deppe, “Low-threshold high- T_0 1.3 μm InAs quantum-dot lasers due to p-type modulation doping of the active region,” *IEEE Photon. Tech. Letts.*, vol. 14, pp. 1231-1233, 2002
- [83]: S. Fathpour, Z. Mi, P. Bhattacharya, A. R. Kovsh, S. S. Mikhlin, I. L. Krestnikov, A. V. Kozhukhov and N. N. Ledentsov, “The role of Auger recombination in the temperature-dependent output characteristics ($T_0 = \infty$) of p-doped 1.3 μm quantum dot lasers,” *Appl. Phys. Letts.*, vol. 85, pp. 5164-5166, 2004
- [84]: I. P. Marko, N. F. Massé, S. J. Sweeney, A.D. Andreev, A. R. Adams, N. Hatori and M. Sugawara, “Carrier transport and recombination in p-doped and intrinsic 1.3 μm InAs/GaAs quantum-dot lasers,” *Appl. Phys. Letts.*, vol. 87, art. no. 211114, 2005
- [85]: T. J. Badcock, R. J. Royce, D. J. Mowbray, M. S. Skolnick, H. Y. Liu, M. Hopkinson, K. M. Groom and Q. Jiang, “Low threshold current density and negative characteristic temperature 1.3 μm InAs self-assembled quantum dot lasers,” *Appl. Phys. Letts.*, vol. 90, art. no. 111102, 2007
- [86]: S. Mokkaṭpati, M. Buda, H. H. Tan and C. Jagadish, “Effect of Auger recombination on the performance of p-doped quantum dot lasers,” *Appl. Phys. Letts.*, vol. 88, art. no. 161121, 2006
- [87]: C. Y. Jin, T. J. Badcock, H. Y. Liu, K. M. Groom, R. J. Royce, D. J. Mowbray and M. Hopkinson, “Observation and modelling of room-temperature negative characteristic

temperature 1.3 μ m p-type modulation doped quantum dot laser,” IEEE Jnl. Quant. Elect., vol. 42, pp. 1259-1265, 2006

[88]: Ryan Alexander, “GaAs based quantum dot lasers for 1.3 μ m optical communications”, in PhD thesis, University of Sheffield, pp. 111-120, submitted 2010

[89]: K. M. Groom, A. I. Tartakovskii, D. J. Mowbray, M. S. Skolnick, P. M. Smowton, M. Hopkinson and G. Hill, “Comparative study of InGaAs quantum dot lasers with different degrees of dot layer confinement,” Appl. Phys. Letts., vol. 81, pp. 1-3, 2002.

[90]: M. Sugawara, K. Mukai, and Y. Nakata, Appl.Phys.Lett. 75,656, 1999

[91]: Atsushi Konuma, Mitsuyoshi Shibata, in “よくわかる半導体レーザ” , Engineering Books Co., Ltd., pp. 111, 1995

[92]: A. V. Uskov, I. Magnusdottir, B. Tromborg, J. Mørk and R. Lang, “Line broadening caused by Coulomb carrier–carrier correlations and dynamics of carrier capture and emission in quantum dots,” Appl. Phys. Letts., vol. 79, pp. 1679-1681, 2001

[93]: N. Peyvast, K. Zhou, R. A. Hogg, and D. T. D. Childs, “Dominant role of many-body effects on the carrier distribution function of quantum dot lasers”, Appl. Phys. Express 9, 032705, 2016

[94]: G. Park, D. L. Huffaker, Z. Zou, O. B. Shchekin, and D. G. Deppe, “Temperature Dependence of Lasing Characteristics for Long-Wavelength (1.3- μ m) GaAs-Based Quantum-Dot Lasers”, IEEE Photonics Technol. Lett. Vol. 11, No. 3 301, 1999

[95]: I. P. Marko, A. R. Adams, S. J. Sweeney, I. R. Sellers, D. J. Mowbray, M. S. Skolnick, H. Y. Liu, and K. M. Groom, “Recombination and loss mechanisms in low-threshold InAs/GaAs 1.3 μ m quantum dot lasers,” in Proc. 19th IEEE Int. Semiconductor Laser Conf., Matsue, Japan, Sep. Paper ThB4, 2004

[96]: S. Melnik, G. Huyet and A. V. Uskov, “The linewidth enhancement factor α of quantum dot semiconductor lasers,” Opt. Express, vol. 14, no. 7, pp. 2590-2595, 2006

[97]: D.L. Huffaker and D.G. Deppe, “Electroluminescence efficiency of 1.3 μ m wavelength InGaAs/GaAs quantum dots,” Appl. Phys. Lett., vol. 73, pp. 520–522, 1998

[98]: A. Fiore and A. Markus, “Differential Gain and Gain Compression in Quantum-Dot Lasers”, IEEE JQE, Vol. 43, No. 3, pp. 287-294, 2007

[99]: M. Grundmann and D. Bimberg, “Theory of random population for quantum dots,” Phys. Rev. B, vol. 55, pp. 9740–9745, 1997

[100]: K. Petermann, “External optical feedback phenomena in semiconductor lasers”, IEEE J Selected To. In Quantum Elect., Vol. 1, No. 2, 1995

- [101]: G. P. Agrawal, G. H. Duan, and P. Gallion, “Influence of refractive index nonlinearities on modulation and noise properties of semiconductor lasers”, *Electron Lett.* Vol. 28, No. 19 pp. 1773–1774, 1992
- [102]: F. Girardin, G. H. Duan, and P. Gallion, “Linewidth rebroadening due to nonlinear gain and index induced by carrier heating in strained quantum-well lasers”, *IEEE Photon. Tech. Lett.* Vol. 8, No. 3, pp. 334–336, 1996
- [103]: H. Olesen, B. Tromborg, H. E Lassen, X. and Pan, “Mode instability and linewidth rebroadening in DFB lasers”, *Electron. Lett.* Vol. 28, No. 5, pp. 444–446, 1992
- [104]: X. Pan, B. Tromborg, and H. Olesen, “Linewidth rebroadening in DFB lasers due to weak side modes”, *IEEE Photon. Technol. Lett.* Vol. 3, No. 2, pp. 112–114, 1991
- [105]: M. Okai, M. Suzuki, T. Taniwatari, and N. Chinone, “Corrugation-Pitch-Modulated Distributed Feedback Lasers with Ultranarrow Spectral Linewidth”, *Jpn. J. Appl. Phys.* 33, 2563–2570, 1994
- [106]: H. Wenzel, H. J. Wunsche, and U. Bandelow, “Linewidth rebroadening in semiconductor lasers due to lateral spatial holeburning” *Electron. Lett.* Vol. 27, No. 25, pp. 2301–2302, 1991
- [107]: Cisco GPON SFP Datasheet, April 25, 2016, document ID:1461606040226191

Chapter 4

Proposal for a Common Active Layer In(Ga)As Quantum Dot Electro-Absorption Modulated DFB Laser at 1.3- μm

4.1 Introduction

In the previous two chapters the gain and absorption characteristics of state-of-the-art quantum dot (QD) active media were experimentally investigated, which confirmed the unique spectral shape that is caused by the QDs delta function like density of states (DOS). As gain/absorption spectra have been studied, the prospects of utilizing the material for modulation applications can be investigated with a device application in mind. Accordingly, prospects of a new path to high-speed and frequency-chirp-managed modulation are explored by considering the monolithic integration of a novel common QD active layer electroabsorption modulated (EAM) laser.

Demonstrating a temperature-insensitive [1] and an ultra-low [2] threshold current, and

potential tolerance to optical feedback [3], QD active medium is a desirable option for uncooled and isolator-free utilization in fiber optic telecommunication. Nonetheless, as seen in chapter 3, QD Fabry-Perot lasers present a broad lasing spectrum attributed to the interaction of inhomogeneous and homogeneous linewidths [4], and also damping-limited thus relatively moderate direct modulation rates as will be investigated in chapter 5 and also reported in [5]. GaAs-based QD distributed feedback lasers (DFBs) have demonstrated 10 *Gbps* direct modulation under a wide temperature of operation, and although lower than QW equivalents, exhibiting linewidth enhancement factor values of ~ 1 [6].

Direct modulation in a long-haul optical telecommunication system is limited, not because of the modulation bandwidth limitation but due to the frequency (wavelength) chirp produced under direct modulation. The chirping of a single-mode DFB laser limits the transmission distance in high-bit-rate systems because of the chromatic dispersion of the standard silica-based optical fiber. This will eventually broaden the signal down the transmission line, which may cause cross-talk and error in recording 0's and 1's at the decision level. Therefore, the target is to realize high-speed modulation with a negative frequency chirp to counter signal broadening.

It is also noteworthy that directly modulating laser devices by modulating the drive current enhances the carrier/photon density coupling, which increases the LEF and therefore the dynamic frequency chirp, consequently external modulation is more desirable. In 2000, the first coast-to-coast 10 *Gbps* transmission system was installed in the US. The preferred optical transmitter technology was based on Lithium Niobate (LiNbO) Mach-Zehnder modulation for these long-haul systems. The main advantages, at the time, which had contributed to the dominance of LiNbO over electro absorption modulated lasers (EMLs) were the low yield of EMLs due to less mature technology, the ability of LiNbO to reliably achieve moderately high output power, and the ability of LiNbO to modulate an optical signal while maintaining a constant chirp parameter over the full range of drive voltage [7]. As additional long-haul links and components and metropolitan systems were installed, cost and size became more important, and demonstrations of EMLs have raised confidence. Due to the shorter interaction length, convenient integration with the laser chip, and lower drive voltages, EMLs enable lower cost and size compared to a laser plus a LiNbO. It must be noted that the principle of modulation operation along with the aforementioned modulator and also the QD and QW EAMs were explained in chapter 2, under section 2.4: Modulation. Metro systems are expected

to span distances of up to 200 km and will subsequently not demand extinction ratios (defined in the following section 4.2) beyond 10 dB. However, dispersion-compensation-free spans in the range of 200-km for 10 Gbps communications are very desirable for metro rings. For this reason, chirp characteristics are highly imperative.

4.1.2 Extinction ratio and insertion loss

In telecommunications, extinction ratio (ER) is the fraction of the two optical power levels of a signal generated by an optical source. It is usually expressed in dB and considering fig. 4.1 which depicts a typical absorption spectrum expected from a QW system, ER can be written as:

$$ER = R_{on/off} = \frac{P_{out}(V_{on} = 0)}{P_{out}(V_{on} = V_b)} = \frac{e^{-\alpha(0)L}}{e^{-\alpha(b)L}}$$

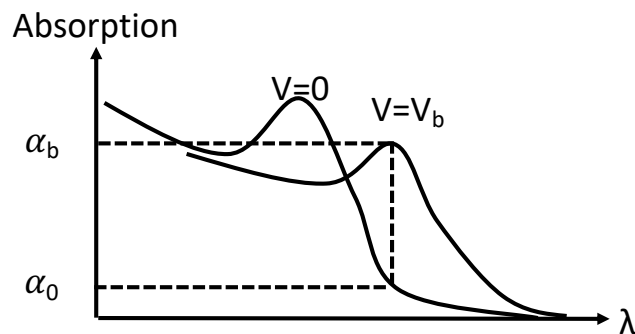


Figure 4.1: Depicted QW QCSS for the presentation of extinction ratio

Extinction ratio can be made as large as possible by increasing the length of the modulator. However, as a trade-off propagation loss becomes an issue. Correspondingly, insertion loss refers to the loss of signal power due to the insertion of a device in a transmission line or an optical fiber and can be written as:

$$IL = \frac{P_{in} - P_{out}(V = 0)}{P_{in}} = 1 - e^{-\alpha(0)L}$$

As expected, longer devices have a larger insertion loss associated with them.

4.2 Background and motivation

In direct modulation of standard QDs, the limitation arises from the occupation of states in the barrier and wetting layer at room temperature by the electrons injected into the active region (hot carrier effect). The occupation of these undesirable states, in the conduction band, increases gain compression, which causes a reduction in the modulation bandwidth. Furthermore, thermal hole broadening, in the valence band, results in tightly spaced energy levels. This could substantially increase the nonradiative recombination rates, thus reducing gain. The former hot carrier effects and this latter hole broadening result in a decrease in gain and differential gain of QD lasers, therefore reducing the direct modulation bandwidth. To alleviate these limitations, tunneling injection has been proposed to reduce hot carrier effects [8-, 9-]. And also, p-doping has been proposed as solution to hole state broadening at room temperature [10-, 11-]. While p-doping and tunnel injection were successfully demonstrated to enhance the modulation performance of QD lasers, a combination of these methods is often required and the latter tunnel injection is dependent upon complicated growth procedures. This makes it particularly difficult to achieve high modulation bandwidths at the communication wavelength of 1.3 μm .

On the other hand, narrow linewidth DFB lasers enable high bit-rate transmission along with reduced temporal broadening of the pulse as it propagates through the chromatically dispersive fiber. Nonetheless, the relatively large positive (red) chirp attributed to the change in the carrier density of a directly modulated laser precipitates pulse broadening. As mentioned above, because of the smaller chirp from optical modulators, external modulation is desirable. Even with non-dispersion shifted fibers, chirp-free pulses experience broadening, attributed to the Fourier components of the pulse itself [12]. Negative (blue) chirped pulses can extend the transmission distance since the optical pulses would primarily be compressed temporally by the dispersion as they propagate through the fiber.

A well-renowned track for obtaining high ER, high-speed, and low chirp InP-based devices is through the utilization of QW-DFB monolithically integrated electro-absorption modulated laser (EML) devices [13]. This method relies upon photonic integration technologies to spatially vary the band-gap, such as selective area growth [14], butt-coupled regrowth [15], or intermixing [16]. Nevertheless, such devices have not been achieved in GaAs-based QD

structures, seemingly due to the perceived prerequisite for the spatial modification of the band-gap for the modulator and gain sections.

More recently InP-based QW DFB-EMLs have been realized using a common MQW active layer structure for these two sections [17]. Utilizing these structures decrease coupling losses, and substantially simplifies the manufacturing procedure, which will ultimately reduce possible failure mechanisms and also cost. Thus, it is timely to explore the opportunities for monolithic integration of GaAs-based DFB-EMLs using a common active media that can be realized by QDs instead.

4.3 Gaps in knowledge

Presently, the number of reports on QD-based EAMs are limited in the literature [18-21]. In [18] the electro-absorption properties of a ten-layer-stack single-mode 1.3 μm QD waveguide was investigated. Although 10 V is quite large for electro-absorption modulator purposes as compared to QWs (2-3 Vpp), the corresponding electric fields are around 260 kV/cm at 10V. This is attributed to the relatively thick, (33 nm in [18]) GaAs spacer layer in each period of the QD stacks, which makes up a sizable intrinsic layer thickness. Therefore, by reducing the spacer layer thickness, a reasonable bias voltage may achieve the same QCSS. As such, a 1.4 nm GaP tensile strain compensation layer was deposited in each period of the QD layers which helped achieve an extinction ratio of 13 dB at 5 V. in [19] a QCSS is reported for In(Ga)As QDs with no substantial broadening of the transition. A shift of 11 meV was reported under an applied field of 270 KV/cm (10 V), the dot ground state red-shifts by 11 meV at 1.3 μm , which yielded a maximum refractive index change of 0.001 below the bandgap. In [20] a 10-layer stack QD EAM was utilized to achieve a 17 GHz modulation bandwidth and an extinction ratio of 18 dB under an applied bias of 9 V (QCSS of 15 nm). In [21], they made use of an external tunable laser for the light source and a separate modulator section which helped achieve a clear eye opening for a 4.8 Gbps data transmission with a fixed carrier wavelength of 1.6 μm and 7 Gbps at 1.29 μm . The potential of using QDs as optical modulators have been reported in InAs QDs grown on a Si substrate [22]. An extinction ratio of 5.1 dB at 1310 nm under a reverse bias of 20 V was reported.

A distinctive property of QD EAMs due to the unique shape of their DOS was previously

proposed and modeled, which utilizes a novel modulation arrangement promising negative chirp values [12].

Figure 4.2 a) shows the absorption spectra of the QDs as modeled in [12]. They assumed a Gaussian-shaped spectrum with a broadening of 34 meV, whereas a broadening of 28meV was measured in the QDs here attributed to the inhomogeneous broadening precipitated by the size and composition variation of the dots. Between the two absorption peaks, is a region with a small absorption coefficient due to the QD's discrete energy levels. By fine-tuning the signal wavelength to the maximum of the absorption peak without application of E-field, a transmission can then be obtained when the E-field is applied. As such, since the transmission wavelength is on the shorter wavelength (blue side) of the absorption peak, the change in the refractive index yields a negative alpha value. Achieving this negative wavelength chirp helps compress the optical pulse in the fiber transmission countering the inherent chromatic dispersion in standard single mode fibers.

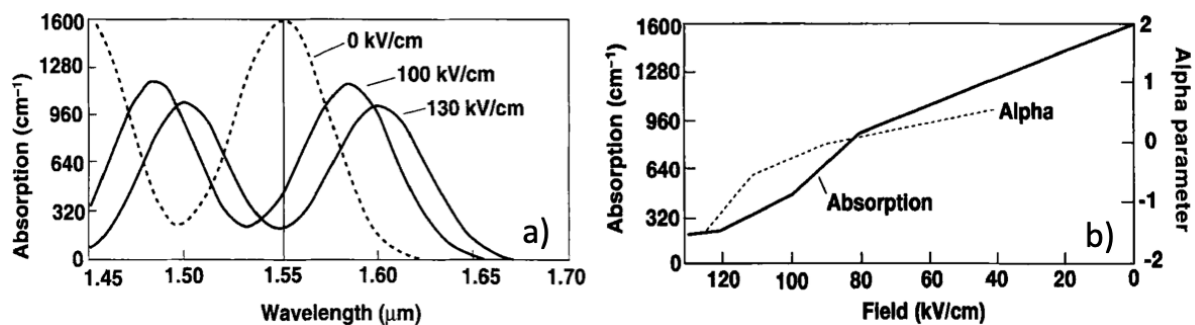


Figure 4.2: a) Simulated absorption spectra of InAs QDs. Inhomogeneous broadening value of 34 meV (full width) is presumed. The dotted line represents the absence of the electric field, and b) the calculated absorption coefficient and the alpha parameter [12]

Figure 4.2 b) demonstrates the calculated alpha parameter and the change in the absorption coefficient with respect to the applied electric field. The alpha parameter is negative for a high electric field of 130 to 80kV/cm, and it shifts to positive at lower fields. This increase will not be problematic since the light is absorbed by QDs under the low field.

The analysis carried out in [12] is a preliminary but provides an attractive approach for blue-chirp signal generation. The researchers assumed a quantum confined Stark shift (QCSS) identical to that of a QW; whereas in QDs, Coulomb charge effects may have some influence

on the QCSS due to the higher localization of carriers. The presumed inhomogeneous broadening of 34meV is based on the S-K growth mode. The progress of growth technology has reduced this, and a narrower broadening largely reduces the absorption loss between discrete levels to yield a larger modulation extinction ratio. Currently, modulators that employ QDs as active elements have not found a widespread application, considering the problems to be addressed. Nevertheless, they are worth more detailed investigation because of the need for controlled-chirp modulation for longer-span transmission systems.

In this comparatively concise chapter, the spectroscopic study of state-of-the-art In(Ga)As/GaAs QD material carried out in chapter 2 is utilized in order to investigate the different mechanisms for the operation of a common QD active layer DFB-EML. Examination of the absorption and gain spectra (from -10 to 85 °C) corroborates the exclusive delta-function-like DOS of the QDs in the profiles of both gain and absorption spectra. Utilizing this distinctive shape, I will investigate the prospects for a number of modulation schemes, which depend on the selected DFB wavelength detuning from the gain peak. Both modulation arrangements of conventional [23], where signal is absorbed at high bias voltage, and novel [12], where signal is transmitted at the higher bias voltage will be investigated.

I will then probe the effect of EML length on the corresponding ER and the associated insertion losses (IL) and demonstrate the change in absorption spectra which would lead to various chirp values at these different DFB wavelengths. Subsequently, reflecting upon my findings, I will conclude that a monolithically-integrated QD DFB-EML is feasible and compare some of its key figures of merit with a similar design which employed QWs in the active medium.

It will be shown that, under red detuning from the gain peak, standard EML operation is realized with the expected positive chirp and with no signal amplification necessary. On the other hand, operation in the blue detuning regime could achieve the aforementioned proposed modulation scheme [12] along with negative or blue chirp. Nevertheless, blue chirp operation would require signal amplification that could be realized by an amplifier section.

In what follows, firstly the proposed QD-DFB-EML device is presented and the test material outlined. Subsequently I delve into the experimental results and the corresponding analysis. A conclusion section is provided at the end to summarize the chapter results, and finally possible

future work is proposed.

4.4 Proposed device

Figure 4.3 provides a schematic representation of the proposed device incorporating a DFB laser integrated with an EAM with multi-section contacts. Reverse bias and modulation voltages are expected to be applied to the EAM section and continuous currents to the DFB laser. It is underlined that such a proposed structure does not depend on spatial variation in the epitaxial material through e.g. selective area growth, regrowth, or intermixing processes.

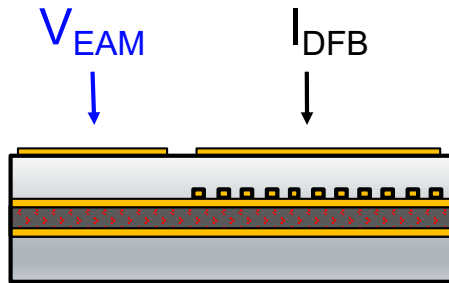


Figure 4.3: Schematic representation of the integrated EAM-DFB device

In order to assess the possible characteristics of such a structure, the E-field and temperature dependent opto-electronic properties of state-of-the-art commercially available epitaxial material are investigated. As explained in chapter 2, the structures were grown by molecular beam epitaxially consisting of 8 stacks of QD layers each comprised of self-assembled InAs dots. As shown in chapter 2, an areal density of 5.9×10^{10} is achieved through the growth of highly uniform QDs [24]. The materials were fabricated into a $375 \mu\text{m}$ long fiber pigtailed single-mode ridge-waveguide laser and optical access mesa diodes with an annular contact diameter of $400 \mu\text{m}$ for gain and absorption [25] measurements, respectively.

4.5 Results and analysis

Figure 4.4 (a) shows the net modal gain spectra as a function of energy at 25°C . Data is from the $375\text{-}\mu\text{m}$ -long fiber-pigtailed $3\text{-}\mu\text{m}$ ridge-waveguide laser, which was measured by the Hakki-Paoli method [26] for currents from 1 to 6.8 mA . Gain spectra are truncated where

measurement falls into the noise floor (where QDs do not have gain). The threshold current is at 6.85 mA or 608 A/cm^2 . Total internal losses can be assessed from the low energy tail [27] as indicated on fig. 4.4 (a) and amount to $3.5 \pm 0.5 \text{ cm}^{-1}$. The peak in absorption at low current is at 965 meV with a net modal loss of 50 cm^{-1} at 1 mA and a full width at half maximum (FWHM) amounting to 25 meV . The peak in gain in the vicinity of threshold occurs at 952 meV , showing a 12 cm^{-1} net modal gain and FWHM of 20.5 meV . The threshold modal gain is $\sim 15 \text{ cm}^{-1}$, $\sim 1/3$ of the saturated gain to maximize the modulation rate of the laser [5].

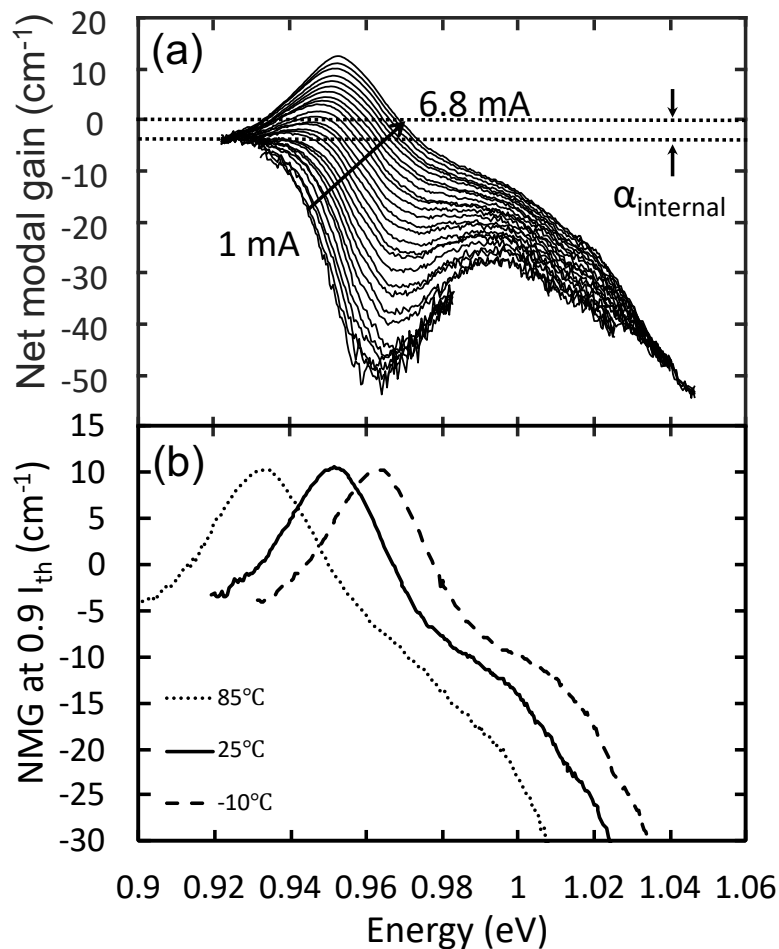


Figure 4.4: (a) Hakki-Paoli measurement of net modal gain (NMG) spectra (b) gain spectra at different temperatures at 90 % of threshold current as a function of energy

A net modal loss of $\sim 27 \text{ cm}^{-1}$ at $\sim 995 \text{ meV}$ is observed, which is mid-way between the first excited state and ground state (GS). This is the subject of a separate structural and simulation-based study [28]. Furthermore, the energy difference between the peak in absorption (965 meV) and the peak in gain (952 meV) is $\sim 13 \text{ meV}$ with an increase in the FWHM of $\sim 5 \text{ meV}$. This can be attributed to the many-body effects causing additional broadening and a renormalization

shift to the transition energy. This shift and the corresponding broadening continue as more carriers are added by increasing current [29].

Figure 4.4 (b) presents gain spectra at 5.9 mA (0.90 I_{th}), 6.1 mA (0.89 I_{th}), and 10.2 mA (0.91 I_{th}) at -10, 25, and 85 °C, respectively. Current dependence of net modal gain is effectively identical to that shown in fig. 4.4 (a). A redshift of 0.33 meV/°C is observed in the gain peak as temperature is increased due to shrinkage of the band-gap.

As presented in chapter 2, normal incidence photocurrent (PC) as a function of bias was investigated for the same material in the optical access mesa diodes. In-plane QD PC analyses have shown that GS emission possesses a TE polarization as the lowest energy transitions are predominantly heavy-hole in character since the light-hole is pushed way down due to the high strain. Hence, the polarization dependence of the in-plane and the normal incidence PC are expected to be identical [30].

The NML spectra is deduced from the short circuit (0 V) PC data, which needed to be corrected for non-ideal carrier escape at low E-field [25] and normalized to the maximum value of absorption found in fig. 4.4 (a). Considering, at a current of 0.9 x I_{th} the bias across the device is 0.93 V. Adding this point to the shift in the deduced ground state net modal loss as a function of bias elaborates the deduction process better. As such fig. 4.5 plots the peak net modal loss as a function of reverse bias with a linear fit for the deduction of the amount of NML.

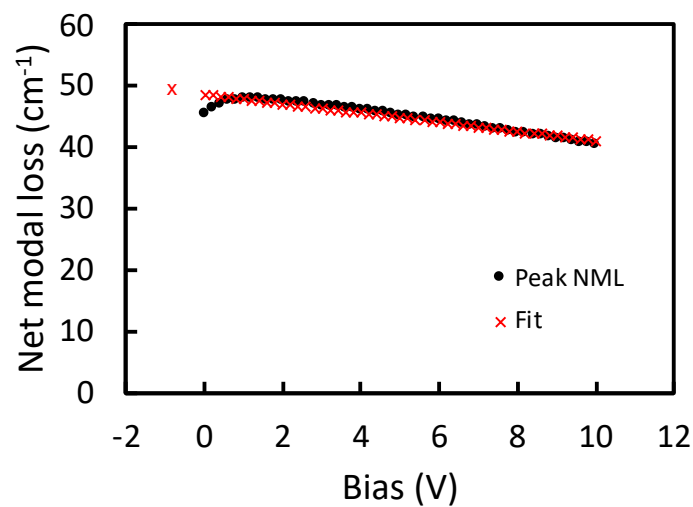


Figure 4.5: Peak NML as a function of reverse bias

Furthermore, the spontaneous emission spectra at 1 mA and 99 % of threshold ($\sim 1 - 2$ e-h pairs per QD) were compared. Figure 4.6 plots the spontaneous emission in linear mW units as a function of energy.

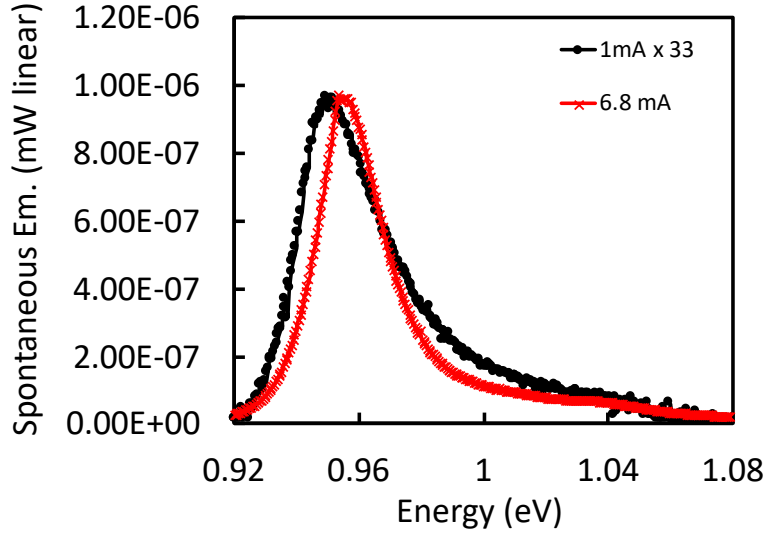


Figure 4.6: Spontaneous emission as a function of energy

From the graph, the 1mA spectrum was rescaled 33 times compared to the 6.8mA spectrum. A carrier occupancy of < 0.04 e-h pairs per dot at 1 mA can therefore be deduced from fig. 4.6 ($1/33 = 0.03$). As a result, the QDs can be assumed to be essentially empty at this drive current.

Figure 4.7 (b) shows the deduced net modal loss for the EAM section as a function of reverse bias at 3 V increments. As expected from fig. 4.5, an essentially linear shift of the absorption peak can be seen with bias. As stated previously, this is ascribed to the permanent dipole moment attributed to the QDs' form asymmetry because of the indium composition variation in the vertical direction [30]. It should also be noted that the absorption is resilient at high E-fields owed to strong carrier localization [25].

Figure 4.7 (a) re-plots the gain spectrum presented in fig. 4.4 (a) to explain the operation of the proposed electro-absorption modulated DFB laser. The gain peak wavelength is marked as λ_{Center} with the λ_{Red} at 10 meV to the red side and λ_{Blue} 30 meV to the blue side. It is noted that a 10 layer stack In(Ga)As QD-DFB exhibits an energy shift of $0.08 \text{ meV}/^\circ\text{C}$ [6].

Under the relatively low current density of $0.6 \text{ kA}/\text{cm}^2$ shown in fig. 4.7 (a), no gain is observed

at the marked blue detuning of 0.98 eV . Yet, gain at 0.98 eV can be reached at greater drive currents ($5 - 10 \times J_{th}$) from identical [6, 31] or similar [32] material.

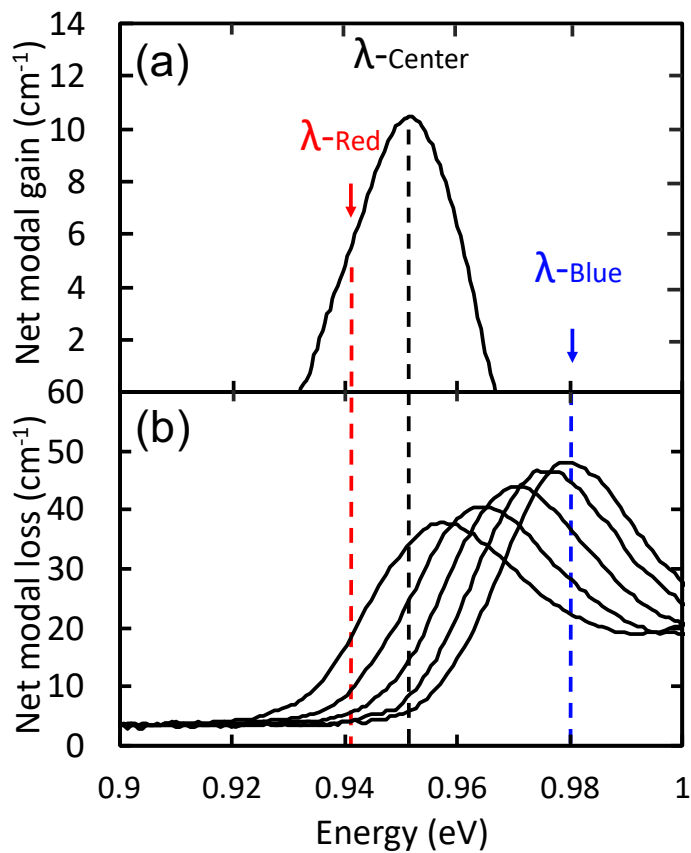


Figure 4.7: (a) Positive gain region at 90 % of threshold current (b) deduced net modal loss (NML) of the same active material as a function of energy

Figure 4.8 plots the net modal loss at the selected detuning wavelengths as a function of bias.

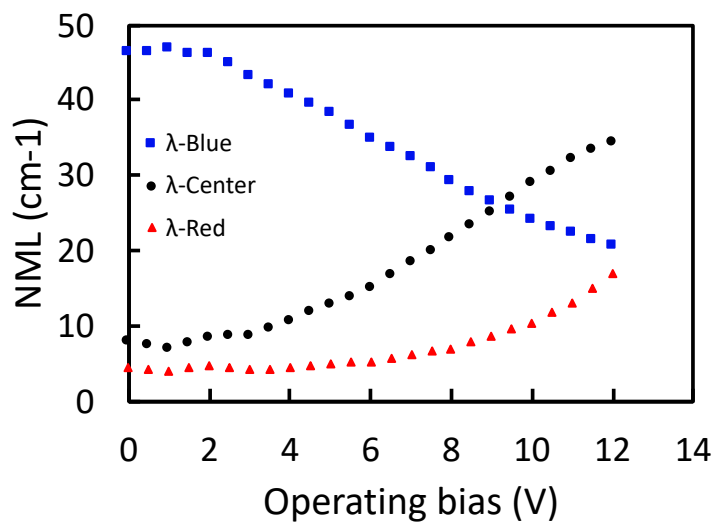


Figure 4.8: Net modal loss at λ- red, center, and blue as a function of operating bias

The peak in absorption is reached at 12 V from the λ_{Red} and λ_{Center} , and at 1 V for the λ_{Blue} . The smallest absorption is at 12 V for λ_{Blue} , and at 1 V for the λ_{Red} and λ_{Center} detuning regimes.

By detuning the DFB at λ_{Blue} a novel EML configuration, where signal is absorbed in the lower bias and transmitted at the higher one, could be achieved. This would provide negative (blue) chirp. Nonetheless, this mode of operation would need signal amplification that could be realized by adding a semiconductor optical amplifier (SOA) section of the same active layer.

On the other hand, standard EML operation could be achieved for λ_{Center} and λ_{Red} exhibiting the predicted positive or red chirp but without needing amplification. On the other hand, as seen in chapter 2, due to the onset of impact ionization at 15 V [25], I am limited in the applied reverse bias, and hence possible further red detuning.

Figure 4.9 demonstrates the deduced net modal loss spectra under the chosen biases as a function of energy indicated for λ_{Red} , λ_{Center} , and λ_{Blue} . The relevant points in the spectra are highlighted with squares and circles to represent ‘1’ and ‘0’ signals, respectively. It must be noted that, in order to circumvent a substantial p-i-n diode capacitance penalty at 0 V , this bias is suggested to be avoided for EAM purposes. I acknowledge that these voltage swings are comparatively large (*c.f.* ~ 3 V in QWs). This is attributed to QDs lower rate of Stark shift [25], which is due to the lower dimensionality and the parabolic shape of carrier confinement as compared to the QW’s square well shape.

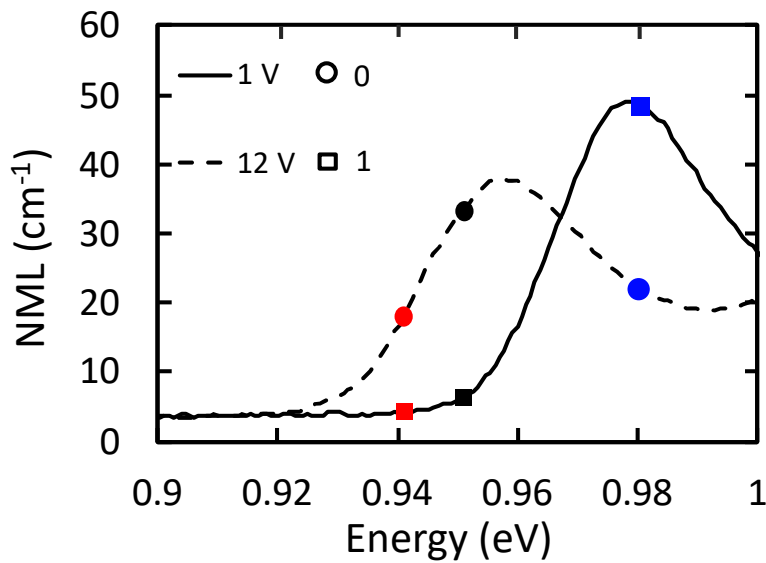


Figure 4.9: Block (‘0’) and transmit (‘1’) scheme as circles and squares, respectively

Figure 4.10 presents the corresponding values of ER and IL acquired from the absorption values at the chosen bias voltages for the ‘1’ and ‘0’ signals as a function of modulator length.

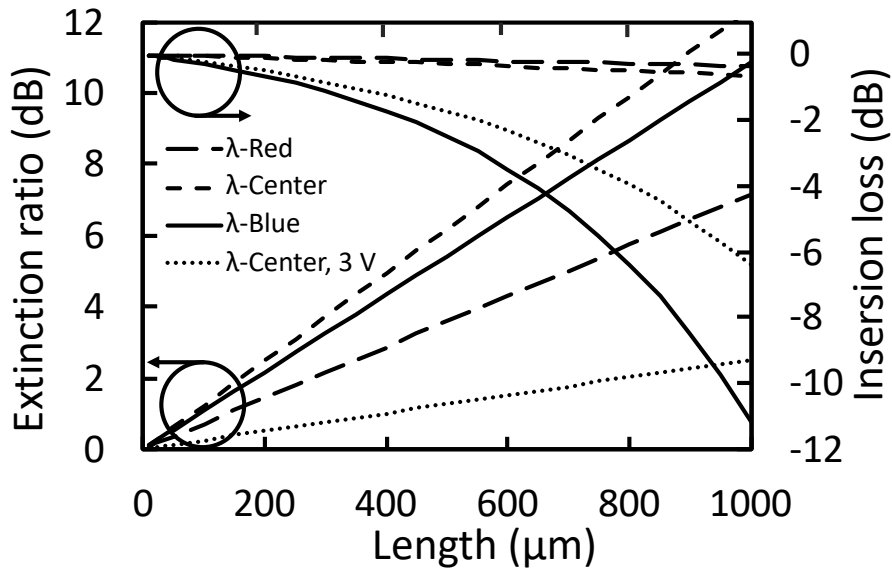


Figure 4.10: ER and the IL vs modulator length for the different detuning regimes. Dotted line stems from a 3 V pk-pk modulation for comparison

As expected, increasing the chip length triggers a trade-off between IL and ER. The λ_{Red} regime displays lower values of ER, while λ_{Blue} and λ_{Center} demonstrate higher, more comparable values at shorter EAM lengths.

It should be noted that, the modulation bandwidth of an EAM is generally limited by the RC time constant from its junction capacitance. Consequently, the modification of the structural parameters of the EAM is required in order to bring the capacitance down. However, increasing the modulation bandwidth comes at a trade off with other important figures of merit such as the ER, IL, and required drive voltage. 56 Gbps operation has been reported with an ER of ~ 10 dB employing a common MQW structure in an 80- by 5- μm ridge waveguide structure. Also demonstrating f_{3dB} of 31 GHz with an IL of 3 dB and an output power under modulation of 1 mW utilizing a 2.5 V pk-pk driver [17]. With waveguide geometry calculations in mind (considering the capacitance of flat, parallel plates of area A and separation d given by: $C = \frac{\epsilon\epsilon_0 A}{d}$, where ϵ is the permittivity of the dielectric material, ϵ_0 the permittivity of free space) the non-optimized device under investigation here would exhibit ~ 3 times the capacitance (~ 27 fF), which suggest 15-20 Gbps operation should be possible. For an ER of 10 dB, a modulator

length of $950 \mu\text{m}$ is needed for the blue regime. In order to achieved a similar IL value, either a DFB with output power of 2.75 mW or an SOA section which provides a gain of 12 dB ($920 \mu\text{m}$) is necessary. Furthermore, the modulation rate could be improved through higher amount of absorption from each QD layer and a larger intrinsic region thickness to reduce the capacitance. In other words, there is a persistent need for epitaxial solutions to simultaneously decrease the inhomogeneous linewidth and also increase areal dot density. The former would increase the ER while the latter would permit a decrease in the active device length and thus a further reduction in capacitance and dynamic dissipation and thus a better IL. Strain balancing of the QD layers may similarly achieve this through close vertical stacking of the QDs [33].

Figure 4.11 plots the change in absorption under modulation with respect to energy between 1 and 12 V. Colored circles indicate the values at the proposed detuning wavelengths.

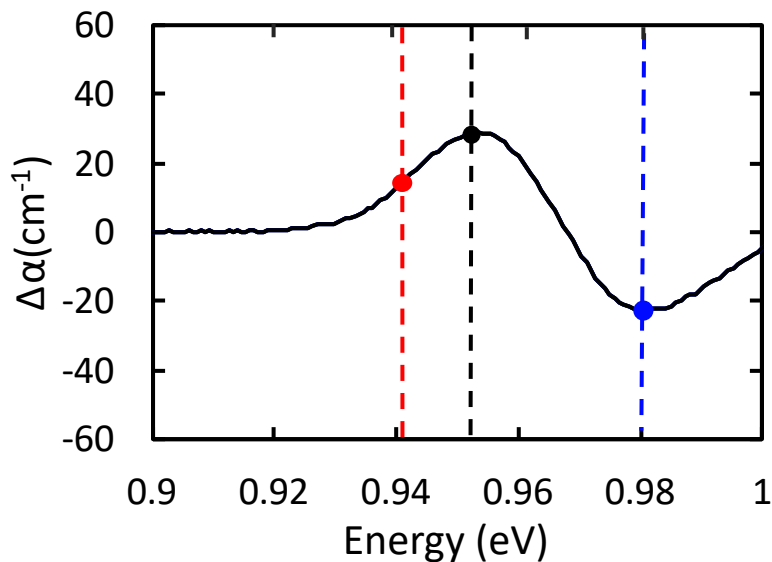


Figure 4.11: Change in absorption spectra as a function of energy

The negative and positive chirp regions will be on the high and low energy sides of the peak in $\Delta\alpha$, respectively from the Kramers-Kronig relations. As such, since the modulation wavelength is on the negative side of $\Delta\alpha$, the obtained chirp will be negative. This is achieved when the DFB is detuned at the λ_{Blue} regime. Accordingly, the DFB-EML would operate optimally in the λ_{Blue} . This would significantly reduce signal degradation caused by chromatic dispersion which is characteristic of standard single-mode-fibers (SMF) and also circumnavigate the requirement for pre-chirp management, thus increasing the transmission distance and reduce the cost of the transmission line.

In spite of the fact that the minimum dispersion window is at $1.3 \mu\text{m}$ in standard SMFs, QDs can cover all of the O- to L- band and the equivalent principle of operation applies to EAMs at this wavelength range. It is noted that the operation scheme and the available chirp sign may be further expanded with temperature control and possible integration with an SOA section as it is known that they also provide negative chirp when operated in the saturated regime [34].

With respect to device geometry, in order to operate at the blue-detuning regime for blue chirp, an EAM section length of $950 \mu\text{m}$ is expected to provide an ER of 10 dB at 15-20 Gbps. With respect to temperature control, from fig. 4.7, at 25°C the absorption peak is on the blue-side of the DFB's Bragg wavelength. As temperature increases, the absorption shifts to lower energies. Because of the initial detuning of the absorption edge relative to the gain band, for a medium range of temperatures (i.e. $25 - 65^\circ\text{C} \sim 12 \text{ meV}$), the device's ER decreases from 10 to 6.4 dB (i.e. from λ_{Center} to λ_{Red} , for a device length of $800 \mu\text{m}$). However, IL remains largely the same (i.e. from -0.3 to -0.5 dB, for a device length of $800 \mu\text{m}$).

4.5 Conclusion

An investigation of the optical gain and absorption spectra was carried out on GaAs-based QD materials incorporated as the active layer in a laser and mesa diodes for the purpose of examining the viability of a novel integrated common QD-active layer DFB-EML. It was demonstrated that with appropriate detuning wavelengths, different EML operation arrangements could be harnessed. Conventional EML operation could be achieved which is accompanied with the expected positive chirp, but without the need for signal amplification. DFB operation in the blue-detuning regime would enable novel EML operation producing blue chirp. The insertion losses, in this approach of operation, could be countervailed by an SOA section. Compact semiconductor waveguides have significant coupling losses associated between the different components (laser, modulator, etc). It can therefore be envisaged that a monolithically integrated device as outlined in this chapter would compensate for the optical power loss of the device upon insertion. This chapter's experimental results highlight the potential of GaAs-based QD material for a chirp-managed common active-layer DFB-EMLs at $1.3 \mu\text{m}$ as an alternative to the InP platform and their QW counterparts.

4.6 Future work

Carrying out the chirp calculation from the Kramers-Kronig relation will provide a more precise account of the negative chirp under modulation. Furthermore, in order to evaluate the data generation an electrical pulse pattern generator could be employed and the transmission may be characterized utilizing a network analyzer.

On the other hand, as technology matures, the QD areal density and also uniformity (inhomogeneous broadening) are expected to improve, which would allow a reduction in device's length and an increase in the ER, respectively. Higher modulation bandwidth is also expected to be achieved following from the capacitance reduction argument above.

Ultimately, optimizing the structure considering the findings outlined in this chapter in order to fabricate the proposed device is expected to be rewarding considering the lower coupling losses associated with the monolithic integration of devices, the negative chirp under modulation, and the QD's temperature insensitive operation.

References

- [1] S. Fathpour *et al.*, “The role of Auger recombination in the temperature-dependent output characteristics ($T_0=\infty$) of p-doped 1.3 μm quantum dot lasers,” *Appl. Phys. Lett.*, Vol. 85, No. 29, Nov. 2004, pp 5164-5166.
- [2] H.Y. Liu *et al.*, “High-performance three-layer 1.3- μm InAs–GaAs quantum-dot lasers with very low continuous-wave room-temperature threshold currents,” *IEEE Photon. Tech. Lett.*, Vol. 17, No. 6, Jun. 2005, pp. 1139-1141.
- [3] H. Su *et al.*, “High external feedback resistance of laterally loss-coupled distributed feedback quantum dot semiconductor lasers,” *IEEE Photon. Tech. Lett.*, Vol. 5, No. 11, Nov. 2003, pp. 1504-1506.
- [4] M. Sugawara *et al.*, “Effect of homogeneous broadening of optical gain on lasing spectra in self-assembled $\text{In}_x\text{Ga}_{1-x}\text{As}/\text{GaAs}$ quantum dot lasers,” *Phys. Rev. B.*, Vol. 61 No. 11, Mar. 2000, pp. 7595-7603.
- [5] M. Ishida *et al.*, “Photon lifetime dependence of modulation efficiency and Q factor in self-assembled quantum-dot lasers: Impact of capture time and maximum modal gain on modulation bandwidth,” *App. Phys. Lett.*, Vol. 85 No. 18, Nov. 2004, pp. 4145-4147.
- [6] K. Takada *et al.*, “10.3-Gb/s Operation over a wide temperature range in 1.3- μm quantum-dot DFB lasers with high modal gain,” in *Proc. 2010 Conf. on Opt. Fib. Com. (OFC/NFOEC)*.
- [7] J. S. Barton, E. J. Skogen, M. L. Masanovic, S. P. Denbaars, and L. A. Coldren, “A widely tunable high-speed transmitter using an integrated SGDBR laser-semiconductor optical amplifier and Mach-Zehnder modulator,” *IEEE J. Sel. Top. Quan. Electron.*, Vol. 9, No. 5, Sep./Oct. 2003, pp. 1113–1117
- [8] P. Bhattacharya and S. Ghosh, “Tunnel injection $\text{In}_{0.4}\text{Ga}_{0.6}\text{As}/\text{GaAs}$ quantum dot lasers with 15GHz modulation bandwidth at room temperature,” *Appl. Phys. Lett.*, 80(19), 3482, May 2002
- [9] T. Chung, G. Walter, and N. Holonyak, “Coupled strained-layer InGaAs quantum-well improve- ment of an InAs quantum dot AlGaAsC-GaAsC-InGaAsC-InAs heterostructure laser,” *Appl. Phys. Lett.*, 79(27), 4500, December 2001
- [10] O. B. Shchekin and D. G. Deppe, “The role of p-type doping and the density of states on the modulation response of quantum dot lasers,” *Appl. Phys. Lett.*, 80(15), 2758–2760, April 2002

- [11] L. V. Asryan and S. Luryi, "Tunneling-injection quantum-dot laser: Ultrahigh temperature stability," *IEEE J. Quantum Electron.*, 37(7), 905, 2001
- [12] R. Sahara *et. al.*, "Proposal for quantum dot electroabsorption modulator," *IEEE Photon. Tech. Lett.*, Vol. 8, No. 11, Nov. 1996, pp. 1477-1479.
- [13] K. Hasebe *et. al.*, "Directly frequency modulated DFB laser integrated with EA modulator for extended transmission reach," in *Proc. Eur. Conf. Opt. Comm.*, Sep. 2010, paper Th.9. D.5.
- [14] N. Ngo *et. al.*, "Electroabsorption modulated laser integrated with a semiconductor optical amplifier for 100-km 10.3 Gb/s dispersion-free-penalty-free transmission," *J. Lightwave Tech.*, Vol. 31, No. 2, Jan. 2013, pp. 232-238.
- [15] T. Fujisawa *et. al.*, "1.3 μm , 50 Gbit/s electroabsorption modulators integrated with DFB laser for beyond 100G parallel LAN applications," *Electron. Lett.*, Vol. 47, No. 12, Jun. 2011, pp. 708-710.
- [16] E.J. Skogen *et. al.*, "Monolithically integrated active components: A quantum-well intermixing approach," *IEEE J. Sel. Top. Quant. Elec.*, Vol. 11, No. 2, Mar. 2005, pp 343-355.
- [17] M. Theurer *et. al.*, " 2×56 GB/s from a double side electroabsorption modulated DFB laser and application in novel optical PAM4 generation," *J. Lightw. Tech.*, Vol. 35, No. 4, Feb. 2017, pp. 706-710.
- [18] C.Y. Ngo *et. al.*, "Electroabsorption characteristics of single-mode 1.3- μm InAs-InGaAs-GaAs ten-layer quantum-dot waveguide", *IEEE Photon. Tech. Lett.*, Vol. 22, No. 23, Dec. 2010, pp. 1717-1719.
- [19] D.B. Malins *et. al.*, "Electroabsorption and electrorefraction in an InAs quantum-dot waveguide modulator," *IEEE Photon. Tech. Lett.*, Vol.19, No. 15, Aug. 2007, pp. 1118-1120.
- [20] D. Bimberg *et. al.*, "Quantum-dot based distributed feedback lasers and electroabsorption modulators for datacom applications," in *14th International Conference on Transparent Optical Networks*, Jul. 2012.
- [21] N. Yamamoto *et. al.*, "Monolithically integrated quantum dot optical modulator with semiconductor optical amplifier for thousand and original band optical communication," *Japanese J. of Appl. Phys.*, Mar. 2016, Vol. 55, No. 4S, 04EC16.
- [22] I.C. Sandall *et. al.*, "Evaluation of InAs quantum dots on Si as optical modulator," *Semicond. Sci. Technol.* 28, 094002, 2013

- [23] T.H. Wood *et. al.*, “High-speed optical modulation with GaAs/GaAlAs quantum wells in a p-i-n diode structure,” *Appl. Phys. Lett.*, Vol. 44, No. 1, Jan. 1984, pp. 16-18.
- [24] K. Nishi *et. al.*, “Molecular beam epitaxial growths of high-optical-gain InAs quantum dots on GaAs for long-wavelength emission,” *J. Cryst. Growth*, Vol. 378, Sep. 2013, pp. 459-462.
- [25] S.A. Sobhani *et. al.*, “Study of electro-absorption effects in 1300nm In(Ga)As/GaAs quantum dot materials,” in *Physics and Simulation of Optoelectronic Devices XXIV*, Edited by B. Witzigmann, M. Osinski, and Y. Arakawa, Proc. SPIE 9742, Mar 2016.
- [26] B.W. Hakki, and T.L. Paoli, “Gain spectra in GaAs double-heterostructure injection lasers,” *J. Appl. Phys.*, Vol. 46, No. 3, Mar. 1975, pp. 1299-1306.
- [27] R.R. Alexander *et. al.*, “Systematic study of the effects of modulation p-doping on 1.3- μm quantum-dot lasers,” *IEEE J. Sel.Top. Quant. Elec.*, Vol. 42, No. 12, Dec. 2007, pp. 1129-1138.
- [28] I.M.E. Butler, W. Li, S. A. Sobhani, N. Babazadeh, I. M. Ross, K. Nishi, K. Takemasa, M. Sugawara, D. T. D. Childs, and R. A. Hogg, “Size anisotropy inhomogeneity effects in state-of-the-art quantum dot lasers,” *App. Phys. Lett.*, Vol. 113, 012105, Jul. 2018.
- [29] M. Lorke, W. W. Chow, T. R. Nielsen, J. Seebeck, P. Gartner, and F. Jahnke, “Anomaly in the excitation dependence of the optical gain of semiconductor quantum dots,” *Phys. Rev. B* 74, 035334, 2006
- [30] P.W. Fry *et. al.*, “Inverted electron-hole alignment in InAs-GaAs self-assembled quantum dots,” *Phys. Rev. Lett.*, Vol. 84, No. 4, Jan. 2000, pp. 733-736.
- [31] N. Payvast *et. al.*, “Dominant role of many-body effects on the carrier distribution function of quantum dot lasers,”. *App Phys Exp.* Vol 9, 2016, pp. 032705 1-4.
- [32] H. Shahid *et. al.*, “Negative differential gain due to many body effects in self-assembled quantum dot lasers,” *App Phys Lett.*, Vol 99, 2011, pp. 061104 1-3.
- [33] T.S. Roberts *et. al.*, “Strain balancing of metal-organic vapour phase epitaxy InAs/GaAs quantum dot lasers,” *IEEE J. Sel.Top. Quant. Elec.*, vol. 3, No. 6, Dec. 2017, pp. 1901208- 1901216.
- [34] T. Watanabe, N. Sakaida, H. Yasaka and M. Koga, "Chirp control of an optical signal using phase modulation in a semiconductor optical amplifier," in *IEEE Photonics Technology Letters*, vol. 10, no. 7, Jul. 1998, pp. 1027-1029

Chapter 5

Relative Intensity Noise: Temperature-Dependent Study of Modulation and External Optical Feedback

5.1 Introduction

The quality of an optical communication system is, to a high degree, interlinked to the quality and performance of the laser source that is employed. The principal characteristics of lasers such as emission wavelength, optical gain and power, spectral linewidth, modulation response, and relative intensity noise (RIN) are some of the key parameters to quantify the system quality. Few of these characteristics have a fairly straight forward description and can be investigated quite simply, such as the output power or the emission wavelength. On the other hand, measurement of some characteristics of the semiconductor lasers, such as the RIN in this case, requires a good understanding of the underlying dynamics and the limitations which exist in the measurement techniques. This is because of the multifaceted and convoluted effects that need to be accounted for and corrected as compared to e.g. the gain and even the linewidth enhancement factor measurements presented previously in this thesis.

Laser diodes are inherently noisy devices, as explained in chapter 3. The necessary condition for lasing operation, as explained in chapter 1, is the atomic population inversion of levels 1 and 2. Assuming a photon propagating through a medium subjected to population inversion, it will experience gain by growing coherently in numbers through stimulated emission. However, this stimulated emission radiation will be contaminated by the spontaneous emission radiation from level 2 to level 1. A fraction of this radiation emitted by spontaneous events will always exist and indistinguishably travel very closely along the same direction of the stimulated emission radiation. The ramifications of this spontaneous emission noise on the laser characteristics are: 1) variation in the emitted optical power per unit area (intensity) and 2) variations in the emitted frequency. These frequency fluctuations give rise to the finite enhancement of the spectral linewidth of laser diodes, which was investigated in chapter 3. On the other hand, the intensity fluctuations are characterized by the RIN which will be considered in this chapter.

Generally, in a transmission communication system, knowledge of the RIN characteristics of the source is crucial because it is a measure of the signal to noise ratio (SNR) of the link. Since optical transmission systems have a critical limitation due to this noise source, it is important to know how it can be defined and measured. RIN is a measure in order to quantify how noisy the laser, as the transmitter of the transmission link, is. Consequently, in order to achieve a certain data rate in the transmission in a digital system, a certain bit error rate needs to be achieved which entails employment of a laser diode with a certain noise performance

This power intensity fluctuation can be observed as depicted in figure 5.1 where the ideal output intensity of a laser diode biased at a D.C. level is presented. All parameters influencing laser operation such as e.g. bias level and temperature are assumed to be constant.

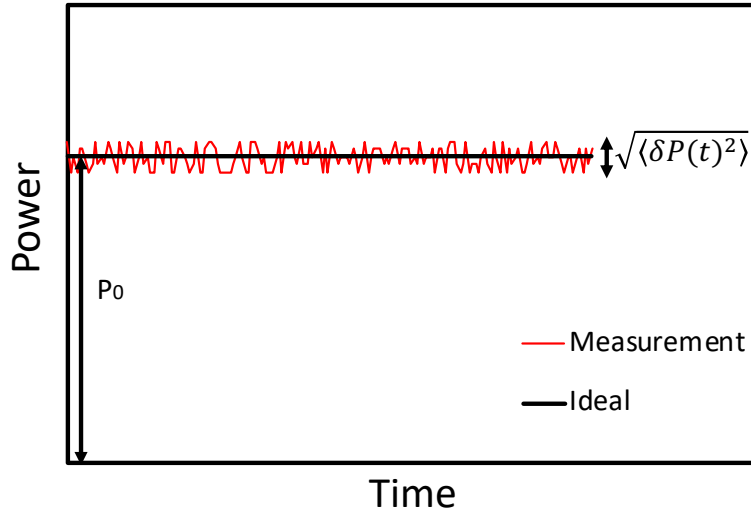


Figure 5.1 Ideal output power of a laser at DC bias and the real laser output power with intensity noise

The intensity noise depicted above can be investigated in terms of the contribution of the intensity variations of the laser to the total electrical noise at the receiver. This electrical noise relative to the electrical signal power quantifies the relative intensity noise (RIN). It can be alternatively viewed as the inverse of the SNR.

In analog applications, the noise is quantified utilizing the electrical SNR. For the laser output illustrated in fig. 5.1, the SNR can be written as:

$$SNR = \frac{m^2}{2} \frac{P_0^2}{\langle \delta P(t)^2 \rangle} \quad 5.1$$

Where, m is the modulation index, $\delta P(t)$ is the optical intensity fluctuations, and the brackets denote a time-averaged value.

A decision level of a “1” or a “0” is recorded at the half point for digital purposes. If the noise goes higher than $P_0/2$, an incorrect acquisition could be made. This can be observed in fig 5.2. Assuming the noise with a Gaussian distribution around the mean power P_0 , in order to reduce the probability of having $|\delta P(t)| > P_0/2$ to less than 1 in a gigabit (a bit-error-rate $< 10^{-9}$), it is required to have an SNR of $\frac{P_0^2}{\langle \delta P(t)^2 \rangle} > (11.89)^2$ [1].

For both analog and digital applications, it is worthwhile to define the RIN of a laser, in the linear format, as:

$$RIN = \frac{\langle \delta P(t)^2 \rangle}{P_0^2}$$

5.2

Where, $\langle \delta P(t)^2 \rangle$ is the mean-squared of the assumed Gaussian noise distribution of the optical intensity fluctuations. Ramifications of RIN on the decision level recognition in a digital system can be observed as depicted in figure 5.2.

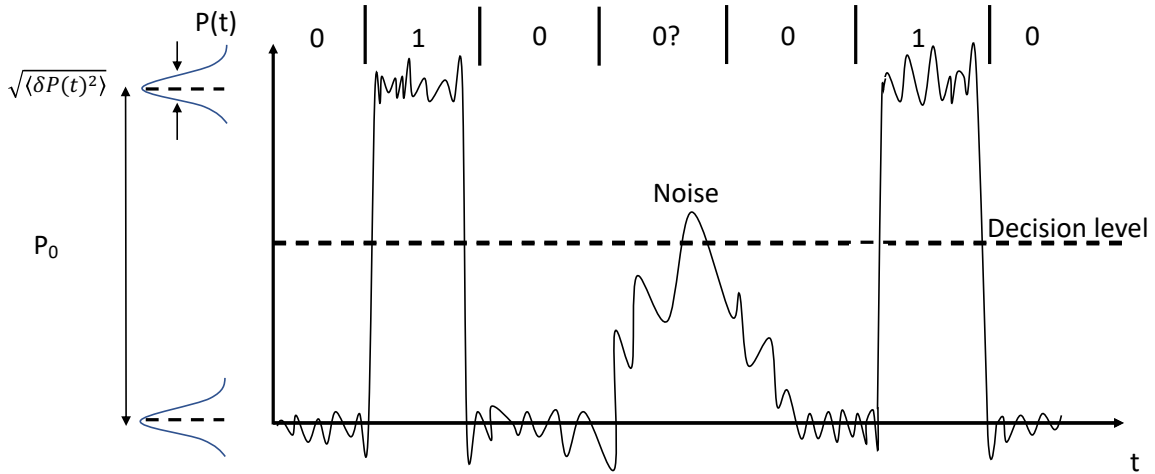


Figure 5.2: Noise in modulated laser signals for digital applications

In digital applications, recording of a “0” or “1” is contingent upon the decision level being at the midpoint, $P_0/2$. If noise exceeds the $P_0/2$ level in Fig. 5.2, a false recording might be made.

RIN is usually presented in decibels units, $10\text{Log}_{10}(\text{RIN})$, as it is a relative measure. In practice, if a particular electrical SNR is the prerequisite in an analog application, equation 5.1 can be used to define the highest permissible RIN (e.g. if the required SNR > 50 dB with $m=1$, then maximum laser RIN < -53 dB). Alternatively, in digital applications, for a BER < 10^{-9} the laser must have RIN < - 20.5 dB [1].

RIN is often normalized to a 1 Hz bandwidth in order to make it more convenient to compare the intensity fluctuations of a given laser when receivers with different bandwidths are considered:

$$RIN = 10\text{Log}_{10} \left[\frac{\langle \delta P(t)^2 \rangle}{P_0^2} \right] - 10\text{Log}_{10}[\Delta f] \text{ (dB/Hz)} \quad 5.3$$

Therefore, considering the required bandwidth is 0.75 of the link bit rate [2], for a 2.5 GB/s link we have:

$$RIN = -20.5 - 10\text{Log}_{10}[1.875 \times 10^9] = -113.2 \text{ dB/Hz} \quad 5.4$$

Alternatively, for a 10 GB/s link we have:

$$RIN = -20.5 - 10\text{Log}_{10}[0.75 \times 10^{10}] = -119.2 \text{ dB/Hz} \quad 5.5$$

In practice, RIN is a very convenient parameter to probe the performance of an optical system. As mentioned above, in analog systems, defining the SNR through RIN, or in digital systems, relating it to the BER will help to qualify the transmission line.

If RIN is the prominent noise source, and limited by shot noise, which will be considered in what follows, equation 5.2 may for simplicity be written as $RIN_{\min} = 2h\nu/P$ for the minimum RIN of a laser [10]. Where, the factor 2 accounts for both of the facets emitting, ν is the frequency of emission, and P is the laser output power. As such, a 1mW laser beam at a wavelength of 1300 nm with intensity noise is expected to exhibit a RIN floor of -154 dB/Hz. It must be noted that, the intensity noise is measurable only if it exceeds the receiver's noise floor. The combination of the receiver's components electronics comprises this noise floor e.g. thermal noise, shot noise of the photodiode, noise from electrical amplifiers (noise figure), noise from electrical spectrum analyzer, etc. As a result, it is more practical to define the RIN of the laser in the electrical domain. The aforementioned noise sources will be individually considered in what follows in the measurement section.

With respect to external feedback resilience of a laser in optical fiber networks, the semiconductor laser source may be perturbed by unintentional reflections from various refractive index interfaces such as fiber connectors, fiber-chip connections, waveguide crossings, regrowth interfaces, or if the fiber is simply unplugged and from the reflection at end of the fiber connector. Outside of a very few number of cases where feedback can be useful, e.g., for obtaining linewidth reduction, the majority of feedback amplitude, phase, and time delay cases have unwanted consequences such as increased intensity noise, linewidth broadening, and mode hopping. This is detrimental to data communication systems as laser

intensity and phase noise increase the bit error rate and therefore limit the data transmission rate in fiber-optic communication networks. Therefore, investigation of the RIN subject to various levels of external optical feedback would provide an important insight into the experimental quantification of the anticipated feedback resilience of QD devices.

Because of the highly damped modulation responses of QD lasers [3], the published RIN reports in the literature are scarce and the handful reported are heavily noisy. RIN under external feedback has been reported on even less. As a result, a high-resolution investigation of the state-of-the-art QD material RIN spectra, at a range of temperatures for the first time, and subject to various levels of feedback is timely. In this chapter, the motivation that prompted this study is detailed out prior to providing the gaps in knowledge in order to more clearly place this work in perspective. Subsequently the measurement of RIN is explained along with various noise sources that convolute the results and need to be corrected, before providing some of the major techniques employed for RIN measurements. RIN measurement under external optical feedback is then outlined, before delving into the results. A discussion successively follows to reflect upon the findings prior to the conclusions and the future work sections to summarize this chapter and provide desirable continuation to this study that extended outside of the scope of this work, respectively.

5.2 Background and motivation

The motivation for this experimental chapter of this work originate from the semiconductor lasers developed at QD Laser Inc., Japan. Researchers at this institute commercialized state-of-the-art high-speed quantum dot lasers emitting at the near infra-red telecommunications optical windows of the O and C bands. Since these devices are primarily intended for the future short-range communication standards, their dynamic properties especially their intensity noise performance would be valuable to investigate.

In modern telecommunications, as the number of end-users is constantly increasing, the demands on the optical transmitters and lasers are always on the rise. Depending on the application, each characteristic of the laser can be crucial. Implementation in fiber-optic communications, where the demand for boosting data-rates are astronomical, is among one of the principal applications in which lasers play a key role. Low RIN values are advantageous

for carrying broadband data with low bit error rate. In addition, lasers with high spectral purity, coherence length and time, etc. are essential for very precise measuring and sensing applications, such as interferometric measurements.

Moreover, the information that can be extracted from the measured RIN spectra in the electrical domain provides a good insight into intrinsic dynamic characteristics of a laser without the parasitic and non-linear effects which are inherent in small-signal-modulation measurements, as described previously in Appendix A.1, laser theory, small signal modulation (SSM) subsection. RIN spectra may be used to determine a number of key parameters of laser operation such as the relaxation oscillation (RO) frequency, K-factor limited bandwidth, and the D-factor modulation efficiency describing the RO frequency behavior with drive current. It must be noted that conventionally, these parameters are extracted from the small-signal intensity modulation response (S_{21}) of the laser, where package and connection parasitic need to be considered and corrected for.

Unlike bulk or quantum wells (QW), quantum dot (QD) material possess a delta function like density of states [4] which leads to a number of technological advantages such as an ultra-low [5] temperature insensitive threshold current [6], and a very small amplitude-phase coupling or linewidth enhancement factor (LEF) [7]. The latter is attributed to QD's symmetric gain curves leaving refractive index essentially unchanged with carrier density, while exhibiting a coincident material and differential gain peak [8].

The RO peak is attributed to a coupling effect between the carrier and photon densities. As such, any increase in carrier density precipitates an increase in the optical gain and thus the photon density. Conversely, this increase in photon density contributes to recombination of carriers through stimulated emission in the cavity. Accordingly, the optical gain saturates, which results in the photon density to decrease. With photon reduction, the saturation effects will in turn be reduced and the carrier density increases again. This resonance process, so called relaxation oscillation, is strong for a specific frequency which is close to f_r [9].

In QW lasers, the carriers have a virtually zero relaxation time to the ground state [3] due to the electron degeneracy much higher than 2 in the ground state as discussed in chapter 3. As a result, there is a comparatively marginal damping of the frequency response from carrier-photon oscillations in the cavity. This subsequently leads to well-defined relaxation oscillation

(RO) peak in the RIN spectrum. As the number of available carriers increases, with increase in the drive current, the carrier lifetime reduces and as a result the RO peak shifts to higher frequencies until the system reaches the point of its fastest intrinsic recovery speed [10], *c.f.* Eqn. A.22.

In QD lasers, on the other hand, there is an intrinsic relaxation time between each state (the wetting layer and the excited) as well as an effective relaxation time to the ground state, contingent upon the ground state occupation probability with an electron degeneracy of only 2. This leads to a comparatively heavier damping of the carrier-photon interaction in the waveguide which precipitates RO peaks that might not be very well pronounced [11].

Also inherent in the the S-K growth mode of self-assembling QDs is the inhomogeneous nature of the dot ensemble i.e. each dot will have a slightly different RO peak which will not only act to broaden and reduce maximum achievable gain, but also further broaden the RO response.

High damping rates are advantageous in reducing RIN levels and also feedback instabilities of QD lasers compared to their QW counterparts as the peak RIN of a laser under optical feedback is limited by the inverse of the damping rate of the relaxation oscillations: $RIN_{\text{peak}} = 1/\gamma$ [12]. With regard to mitigation of the unwanted external optical feedback effects, traditionally, external Faraday rotation based optical isolators have been utilized. Nonetheless, the incorporation of an isolator increases process complexity and package size, reduces output power, and increases the cost of the system considerably. Therefore, isolator-free laser source operation is desirable both from an economic and a system performance standpoint.

The experimental results presented in chapter 3 on the state of the art InAs/GaAs QD lasers indicate an essentially zero LEF across all of the positive gain region and also up to the threshold current at all measurement temperatures. Therefore, the devices are also expected to demonstrate a rather high resilience towards external optical feedback, since the critical feedback ratio for coherence collapse, which is a regime in which the laser's linewidth under feedback drastically broadens to several GHz, is inversely proportional to the fourth power of the LEF as derived in [13]:

$$f_{\text{Critical}} = \frac{\tau_L^2 (Kf_r^2 + \gamma_0)^2}{16|C_e|^2} \left(\frac{1+\alpha^2}{\alpha^4} \right) \quad 5.6$$

Where, τ_L is the roundtrip delay within the gain cavity, α is the LEF, $|C_e| = (1-R) / (2\sqrt{R})$ is the coupling efficiency from the laser to the external cavity, $\gamma = Kf_{ro}^2 + \gamma_0$ is the damping rate of the relaxation oscillations with f_{ro} being the resonance frequency, K the K- factor, and γ_0 is the damping factor offset, which accounts for the electron lifetime $= \frac{1}{\tau_e}$, where τ_e is the electron lifetime [14]. Feedback is defined as the ratio of the reflected power over the emitted power. In the case of optical fiber transmissions, the coherence collapse leads to a strong degradation in the bit error rate when the laser is employed as a transmitter.

Referring to eqn. 5.6, it can be inferred that the critical feedback level fundamentally depends on the damping rate, γ_0 . The heavier the damping, the larger the critical feedback level would be for the onset of the coherence collapse.

In order to run a preliminary comparison between QDs vs QWs, fig. 5.1 plots Eqn. 5.6 for two different values of the K factor characteristic of either QD lasers ($K=1.3$ ns) [3] or QW lasers ($K=0.3$ ns) [14], with everything else kept constant at $\tau_L=4$ ps, $f_r=3$ GHz, $\gamma_0=0.6$ GHz, $R=0.3$. This is because K-factor describes the damping of a laser's response.

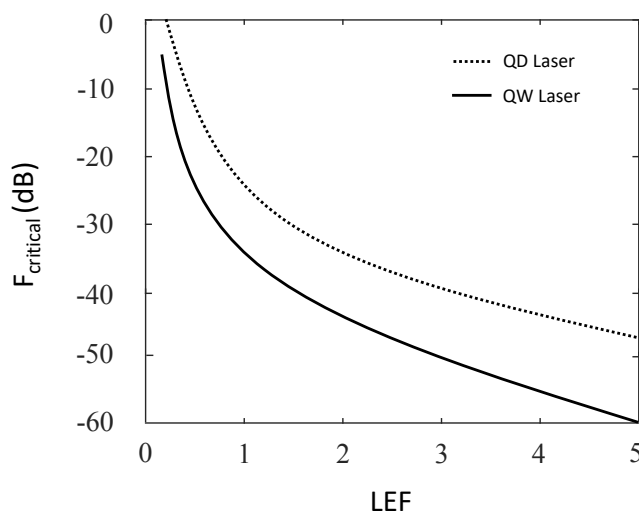


Figure 5.3 numerical evaluation of eqn. 5.1 with fixed values of $\tau_L=4$ ps, $f_r=3$ GHz, $\gamma_0=0.6$ GHz, $R=0.3$

It can be inferred from Fig. 5.3 that the difference in the K factor alone is predicted to result in over 10 dB of increase in f_{crit} for QD lasers compared to QWs. Furthermore, taking into account that QD lasers can exhibit lower LEF values, even larger increases to the critical feedback level

for coherence collapse are expected. In fact, Eqn. 5.6 suggests that no coherence collapse occurs if the LEF approaches zero.

Accordingly, with the demonstration of an ultra-low and temperature-insensitive threshold current [5,6] and potential tolerance to optical feedback [11], QD active media are strong candidates for cooler- and isolator-free operation in optical transmitters. The latter is the direct subject of investigation for this experimental chapter of this project.

The modulation capabilities of devices are evaluated by analyzing the free-running RIN spectra, which are parasitic-free. On the other hand, RIN under external optical feedback also provides a good insight into the degree of resilience towards external optical feedback since RIN levels increase in line with the amount of feedback.

5.3 Gaps in knowledge

As outlined in this section, RIN measurements of QD lasers are scattered in the published reports while analysis of RIN spectra can rarely be found. This is attributed to the highly damped modulation response that leads to very low RIN levels. RIN measurement of QD lasers were first presented in [15] and [16]. No resonance peak was observed in these relatively long-cavity (2.5 mm) devices due to high damping. The completely damped response resulted in RIN levels of -160 dB/Hz, with a flat profile to within ± 2 dB/Hz in the 0.1–10 GHz range. The RIN spectra of QD lasers with a clear and distinct peak were presented by Capua et al. [17]. The resonance peak was around 3 GHz at 1.7 mW for a 1 mm device. However, periodic oscillations at high frequencies limited further analysis.

First RIN analysis of QD lasers was presented by Martinez et al. [18]. The InAs/InP QD lasers grown on a specific InP (3 1 1) B substrate emitted at 1.52 μm . The clear resonance peak at maximum of 3.8 GHz from 1.1 mm device indicated less damping than InAs–GaAs QD lasers. Additionally, A RIN level as low as -160 dB/Hz was experimentally measured with from InAs/InP QD lasers [19]. On a different note, a QD comb laser with RIN levels ranging from -120 to -145 dB/Hz in the 0.1-10 GHz frequency band was also proposed for applications in wavelength-division multiplexing and passive optical networks [20].

More recently, it was shown that QDs directly grown on Germanium exhibit RIN levels as high as -80 dB/Hz however, with strong RO peaks around 1 and 9 GHz [21]. The low damping is reported to be associated with the QD size dispersion and residual strain. The RIN spectra were convoluted by mode partition effects which are attributed to the dual mode lasing reported to be also due to large the inhomogeneity of the QDs. Furthermore, it has also been reported that, the RIN of a QD laser emitting on the pure ES emission is more damped than that of the GS one [22]. Finally, it has been most recently reported in a theoretical study of QD laser RIN characteristics, that excited state (ES) carrier noise contribution can be mitigated by using QD lasers with a larger GS-ES energy separation, which leads to a substantial reduction in RIN [23].

With regards to the investigation of the resilience to external optical feedback, previous reports have indicated that $1.3\ \mu\text{m}$ InAs/GaAs QD lasers can outperform QW counterparts with a coherence collapse threshold as high as -8 dB [11], which was 20-30 dB higher than an AlGaInAs QW laser [24]. This tolerance has been attributed to the highly damped relaxation oscillations which are in turn due to the high gain compression resulting from dot-wetting layer carrier dynamics [25] and the smaller amplitude-phase coupling (LEF) in QD lasers.

Additionally, the strong damping associated with the GS transition as compared to the ES was reported on multi-mode GaAs-based QDs to prevent non-stabilities in the optical spectra, i.e. a sudden considerable broadening, even at the largest feedback ratio, which was at 5.9 % [26]. Furthermore, the higher tolerance of GS to feedback instabilities was also shown experimentally in [27], however, not only the RIN levels reported are difficult to compare as they are not normalized to the bandwidth of measurement as required for comparison (dB/Hz), but also the effect of feedback on their RIN spectra was peculiar in that it produces a spectrum above the free-running spectrum which seem to exhibit a well-defined RO peak, rather than the expected microwave oscillations resulting from the compound cavity with a mode-spacing that corresponds to the length of the external cavity. Most recently, it was reported that a QD laser epitaxially grown on silicon exhibits RIN levels between -130 dB/Hz to -150 dB/Hz while subject to various levels (-10 to -60 dB) of optical feedback [28].

It is expected that the heavily damped response along with the size inhomogeneity inherent in QD active material produce flat RIN spectra from QD lasers with no clear RO peaks. This would also make the feedback effects more complex to investigate as the expected increase in

RIN spectra are reported to exhibit sporadic characteristics. Additionally, the limited published reports in the literature that investigate feedback, outlined above, demonstrate various effects on the spectra due to the feedback rather than a pattern or a norm. These have been attributed to a number of factors such as QD size dispersion creating multiple RO peaks and highly noisy spectra, periodic oscillations at high frequencies limiting further analysis, and the fundamentally highly damped QD response. Furthermore, as QD lasers present operational temperature insensitivity, probing their noise behavior at elevated temperatures is desirable in order to gauge their prospects of operation in harsh environments. This is also missing in the literature.

It is therefore timely to investigate the gaps in knowledge outlined above in QD RIN on the state-of-the-art 1300 nm QD material, which have been shown to exhibit essentially zero, temperature-independent alpha factors in chapter 3.

In this chapter temperature-dependent RIN spectroscopy of the state-of-the-art QD lasers is carried out at a temperature range beyond the current standards' commercial window [29] to establish noise characteristics and modulation capabilities at elevated temperatures. Subsequently, the external optical feedback effects are investigated under various feedback ratios and for the first time at different temperatures. An increase in RIN with feedback is observed in the form of compound cavity modes with a mode-spacing dictated by the length of the external cavity.

5.4 Measurement of RIN

As previously explained, RIN is measured through direct detection in the electrical domain. A photodetector is used in order to convert the optical noise power into an electrical signal. The target of measurement is the spectrum of this electrical noise signal with respect to frequency. An electrical spectrum analyzer (ESA) is utilized to record the spectra.

Since the output photocurrent from the detector is usually a weak signal, an amplifier is required to be placed after the detector. This amplification should be high enough to meet the sensitivity of the ESA, i.e. above its noise floor. It must also be noted that as amplifiers add their own noise (noise figure) to the total system noise, low noise amplifiers should be utilized to minimize this. There is a tradeoff between noise and bandwidth in amplifiers [30].

In practice, RIN measurement is constrained to certain limitations, which would need to be quantified and compensated. There are different methods to overcome these limitations, which will be discussed in what follows.

Figure 5.4 shows the RIN measurement set-up employed for recording the free-running spectra. The light is converted in the photodetector to an electrical signal (OE). The resultant photocurrent is subsequently divided into its A.C., which carries the noise (RF), and D.C. components, from which the relative power is calculated.

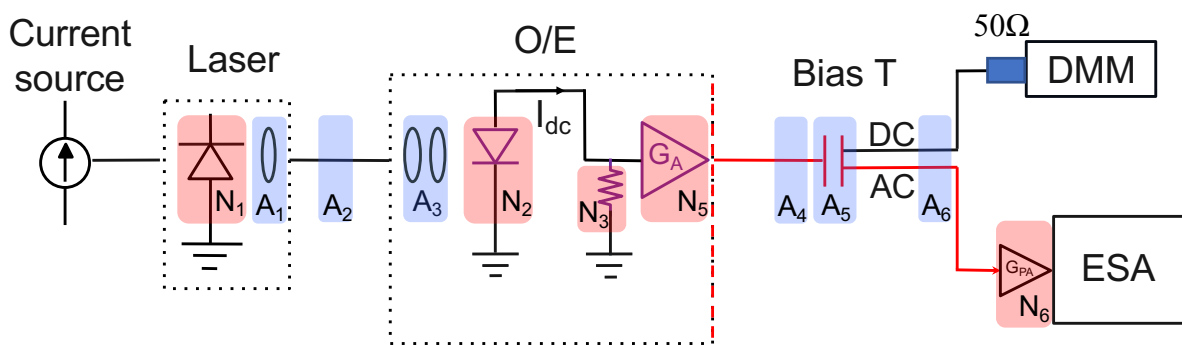


Figure 5.4: Free-running laser RIN measurement set-up, sources of additional noise (red-shade) and attenuation (blue-shade) are highlighted

Bias was provided by a DC current source, Keithley 2400 series, the laser devices under test were put on a mount and suspended on an optical bench. The temperature was kept constant with a Pt100 thermistor inside and a thermo-electric cooler underneath the mount as explained previously in the gain measurement section of chapter 3.

The output light of the laser is coupled to a standard single-mode fiber (SMF-28, 1 m long) via lens fiber pigtail package for the HR (375 μm) coated and as cleaved (750 μm) devices. This coupling system has a loss of 25.8 %, derived by measurement. The fiber guides the light to the Agilent 11982A (1200 to 1600 nm) low noise optical/electrical lightwave converter, whereby the photodetector converts it from an optical power into an electrical current. The O/E system provides a dc coupling with 20 dB of electrical gain with a 15 GHz bandwidth.

The noise terms highlighted from N1 to N6 account for laser noise, detector shot noise, thermal noise, and amplifiers noise figures, respectively. A1 through to A6 denote any coupling

losses/attenuations down the measurement system. These noise and attenuation terms will be explored in more detail in what follows.

The high-speed photodetector which is utilized for these high-speed lasers typically has a small area. As a result, in order to conduct a very precise measurement, it is very critical that the output light of the laser, can be captured completely and be sent through a fiber, to hit the effective area of the photodetector. As such, there may be an underestimation in the measurement of non-fiber-pigtailed light source systems, if employing the same set-up as presented here.

The electrical signal is analyzed using an electrical spectrum analyzer (ESA), Agilent E4440A, which displays the power spectral density (PSD) of the photocurrent as a function of frequency. Considering equation 5.2, the square of the ratio of the optical powers is equivalent to the ratio of the recorded electrical powers. For measurement purposes 5.2 can be rewritten as:

$$RIN = \frac{N_{elec}}{P_{Avg(elec)}} \text{ dB/Hz} \quad 5.7$$

Where, N_{elec} is the PSD of the photocurrent over a normalized 1 Hz bandwidth, and $P_{Avg(elec)}$ is the average power of the photocurrent calculated from the digital multimeter reading.

As far as the photocurrent is concerned, following the photodetector the a.c. and d.c. components of the photocurrent must be separated. A bias tee which is a d.c. blocking unit is placed between the lightwave converter and the preamplifier to filter out the large d.c. term for the relative calculation. The d.c. term might also have saturation effects on the preamplifier. The average d.c. voltage is detected on the digital multimeter from which the average power of the photocurrent can be calculated.

The a.c. signal is amplified prior to detection by the ESA as the signal as is hits the noise floor of the ESA in the higher frequencies. For all of the free running RIN measurements in this project, a Keysight 87405C preamplifier with a bandwidth of 18 GHz (< 0.1 GHz), a maximum gain of 27 dB across the bandwidth, and a comparatively small maximum noise figure of 7 dB across the bandwidth is employed. Despite of the increase in the sensitivity of the measurement system, the total pre-amplifier gain and noise figure will be not present a flat frequency response across the range of measurement as will be shown later in the results through their

S_{21} parameters. Hence, if gain compensation is not implemented carefully, such fluctuations in the total gain spectrum of the amplifier will precipitate fluctuations in the RIN trace. Finally, the ESA measures and records the spectrum of the amplified a.c. signal, which is the total noise term.

It must be noted that, the voltage responsivity, r_v , is normally provided at the reference plane after the photodiode, and is required to calculate shot noise. However, in the case of the Agilent 11982A unit employed here, the amplifier is an integral part of the lightwave converter. Consequently, the responsivity is given from the reference plane located after the amplifier, which is indicated with a dashed red line on the right-hand side of the O/E converter in fig. 5.4. As such, the expression for responsivity should contain the gain, G_A , of the amplifier as $r_v = r_{G_A R_L}$. This will be covered in section 5.5.1, Subtraction method.

5.4.1 Limitations of RIN measurement

In practice, extra noise sources from individual electrical components utilized in the measurement system superimpose the pure laser intensity noise. Dark current from the photodetector, thermal noise from the electrical components such as amplifiers and ESA are the additional sources that combine with the laser intensity noise. Moreover, there is another noise source corresponding to the quantum nature of the light, the shot noise. The total noise power recorded from the ESA is comprised of the summation of the aforementioned individual noise terms and can be written as:

$$N_{Total}(f) = N(f)_{Laser} + N(f)_{Thermal} + N(f)_{Shot} \text{ (W/Hz)} \quad 5.8$$

Care must be taken to include the effects of photodiode responsivity, the gain and noise effects of the amplifiers, and most importantly the frequency response corrections of each component contributing to the total noise measured from the system. Thus, RIN measured from the system will inherently be higher than RIN of the laser due to the contribution of thermal noise and shot noise. While the spectrum recorded in the ESA is the total system noise, it is valuable to compartmentalize the quantification of the individual contributions of the laser, shot, and the thermal noise. A discussion of each of these noise sources follows.

5.4.1.1 Laser noise

Laser intensity noise, $N_{(Laser)}$, which is the target of measurement, signifies the noise produced by the laser diode. As mentioned earlier, it arises from random spontaneous emission events introduced into the lasing mode and is dependent on structural parameters. Additionally, external influences, such as modulation frequency, the driving bias directly affect the noise levels. On the other hand, the incidence of external optical reflections or feedback into the laser will increase this noise. Commonly, in QW lasers, the largest portion of the laser intensity noise spectrum rises from the peak at the relaxation oscillation frequency.

5.4.1.2 Shot noise

Shot noise (N_{Shot}) or Poisson noise places a limit on the observed intensity noise. It is a quantum noise arising from the discrete nature of photons arriving at the detector's surface. For a system at a specific temperature, thermal noise is typically constant, but shot noise is a function of average power. The generated noise is directly related to the amount of light incident on the photodetector. The shot noise power from the photodetector is:

$$N_{Shot} = 2qI_{dc}R_L\Delta f \text{ W/Hz} \quad 5.9$$

Where, q is the electron charge, I_{dc} the detected photocurrent, R_L is the load resistance at the input of the amplifier, and Δf is the bandwidth of measurement for spectral density.

For instance, with a load resistance of 50 ohms, a photocurrent of 1nA will produce a shot noise power of 1.6×10^{-17} mW or -168 dB/Hz.

5.4.1.3 Thermal noise

In the measurement system, the amplifiers and the electronic components after the photodetector generate thermal noise ($N_{Thermal}$), also known as Johnson-Nyquist noise. Thermal noise is produced due to thermal agitation of the charge carriers within an electrical conductor. This type of noise occurs regardless of the applied voltage since the charge carriers vibrate as

a result of their temperature. Thermal noise puts a limit on the sensitivity of the receiver and also limits the effective distance between receiver and transmitter in digital and analog systems.

Thermal noise can be expressed in several ways. It is often described as a noise power and because the system circuit is 50-ohm impedance-matched, the noise power generated transfers to the whole of the circuit, i.e. each component dissipates noise in both itself and the other components and the noise power can be expressed as:

$$N_{Thermal} = 4K_B T \Delta f \text{ W/Hz} \quad 5.10$$

Where, K_B is Boltzmann constant and T is the temperature in Kelvin. Thermal noise is expressed in dB and at room temperature has a value of -174 dBm/Hz.

In order to decrease the thermal noise effects at the receiver, low noise amplifiers are usually employed following the photodetector, which is the case in the lightwave O/E converter utilized. ESAs are commonly employed in lightwave measurements. However, most ESAs exhibit noise figures of at least around 30 dB. Placing a preamplifier at the ESA's input would make a cascade amplifier system and reduce the overall noise figure. This would improve the sensitivity of measurement and hence the lightwave-signal-measuring ability of the ESA. Standard noise figures for amplifiers vary from a few dB for narrowband amplifiers (above the -174 dBm/Hz N_{th} limit at room temperature), to as much as 15 dB for wideband amplifiers. Consequently, there is a tradeoff between sensitivity (low noise figure) and bandwidth when selecting an amplifier.

The value of the laser intensity noise is found from equation 5.11 via subtracting the shot and thermal noise powers from the total system noise power as:

$$N_{Laser}(f) = N(f)_{Total} - N(f)_{Thermal} - N(f)_{Shot} \text{ (W/Hz)} \quad 5.11$$

In the particular case of the laser noise starkly surpassing the shot or thermal noise limits, the total system noise is effectively equivalent to the laser intensity noise i.e. $RIN_{Laser} = RIN_{System}$. Conversely, by the improvement of the semiconductor laser technology the intensity noise levels have decreased. This leads to contributions from the shot and thermal-noise sources becoming more substantial in RIN measurements. It must be noted that, the contribution of any

one of the individual three noise terms will dominate if it is about 5 - 10 dB greater than the other terms. As equation 5.8 shows, the total noise is comprised of the sum of these three noise terms and more.

As an example, a laser-intensity-noise-dominated system was reported by the characterization of a Fabry-Perot laser at 1 mW of output power. The total system noise (N_{Total}) was at -145 dBm/Hz, the thermal noise (N_{thermal}) was -168 dBm/Hz, and the shot noise (N_{shot}) at -169 dBm/Hz (for $I_{\text{dc}} = 0.8$ mA) [31]. Transforming to linear form and removing the shot and thermal noise terms from the total system noise yielded the laser intensity noise. It was found to be just 0.04 dB under the total system noise. For this F-P laser, the total system noise is essentially completely comprised of laser intensity noise. For shot and thermal noise terms to add more than 1 dB to N_{total} , the N_{Laser} would need to be brought down by 15 dB to the value of about -160 dBm/Hz. Therefore, boosting the performance of such a system would necessitate addressing of the laser performance alone.

5.4.1.4 Mode partition noise

Another feature that may be seen in some semiconductor laser RIN spectra is due to mode partition noise [32]. This characteristic, not to be mistaken for the RO peak, occurs at low frequencies. The as-cleaved laser diodes have a reflectance of 34% of the light back into the cavity on each round trip. As a result, in a non-DFB laser, as is the case here (F-P), some of the cavity modes will be reflected back and others transmitted through the facet. Those reflected modes gain more dominance in the next cavity round trip and subsequently they are transmitted out and then another mode is reflected back which then becomes more dominant. This dynamic and the competition between modes for carriers causes phase jitters attributed to mode hopping which results in mode flickering. It is this constant swopping between the modes that precipitates mode partition noise. As will be seen later in the RIN spectra, mode partition noise effects are prevalent in the lower frequencies.

5.5 Measurement methods

Different techniques can be utilized to measure the RIN of a laser. While RIN is often measured directly in the electrical domain as described previously, indirect measurements based on the

optical spectrum can also be employed for RIN estimation with less accuracy. In this section a number of techniques are described for the direct measurement of RIN using an ESA.

The subtraction method, presented in section 5.5.1, calibrates for different noise sources separately and subsequently subtract, in linear units, each term from the total noise term. In the second method discussed in section 5.5.2, as the RIN value at a specific frequency is the target of measurement, the system is calibrated for shot noise more accurately. In the final method, section 5.5.3, a calibration technique for the system background noise is described whereby a low noise reference laser is employed, which helps achieve a highly sensitive calibration system.

5.5.1 Subtraction method

This is the method used in this work. Extra noise sources are considered individually and subtracted from the total RIN using this method.

Thermal noise is quantified when the laser is turned off so there is no light incident on the photodetector. This term comprises the dark photocurrent of the detector and noise from the thermal noise sources of the electronics (total background noise). N_{th} is then calculated considering the system frequency response and the amplifier gain.

On the other hand, shot noise is calculated from the dc photocurrent with the laser turned on. The dc average voltage is detected using a digital multimeter after the dc block, as it was shown in the measurement setup. This terminal gives the voltage of the dc electrical signal. A voltage-drop of 0.2 mV across the bias tee terminals, and a read of 0.5 mV with the laser turned off, attributed to the total background noise including the detector dark current, are also accounted for in V_{dc} for the analysis.

As mentioned before, and because the photodetector is an integral part of the O/E converter, the voltage responsivity is thus given from the reference plane located after the amplifier, which is indicated with a dashed red line on the right-hand side of the O/E converter in Fig. 5.4. Therefore, the detector responsivity is calculated considering the amplifier gain as:

$$r = \frac{r_v}{G_{ARL}} \left(\frac{A}{W} \right) \quad 5.12$$

Where, r_v is the O/E voltage responsivity, G_A is the voltage gain of the integral amplifier of the OE converter (10 dB), and R_L is the load resistance (50 Ω). As such, for 1 mW of optical laser power, the lightwave system's voltage responsivity (r_v) is recorded to be 356 V/W, which corresponds to a detector responsivity (r) of 0.71 A/W.

Consequently, the photocurrent at the reference plane indicated in figure 5.4 can now be calculated through:

$$I_{dc} = r \frac{V_{dc}}{r_v} (A) \quad 5.13$$

Where, V_{dc} is the recorded voltage on the multimeter.

On the other hand, the shot noise power spectral density is calculated via equation 5.9. After accounting for the frequency response of the converter, dc blocking unit, and the preamplifier, these noise terms are subtracted from the total measured noise spectrum in linear units and ultimately RIN in dB may be found relative to the electrical power at the reference plane. Great care must be taken when using this subtraction method to determine RIN_{Laser} . In subtracting small numbers from small numbers, errors in values that are close to the excess-noise value of the laser can have large effects. Errors in the amplitude accuracy of the frequency response of the diode can also cause exaggerated effects. Consequently, it is essential to consider the total system's frequency response before making noise subtractions.

The system instruments' frequency responses must be corrected since they do not have a flat frequency gain over the entire spectrum, making it essential to compensate the result for these parameters. As a result, the frequency response of the lightwave system, the bias-T, the RF cables, and the microwave amplifiers, have to be characterized. In this project, S_{21} (transmission) measurements are carried out for compensating for the electrical gain, and the results are subtracted from the spectrum recorded using the ESA.

5.5.2 Quantum noise calibration method

The difficulty with the subtraction technique is that there is a need to determine several parameters of the system, such as the frequency response of the different components and individual noise contribution from each element of the measurement system, which is a non-trivial task. The accuracy of such technique may be limited due to the fact that one has to rigorously account for all of these parameters. Also, it must be ensured that the impedance mismatch losses between the instruments are minimized or at least characterized very accurately to prevent electrical reflections rendering shot noise calculations wrong [32].

Nevertheless, there is an adjustment mechanism, in the shot noise calibration method, that addresses these system parameters and improves the accuracy of the measurement. This technique is predicated on the fact that at a fixed bias current, when reducing the optical power by a variable optical attenuator (VOA), different noise sources increase differently. As it is illustrated in figure 5.5 a), thermal noise is not dependent on optical power, thus changing the power using a VOA will not change thermal noise. Furthermore, shot noise increases linearly (10 dB/decade) and laser intensity noise term increases quadratically (20 dB/decade). Ultimately, the total electrical noise as a function of detected photocurrent is calculated utilizing a system transimpedance term, which is comprised of all the noise sources, connecting the laser intensity noise at the photodetector through the measurement system components to the data recorded by the ESA.

The advantages of this method are lower uncertainty and a self-calibrating mechanism. Conversely, there are also a number of limitations. Noticeably, the measurement procedure is rather time consuming as a series of photocurrent points must be measured, but more significantly, this method can only be utilized in a shot-noise limited system. As such, it is not suitable for my detection system as the detection system is thermally-limited. This means that even at highest detected optical power, our system is limited by thermal noise. A shot noise limited system would entail lasers with much higher output powers, or use of electronics with much lower noise figures.

5.5.3 Low noise reference laser calibration method

This method is quite similar to the previous method, however the transimpedance of the detection system is extracted more simply. A low-RIN light source, e.g. a low RIN laser, can be used in this method to calibrate the detection system. Therefore, the transimpedance term will have a negligible laser noise term. Given the thermal noise is considered individually when there is no light on the photodetector, the remaining parts of the transimpedance term can be more accurately calibrated. For instance, in [33], a solid-state laser was utilized as reference with an electronic loop to control the pump current so as to reduce the intensity noise. The device exhibits negligible RIN for frequencies above that of the relaxation oscillation. Subsequently, the DUT replaces the reference laser and its RIN extracted.

5.5.4 RIN under external optical feedback

In an optical telecommunications system, the distance to feedback is likely to be much larger than the coherence length of the FP laser. If the product of the frequency of the external cavity f_{ext} and the relaxation oscillation frequency f_{RO} is such that $f_{\text{ext}} \cdot f_{\text{RO}} > 1$, i.e. the external cavity's round-trip time is larger than $1/f_{\text{RO}}$, then the coherence collapse is independent of the external cavity's length. Otherwise, extending the length of the external cavity from e.g. 10 m to 10 km would be a very different dynamic. This is the reason the standards suggest investigation of the feedback effects from a distant reflector. The critical feedback strength is typically modelled to increase with J/J_{th} [34]. On the other hand, the effects of feedback from close reflections, i.e. with $f_{\text{ext}} \cdot f_{\text{RO}} < 1$, are considerably smaller on the intensity noise [14].

Fig. 5.5 provides a schematic representation of the experimental setup for the QD laser subject to external optical feedback. The laser mount is fixed on a suspended optical bench to minimize environmental perturbations. The output of the laser in the left-hand side is fed back to the laser cavity through a 100 % reflecting Au coated mirror to form an external cavity with length $L_{\text{ext}} = 11.7$ m or $f_{\text{ext}} = 8.8$ MHz, considering a core refractive index of 1.46. The laser cavity lengths are 375 and 750 μm as before and the ridge waveguides are both 3 μm wide.

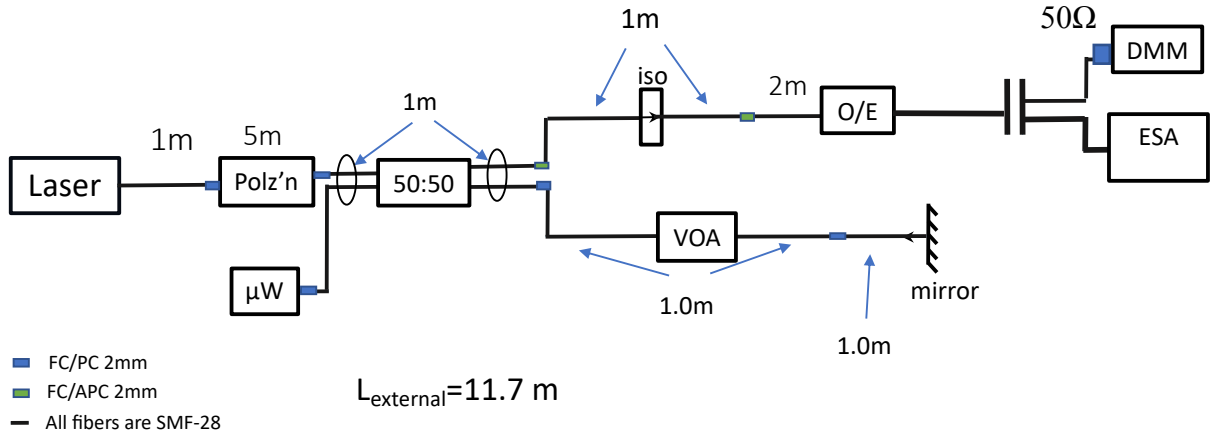


Figure 5.5 Experimental setup of the QD laser under external optical feedback. Polz'n: polarization control, 50:50 symmetric beam splitter, uW: power meter, iso: isolator, VOA: variable optical attenuator, O/E: optical/electrical signal converter; ESA: electrical spectrum analyzer; DMM: digital multimeter.

The length of the external cavity, 11.7 m, satisfying the long external cavity condition. A variable optical attenuator is used to adjust the feedback strength, which is the ratio of the reflected power measured by the power meter to the laser output power as [14]:

$$F_{feedback} = \frac{P_{Reflected}}{P_{Laser-Out}} \tag{5.14}$$

Assuming the polarization of the fed-back light is the same as the polarization of the emitted light, the feedback ratio in the arrangement shown in Fig. 5.5 corresponds to:

$$F_{feedback} = \eta^2 R_m \tag{5.15}$$

Where, R_m is the mirror reflectivity and η encompasses the coupling efficiency considering all the connections on the path towards the mirror. This includes the coupling efficiency from the laser to the fiber (and from the fiber to the laser due to reciprocity), the coupling loss at the fiber connectors, the losses into the polarization control and the beam splitter, and the coupling loss by controlling the VOA. The ratio of optical feedback is corroborated additionally with the power meter using Eqn. (5.14). It must be noted that, A coupling of 25.8 % from chip to fiber means feedback to chip is limited to -12 dB (due to reciprocity). All numbers quoted from hereon are for feedback from fiber back into the fiber and do not include the stated -12 dB

unless otherwise stated. For the purposes of comparison to literature or gauging against the specifications, these numbers are considered.

The polarization controller in the feedback path allows matching the polarizations of the emitted and reflected light and maximizes the effects of the optical feedback. It must be noted that the polarization is adjusted regularly by gauging the noise spectrum in real time for maximum effect and also ensuring that the power meter reads the highest number as polarization is adjusted this will be demonstrated in the results section. The isolator is to prevent any unwanted reflections back into the measurement loop.

Ultimately, the optical signals are captured by the photodetector, which is integrated with an amplifier inside of the O/E lightwave converter and subsequently the RF signal is analyzed by the ESA. The preamplifier is removed as IEEE 802.3ah specifies a RIN setup based on an RF power meter with an AC coupler cut off < 1 MHz and the preamp's cut off is at 0.1 GHz, the bias-T's is at 0.1 MHz. The reason for this specification is that in practice noise is often enhanced at lower frequencies as will be discussed later on due to subtle effects that will be observed in fig 5.9 for the laser on noise power spectral density and discussed in the results section. Furthermore, in a transmission system the semiconductor lasers are biased at high current levels and as discussed before and as will be observed in the next section, the QD lasers' RIN spectra are highly damped particularly at higher currents. The result of external optical feedback is the formation of a resonant spectrum with peaks at multiples of external cavity frequency ($1 / \tau_{ext}$) on top of the regular ($f_{ext} = 0$) spectrum, which decay below 1 GHz. Contrariwise, the maximum of the superimposed noise spectrum is typically around the relaxation oscillation peak for QW lasers [14].

Additionally, the IEEE 802.3ah standard sets the highest limit for RIN optical modulation amplitude (OMA) under an external optical feedback ratio of -12 dB. The RIN_{OMA} is defined as the ratio of the average noise power to the electrical modulation power of a square wave:

$$RIN_{OMA} = \frac{(N_1 + N_0)/2}{P_{mod}} \quad 5.16$$

Where, N_1 and N_0 are the power spectral densities of the corrected on and off powers photocurrent over a normalized 1 Hz bandwidth, and P_{mod} is the modulation power [35]:

$$P_{mod} = \frac{(P_1 - P_0)^2 r^2}{4} R_L \quad 5.17$$

Since RIN_0 is always higher than RIN_1 , as shown in fig. 5.22 (note the height of the lower vs higher power RIN spectra), the corresponding RIN_0 spectra are investigated for the worst-case scenario of RIN_{OMA} under external optical feedback.

5.6 Results

In this section clear RIN spectra of the state-of-the-art QD lasers, solitary and particularly under external optical feedback at a range of temperatures are provided. The latter experimentation is rather scarce in the literature particularly for GaAs based QDs as mentioned in the gaps in knowledge section, and the results are quite nebulous due to the heavily damped response of the QDs. Additionally, there hasn't been any feedback resilience reports carried out on QD lasers at the full commercial temperatures range set out by spec [29]. This is particularly of interest due to the temperature insensitive nature of some of the key parameters of QD lasers e.g. threshold current and LEF.

In the experimental part of this work, the subtraction method, explained in section 5.5.1, was used based on the experimental setup illustrated in figure 5.4. This method was chosen since, as shown figure 5.12, the detection system is thermally limited. As a result, the second and the third techniques outlined in sections 5.5.2 and 5.5.3, respectively are not applicable to my system. Furthermore, at the time of conducting this experiment, I did not have access to a low-noise light source at 1300 nm to employ as a reference light, which is required by the third method.

In this section, firstly the correction processes will be elaborated. The free running RIN results will then be demonstrated and the intrinsic modulation characteristics extracted. Subsequently, RIN results under various levels of external optical feedback are provided and hence analyzed.

5.6.1 Free-running RIN

As it was described before, accurate compensation for the frequency dependent system parameters is paramount for obtaining correct spectra. Consequently, a 2 port S_{21} transmission measurement was carried out from the output of the O/E lightwave converter, to the input of the ESA, including the RF cables (path B as shown in figure 5.6, data presented in fig. 5.8b). Note that in order to compensate for the gain and the frequency response of the preamplifier, the S_{21} of the preamplifier at the ESA input, which includes its gain over the frequency range, is separately acquired from calibration chart and is included in the total S_{21} term. Thereafter, these factors were subtracted from the results obtained by the ESA. For clarity, the electrical side is illustrated in figure 5.8.

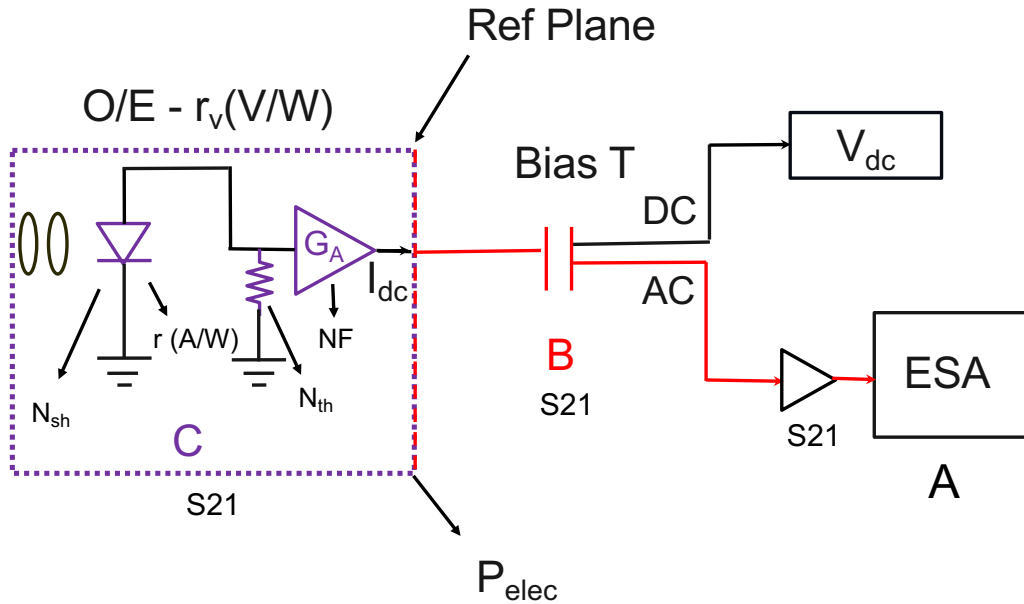


Figure 5.6: Electrical side of the measurement system, relevant correction procedure is highlighted

Considering the previous explanation regarding V_{dc} in the subtraction method in section 5.5.1, it is worth noting the equations that were used to calculate the photocurrent and electrical power at the reference plane indicated in figure 5.8:

$$P_{opt} = \frac{V_{dc}}{r_v} \text{ (W)} \quad 5.18$$

$$I_{dc} = r P_{opt} \text{ (A)} \quad 5.19$$

$$P_{elec} = I_{dc}^2 R_L = (r P_{opt})^2 R_L \text{ (W)} \quad 5.20$$

For instance, for a 1mW of 1300nm optical laser power coupled into the converter, a V_{dc} of 356 mV is detected into 50 ohms corresponding to an I_{dc} of 7.12 mA with an electrical power of 2.53 mW at reference plane.

The shot and thermal noise terms, shown above in the O/E (part C), and defined in their respective sections previously, are both amplified due to the integral amplifier in the lightwave system. These are corrected for accordingly utilizing the S_{21} spectrum provided in the converter calibration chart and also considering G_A , power gain of 20 dB (at 1 GHz).

The resolution bandwidth (RBW) of the ESA should be set as low as possible, to give the highest precision and also the best sensitivity. In [36], the explanation about how RBW is related to the sensitivity of the ESA can be found. In practice, it was observed that RIN values are dependent on RBW setting. If it is set to a high value, ESA will give higher RIN values. It is also essential to use a consistent RBW for all measurements naturally due to the higher uncertainty if different RBWs are used. Thus, 120 kHz was chosen for RBW which gives a reasonable sweep time while resolving the smallest features (~ 200 kHz of FWHM).

Throughout the measurement for all RIN spectra a total number of 8192 data points is taken per spectrum. Moreover, there is an internal attenuator at the input of spectrum analyzers. In the case of measuring noise, setting this attenuator to zero attenuation results in the best instrument sensitivity [36]. Additionally, the noise marker function should be activated on the ESA. This function has several features, such as assigning a +2dB correction factor that is considered in all noise measurements [36].

Figure 5.7 shows the power spectral densities of the different noise sources recorded by the ESA at an RBW of 120 kHz with the 375- μ m-long laser biased just above its threshold (6.85 mA) at 7mA at a temperature of 25C. The system background when the laser is turned off along with the ESA noise floor (blue line) are also plotted. The total noise (red line) is made up of the external noise sources amplified by the O/E (black line).

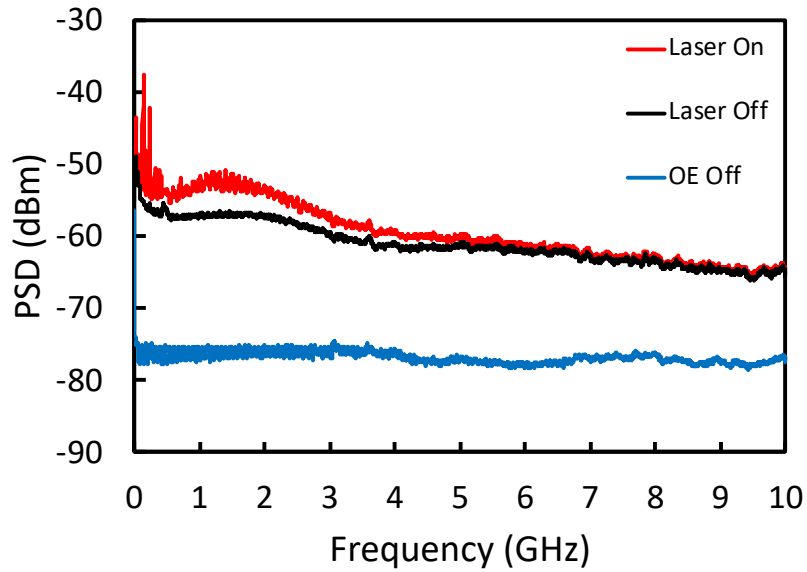


Figure 5.7: Measured power spectral densities of different noise sources at 7 mA of the short device at 25 C

It can be seen from fig. 5.7 that laser intensity noise exceeds that of the other aforementioned noise terms by up to 7 dB at 1 GHz and is more than 20 dB above the ESA noise floor (blue line). This is the point where the spectral density of the laser noise exhibits a clear RO peak located at 1.3 GHz at the highest point. This indicates a laser noise dominated RIN measurement.

The measured noise spectrum subsequently decays before falling into the noise floor at around 4.5 GHz. The rise in noise in the low frequencies, in the red line, is due to mode partition noise, which is discussed once the RIN with respect to output power is presented in fig 5.12. The 20 dB gain of the preamplifier is also evident in the difference between the ESA noise floor and the measured noise spectra. The difference of these spectra is also utilized to crosscheck for the frequency response of the amplifier in the O/E converter.

In order to correct for the frequency response of the preamplifier and the bias tee, 2 port S21 transmission measurements were carried out, and the results were obtained utilizing a Keysight E8362B network analyzer and are presented below. Note that, as mentioned before, the calibration chart was used for the O/E converter response accounting for its integral amplifier gain (20 dB) and noise figure (5 dB).

Figure 5.8 plots the transmission response of the preamplifier and the bias tee at the frequency range of 0.1 GHz to 10 GHz. These spectra are later utilized in the analysis and subtracted from the noise spectra presented in figure 5.9 to correct the frequency varying response of the relevant components.

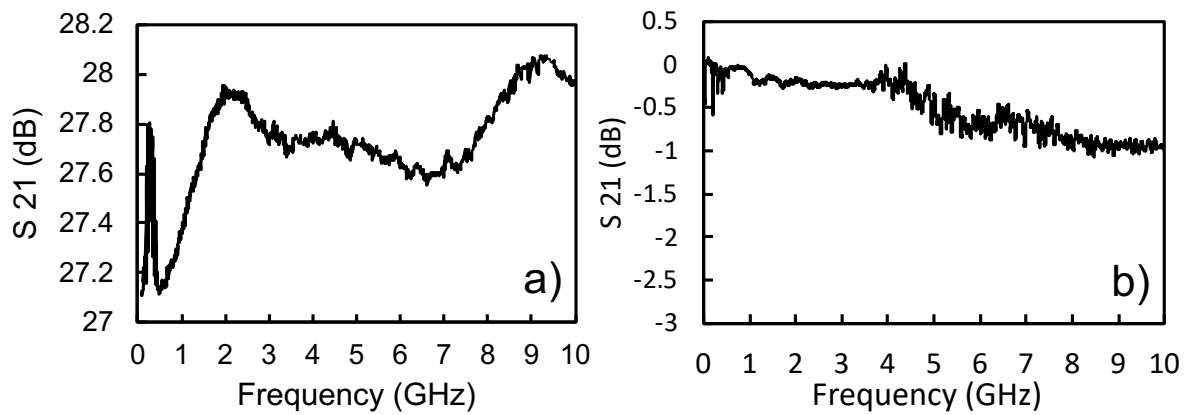


Figure 5.8: a) S₂₁ parameter of the preamplifier and b) the bias Tee both with cables attached

It must be noted that as the amplifier and the photodetector inside of the lightwave converter cannot be treated separately, the S₂₁ of the Agilent 11982A O/E unit is presented in fig. 5.9 a). On the other hand, the preamplifier's noise figure exponentially decreases from 6.1 dB at 0.1 GHz to 2.5 dB at 10 GHz. This is plotted in fig. 5.11 b) below.

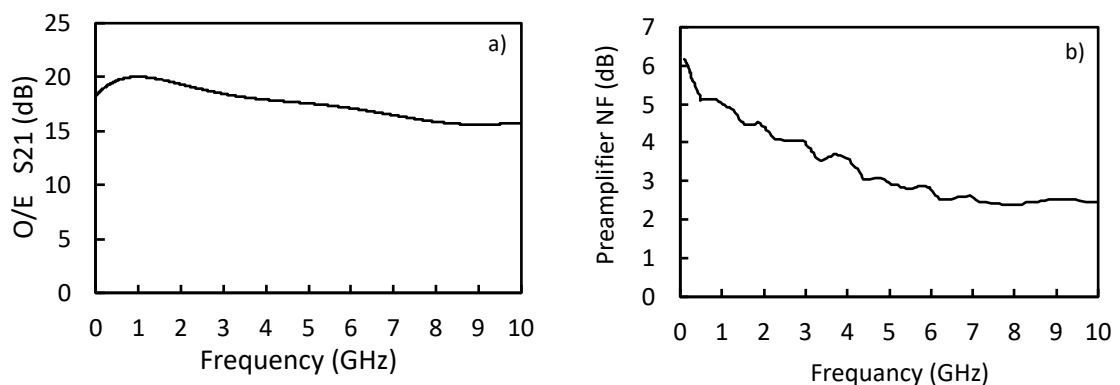


Figure 5.9: Noise figure characteristics of the 87405C preamplifier

Fig. 5.9 b) was generated from the measured data in the calibration chart for the Keysight 87405C preamplifier module.

In order to investigate the amplified shot and thermal noise, consider figure 5.12 with the different noise sources including the thermal noise (solid black line). On the other hand, the shot noise of the photodiode (dashed line) is more than 20 dB smaller. This, however, is the limiting factor at higher powers.

Figure 5.10 illustrates the power spectral densities in mW/Hz for more clarity of the different noise sources at 6.9 mA (0.03 mW). The amplifiers' gain and noise figures influence are already accounted for.

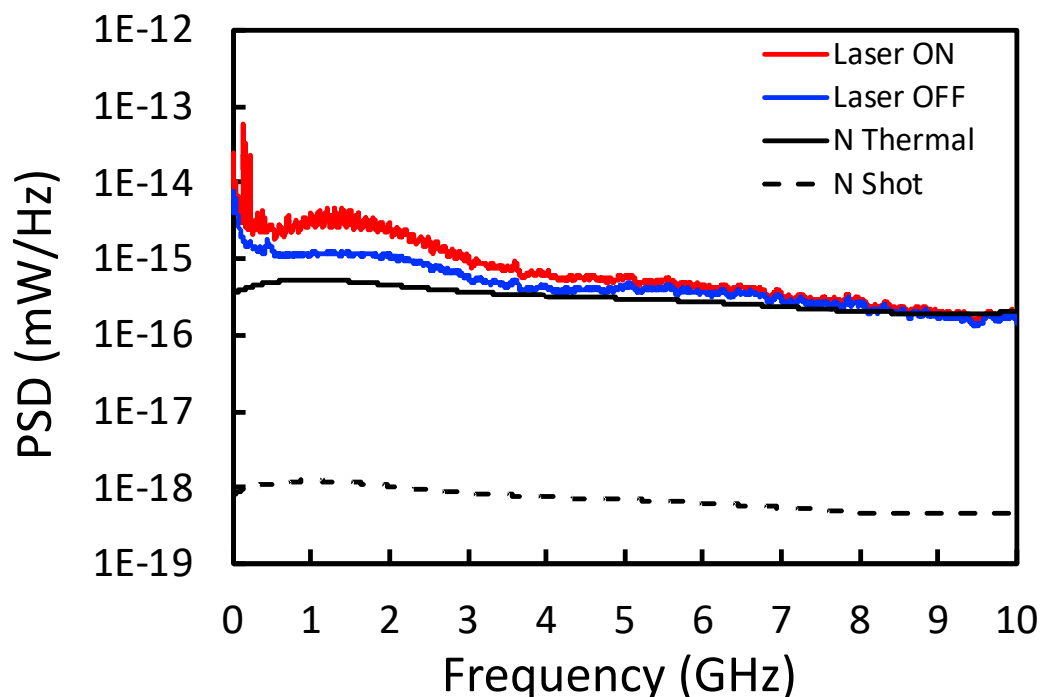


Figure 5.10: Measured power spectral densities of different noise sources at 6.9 mA

The total noise (solid red line) is dominated by the intrinsic laser noise (target of measurement) and the thermal noise (solid black line), while the shot noise of the photodiode (dotted line) is more than 20 dB smaller and hence is negligible. This spectral density shows a clear resonant peak around 1.2 GHz. The increase at lower frequencies is due to the composite effect of the mode partition noise and the 1/f noise. That is why this effect is more pronounced in the laser-on spectra compared with the turned-off laser background.

In what follows, the RIN spectra of fiber pigtailed QD lasers with length of 375 μm with the HR/HR coating will be presented. However, prior to delving into the RIN spectra as a function

of drive current, let us consider the difference in the QW and QD laser specific transfer functions.

Figure 5.11 plots the measured RIN at 0.05 mW from the 375 μm laser along with the calculated RIN spectrum utilizing both the QW SSM transfer function and the QD specific transfer function, which is the modified version of the classical to account for the increase in the lower frequencies as explained in [37]. The QD transfer function used to fit the RIN spectra is:

$$RIN = \frac{\frac{H}{\omega^2} + A\omega^2 + B}{(\omega - \omega_r^2)^2 + \gamma^2\omega^2} \quad 5.21$$

Where, $(2\pi)\omega_r$ accounts for the RO frequency, γ the damping factor, A and B are the Langevin noise terms, and H accounts for the increase in the lower frequencies. Subsequently, RO frequency and damping factor are extracted for further analysis.

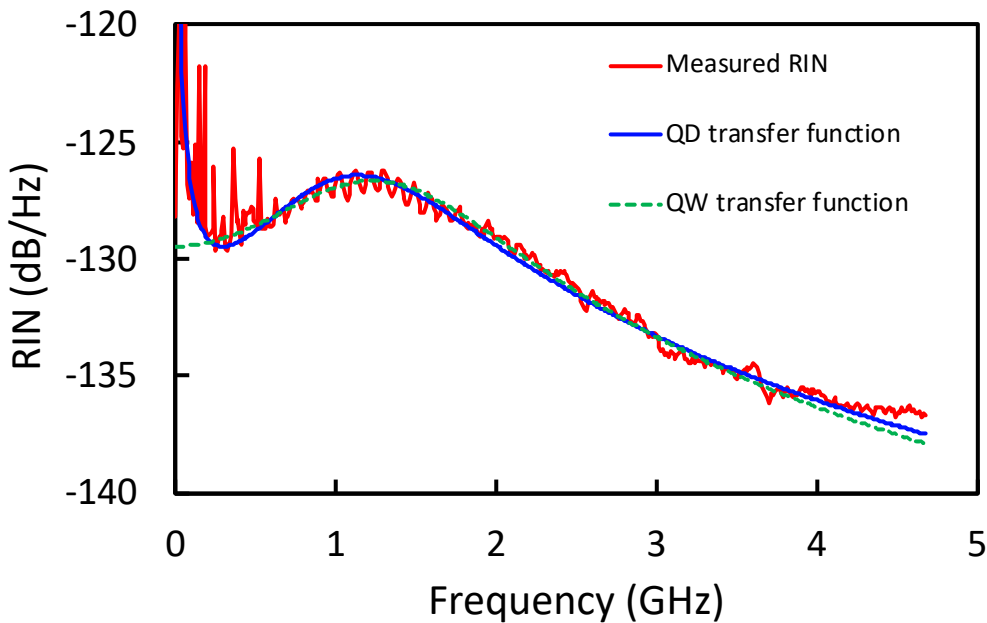


Figure 5.11: Measured and corrected for RIN spectra using the subtraction method from the 375 μm laser at 25C (solid red line), the calculated spectra using QW RIN transfer function for a semiconductor laser (green dashed line), and the QD transfer function (solid blue line)

Figure 5.12 plots the RIN with their corresponding QD transfer function fits as a function of frequency at 25 C for the 375 μm device.

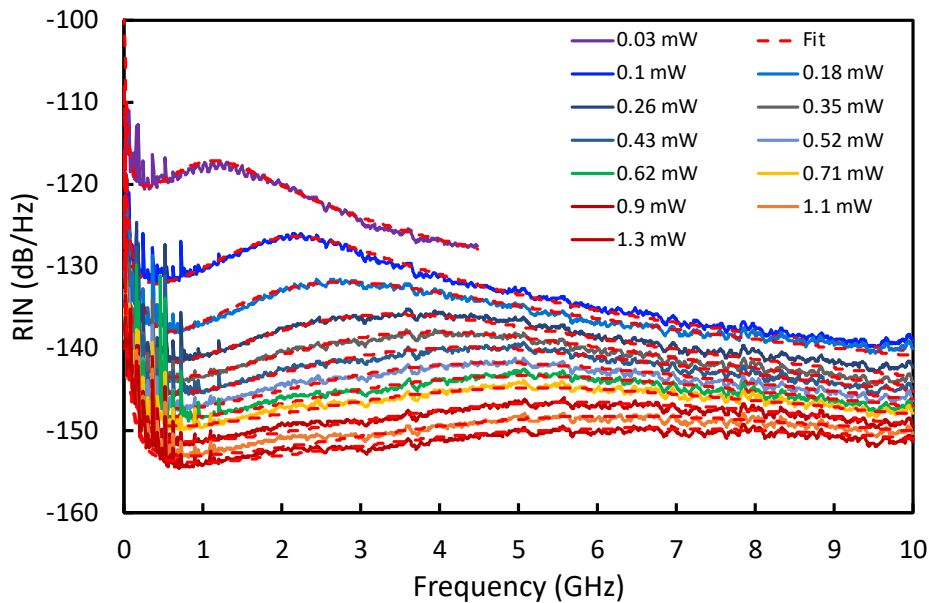


Figure 5.12: Measured and corrected for RIN spectra with the QDSTF fits at 25C (7 - 22 mA)

As observed in fig. 5.7 the laser spectrum falls into the noise floor at around 4.5 GHz, for lower currents just above the threshold (0.03 and 0.05 mW). As such the low power RIN spectra presented here will be truncated before falling into the noise floor.

From fig. 5.7, typical behavior from FP lasers is observed. As explained in the introduction section, the carrier recovery process is hindered by the carrier-photon coupling that generates intensity noise, which is highest at the resonance around the relaxation oscillation peak in the RIN spectra, at 1.2 GHz from 0.03 mW output power. This is most pronounced just above threshold with the presence of more spontaneous emission and reduces as laser is driven harder and output power is increased. By increasing the drive current (available number of carriers), the relaxation oscillation peak increases in frequency and its peak is reduced until the system arrives at its fastest intrinsic recovery speed (7.2 GHz) at higher currents (1.3 mW). This is attributed to the reduction in carrier lifetime, and an increase in the optical SNR, respectively. The persistent nudges in the spectra at 2.4, 3, 3.7, 5, and 5.7 GHz may be attributed to the WiFi router signal interfering with the RF cables and other electrical interference that repeat.

Figure 5.13 plots the maximum f_{RO} RIN level as the current is increased from the presented data in fig. 5.12 at a higher current range and lower increment for clarity. RO peak RIN height

is plotted down to -156 dB/Hz at 50 mA. RO RIN peak is below -140dB/Hz at 12 mA (0.1 mW) and RO RIN peak is at -150 dB/Hz at 1mW of output power.

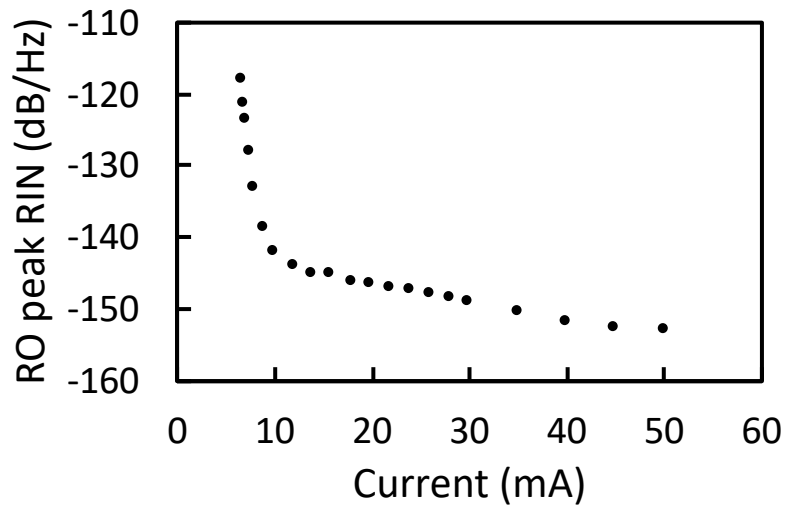


Figure 5.13: RO peak RIN level as a function of current for the short device at 25 C

This is the reason the critical feedback strength is typically modelled to increase with J/J_{th} [40] as mentioned before in section 5.5.4.

On the other hand, from the spectra in fig 5.12 it can be observed that the critical noise-contributing portion of the spectra is below 1 GHz. This part presents a greater source of noise than even the RO peak. This increase in noise in low frequencies is attributed to mode partition noise predominantly and increases with output power and develops as the dominant source of noise in spectra. These findings are consistent with [21 and 22]

Figure 5.14 presents the low frequency part of the RIN spectra at higher powers for both devices. The increase in the noise spectra at lower frequencies is evident in both devices. The spikes on the data presented in fig. 5.16 may be attributed to electrical interference.

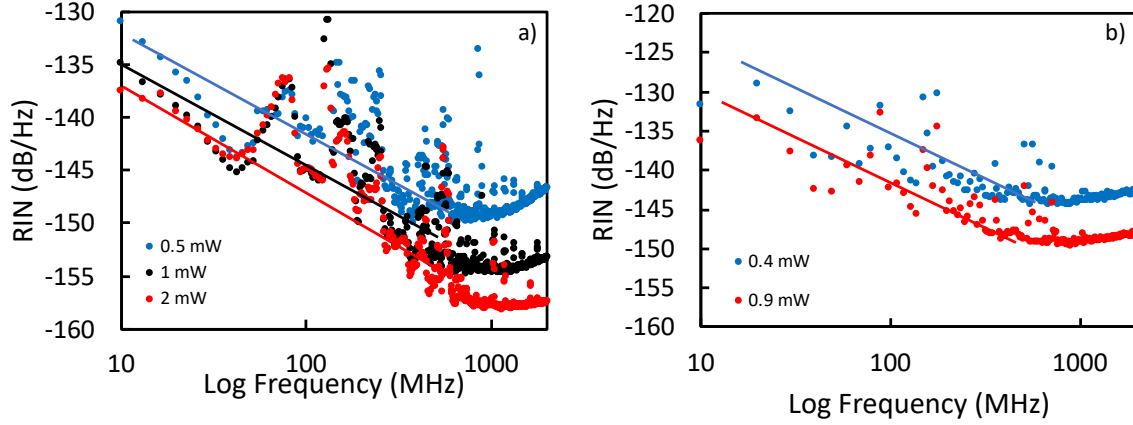


Figure 5.14: Low frequency mode partition noise in the RIN spectra for a) the short device and b) the long device at 25 C

As given in Eqn. 5.6 for the damping rate, the K-factor describes the damping of the response, and as such is an important parameter in the characterization of high-speed lasers. Due to the fact that the damping rate increases proportional to f_r^2 , *c.f.* A.22, as the laser is driven harder with current with the goal of increasing f_r^2 , the response flattens out as presented in Fig. 5.12. The damping factor offset γ_0 is more significant at low powers where the RO frequency is low. In practice, K and γ_0 are utilized as fitting parameters that are extracted from the laser's RIN spectrum.

At high powers, above 1mW in Fig 5.12, the spectrum flattens out as the damping rate becomes large enough and the response drops below the 3-dB cutoff (the RO peak) at frequencies less than f_{ro} . Consequently, there is an intrinsic maximum achievable bandwidth. The modulation bandwidth can be determined at either of these limits i.e. for low damping at lower powers as well as the maximum possible bandwidth at high powers (K-factor limited), respectively we have [38]:

$$f_{3\text{-dB-limited}} = \sqrt{1 + \sqrt{2}} f_r, \quad \left(\frac{\gamma}{f_r} \ll 1\right) \quad 5.22$$

$$f_{3\text{-dB max}} = \sqrt{2} \frac{2\pi}{K}, \quad \left(\frac{\gamma}{f_r} = \sqrt{2}\right) \quad 5.23$$

Fig. 5.15 show the RIN parameters extracted for analysis via the intrinsic frequency response transfer function for the 375 um QD laser at 25 C. The modulation efficiency or the D-factor which describes the intrinsic modulation characteristics of the device, essentially quantifies the

rate at which the resonance frequency increases with current as defined in Eqn. A.26. Subsequently, f_{ro} is plotted as a function of square root of the incremental current in figure 5.15 a).

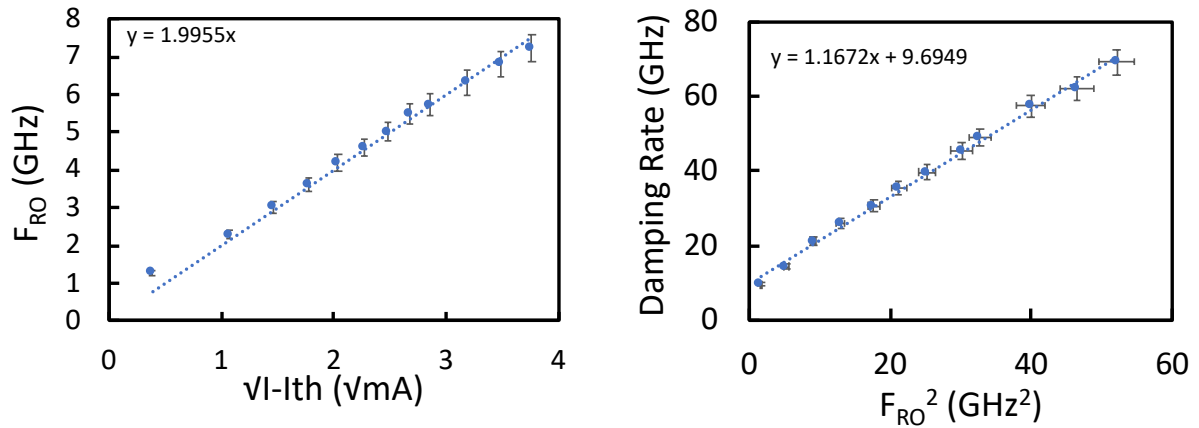


Figure 5.15: a) RO frequency vs square root of incremental current. b) damping frequency as a function of resonant frequency squared

Investigation of the damping coefficient versus resonance frequency squared, presented in fig 5.15 b), determines the slope parameter i.e. K-factor as defined in eqn. A.23, for the damping factor. The K-factor can be used to calculate the maximum K-factor limited bandwidth using eqn. 5.23. Because I am concentrating on the laser performance above threshold and as lasers are run at currents considerably higher than their threshold in practice, the maximum K-factor limited bandwidth is used as the figure of merit here.

From fig. 5.15 b), at 25 C, the K-factor is 1.16 ns which implies a modest modulation speed attributed to strong damping. f_{RO} at 1.1 mW is at 7 GHz which entails a maximum 3-dB bandwidth of 11.18 GHz. While the K-factor limited bandwidth is 8 GHz, which sets the experimental limit of direct modulation on the device. It must be noted that, the curve becomes more non-linear as current is increased meaning that the actual RO frequency shifts faster than the damping. The modulation efficiency, the D-factor, is $2 \text{ GHz}/\text{mA}^{1/2}$.

The RIN spectral analysis of the modulation characteristics through the QD frequency response transfer function for the 375 μm QD laser at a range of temperatures is shown below. Figure 5.16 a) plots the RO frequency as a function of square root of the incremental current and b)

the damping rate vs square of the RO frequency for the extraction of the D- and K-factor, respectively.

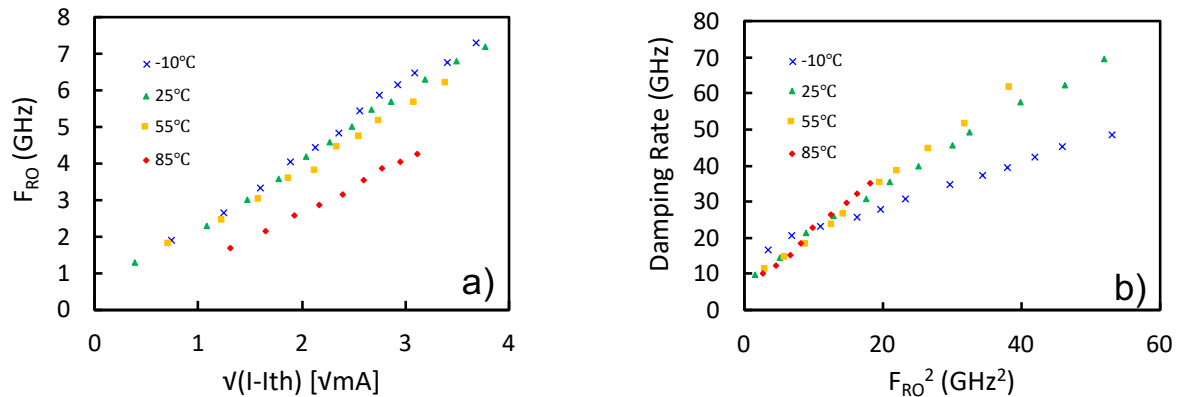


Figure 5.16: a) RO frequency vs square root of incremental current. b) damping frequency as a function of resonant frequency squared

It can be observed from fig. 5.18 a) that, a proportional dependence exists at low injection current however, as the current injection is increased, and at all temperatures, the RO frequency shows a decreased slope. This is attributed to gain saturation also observed in [22]. Furthermore, this gain saturation results in a reduction in differential gain or an increase in gain compression which is primarily attributed to the delayed carrier relaxation process in QDs as explained in chapter 3.

On the other hand, as temperature is increased, for a given $\sqrt{(I - I_{th})}$ f_{ro} shifts to lower frequencies which may be attributed to the thermal expansion of the laser cavity. And also, since f_{ro} is directly proportional to the photon density in the cavity (N_p), referring to eqn. A.22 and in [39], as temperature is increased N_p reduces due to carrier thermalization to higher energy states, whereby they are more likely to recombine non-radiatively in QDs [40] which also reduces f_{ro} .

Correspondingly, damping rate increases with increasing temperature, as seen in fig. 5.18 b). It can be observed that at low powers the damping rate is very similar for the above 0 characteristics, however there is higher damping at -10 C. This may be attributed to the relatively small homogeneous broadening tightening the RO correlation of the dots with different sizes. Thus, dots that have an optical gain above the lasing threshold start lasing

independently, with different resonant oscillation frequencies which acts to further broaden the RIN spectrum.

As the laser is driven harder, above 10 GHz on the f_{ro}^2 scale of fig. 5.16 b), with temperature increasing, there is higher damping at a given drive current and the spectrum flats out at lower f_{ro}^2 values. Further dampening the response is another result of the aforementioned carrier thermalization to higher states as temperature is increased. This is corroborated in the investigation of the carrier lifetime which increases with temperature as shown in fig. 5.17 b).

Figure 5.17 plots the K- and D- factor analysis with respect to temperature indicating the limits of f_{ro} limited and the K-factor limited f_{3dB} at -10 and 85 and the corresponding electron lifetime as a function of heatsink temperature

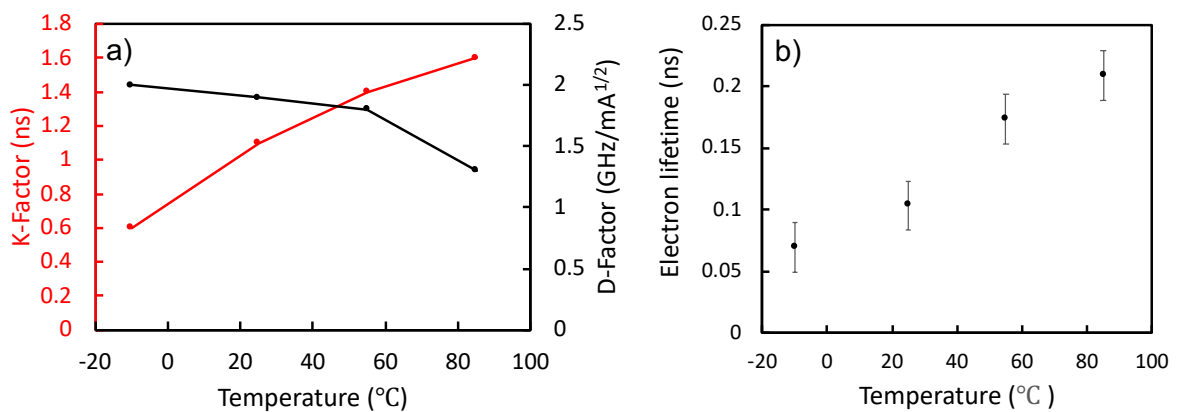


Figure 5.17: a) K- and D- factor as a function of mount temperature. Limits of f_{3dB} are numerate on the plot at -10 and 85 C b) Electron lifetime vs heatsink temperature

It can be seen from fig. 5.17 a) that the modulation efficiency (the D-factor) decreases as temperature is increased which is triggered by an increase in the damping rate as explained above (K-factor). Although this is detrimental to the modulation capabilities of the device at elevated temperatures, a further increase in the damping rate can be beneficial in significantly increasing the laser's resilience to external optical feedback as discussed before in the presentation of Eqn. 5.6.

The RIN spectra for the 750 μm device was only extractable at 25 C as it fell below the ESA noise floor at the other temperatures presented for the short device.

Figure 5.18 presents the RIN spectra with their corresponding transfer function fits as a function of frequency at 25 C for the 750 μm device.

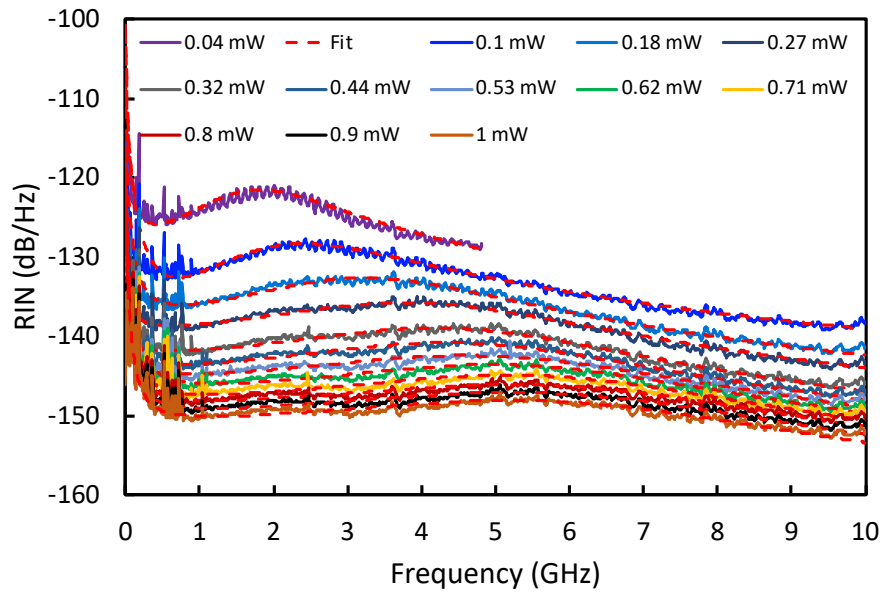


Figure 5.18: Measured and corrected for RIN spectra with the QD transfer function fits at 25C (12 - 48 mA)

Again, as before, the same trend follows for the 750 μm FP laser, namely, RO peak reduces with increasing current due to increasing OSNR. RO peak shifts to higher frequency due to reducing carrier lifetime and the mode partition noise at low frequencies. The device exhibits comparatively lower noise than the shorter device.

Fig. 5.19 plots the RIN analysis using the QD specific transfer function fits for the 750 μm QD laser at 25 C for the extraction of K- and D-factors.

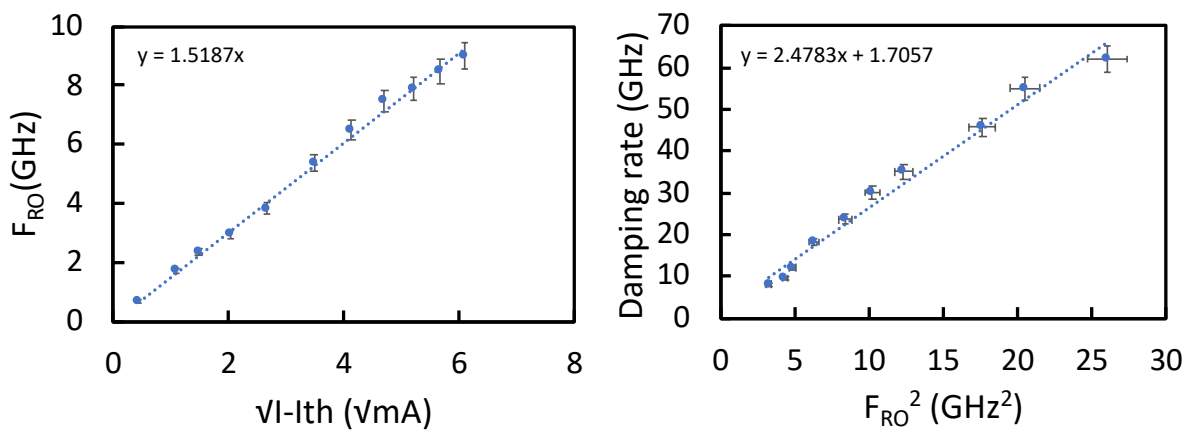


Figure 5.19: a) RO frequency vs square root of incremental current. b) damping frequency as a function of resonant frequency squared for the long device at 25 C

A modulation efficiency of $1.5 \text{ GHz/mA}^{1/2}$ is achieved at 25 C with a relatively large K-factor value of 2.5 ns, which is attributed to heavier damping in the 750 μm device. There are large uncertainties from data fitting, which is due to the smaller signal above the ESA background noise floor.

In order to compare the devices at two lengths F_{RO} and the corresponding RIN levels is investigated with respect to output power and current density.

Figure 5.20 plots the F_{RO} characteristics for the 375 and 750 μm devices.

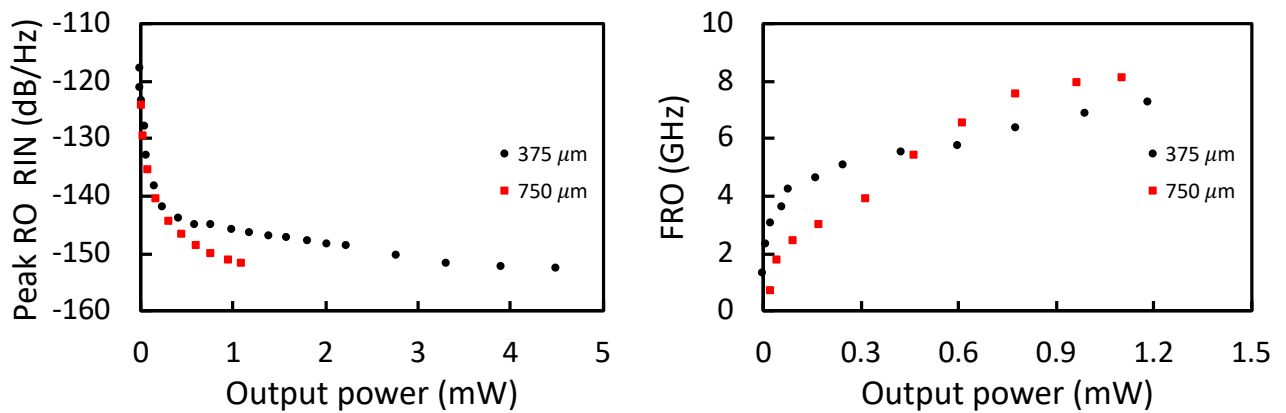


Figure 5.20: a) RO frequency and b) peak RIN vs output power for both devices at 25 C

From fig. 5.20 a) the 750- μm device exhibits a lower peak RIN by ~ 5 dB with respect to output power. In fig. b) the long chip also shows a better performance in terms of RO frequency vs output power. This behavior may be attributed to the fact that the short chip exhibits higher noise due to the HR/HR coating reflecting more power into lasing, which also means reflecting back more spontaneous emission as compared to the both as cleaved facets in the long chip.

Figure 5.21 plots the modulation efficiency characteristics for both devices with respect to current density.

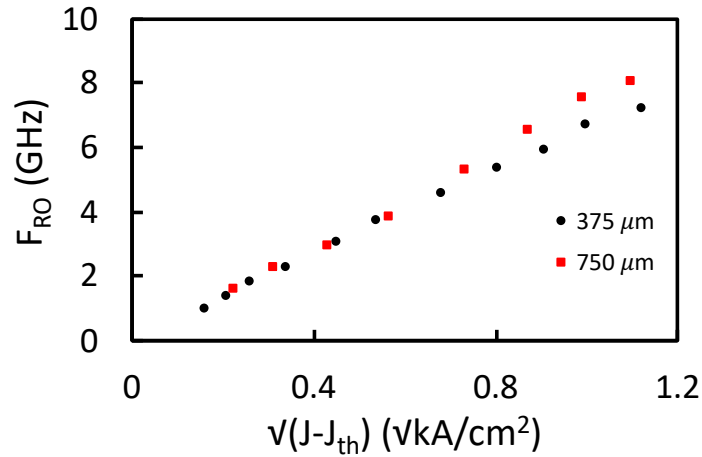


Figure 5.23: RO frequency vs square root of incremental current density for both devices at 25 C
Both devices exhibit a similar modulation efficiency performance when investigated as a function of the square root of incremental current density, $J-J_{th}$.

5.6.2 RIN under external optical feedback

In order to investigate the RIN spectra under various levels of external optical feedback, it is worth outlining the IEEE 802.3ah specifications [2] as related to this work. For a 2.5 Gbps optical link module (in the range of 1260-1360 nm), the minimum and maximum launch powers are specified at -9 and -3 dBm i.e. 0.12 and 0.5 mW, respectively with a required minimum extinction ratio (ER) of 6 dB in a standard single mode fiber configuration and a maximum RIN_{OMA} of -113 dB/Hz (eqn. 5.4) for -12 dB of back reflection. I have also defined a case for a maximum ER of infinity. For clarity these power levels are illustrated on the light-current graph of the device in figure 5.22 below.

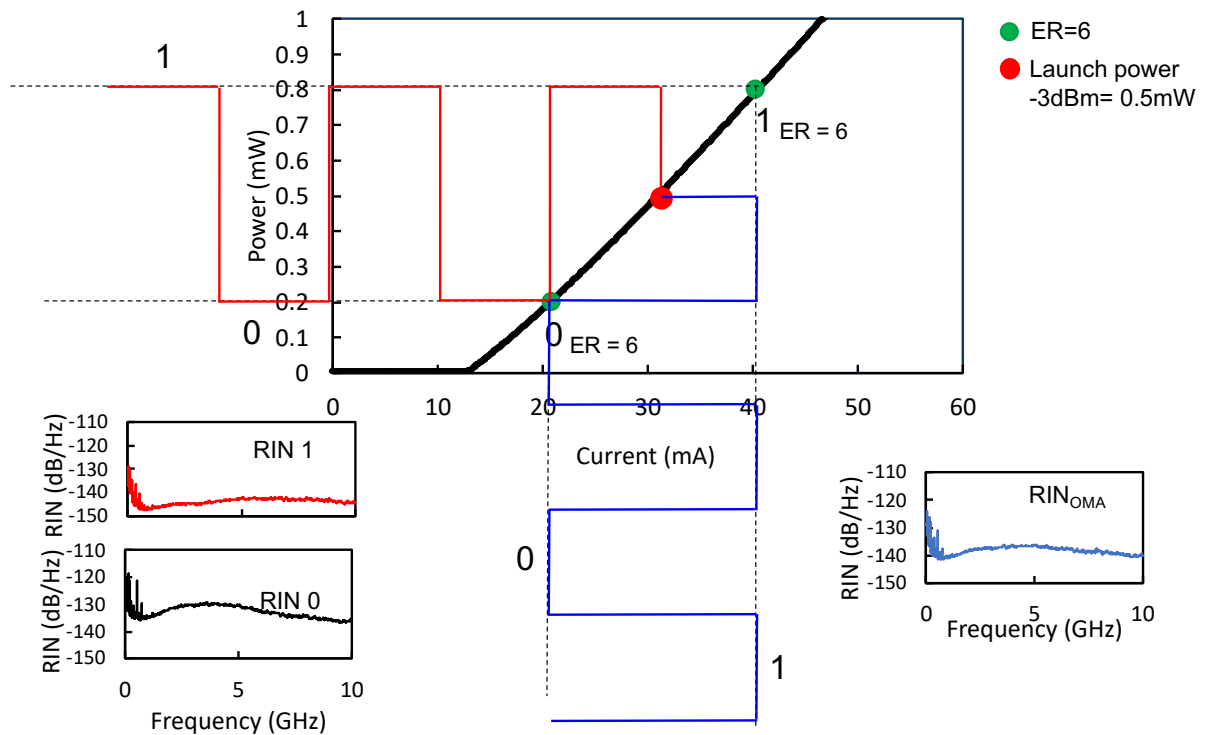


Figure 5.22: L-I characteristics of the device with the 0 and 1 launch powers considering an ER of 6 dB. Bottom left-hand-side shows the 1 and 0 level RIN spectra, respectively, and the bottom right-hand-side show the corresponding RIN_{OMA}

The free-running 1 and 0 RIN spectra and the corresponding RIN_{OMA} spectrum are illustrated to elaborate the higher RIN_0 levels. As external optical feedback produces a spectrum that is superimposed on top of the free-running spectrum the RIN_0 under feedback is investigated for the worst-case intensity noise scenario against the specification.

Firstly, in order to ensure that the correct polarization of light is being fed back into the laser cavity, the PSD spectrum is investigated with respect to the change in the polarization controller for maximum effect on the external cavity modes.

Figure 5.23 shows the low frequency portion of the PSD of the short device at 1mW under -16 dB of feedback with varying the polarization of the feedback light.

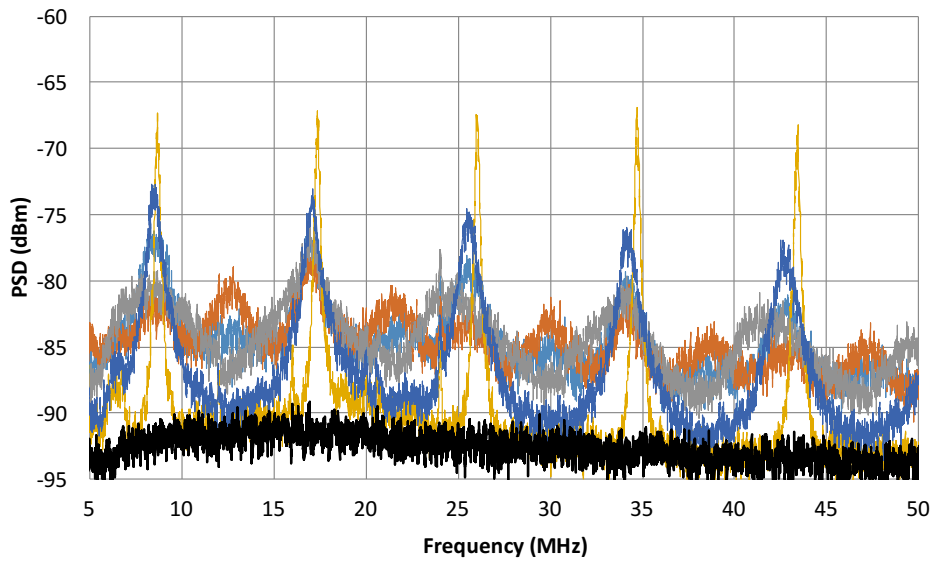


Figure 5.23: Effect of the polarization control on the external cavity modes PSD vs frequency short device

It can be seen that by changing the polarization of the light being fed back into the laser, the external cavity peaks can be altered. The ESA background is shown in black. It is possible to minimize the peaks (reduce by 10 dB) at the expense of the average noise level (increased by 5dB). Extra harmonics may also be promoted.

On the other hand, light vs current characteristics are also indicative of the effect of polarization control on output power. The polarization is adjusted to obtain the highest and lowest powers.

Figure 5.24 plots the L-I characteristics of the short device at 25 C under feedback with varying the polarization control for the highest destructive interference (black line in fig 5.25) and highest constructive interference (yellow line) effect.

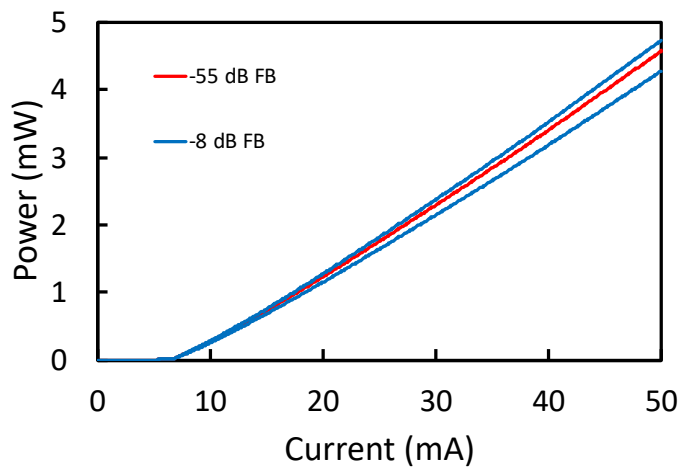


Figure 5.24: Light vs current for the short device under high and lowest (free running) feedback regimes

It can be observed from the graph above, that with polarization control the output power can be altered by +3.0 or -6.0% as compared to the lowest level of feedback (free running) case.

Figure 5.25 presents the RIN spectra of the short device at 1 mW under highest and the lowest amounts of feedback.

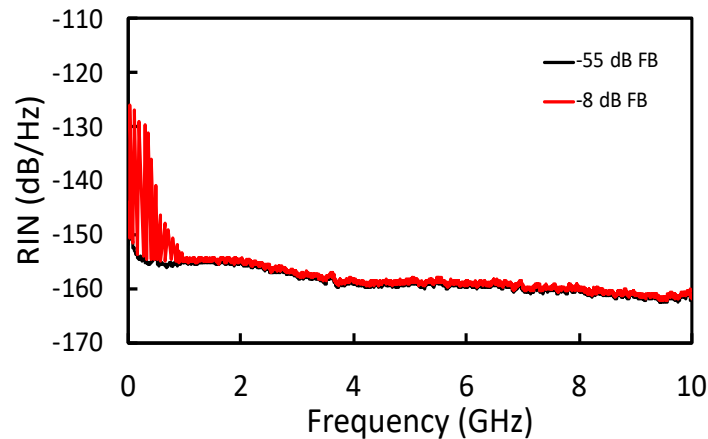


Figure 5.25: Light vs current for the short device under high and lowest (free running) feedback regimes

The feedback does not seem to change the high frequency RIN spectra as substantially as it does for the lower frequencies. The changing portion is at the low frequency part ($1/\tau_{\text{round-trip}}$ of external cavity – 8.8 MHz) and its harmonics. The harmonics decay down to the noise floor below 1 GHz, which may be attributed to the loss in the external cavity.

Figure 5.26 presents the low frequency part of fig 5.27 at 25 C from 0.1 to 200 MHz.

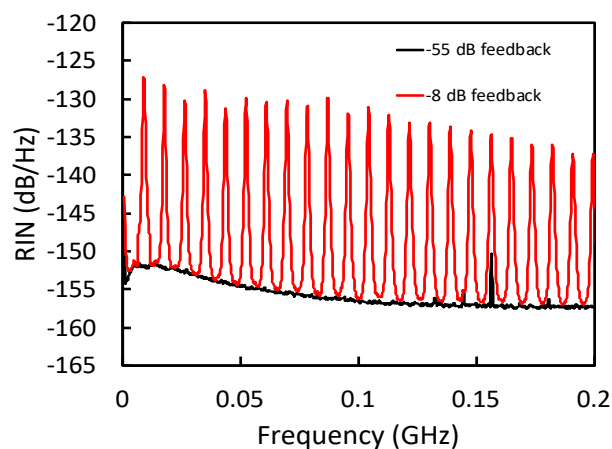


Figure 5.26: Measured low frequency RIN at weak and strong feedback levels at 1mW

The spectra were video averaged over 20 scans to resolve the spectral features better. The feature around 160 MHz may be due to the interference from the maritime mobile services as the frequency band 156.8375 - 161.9375 MHz is dedicated to mobile signals, except aeronautical [41].

Under strong feedback, enhanced RIN peaks separated by the external cavity roundtrip frequency of $1 / \tau_{\text{ext}} = 8.8$ MHz can be observed. Thus, the effect of feedback is formation of a resonant structure with peaks at multiples of $1 / \tau_{\text{ext}}$ superimposed on the low feedback regime spectrum with a pronounced maximum at the relaxation resonance frequency which is now pushed down to 8.8 MHz. On the other hand, with increasing feedback the round-trip peak shifts to higher frequency.

Figure 5.27 presents the fundamental harmonic at 8.8 MHz as feedback strength is increased. From data presented in the inset a shift of 6 kHz/dB is deduced.

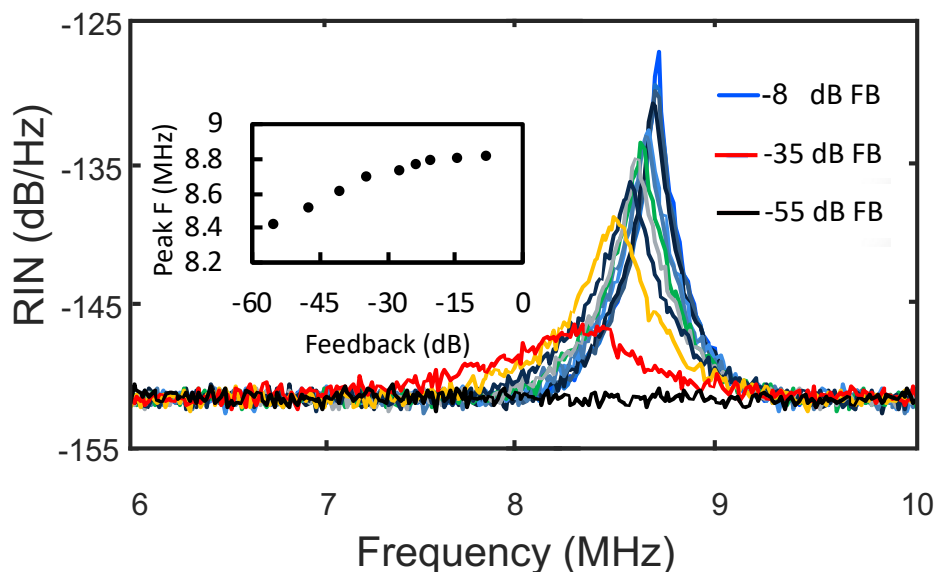


Figure 5.27: Fundamental harmonic shift with feedback strength with respect to frequency, inset shows peak frequency as a function of feedback strength

Moreover, 5 and a 10 m patch fiber cords were inserted into the 11.7 external cavity, which changed the round-trip frequency from 8.78 to 6 and 4.7 MHz, respectively as expected. The feedback level for the oscillations at 5 dB height was unchanged at -35 dB. With the addition of a 12.8 km fiber into the external cavity feedback branch, the feedback sensitivity in a

practical situation (10 km) may be investigated. Figure 5.28 presents the RIN spectrum measured under -20 dB of reflection from 12.8 km away for 1 mW of laser output power.

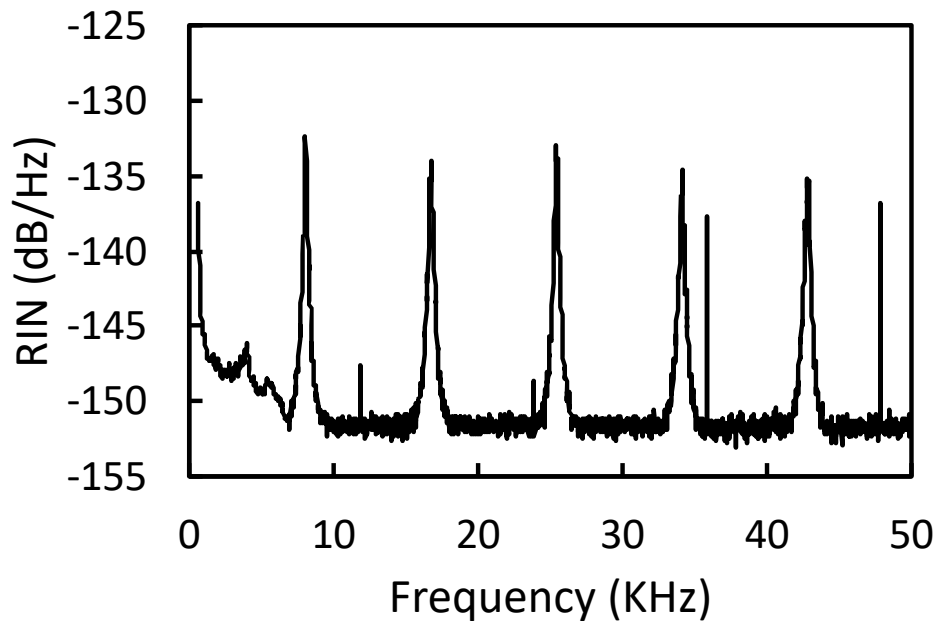


Figure 5.28: RIN spectrum under -20 dB of reflection from 12.8 km away for the short device at 25 C

It can be seen that the round-trip frequency is 8 kHz as expected ($1/\tau_{\text{round-trip}}$). Under this regime, external cavity peaks start appearing at -30 dB of reflection ($\sim 0.08\%$ R). As such, feedback sensitivity seems to be better by about 5 dB, which may be attributed to the attenuation by the external cavity keeping the external cavity modes below the ESA noise floor. Consequently, it may be assumed that feedback sensitivity is independent of length under the incoherent feedback regime (above 10 m here).

With regard to the investigation of the effects of external feedback on the optical spectrum, the laser is expected to exhibit spectral broadening, which is reported for QW lasers [14]. Figure 5.29 plots the optical spectra of the free running laser and under highest level of external feedback.

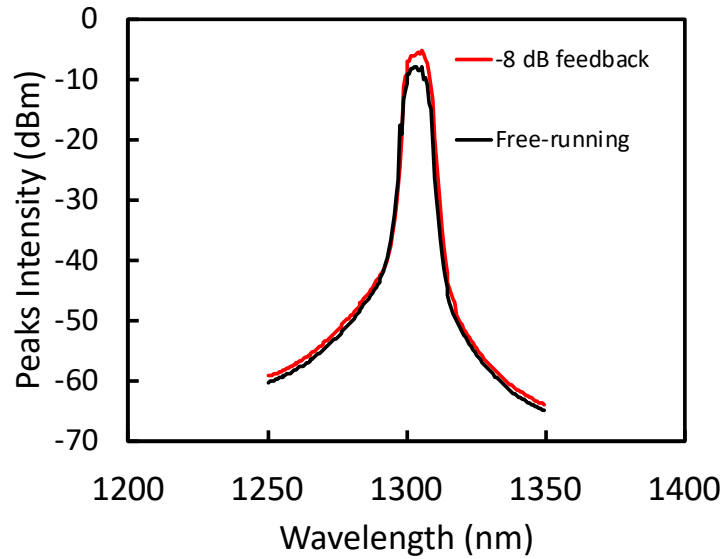


Figure 5.29: Optical spectra of the free running and subject to external feedback of the laser

The under-feedback spectrum exhibits a finite amount of higher emitted power under feedback as expected and although the OSA resolution is insufficient for resolving individual mode's broadening, with no significant difference in the measured envelope linewidth between the spectra.

Another effect on the optical spectrum to be investigated is on the individual F-P modes as the feedback is increased.

Figure. 5.30 plots the electroluminescence spectra as a function of wavelength with varying levels of feedback.

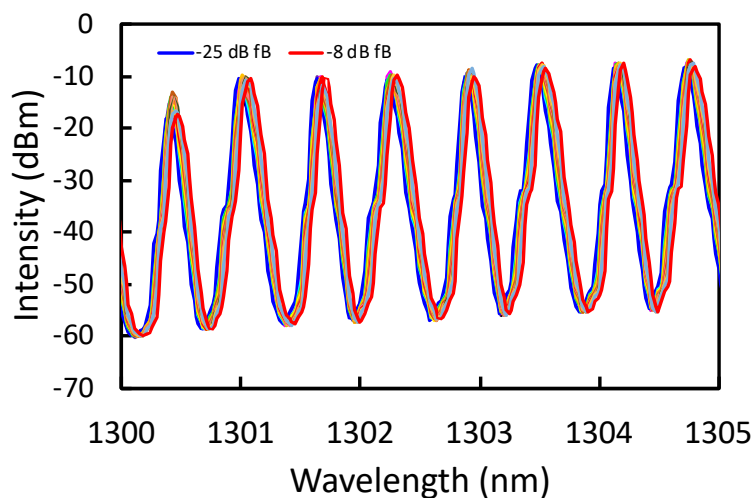


Figure 5.30: Effect of feedback on the modes in the optical spectra

It can be seen that the FP modes shift to longer wavelengths. Consequently, the Hakki-Paoli gain spectrum will also shift to longer wavelengths.

Figure 5.31 plots the shift of an individual F-P mode as the feedback strength is increased. A shift of 4 pm/dB can be deduced from the data presented in fig. 5.31.

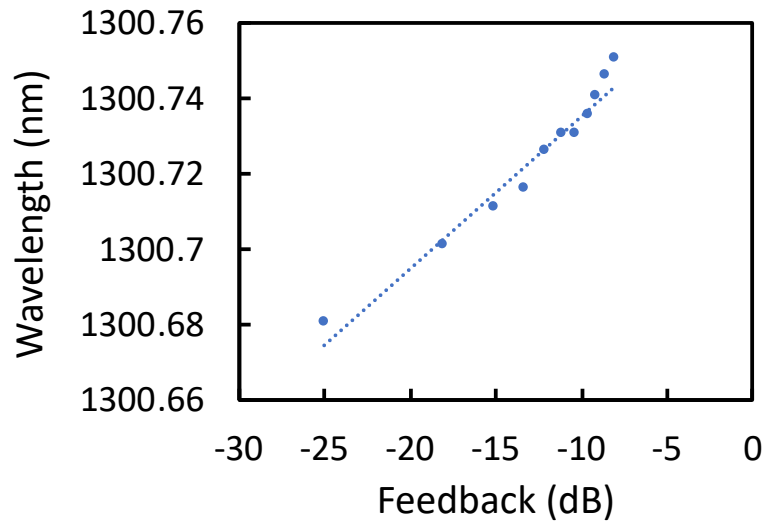


Figure 5.31: F-P mode wavelength shift as a function of feedback strength

Figure 5.32 plots the RIN_0 spectra (0.2 mW) of the 375- μm device vs frequency in the range of 0.0001 to 1 GHz at 25C under various levels of external optical feedback.

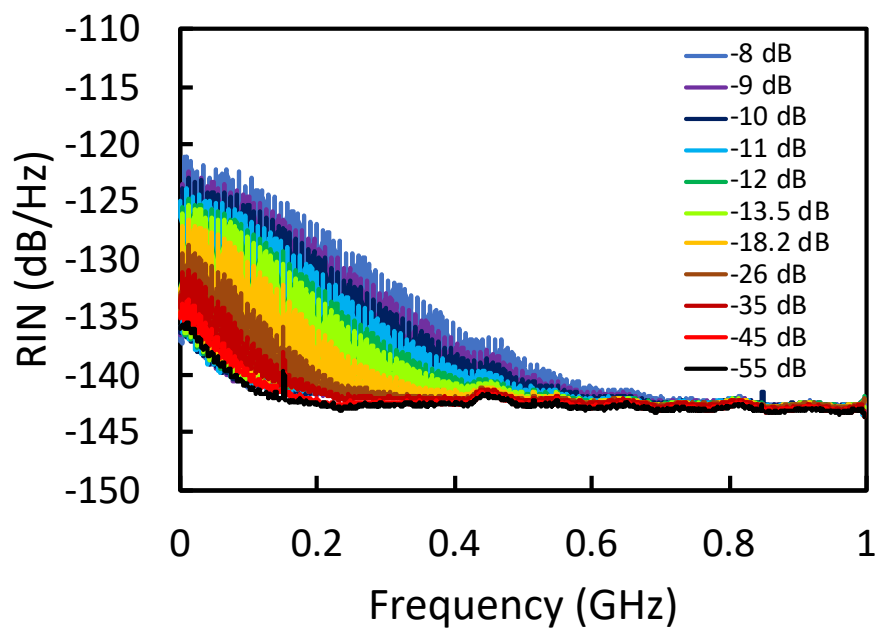


Figure 5.32: RIN_0 under various levels of external optical feedback as a function of frequency of the 375 μm device at 25C

As feedback strength is increased from -55 to -8 dB, the round-trip oscillations of the external cavity increase above the free running case (-55 dB). Furthermore, the frequency range of the harmonics increases with increasing feedback strength. Maximum RIN enhancement due to feedback occurs around fundamental harmonic at 8.8 MHz and decays down to the noise floor at around 700 MHz. The features at 800 and 850 MHz may be attributed to the mobile broadband services [41].

Figure 5.33 provides, for the purpose of clarity, the data presented in fig. 5.32 in a 3-D format so that the rise of the external cavity modes above the free running case at -55 dB of feedback may be better viewed.

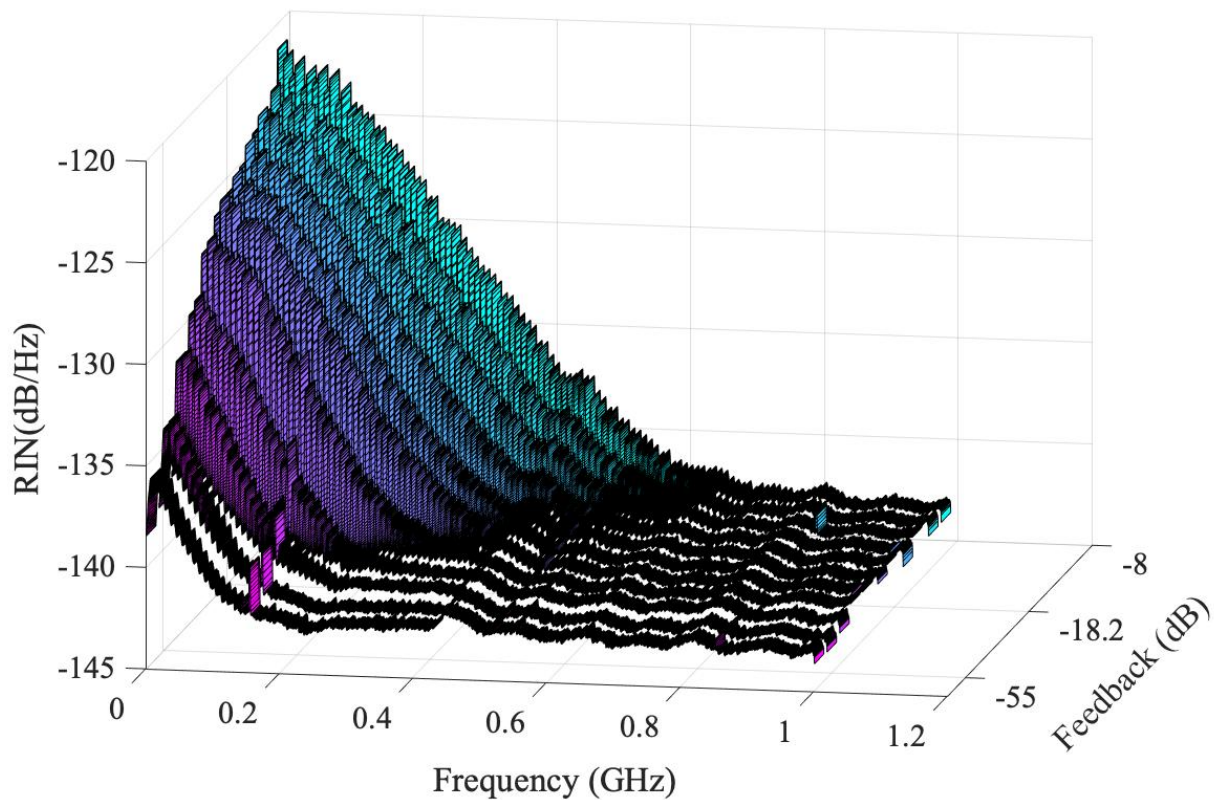


Figure 5.33: RIN_0 under various levels of external optical feedback as a function of frequency of the 375 μm device at 25C with and ER of 6 feedback strength is on the z axis

The RIN at 8.8 MHz and also the integrated RIN over 0.75 of the bandwidth is calculated and plotted in fig. 5.34 for comparison.

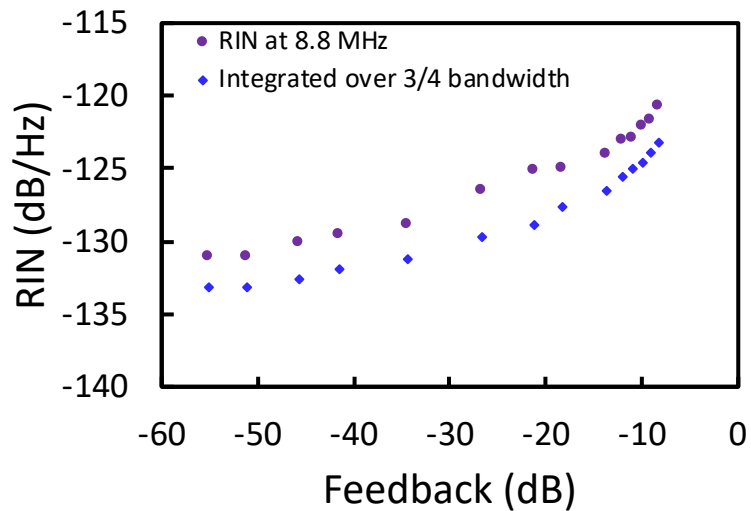


Figure 5.34: Peak RIN and the integrated amount over $\frac{3}{4}$ of bandwidth for the 375 μm device at 25C with an ER of 6 dB

The integrated RIN is lower than the peak RIN by ~ 2 dB. The IEEE 802.3ah specification sets the maximum allowable amount of RIN for a 2.5 Gbps link under -12 dB of reflection at -113 dB/Hz.

Similarly, figure 5.35 plots the RIN_0 spectra (0.2 mW) of the 750- μm device vs frequency in the range of 0.0001 to 1 GHz at 25 C under various levels of external optical feedback.

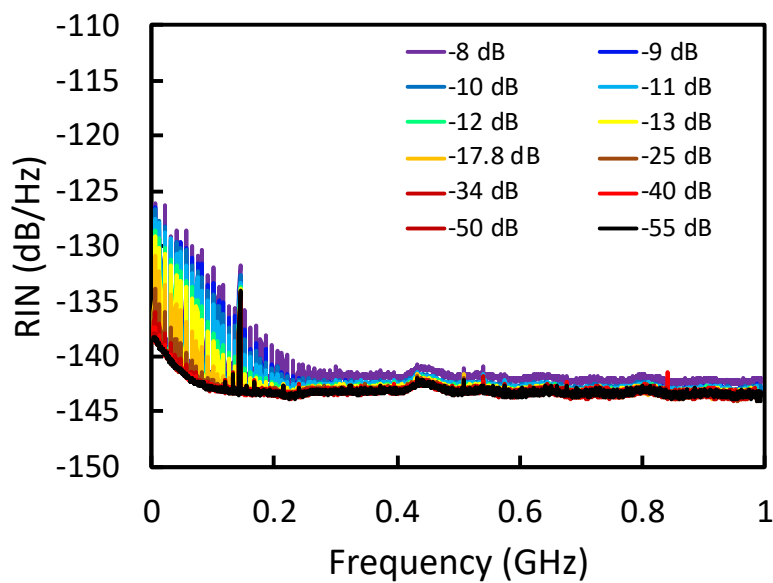


Figure 5.35: RIN_0 under of feedback as a function of frequency of the 750 μm device at 25C

Accordingly, the peak RIN and also the integrated RIN over 3/4 of the bandwidth is calculated and plotted in fig. 5.36 below for comparison.

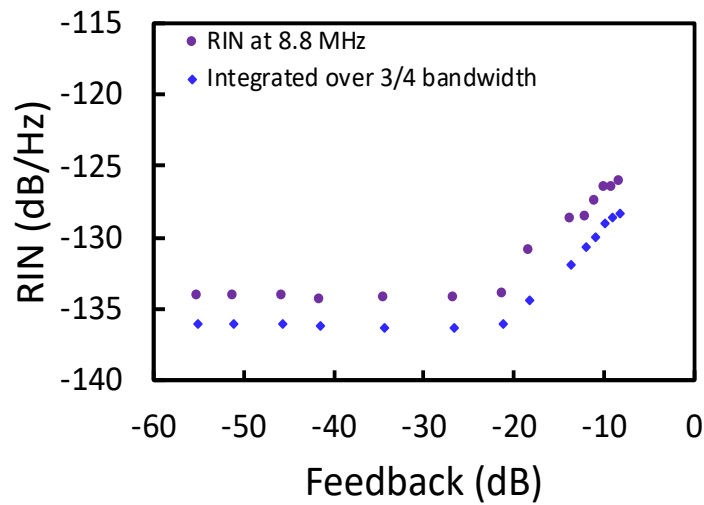


Figure 5.36: Peak RIN and the integrated RIN over $\frac{3}{4}$ of bandwidth for the 750 μm device at 25C

It can be observed from figure 5.38 that RF power scales with feedback strength above -20 dB of reflection. It should also be noted that the oscillation peaks below ESA noise floor cannot be resolved, as such data presented in fig. 5.36 less than -20 dB worth of feedback is essentially showing the noise floor.

The integrated RIN_0 over $\frac{3}{4}$ of the bandwidth as a function of temperature for both device lengths at -12 dB of reflection is consequently presented in figure 5.37.

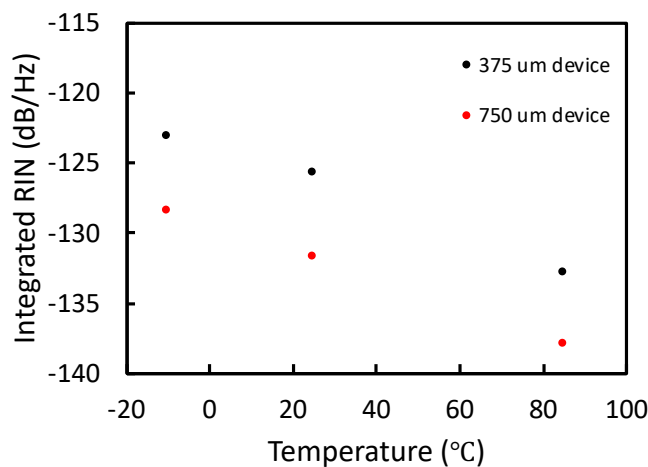


Figure 5.37: The integrated amount over $\frac{3}{4}$ of bandwidth for the 375 and 750 μm devices at the mount temperature range of measurement

It can be concluded from Fig. 5.37 that the increase in total integrated RIN induced by optical feedback is at least 10 dB under the limit of -113 dB/Hz in the worst case and thus both devices meet the specification at the temperature range of measurement for a 2.5 Gbps link.

Although a clear route to chaos is not observed in the presented results, if the threshold for instability is assumed to be a 5 dB level increase in the external cavity peaks above the free-running case, from fig. 5.36 it can be inferred that the short laser exhibits a threshold of -25 dB (0.03 % R). Including the chip to fiber coupling loss of 25.8 % (total of -12 dB of back reflection), this is -47 dB in total (i.e. chip to chip). From fig. 5.38, it can be seen that, the long laser shows a threshold of -15 dB (0.3 % R). This is -33 dB for chip to chip in total considering the chip to fiber coupling. This difference may be attributed to the overall higher amount of noise reflected back into the HR/HR coated shorter device.

As mentioned before, the decrease in sensitivity at low powers is due to the external cavity peaks being below the ESA noise floor. Therefore, it can be inferred from presented data that the critical feedback strength is independent (or weakly dependent) on the output power contrary to what the literature suggested [13, 14].

5.7 Discussion

As far as the free running results are concerned, in comparison with some landmark results, a D-factor of 0.66 GHz / mA^{1/2} was reported in [3] and 2.2 GHz / mA^{1/2} in [22] but the latter is only considered for the two of the lowest drive current points, the total D-factor can be calculated and is 0.33 GHz / mA^{1/2}. In [42] a D-factor value of 0.1 GHz / mA^{1/2} at room temperature was reported to correspond to a differential gain value of 11.1 cm² which is 10 times larger than previously reported in [43]. Consequently, with a D-factor value of 1.99 GHz / mA^{1/2} measured at 25 C in my device, it can be inferred that the differential gain in the measured device here is at least 20 times larger than reported in [43].

On the other hand, K-factor of 0.82 ns was reported in p-doped QD lasers [44], [45] and estimated at 0.5–0.6 ns in p-doped tunnel-junction QD lasers in the 1.3 μm range [46]. A K-factor of 1.3 ns at 25 C was reported in [3] which agrees with the K-factor of 1.16 ns found here at 25 C as the QDs were grown in a very similar way. This higher K-factor can be

attributed to the slightly lower uniformity and areal density of the dots in [3] resulting in higher damping. These large K-factor values of QD lasers, which are about 2–3 times the values of optimized InP-based multiple QW lasers [47], [48], are attributed to the highly damped frequency response which precipitates a low modulation bandwidth [49] as demonstrated in the measurement section. Consequently, it can be deduced that the maximum bandwidth of QD lasers is fundamentally limited by the K-factor. The maximum modulation bandwidth limited by the K factor is 8 GHz, which is lower than the measured f_{ro} limited 11.8 GHz at 1.2 mW in fig. 5.17. This narrower measured bandwidth is due to the saturation of the relaxation frequency at high drive currents, which is attributed to the delayed carrier relaxation in QD lasers.

With respect to the measurements under external optical feedback, the noise spectrum rises immediately from the top of the free-running spectrum in Fig. 5.26. In QW lasers on the other hand, the feedback spectrum is positioned at least 5 dB above the weak feedback spectrum [28] which adds to RIN enhancement under feedback. Furthermore, the RIN values of the QD lasers at the highest level of feedback (-8 dB) correspond with QW lasers values at nearly 20 dB weaker feedback levels.

Interestingly, the devices under investigation here do not exhibit a clear route to chaos. Instead, the dynamics evolve from a stable solution to periodic oscillations without any chaotic pulsations, irrespective of the feedback level. Conversely, it has been estimated that the threshold is between -40 to -30 dB for the heterogeneously integrated QW lasers studied in [28], which agrees with previous reports of traditional III-V QW lasers [14]. Contrariwise, it is more difficult to estimate this for the QD lasers here as the RIN increase is much smaller. Previously, QD lasers emitting at 1.3 μm were reported to demonstrate coherence collapse at -14 and -8 dB of external feedback ratio, for a 300 μm HR/HR coated DFB laser and a 1500 μm as-cleaved Fabry–Pérot laser, respectively [50, 11]. Coherence collapse is not observed in the QD lasers studied here attributed to the high areal density and uniformity of these state-of-the-art material providing high differential gain. Since the linewidth enhancement factor, which is also a measure of feedback sensitivity of lasers as explained in eqn. 5.6, is inversely proportional to the differential gain a much lower coupling between the carrier and photon densities occurs that precipitates a lower enhancement of the intensity noise under external feedback. Additionally, eqn. 5.6 also predicts a lack of coherence collapse given the LEF approaches zero, which is the case here.

It must also be noted that, as the RIN under feedback is investigated above threshold, subtle effects such as gain compression are expected to increase the LEF as explained in chapter 3. Therefore, in order to investigate the possibility of coherence collapse, a more precise determination may be made by examining the high-resolution optical spectra for the occurrence of satellite modes appearing at multiples of the relaxation oscillation frequency away from the main lasing mode [51] to further analyze the possibility of coherence collapse. However, I am limited in the pursuit of this endeavor by my current setup and the resolution available on the optical spectrum analyzer.

5.8 Conclusions

The dynamic characteristics of the In(Ga)As/GaAs QD lasers were investigated through the parasitic free RIN measurement of the free running laser before studying the reflection sensitivity of the devices under various levels of external optical feedback. Investigation of the RO frequency and the damping rate allowed for the extraction of the dynamic parameters of K-factor and D-factor. The damping limited bandwidth was 15 GHz at -10 °C and reduced with increasing temperature to 6 GHz at 85 °C, which may be attributed to carrier thermalization to higher states whereby they are more likely to recombine non-radiatively in QDs [40]. The modulation efficiency (D-factor) is 2 GHz/mA^{1/2} at -10 °C and decreases with increasing temperature to 1.3 GHz/mA^{1/2} at 85 °C. The relatively higher values of D-factor correspond to the high differential gain provided by the high uniformity of this QD material.

Compared to quantum wells, these quantum dot lasers demonstrated nearly 30 dB reduction in sensitivity to back reflection alongside maintaining low levels of RIN over the full feedback range. My results demonstrate the prospects of isolator free operation of quantum dot lasers for future photonics systems where back reflections must be inhibited particularly in fiber telecommunication which along with the prospects of running the devices cooler-free in a transmission system would prove beneficial in terms of lowering system complexity, power penalty, and the end cost of the total system considerably.

5.9 Future work

It would be very interesting to investigate the dynamic properties of the same QD active material incorporated in a DFB laser, since as mentioned in chapter 3, the inclusion of the Bragg grating along the whole of the cavity improves the laser performance in terms of spontaneous emission noise. On the other hand, the devices studied here were HR/HR coated and consisted of 8 stacks of QD layers. Using a laser with higher number of stacks is expected to improve gain, which would further decrease the LEF thereby making the devices even more resilient towards external optical feedback.

On the other hand, it would be desirable to simultaneously record the optical spectrum with the incorporation of a high resolution OSA in the detection path using a beam splitter before the lightwave converter.

As previously mentioned, there was no low noise reference source available at the time of measurement. LNRL calibration method could be employed using e.g. an erbium doped fiber amplifier (EDFA) with a known noise characteristic. Extraction of RIN spectra will be streamlined as the system response is recorded using the LNR source (EDFA) and the total noise spectrum is then corrected for laser noise only by subtracting the system response. This will be much quicker than the subtraction method where every noise source and component response is accounted for individually for correction, but is expected to be less accurate comparatively.

References

- [1]: A. Yariv, P. Yeh “Photonics: Optical Electronics in Modern Communications” 6th edition, Oxford University Press, New York, p.499, 2007
- [2]: IEEE Standard 802.3ah: Amendment to IEEE Std. 802.3-2004 as amended by IEEE Stds. 802.3ae-2002, 802.3af-2002, 802.3aj-2003 and 802.3ak-2004
- [3]: Ishida M, Hatori N, Akiyama T, Otsubo K, Nakata Y, Ebe H, Sugawara M, Arakawa Y,” Photon lifetime dependence of modulation efficiency and K factor in 1.3 μm self-assembled InAs/GaAs quantum-dot lasers: Impact of capture time and maximum modal gain on modulation bandwidth”, Appl. Phys Lett, 85 p. 4145, 2004
- [4]: Y. Arakawa and H. Sakaki, “Multidimensional quantum well laser and temperature dependence of its threshold current,” Appl. Phys. Lett., Vol. 40, No. 11, Mar. 1982, 939-941.
- [5]: H.Y. Liu et. al., “High-performance three-layer 1.3 μm InAs–GaAs quantum-dot lasers with very low continuous-wave room-temperature threshold currents,” IEEE Photon. Tech. Lett., 17, no. 6, Jun. 2005, 1139-1141.
- [6]: S. Fathpour et. al., “The role of Auger recombination in the temperature-dependent output characteristics ($T_0=\infty$) of p-doped 1.3 μm quantum dot lasers,” Appl. Phys. Lett., 85, no. 29, Nov. 2004, 5164-5166.
- [7]: T.C. Newell et. al., “Gain and Linewidth Enhancement Factor in InAs Quantum-Dot Laser Diodes,” IEEE Photon. Tech. Lett., 11, no. 12, Dec. 1999, 1527-1529.
- [8]: D. Bimberg et. al, “InGaAs-GaAs quantum-dot lasers,” IEEE J. Sel. Topics Quantum Electron., 3, no. 2, Apr. 1997, 196–205.
- [9]: R. Hui and M. O’Sullivan, Fiber Optic Measurement Techniques, Academic Press, Boston, USA, p. 259–363, 2009
- [10]: L. A. Coldren and S. W. Corzine, “Diode lasers and photonic integrated circuits,” 2nd edition, Willey, 1995
- [11]: D. O'Brien, S. P. Hegarty, G. Huyet, J. G. McInerney, T. Kettler, M. Laemmlin, D. Bimberg, V. M. Ustinov, A. E. Zhukov, S. S. Mikhlin and A. R. Kovsh, “Feedback sensitivity of 1.3 μm InAs/GaAs quantum dot lasers,” Elect. Letts., vol. 39, no. 25, pp. 1819- 1820, 2003.
- [12]: J. Wang and K. Petermann, “Noise analysis of semiconductor lasers within the coherence collapse regime,” IEEE J. Quantum Electron. 27, 3–9, 1991
- [13]: H.Helms and K.Petermann, “A simple analytic expression for the stable operation range of laser diodes with optical feedback,” IEEE J. Quantum Electron., vol. 26, pp. 833-836, 1990

- [14]: K. Petermann, "External optical feedback phenomena in semiconductor lasers," *IEEE J. Sel. Top. Quantum Electron.* 1, pp. 480–489, 1995
- [15]: P. Resneau, M. Calligaro, S. Bansropun, O. Parillaud, M. Krakowski, R. Schwertberger, A. Somers, J. P. Reithmaier, and A. Forchel, "High power, very low noise and long term ageing 1.55 μm InP-based Fabry-Perot quantum dash lasers under CW operation," in *Conf. Lasers Electro-Opt.* pp. 1805–1807, 2005
- [16] M. Krakowski, P. Renseau, M. Calligaro, H. Liu, and M. Hopkinson, "High power, very low noise, CW operation of 1.32 μm quantum-dot Fabry-Perot laser diodes," presented at the presented at the 20th IEEE Int. Semicond. Laser Conf., Kohala Coast, HI, Paper TuC4.
- [17]: A. Capua, L. Rozenfeld, V. Mikhelashvili, G. Eisenstein, M. Kuntz, M. Laemmlin, and D. Bimberg, "Direct correlation between a highly damped modulation response and ultra low relative intensity noise in an InAs–GaAs quantum dot laser," *Opt. Exp.*, vol. 15, pp. 5388–5393, 2007.
- [18]: A. Martinez, K. Merghem, S. Bouchoule, G. Moreau, A. Ramdane, J.-G. Provost, F. Alexandre, F. Grillot, O. Dehaese, R. Piron, and S. Loualiche, "Dynamic properties of InAs–InP (311)B quantum dot Fabry-Perot lasers emitting at 1.52 μm ," *Appl. Phys. Lett.*, vol. 93, p. 021101, 2008.
- [19]: F. Lelarge et al., "Recent advances on InAs/InP quantum dash based semiconductor lasers and optical amplifiers operating at 1.55 μm ," *IEEE J. Sel. Topics Quantum Electron.*, vol. 13, no. 1, pp. 111–124, Jan./Feb. 2007.
- [20]: A. Kovsh, "Quantum-dot comb laser with low relative-intensity noise for each mode," *SPIE Newsroom*, Jun. 2008
- [21]: Y.-G. Zhou, C. Zhou, C.-F. Cao, J.-B. Du, Q. Gong, and C. Wang, "Relative intensity noise of InAs quantum dot lasers epitaxially grown on Ge," *Opt. Express*, vol. 25, no. 23, pp. 28817–28824, 2017.
- [22]: G. Lin, H.-L. Tang, H.-C. Cheng, and H.-L. Chen, "Analysis of relative intensity noise spectra for uniformly and chirpily stacked InAs–InGaAs–GaAs quantum dot lasers," *J. Lightw. Technol.*, vol. 30, no. 3, pp. 331–336, Feb. 1, 2012.
- [23]: J. Duan, X. Wang, Y. Zhou, C. Wang and F. Grillot, "Carrier-Noise-Enhanced Relative Intensity Noise of Quantum Dot Lasers," in *IEEE Journal of Quantum Electronics*, vol. 54, no. 6, pp. 1-7, 2018
- [24]: G. Huyet et. al, "Quantum dot semiconductor lasers with optical feedback," *Phys. Stat. Sol.* 201, no. 2, Jan. 2004, 345–352.

- [25]: A.V. Uskov et al., “Theory of a self-assembled quantum-dot semiconductor laser with Auger carrier capture: quantum efficiency and nonlinear gain”, *Appl. Phys. Lett.*, 73, no. 11, Sep. 1998, 1499–1501
- [26]: H. Huang, D. Arsenijević, K. Schires, T. Sadeev, D. Bimberg, F. Grillot, “Multimode optical feedback dynamics of InAs/GaAs quantum-dot lasers emitting on different lasing states”, *J AIP Advances*, 125114, V 6, N 12, 2016
- [27]: H. Huang K. Schires, F. Grillot, D. Arsenijević, T. Sadeev, D. Bimberg, “InAs/GaAs excited state quantum-dot transmitters operating under long-delayed optical feedback” *SPIE Photonics Europe*, 9892, 2016
- [28]: A. Y. Liu, T. Komljenovic, M. L. Davenport, A. C. Gossard, and J. E. Bowers, “Reflection sensitivity of 1.3 μm quantum dot lasers epitaxially grown on silicon,” *Opt. Express*, vol. 25, no. 9, pp. 9535–9543, 2017
- [29]: Cisco GPON SFP Datasheet, April 25, 2016, document ID:1461606040226191
- [30]: “Lightwave signal analyzers measure relative intensity noise,” Product Note 71400-1, Agilent Technologies, 2000
- [31]: “Digital Communication Analyzer (DCA), Measure Relative Intensity Noise (RIN)”, Keysight Technologies, application note, no number, 2014
- [32]: L. A. Coldren and S. W. Corzine, “Diode lasers and photonic integrated circuits,” 2nd edition, Wiley, pp. 301, 1995
- [32]: C. M. Miller and L. F. Stokes, “Measurement of laser diode intensity noise below the shot noise limit”, Boulder, CO: NIST Symp. on Optical Fiber Measurements, 1990
- [33]: J. Poette, P. Besnard, L. Bramerie and J. Simon, “Highly-sensitive measurement technique of relative intensity noise and laser characterization”, *Proc. of SPIE*, Vol. 6603, 66031R-10, 2007
- [34]: C Otto, B Lingnau, E Schöll, and K Lüdge, “Manipulating coherence resonance in a quantum dot semiconductor laser via electrical pumping”, *Optics Express* Vol. 22, Issue 11, pp. 13288-13307, 2014
- [35]: “Spectrum Analysis Basics”, Keysight Technologies, application note 150, 2016
- [36]: “E4440A - User’s and Programmer’s Reference Volume 1 Core Spectrum Analyzer Functions PSA Series Spectrum Analyzers” Agilent Technologies, 2011
- [37]: J. Hayau, P. Besnard, O. Dehaese, F. Grillot, R. Piron, S. Loualiche, A. Martinez, K. Merghem, and A. Ramdane "Effect of the wetting layer on intensity noise in quantum dot laser," 2009 35th European Conference on Optical Communication, Vienna, pp. 1-2, 2009

- [38]: L. A. Coldren and S. W. Corzine, “Diode lasers and photonic integrated circuits,” 2nd edition, Wiley, pp. 201, 1995
- [39]: L. A. Coldren and S. W. Corzine, “Diode lasers and photonic integrated circuits,” 2nd edition, Wiley, pp. 263, 1995
- [40]: Y. Arakawa and H. Sakaki, “Multidimensional quantum well laser and temperature dependence of its threshold current,” *Appl. Phys. Letts.*, vol. 40, pp. 939-941, 1982
- [41]: Acquired from Ofcom on 20 April 2019 <https://www.ofcom.org.uk/spectrum/information/uk-fat>
- [42]: Zhao HX, Yoon SF, Tong CZ, Liu CY, Wang R, Cao Q. “Thermal Effects and Small Signal Modulation of 1.3- μm InAs/GaAs Self-Assembled Quantum-Dot Lasers”, *Nanoscale Res Lett.* 6(1):37, 2011
- [43]: Kuntz M, Ledentsov NN, Bimberg D, Kovsh AR, Ustinov VM, Zhukov AE, Shernyakov YM, “Spectrotemporal response of 1.3 μm quantum-dot lasers”, *Appl. Phys. Lett.* 81:3846, 2002
- [44]: K. Otsubo, N. Hatori, M. Ishida, S. Okumura, T. Akiyama, Y. Nakata, H. Ebe, M. Sugawara, and Y. Arakawa, “Temperature-insensitive eye- opening under 10-Gb/s modulation of 1.3- μm p-doped quantum-dot lasers without current adjustments,” *Jpn. J. Appl. Phys.*, vol. 43, pp. L1124–L1126, 2004
- [45]: A. Fiore and A. Markus, “Differential gain and gain compression in quantum-dot lasers,” *IEEE J. Quantum Electron.*, vol. 43, no. 4, pp. 287–294, 2007
- [46]: S. Fathpour, Z. Mi, and P. Bhattacharya, “High-speed quantum dot lasers,” *J. Phys. D*, vol. 38, pp. 2103–2111, 2005
- [47]: H. Lu, C. Blaauw, B. Benyon, G. P. Li, and T. Makino, “High-power and high-speed performance of 1.3- μm strained MQW gain-coupled DFB lasers,” *IEEE J. Sel. Topics Quantum Electron.*, vol. 1, no. 2, pp. 375–380, 1995
- [48]: T. Fukushima, R. Nagarajan, M. Ishikawa, and J. E. Bowers, “High- speed dynamics in InP based multiple quantum well lasers,” *Jpn. J. Appl. Phys.*, vol. 32, pp. 70–83, 1993
- [49]: M. Ishida, Y. Tanaka, K Takada, T. Yamamoto, H.Z. Song, Y. Nakata, M. Yamaguchi, K. Nishi, M. Sugawara, and Y. Arakawa, “Effect of carrier transport on modulation bandwidth of 1.3- μm InAs–GaAs self-assembled quantum-dot lasers,” in *Proc. 22th IEEE Int. Semicond. Laser Conf.* pp. 174–175, 2010
- [50]: H. Su, L. Zhang, A. L. Gray, R. Wang, T. C. Newell, K. Malloy, and L. F. Lester, “High external feedback resistance of laterally loss-coupled distributed feedback quantum dot semiconductor lasers,” *IEEE Photon. Technol. Lett.*, vol. 15, no. 11, pp. 1504–1506, Nov. 2003

[51]: R. Tkach and A. Chraplyvy, "Regimes of feedback effects in 1.5- μm distributed feedback lasers," *J. Lightwave Technol.* 4, 1655–1661, 1986

Chapter 6

Summary and Future Work

This chapter provides a brief account of the conclusions and future works from each experimental chapter in order to conclusively expand understanding of the results carried out to improve the performance of QD material, enable future device optimization, and to outline possible continuation to this work.

6.1 Summary

This thesis was predicated upon the empirical analysis of the static and dynamic performance of the state-of-the-art In(Ga)As/GaAs QD material for the purposes of better understanding the physical mechanisms behind their operation so as to advance the next generation of lasers, detectors, and modulator devices.

The key consequences of 3-D confinement of carriers in QDs include a delta function like density of states which regulates the gain and absorption spectra. Though, inhomogeneous broadening acts to broaden the delta-functions attributed to the QDs shape and size dispersion, QDs are still useful in obtaining a number of technological advantages over the higher dimensional quantum confined structures.

It has been simulated previously [1], that due to the gaussian nature of the absorption spectrum in QDs, they can be utilized in a novel modulation scheme whereby blue or negative wavelength chirping can be obtained on the modulated signals. In order to investigate the viability of such an electro absorption modulator preliminary, in Chapter 2, the optical absorption properties of the 1.3 μm QDs incorporated in mesa diodes were studied using photocurrent (PC) spectroscopy. The peak intensity and shift of the energy states have been

contrasted against quantum well reports in the literature. The comparison of QDs shift of PC peaks investigated in this work to a number of QW absorption reports showed that the QDs maintain a high peak absorption up to high E-fields (close to breakdown), and exhibit a lower Stark-shift as compared to their QW counterparts. This is attributed to the strong carrier localization in QDs. The absorption was shown to remain strong until impact ionization effects (in the GaAs intrinsic region) occur above 15V (340 kV/cm). Then I went on to discuss possible applications in which such properties may be exploited for absorption-based devices. Thus, prospects for employment in an EAM with potential of producing blue chirp under modulation were initially studied. And also, potential application for a separate amplification and multiplication SAM-APD with a relatively low dark current and a reasonable avalanche multiplication gain were investigated.

Another consequence of discrete energy level in QDs is the fact that gain spectrum shows a symmetric (Gaussian) shape as compared to the jagged (step-like) shape from QWs. This will cause a no-changing refractive index at the gain peak which is expected to result in very small linewidth enhancement factor (LEF). In chapter 3, the corresponding gain spectra of the same active material incorporated in Fabry-Perot lasers were measured, using Hakki-Paoli method, in order to investigate the LEF at different ambient temperatures. To correctly measure the LEF, only the carrier related modal shift in wavelength was required. A temperature correction technique was utilized to remove the thermal related wavelength shift yielding the measurement of solely the carrier-related LEF. Additionally, Hakki-Paoli method enables employment of a constant junction temperature method to account for the temperature increase as current density is increased.

An imprint of the fluctuations in the laser RMS linewidth with increasing current above threshold was seen for the first time in the corrected modal shift of the QD devices. This correlation can be attributed to spectral hole burning in the lasing mode and a certain degree of non-ideal carrier clamping above threshold varying the inhomogeneous linewidth in an oscillatory manner. These oscillations were moderated via the constant junction temperature method but still visibly persist.

Ultimately, LEF of QD lasers has been calculated from measured data at a range of temperatures. Findings of this chapter demonstrated for the first time essentially zero spectral and current dependent LEF values over all positive net modal gain region of the devices at the

full temperature range of -10 to 85 °C, which goes beyond the commercial window as specified in guidelines [2].

It is noteworthy that the smallest LEF results, utilizing the same experimental method, were previously reported in [3] which studied the effect of p-doping in QD laser dynamics, and the results here are an order of magnitude smaller, attributed to the higher differential gain. As chirp is directly proportional to the LEF, these findings bode well for employment in a pre-chirp managed optical telecommunication system.

In chapter 4, utilizing the findings of chapter 2 and 3 of the optical gain and absorption spectra, the viability of a novel integrated common QD-active layer DFB-EML was examined. It was shown that different EML operation arrangements could be exploited depending upon the chosen detuning wavelength from gain peak. Possibility of conventional EML operation was shown which is accompanied by the anticipated positive chirp, though not needing signal amplification. Operation of the DFB in the blue-detuning regime would enable novel EML operation with blue-chirp modulated signals. In this mode of operation, the insertion losses could be compensated for using an SOA section. This chapter's experimental results underscore the prospects of GaAs-based QD devices for a negative-chirp common active-layer DFB-EMLs at 1.3 μm as an alternative to the InP platform and also QW counterparts.

Since the critical coherence collapse due to external optical feedback into a semiconductor laser is inversely proportional to the fourth power of its α -H parameter, when LEF is small [4], the presented QD lasers, with essentially zero-LEF values, are expected to demonstrated a high resilience towards external optical feedback. This fact served as a strong motivation to not only investigate the free-running relative intensity noise (RIN) characteristics of these QD lasers, but also to consider RIN spectra of the laser subject to varying levels of external optical feedback.

In chapter 6, The dynamic characteristics of the QD lasers were examined via the parasitic free RIN measurement of the free running laser before studying the reflection sensitivity of the devices under various levels of external optical feedback all performed at a range of temperatures. Investigation of the RO frequency versus incremental current as well as the damping rate as a function of the RO frequency resolved the dynamic parameters of K-factor and D-factor, respectively where device modulation parameters are extracted within. The K-

factor limited bandwidth was at 15 GHz at -10 °C and reduces with increase in temperature to 6 GHz at 85 C attributed to carrier thermalization to higher states where they are more likely to recombine non-radiatively in QDs [5]. The extracted D-factor starts at 2 GHz/mA^{1/2} and decreases with increase in temperature to 1.3 GHz/mA^{1/2} at 85 C. The relatively higher values of D-factor correspond to the high differential gain provided by the state-of-the-art QD material.

Compared to QWs, these QD lasers demonstrated nearly 30 dB reduction in sensitivity to back reflection alongside maintaining low levels of RIN over the full feedback range. My results demonstrate the prospects of isolator free operation of quantum dot lasers for future photonics systems where back reflections must be inhibited particularly in fiber telecommunication which along with the prospects of running the devices cooler-free in a transmission system would prove beneficial in terms of lowering system complexity, power penalty, and the end cost of the total system considerably.

The advantages of using QDs as active material for optical telecommunications are the ultra-low and temperature insensitive threshold current, the zero or very small values of LEF, negative-chirp under modulation, and potential tolerance to external optical feedback. These benefits were investigated and confirmed. Considering the results, the QD devices can be incorporated in telecommunication systems with a cooler-free packaging, as pre-chirp managed systems, and most importantly without the need for complicated isolator circuitry to inhibit reflections back into the laser. These benefits will reduce the complexity of the final packaged device, thus reducing the footprint and ultimately bring the cost down.

6.2 Future works

In the absorption study of the photocurrent spectroscopy in chapter 2, it was shown that there is a finite amount of absorption half-way between the GS and ES1 which goes against the predicted transparent regions expected to result from the discrete energy levels. Therefore, growth optimization with the purpose of alleviating this characteristic could significantly improve the ER particularly for the novel EAM configuration scheme. Also conducting this absorption study under different temperatures could provide valuable information particularly about the dark current. It would also be interesting to drive these devices above the breakdown

limit in a pulsed manner to investigate the increase in the multiplication factor for photodetection purposes.

From the study of LEF in chapter 3, investigating the trade-offs involved in a dynamic operation, e.g., under modulation and above threshold would be a desirable extension. Additionally, as shown in Fig 3.21, differential gain decreases with increasing temperature due to hot carrier effects. This causes an increase in the LEF which is not readily observable in the results presented here at 85 °C, this is because the final values are very close to zero. It would be attractive to investigate these QD devices LEF performance at higher temperatures as there is interest for these devices to operate in harsh environments often under high temperatures.

Regarding the proposed device in chapter 4, optimizing the structure considering the findings outlined in this chapter in order to realize the proposed device epitaxially is expected to be rewarding. With respect to device geometry, in order to operate at the blue-detuning regime for blue chirp, an EAM section length of 950 μm is expected to provide an ER of 10 dB at 15-20 Gbps. With respect to temperature control, from fig. 5, at 25 °C the absorption peak is on the blue-side of the DFB's Bragg wavelength.

As temperature increases, the absorption shifts to lower energies. Because of the initial detuning of the absorption edge relative to the gain band, for a medium range of temperatures (i.e. 25 - 65 °C \sim 12 meV), the device's ER decreases from 10 to 6.4 dB (i.e. from λ_{Center} to λ_{Red} , for a device length of 800 μm). However, IL remains largely the same (i.e. from -0.3 to -0.5 dB, for a device length of 800 μm).

On the other hand, as technology matures, the QD areal density and also uniformity (inhomogeneous broadening) are expected to improve, which would allow a reduction in device's length and increase the ER, respectively. Higher modulation bandwidth is also expected to be achieved following from the capacitance reduction argument above.

With respect to the RIN investigation in chapter 5, especially under external feedback, I was limited in accurately confirming the absence of coherence collapse attributed to the limited resolution of the OSA. It would be interesting to simultaneously acquire the optical spectrum using a high resolution OSA in the detection path via a beam splitter prior to the lightwave converter.

Additionally, with respect to device optimization considering high resilience against optical feedback, a number of configurations could be useful. Fabry-Perot lasers that have high facet reflectivity exhibit a uniform power distribution down the cavity and therefore spatial hole burning is negligible. Replacing the high reflectivity facets by distributed Bragg reflectors (DBR) with high KL would still maintain low spatial hole-burning as explained in chapter 5. Therefore DBR-lasers with high reflectivity mirrors are highly desirable that provide high tolerance against external optical feedback. Furthermore, gain-coupled or partly gain-coupled distributed feedback (DFB-lasers) exhibit a higher mode stability and less spatial hole burning compared to pure index-coupled devices. Therefore, high KL-gain coupled lasers should be viable given the scattering losses is sufficiently low for high quantum efficiency. Moreover, spatial hole-burning in index-coupled DFB-lasers can be mitigated by nonuniform current injection [6], through introducing multiple phase shifts or by weighted coupling. In particular, very small spatial hole burning is achieved when the coupling strength is small in the center of the device and increases toward the facets [7]. In such a device the reflectivity is concentrated close to the laser facets, so that it resembles a DBR-laser with its low spatial hole-burning. Thus DFB-lasers with weighted coupling, resembling a DBR-laser, are also interesting alternatives for high KL-devices with low feedback sensitivity.

Furthermore, with respect to the measurement, there was no low noise reference source available at the time of measurement. Low noise reference laser (LNRL) calibration method could be employed using e.g. an erbium doped fiber amplifier (EDFA) with a known noise rating. Extraction of RIN spectra will be streamlined as the system response is recorded using the LNR source (EDFA) and the total noise spectrum is then corrected for laser noise only by subtracting the system response. This will be much quicker than the subtraction method where every noise source and component response is accounted for individually for correction.

References

- [1]: R. Sahara, M. Matsuda, H. Shoji, K. Morito, and H. Soda, "Proposal for quantum dot electroabsorption modulator," *IEEE Photon. Tech. Lett.*, Vol. 8, No. 11, pp. 1477-1479, 1996
- [2]: Cisco GPON SFP Datasheet, April 25, 2016, document ID:1461606040226191
- [3]: R. Alexander, D. Childs, H. Agarwal, K. Groom, H.Y. Liu, M. Hopkinson, R.A. Hogg "Zero and Controllable Linewidth Enhancement Factor in p-Doped 1.3 μm Quantum Dot Lasers" in *Japanese Journal of Applied Physics*. 46. pp. 2421-2423, 2007
- [4]: K. Petermann, "External optical feedback phenomena in semiconductor lasers", *IEEE J Selected To. In Quantum Elect.*, Vol. 1, No. 2, 1995
- [5]: Y. Arakawa and H. Sakaki, "Multidimensional quantum well laser and temperature dependence of its threshold current," *Appl. Phys. Letts.*, vol. 40, pp. 939-941, 1982
- [6]: T. Kurosaki, T. Hirono, and M. Fukuda, "Distributed-feedback laser with a high endurance level against optical feedback," in *Proc. OFC '92*, San Jose, pp. 273-274, 1992
- [7]: G. Morthier, K. David, P. Vankwikelberge, and R. Baets, "A new DFB- laser diode with reduced spatial hole burning," *IEEE Photon. Technol. Len.*, vol. 2, no. 6, pp. 388-390, 1990

Appendix

A.1 Laser Theory

For the purpose of establishing the background to progress into the dynamic behavior of the laser in response to perturbation (e.g. current modulation, external feedback, etc.), and gaining an insight into the physics that relative intensity noise is predicated upon, this section will provide an explanation of laser operation from drive current to light output prior to providing the rate equations.

Starting with the carrier injection at a rate of I/q into the laser, where I is the injection current and q is the electron charge. From this carrier rate $\eta_i I/q$ reach the active region, where η_i is the injection (internal) efficiency of the laser. η_i is the fraction of current that produces carriers in the active region. After carriers arrive in the laser cavity, they have a number of possibilities. They can recombine non-radiatively or spontaneously at the rate of N/τ , where $N = R_{nr} + R_{sp}$ is the number of carriers. N/τ may be replaced by $AN + BN^2 + CN^3$. Where A , B , and C account for defect, spontaneous (R_{sp}), and Auger recombination rates, respectively. A fraction of this spontaneous emission then couples into the laser mode of interest at a rate of $\Gamma\beta_{sp}R_{sp}$. Where, Γ is the electron/photon overlap factor, better known as the confinement factor. This arises because the cavity volume occupied by photons is usually larger than the active region volume occupied by electrons. β_{sp} is the spontaneous emission factor, which quantifies the fraction of the coupled spontaneous emission into the lasing mode.

The rest of the carriers recombine through stimulated emission at the rate $v_g g N_p$, of which $\Gamma v_g g N_p$ emit or couple into the mode of interest. Where, N_p is number of photons, v_g is the group velocity of the mode of interest (lasing) considering material and waveguide dispersion, and g is the incremental material gain per unit length due to net generation and amplification of photons through stimulated emission. It should be noted that photons in other

modes can also encourage stimulated recombination of carriers. However, for relevance a single mode is investigated here.

Ultimately, photons in the cavity may be absorbed, which add to carrier density. Stimulated absorption in the active region depletes photons. It must be noted that the gain term, g , in the aforementioned $v_g g N_p$ expression consists of the stimulated emission photons excluding the stimulated absorption reducing photons density through the so-called gain compression factor, which will be discussed later-on when dealing with the differential analysis.

All other photons exit the cavity through one mirror at the rate N_p/τ_p . Where τ_p is the photon lifetime defined in eqn. A.4 below. Of those photons leaving the cavity, only $\eta_0 N_p / \tau_p$ leave through the desired mirror to be collected as useful output power, P_0 , where η_0 is the optical output efficiency of the laser whose product with the injection efficiency constitutes the differential quantum efficiency defined previously. The remainder of the photons exit the cavity via a different mirror or decay by either free carrier absorption in the active region (which does not increase the carrier density), absorption in materials outside the active region, or/and scattering at uneven surfaces [1].

With the above explanations in mind and by setting the rate of change of the carriers and photons, with respect to time, equal to the sum of rates into, minus the sum of rates out of the cavity and active region volumes occupied by photons and electrons, respectively, the rates of change of carrier and photon densities with respect to time can be written as:

$$\frac{dN}{dt} = \frac{\eta_i I}{qV} - \frac{N}{\tau} - v_g g N_p \quad \text{A.1}$$

$$\frac{dN_p}{dt} = \Gamma v_g g N_p + \Gamma \beta_{sp} R_{sp} - \frac{N_p}{\tau_p} \quad \text{A.2}$$

To finish the description above, the output power of the lasing mode can be expressed as:

$$P_0 = \eta_d h\nu \frac{N_p V_p}{\tau_p} \quad \text{A.3}$$

Where, $\eta_d = \eta_i \left[\frac{\alpha_m}{(\alpha_m + \alpha_i)} \right]$ is the optical efficiency, better known as the external differential quantum efficiency, which provides a measure of the conversion efficiency of injected carriers to photons out of the facets. α_m denotes the mirror losses and α_i arise from any internal losses within the cavity. And photon lifetime can be written as:

$$\tau_p^{-1} = v_g(\alpha_m + \alpha_i) \quad \text{A.4}$$

A.1.1 Steady-state solutions

The steady-state solutions of the rate equations, A.1 and A.2, are found by setting the time derivatives to zero. Solving eqn. A.1 for the DC current, and eqn. A.2 for the steady-state photon density:

$$I(N) = \frac{qV}{\eta_i l} \frac{N}{\tau} + v_g g(N) N_p(N) \quad \text{A.5}$$

$$N_p(N) = \frac{\Gamma \beta_{sp} R_{sp}}{\frac{1}{\tau_p} - \Gamma v_g g(N)} \quad \text{A.6}$$

A.1.2 Differential investigation of rate equations

In order to understand the dynamic behavior of lasers in response to a perturbation to the system e.g. current modulation, the time derivative of the density rate equations A.1 and A.2 need to be analyzed. However, apart from the steady-state solutions precise analytical explanations for the whole of the rate equations cannot be acquired. As a result, given the perturbations from the steady-state value are small, a small-signal analysis can be postulated so as to arrive at an approximate analytical solution.

In this sub-section, the rate equations will be investigated predicated on the assumption that dynamic changes in the photon and carrier densities far from their steady-state values are small. Consequently, small-signal responses due to one variable can be investigated in terms of a perturbation to another through solving the differential of the rate equations.

A set of two coupled rate equations is often formulated to analyze the laser's intrinsic dynamic behavior. One expression accounts for the carrier density in the active region, and the other considers the photon density of the lasing mode in the laser cavity. These rate equations are presented below. Considering I, N, N_p , and g , as dynamic variables, the differentials of eqn. A.5 and A.6 become:

$$d \left[\frac{dN}{dt} \right] = \frac{\eta_i}{qV} dI - \frac{1}{\tau_{\Delta N}} dN - v_g g dN_p - N_p v_g dg \quad \text{A.7}$$

$$d \left[\frac{dN_p}{dt} \right] = \left[\Gamma v_g g - 1/\tau_p \right] dN_p + \Gamma N_p v_g dg + \frac{\Gamma}{\tau'_{\Delta N}} dN \quad \text{A.8}$$

Where:

$$\frac{1}{\tau_{\Delta N}} = \frac{dR_{sp}}{dN} + \frac{dR_{nr}}{dN} \approx A + 2BN + 3CN^2 \quad \text{A.9}$$

$$\frac{1}{\tau'_{\Delta N}} = \frac{d\beta_{sp} R_{sp}}{dN} \approx 2\beta_{sp} BN + \frac{d\beta_{sp}}{dN} BN^2 \quad \text{A.10}$$

Considering R is the total carrier recombination rate (spontaneous + stimulated + nonradiative), the differential carrier lifetime, $\tau_{\Delta N}$, depends on the local gradient dR/dN . Conversely, the total carrier lifetime τ depends on the overall slope of R/N . The differential lifetime of carriers that radiate photons into the mode of interest (lasing mode), $\tau'_{\Delta N}$, is typically in the tens of microseconds range and is insignificant in most cases.

$\frac{1}{\tau'_{\Delta N}}$ may be further simplified when considering the largest possible value that it could reach [1]:

$$\frac{1}{\tau'_{\Delta N}} = \frac{v_g n_{sp}}{V_p} \frac{dg}{dN} \left[1 + \frac{g}{n_{sp}} \frac{dn_{sp}}{dg} \right] \quad \text{A.11}$$

Where n_{sp} , is the population inversion factor. Hence, the expression to the right of 1 in the brackets varies between -1 at transparency (pump condition at which photon of energy greater than that of the bandgap traverses the medium without getting absorbed) to 0 at infinite pump levels. Therefore, the expression reduces to the following inequality when considering the maximum possible value [1]:

$$\frac{1}{\tau'_{\Delta N}} \leq \frac{v_g n_{sp}}{v_p} \frac{dg}{dN} \quad \text{A.12}$$

dg , may be viewed in more detail considering it results from variations in photon and carrier densities:

$$dg = a dN - a_p dN_p \quad \text{A.13}$$

Where a and a_p are the gain derivatives from carrier and photon densities, respectively. Note that the negative sign is to reflect that the gain is increased with increasing carrier density and is decreased or compressed with increasing photon density.

A.1.3 Small-signal modulation

As mentioned in the previous section, through substitution of the time varying terms in the coupled rate equations with the first order Taylor expansion, the small signal modulation (SSM) response of eqn. A.5 and A.6 can be investigated in terms of perturbation of one to that of another. Subsequently in order to take the small-signal modulation responses carrier and photon densities to a sinusoidal current modulation $dI(t)$, the following substitutions are made:

$$dI(t) = I_1 e^{j\omega t} \quad \text{A.14}$$

$$dN(t) = N_1 e^{j\omega t} \quad \text{A.15}$$

$$dN_p(t) = N_{p1} e^{j\omega t} \quad \text{A.16}$$

Where I_1 , N_1 and N_{p1} , are the steady state values. d/dt will be substituted by $j\omega$ in order to take the small-signal carrier and photon densities in terms of a sinusoidal current modulation. Substituting for N_1 and N_{p1} and manipulating the rate equations to eliminate dN and dN_p yields a second-order equation after applying Cramer's rule [1]. The small-signal solutions are often given in terms of a transfer function, $H(\omega)$:

$$N_1 = \frac{\eta_i I_1}{qV} \cdot \frac{\gamma_{PP} + j\omega}{\omega_R^2} H(\omega) \quad \text{A.17}$$

$$N_{p1} = \frac{\eta_i I_1}{qV} \cdot \frac{\gamma_{PN}}{\omega_R^2} H(\omega) \quad \text{A.18}$$

Where the transfer function describes the small-signal modulation response in terms of two parameters:

$$H(\omega) = \frac{\omega_R^2}{\omega_R^2 - \omega^2 + j\omega\gamma} \quad \text{A.19}$$

Where, ω_R is defined as the relaxation oscillation frequency and γ as the damping factor. The transfer function, $H(\omega)$, is essentially a second-order low-pass filter with a damped resonance appearing near the cutoff frequency.

The intensity modulation can follow the current modulation up to frequencies near ω_R , with an enhancement in the response existing at the relaxation resonance. After the resonance, the response drops off. The frequency at which the electrical power response drops to half its DC value, $\omega_{3\text{-dB}}$, is known as the modulation bandwidth. To understand how we can maximize the modulation bandwidth, or $\omega_{3\text{-dB}}$, eqn. A.20 and A.21 need to be evaluated

The ω_R and the damping factor from the transfer function eqn. A.19 can be expanded [1]:

$$\omega_R^2 = \frac{av_g N_P}{\tau_p} + \left[\frac{\Gamma a_p v_g N_P}{\tau_{\Delta N}} + \frac{\Gamma \beta_{sp} R_{sp}}{N_P \tau_{\Delta N}} \right] \left(1 - \frac{\tau_{\Delta N}}{\tau'_{\Delta N}} \right) + \frac{1}{\tau'_{\Delta N} \tau_P} \quad \text{A.20}$$

$$\gamma = av_g N_P \left[1 + \frac{\Gamma a_p}{a} \right] + \frac{1}{\tau_{\Delta N}} + \frac{\Gamma \beta_{sp} R_{sp}}{N_P} \quad \text{A.21}$$

Equation A.20 can be simplified for practical cases. For instance, the last term is insignificant compared to the first for $N_p V_p > n_{sp}$ (see equation A.12 and its limit explained above), and hence can be disregarded above threshold where $n_{sp} \sim 1 - 2$ and $N_p V_p \gg 1$. From the remaining terms, two are proportional to N_p , and one is proportional to $1/N_p$. The former dominates above threshold with increase in the photon density. Therefore, the $1/N_p$ term can also be ignored.

Comparing the coefficients of the two proportional terms to N_p , considering $\tau_{\Delta N} \gg \tau_p$ and $a \sim \Gamma a_p$, it can be recognized that $a/\tau_p \gg \Gamma a_p/\tau_{\Delta N}$. Accordingly, the first term dominates over all other terms and ω_R^2 can be broken down to:

$$\omega_R^2 = \frac{av_g N_P}{\tau_p} \quad \text{A.22}$$

As laser performance above threshold is of interest, ω_R is defined using eqn. A.22. This definition of ω_R can also be used to rewrite the damping factor as:

$$\gamma = Kf_R^2 + \gamma_0 \quad \text{A.23}$$

The K-factor describes the damping of the response. The damping factor offset γ_0 becomes more noticeable at low powers where the relaxation resonance frequency is small. K and γ_0 are used as fitting parameters to be extracted from the laser modulation response.

$$K = 4\pi^2\tau_P \left[1 + \frac{\Gamma a_p}{a} \right] \quad \text{A.24}$$

$$\gamma_0 = \frac{1}{\tau_{\Delta N}} + \frac{\Gamma \beta_{sp} R_{sp}}{N_P} \quad \text{A.25}$$

In addition to the K- and the damping factors, the so-called D-factor is another figure of merit. This is also known as the intrinsic modulation factor and quantifies the rate at which the resonance frequency increases with drive current and can be written as:

$$D = \frac{1}{2\pi} \sqrt{\frac{\Gamma a_p v_g N_P}{qV}} = \frac{f_r}{\sqrt{I - I_{th}}} \quad \text{A.26}$$

where I_{th} is the threshold current. D-factor is therefore characterized by plotting f_r as a function of $\sqrt{I - I_{th}}$ and measuring the slope.

The RO peak saturates as injection current increases as explained later-on in the relative intensity noise section. The K- and D-factor characterization is therefore evaluated at current levels just above threshold where RO peaks are most pronounced.

In a QW laser the RO frequency is the dominant limiting factor for a high modulation bandwidth rather than damping factor, however for a QD laser the opposite is true and the damping factor is dominant. The large relaxation oscillation peaks are typical of QW lasers, however due to the higher damping factor for QD lasers the RO response is much flatter and not typically discernable particularly in multi-mode QD lasers.

A.1.4 Equivalent circuit for SSM

The small signal modulation transfer function often contains an additional extrinsic contribution in the form of an extra pole. This is primarily caused by the parasitic capacitance of the laser and by carrier transport effects [2]. For the purpose of relating the impact of the parasitic effect to the small signal modulation transfer function the equivalent electrical circuit model of the laser, which is illustrated in fig A.1, is often approximated by a simple RLC filter. These parasitic effects entail an additional pole with cut-off frequency f_p . This additional term is multiplied by the intrinsic transfer function of the laser, $H(\omega)$, producing the total electrical transfer function:

$$H_{\text{Total}}(\omega) = H(\omega) \cdot H_{\text{parasitic}}(\omega) \quad \text{A.27}$$

Figure 1.10 depicts an equivalent circuit of the laser diode for SSM measurement. circuit is divided into three parts by considering contributions of the bond wire, the package and fixture parasitic, and the intrinsic laser diode. The parasitic from the package and fixture are represented by the inductor and the resistor, L_p R_p , and the capacitors C_{1p} and C_{2p} .

The RF response of the intrinsic laser diode is represented by the capacitor C_i , in parallel with resistor R_i and inductor L_i .

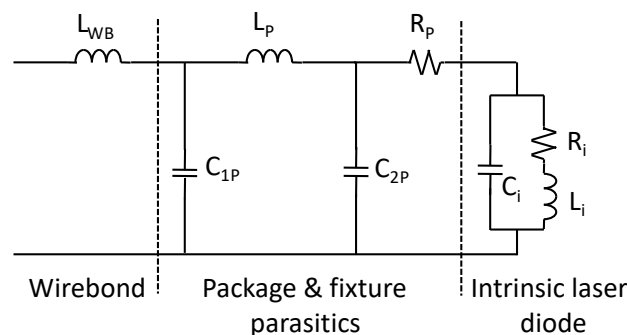


Figure A.1 Equivalent circuit of the laser for SSM considerations.

As the SSM measurements implicitly contain package and bonding responses, these parasitics must then be removed numerically to obtain the correct SSM response.

References

- [1]: L. A. Coldren and S. W. Corzine, "Diode lasers and photonic integrated circuits," 2nd edition, Wiley, 1995
- [2]: R. S. Tucker, "High-speed modulation of semiconductor lasers." IEEE transactions on electron devices, 32(12), 2572-2584, 1985

B.1 Hakki - Paoli Gain and More (Data Analysis) – Matlab Code

As promised in chapter 3, the Matlab code for the extraction of the Hakki-Paoli gain spectra, the spontaneous emission spectra, RMS linewidth, and gain and spontaneous emission full width at half maximum from the raw optical intensity data recorded during measurement is provided here.

```
NC=491; % Number of columns (raw data range)
NP=400; % Number of peaks (fringes)
new_pks=zeros(NP,NC);
new_pks_mw=zeros(NP,NC);
new_waveln=zeros(NP,NC);
new_energy=zeros(NP,NC);
new_val=zeros(NP,NC);
new_val_mw=zeros(NP,NC);
new_val_waveln=zeros(NP,NC);
gamma_i=zeros(NP,NC);
Modal_gain=zeros(NP,NC);
Spon_Emm=zeros(NP,NC);
P_m=zeros(NP,NC);
M_G=zeros(NP,NC);
fwhm=zeros(1,NC);
L=0.0375; % Length of the cavity
R=0.32; % Reflectivity
mode_spacing=0.4; % < free spectral range to resolve all

% For RMS linewidth:

power_mw=10.^(mydata/10);
po=sum(power_mw,1);
lambda_p=bsxfun(@times,wavelength,power_mw);
lambda_c=sum(lambda_p)./po;
D=lambda_c';
```

```

lambdai_lambdac=power_mw.*bsxfun(@minus,
wavelength,reshape(D(:,1,[])).^2);
delta_lambda_rms=sqrt(sum(lambdai_lambdac)./po);

for i=1:NC
    clear pks locs

    [pks,locs]=findpeaks(mydata(:,i),wavelength(),'MinPeakDistance',mode_spacing);

    y= [pks;zeros(NP-length(pks),1)];    % concatenates a new
variable with 000 so matlab won't go nuts
    new_pks(:,i)=y;
    x= [locs;zeros(NP-length(locs),1)];    % concatenates a new
variable with 000 # # # # #
    new_waveln(:,i)=x;

end

for i=1:NC
    clear pks locs
    [pks,locs]=findpeaks(-
mydata(:,i),wavelength(),'MinPeakDistance',mode_spacing);

    y= [pks;zeros(NP-length(pks),1)];    % concatenates a new
variable with 000 # # # # #
    new_val(:,i)=-y;
    x= [locs;zeros(NP-length(locs),1)];    % concatenates a new
variable with 000 # # # # #
    new_val_waveln(:,i)=x;
end
for i=1:NC
    for j=1:NP;

```

```

        if new_pks(j,i)~=0
            new_pks_mw(j,i)= 10^(new_pks(j,i)/10);
            new_energy(j,i)= 1240/new_waveln(j,i);
        end
        if new_val(j,i)~=0
            new_val_mw(j,i)= 10^(new_val(j,i)/10);
        end
    end
end

for i=1:NC
    clear pks locs
    stop_indicator=1;
    j=1;
    while stop_indicator==1
        if new_val_mw(j,i)==0 || new_pks_mw(j+1,i)==0
            stop_indicator=0;
        else
            gamma_i(j,i)=(new_pks_mw(j,i)+new_pks_mw(j+1,i))/2/new_val_mw(
j,i);
            Modal_gain(j,i)=-((1/L)*
log((sqrt(gamma_i(j,i))+1)/(sqrt(gamma_i(j,i))-1))+(1/2/L)*log
(R));

            Spon_Emm(j,i)=(new_pks_mw(j,i)*new_val_mw(j,i))/(0.5*(sqrt(new
_pks_mw(j,i))+sqrt(new_val_mw(j,i))))^2;
            M_G=real(Modal_gain);
            P_m(j,i)=M_G(j,i)/Spon_Emm(j,i);
        end
        j=j+1;
    end
end
end
% for gain spectrum FWHM
for i=1:NC

```

```

half_max = ((max (Spon_Emm(1:375,i)))/2);
check=0;
for j=1:375
    if Spon_Emm(j,i)>half_max && check==0
        index1=j; % saves it
        check=1; % flags it
    end
end
check=0;
for k=1:376;
    if Spon_Emm(377-k,i)>half_max && check==0
        index2=377-k;
        check=1;
    end
end
fwhm(i) = new_waveln(index2,i) -
new_waveln(index1,i);
end

clear x y locs pks i j stop_indicator R L index1 index2
half_max Modal_gain mode_spacing check k NP NC Spon_Emm(j,i) D

```